NOVA SCHOOL OF SCIENCE & TECHNOLOGY

DEPARTAMENT OF MATERIALS SCIENCE

NANOBIOSENSING PLATFORMS WITH SERS AND MIP-BASED TECHNOLOGIES

ANA CAROLINA CARDOSO MARQUES

Master in Biochemistry

DOCTORATE IN NANOTECHNOLOGIES AND NANOSCIENCES

NOVA University Lisbon

November, 2021

NOVA SCHOOL OF SCIENCE & TECHNOLOGY

DEPARTAMENT OF MATERIALS SCIENCE

NANOBIOSENSING PLATFORMS WITH SERS AND MIP-BASED TECHNOLOGIES

ANA CAROLINA CARDOSO MARQUES

Master in Biochemistry

Adviser: Elvira Maria Correia Fortunato
Full Professor, NOVA University Lisbon

Co-advisers: Maria Goreti Ferreira Sales
Associate Professor with Aggregation, University of Coimbra

Bruno Costa-Silva
Doctor, Champalimaud Foundation

Examination Committee:

Chair: Rui Jorge Fernandes Ferreira Santos,
Full Professor, NOVA University Lisbon

Rapporteurs: Thiago Regis Longo César da Paixão,
Associate Professor, University of São Paulo
Tito da Silva Trindade,
Full Professor, University of Aveiro

Adviser: Elvira Maria Correia Fortunato,
Full Professor, NOVA University Lisbon

Members: Eulália Fernanda Alves de Carvalho Pereira,
Associate Professor, University of Porto
Pedro Miguel Cândido Barquinha,
Associate Professor, NOVA University Lisbon
Andreia Cristina Jóia Araújo Cardoso,
Doctor, Imprensa Nacional Casa da Moeda, SA

DOCTORATE IN NANOTECHNOLOGIES AND NANOSCIENCES

NOVA University Lisbon
November, 2021

Nanobiosensing platforms with SERS and MIP-based technologies

Copyright © Ana Carolina Cardoso Marques, NOVA School of Science and Technology, NOVA University Lisbon.

The NOVA School of Science and Technology and the NOVA University Lisbon have the right, perpetual and without geographical boundaries, to file and publish this dissertation through printed copies reproduced on paper or on digital form, or by any other means known or that may be invented, and to disseminate through scientific repositories and admit its copying and distribution for non-commercial, educational or research purposes, as long as credit is given to the author and editor.

Agradecimentos

Em primeiro lugar, quero agradecer à minha orientadora Professora Elvira Fortunato e aos meus coorientadores Professora Goreti Sales e Doutor Bruno Costa-Silva, por me terem permitido realizar este projeto. À Professora Elvira Fortunato por me ter dado sempre todas as condições e mais algumas para a execução deste trabalho e não só, por toda a confiança depositada em mim, por me ter permitido crescer tanto nos últimos anos, por me ter sempre incutido o espírito de resiliência e nunca me ter deixado fraquejar. À Professora Goreti Sales por me ter recebido no seu centro de investigação *Biomark*, mesmo antes do início do doutoramento, pela sua prontidão em ajudar, pelo seu sentido prático e por todas as mensagens de força. Ao Doutor Bruno Costa-Silva, também por me ter recebido no seu grupo de investigação na Fundação Champalimaud, e por sempre responder a todas as minhas dúvidas, mesmo quando não faziam muito sentido.

Ao Professor Rodrigo Martins que, juntamente com a Professora Elvira Fortunato, construiu e impulsionou o que é hoje o CENIMAT&CEMOP, devido à sua incansável dedicação e perseverança.

À Fundação para a Ciência e a Tecnologia por me ter concedido a bolsa de doutoramento (SFRH/BD/115173/2016) que me assegurou estes quatro anos de investigação científica.

Nestes últimos anos tenho tido a imensa sorte de estar rodeada de pessoas com um enorme talento a quem devo muito, e aos quais gostaria de deixar o meu mais sincero agradecimento.

À Alexandra Gonçalves por ser a pessoa maravilhosa que é, por estar sempre disponível para todos os que lhe batem incessantemente à porta do gabinete, por providenciar as melhores condições de trabalho em laboratório do mundo e, acima de tudo, pela amizade dos últimos anos, pela preocupação e por estar sempre presente. À Sónia Pereira por toda a calma que sempre me transmitiu, por todas as conversas e conselhos e pela amizade. À Jóia, pela sua imensa força, por sermos tão diferentes, mas ao mesmo tempo tão iguais e pela sua loucura saudável. Aos restantes marmiteiros: Rita Branquinho, minha *life optimizer*, sempre disponível e com as palavras certas, ao Pedro Barquinha por todas as conversas, bom humor e ensinamentos, à Joana Pinto e à Joana Neto por serem pessoas incansáveis e talentosas e ao João Oliveira pela parvoíce, pela boa-disposição e por todas as conversas e conselhos.

Aos membros da *team* Fortunato, pela constante boa-disposição, entreajuda, companheirismo e pela pontual competição saudável. À Xana, Emanuel Carlos, Sofia Ferreira, Sara Silvestre, Tomás Pinheiro, Maria Morais (Tomás e Maria obrigada por todas as pontas que seguraram principalmente no último

ano!) e João Coelho, o meu muito obrigada. Também à Daniela Gomes e à Ana Pimentel pelos últimos anos, por todos os conselhos, toda a ajuda e pela amizade.

Gostaria também de agradecer à Diana Gaspar, por todas as nossas conversas e piadas subliminares que só nós entendemos e por toda a compreensão e amizade, ao João Resende (o bom filho à casa retorna), pelo seu companheirismo e otimismo e ao Bruno Veigas, por tudo o que me ensinou e pela sua generosidade.

Aos restantes membros e ex-membros do grupo MEON e CENIMAT: Inês Cunha, Beatriz Coelho, Joana Figueira, Paul Grey, Cristina Gaspar, Nuno Ferreira (um obrigada especial), Ricardo Correia, Alexandra Fernandes, Luís Pereira, Hugo Águas, Rui Igreja, Lídia Santos, Adriana Costa (saudades!), minha Samouco, Tomás Calmeiro, Ana Rovisco, Jonas Deuermeier, Tiago Carvalho, Raquel Barras, Sumita Goswami, Raquel Borda d'Água, Ricardo Ferreira, Tiago Mateus, Maria João Oliveira, Guilherme Ribeiro, Pedro Centeno, Tomás Freire, Mariana Matias, Maria Pereira, Cátia Figueiredo, Francisca Andrade, Catarina Martins, Cristina Fernandes, Daniela Salgueiro, aos membros honorários, Pedro Ivo e Neusmar Jr., Andreia Santos, Jenny Boane, Fernanda Carvalho, Marta Corvo e, a todos os restantes! O meu muito, muito obrigada a todos – sou uma sortuda por, nos últimos anos, poder conviver e trabalhar com pessoas tão extraordinárias!

Não posso também deixar por agradecer ao secretariado e à gestão pela prontidão em ajudar: Susana Mendes, Paulo Manteigas, Luís Milhano, Valéria Gomes, Lúcia Mendes e Mafalda Gonçalves – obrigada!

A todos os membros do *Biomark* que direta ou indiretamente participaram neste trabalho, em particular à Rita Cardoso, por toda a colaboração nos últimos anos, pela sua hiperatividade científica, e pela imensa disponibilidade. Quero também agradecer à Gabriela Martins e à Akmaral Suleimenova pelos nossos *side projects*.

Aos membros do *Systems Oncology Group* da Fundação Champalimaud, em particular à Joana Maia, Ana Gregório e Cristian Bodo, por toda a sua ajuda e paciência a introduzirem-me em práticas laboratoriais até então desconhecidas por mim, pela sua boa-disposição e por me terem recebido sempre tão bem.

À Diana, ao Mauro e ao Duarte pelos anos de amizade, festinhas, noitadas, pelas melhores horas de tédio da minha vida, mas, acima de tudo, por estarem sempre, sempre disponíveis mesmo quando não estão presentes e mesmo que as correrias da vida não nos permitam estar tão juntos como no passado.

A todas as amizades feitas nesta vida académica - tive a sorte de conhecer pessoas extraordinárias e maravilhosas.

Ao Sérgio, pelo seu amor, pela sua amizade incondicional, por ser o melhor companheiro para todas as horas, pela sua paciência em aceder a quase todos os meus caprichos nestes últimos treze anos! Seguimos juntos, sempre – e mal posso esperar para descobrir o que mais o futuro nos reserva. À minha família emprestada que agora é minha também (Ana e Pedro Filipe!, Vasco, Giulia, Matteo e Kevin, Isabel, Fernando, Joana, Rodrigo, Sarinha e Johnny e Lai), por nestes últimos anos me fazerem sentir sempre em casa, por todo o seu apoio constante, por tudo o que me ensinaram e, por participarem de todas as minhas alegrias e tristezas.

Aos meus pais, pela educação que me deram, por terem sempre apoiado todas as minhas vontades, mesmo quando não as compreendiam, por me terem permitido ser a pessoa que sou hoje e, chegar onde cheguei, mesmo com todos os sacrifícios e mesmo que isso tenha implicado construir uma vida longe deles. Ao meu irmão pela sua presença e apoio e por todas as alegrias que me dá com a recente alargada família. A toda a restante imensa família, tios, primos e afins, por todas as alegrias, todas as festividades, por todo o amor e pelo companheirismo.

Gostaria de terminar com um beijinho especial para a minha Tia Dulcinha, de quem tenho imensas saudades e de agradecer às minhas avós Preciosa e Altina que, apesar de já não estarem presentes, terem sido mulheres tão fortes e que me passaram valores tão importantes como a generosidade, empatia pelo próximo e humildade. Trago-vos sempre no coração.

"The role of the infinitely small in nature is infinitely great."

- Louis Pasteur

"Begin at the beginning," the King said gravely, "and go on till you come to the end: then stop."

- Lewis Carroll*, Alice in Wonderland*

Resumo

O desenvolvimento de dispositivos analíticos precisos, fiáveis e de baixo-custo é da maior relevância para várias indústrias, desde o diagnóstico médico ao rastreio ambiental. A elevada presença de sistemas de transdução eletroquímicos seguidos dos óticos no mercado dos biossensores deve-se à sua meritória capacidade de oferecer elevada seletividade e sensibilidade, facilidade de fabrico e manuseamento, fácil miniaturização, baixo-custo e versatilidade. Este trabalho centra-se no desenvolvimento de biossensores óticos e eletroquímicos, procurando alternativas ao uso de bioreceptores de origem natural aliado ao uso de técnicas de micro- e nanofabricação que sejam versáteis e de baixo-custo. Como biossensores óticos, foram produzidas plataformas SERS (do inglês *Surface-Enhanced Raman Spectroscopy*) em substratos de celulose, incorporando nanoestruturas capazes de intensificar o sinal de Raman, produzidas tanto por métodos físicos como químicos. Particularmente, seguindo a via química, a superioridade dos substratos de nanocelulose, em ajudar na intensificação do efeito de Raman, em relação a outros tipos de materiais celulósicos foi demonstrada. As plataformas SERS produzidas foram usadas para a deteção do antibiótico tetraciclina, de exossomas de linhas celulares tumorais do cancro da mama e da proteína *spike* do vírus SARS-CoV-2, sem usar bioreceptores de origem natural. O potencial para quantificar e/ou qualificar amostras complexas por espectroscopia de Raman combinado com ferramentas de análise de dados foi demonstrada com sucesso. Como biossensores eletroquímicos, elétrodos de grafeno induzidos por laser (LIG, do inglês *Laser-induced Graphene*) foram produzidos em substratos de poli-imida, sem necessitar de máscaras, e usados como plataforma para a eletropolimerização de materiais biomiméticos, pela tecnologia de impressão molecular polimérica. Em primeiro lugar, os elétrodos LIG foram totalmente otimizados e caraterizados e o seu desempenho eletroquímico foi comparado favoravelmente com elétrodos comerciais impressos por serigrafia. Os polímeros preparados por impressão molecular foram utilizados para a deteção e quantificação do antibiótico cloranfenicol, obtendo um limite de deteção ao nível nanomolar. Finalmente, para mostrar a liberdade de conceção providenciada pelo método escolhido para a produção dos elétrodos, foi também fabricado um sistema de deteção dupla, usado com sucesso para a deteção simultânea de dois compostos químicos (ácido ascórbico e amoxicilina). Os conceitos de biodeteção explorados neste trabalho abrem caminho para o desenvolvimento de dispositivos analíticos robustos e sem bioreceptores de origem natural, com potencial para serem integrados em plataformas multifuncionais autónomas para serem utilizados no ponto-de-tratamento.

Palavras-chave: biossensores; deteção ótica; deteção eletroquímica; espectroscopia de Raman; polímeros de impressão molecular; grafeno induzido por laser

Abstract

The development of accurate, reliable, and inexpensive analytical platforms is of utmost relevance to several industries from clinical diagnosis to environmental screening. The ubiquitous presence of electrochemical followed by optical transduction mechanisms in the biosensor's market is due to their meritorious ability to offer high selectivity and sensitivity, ease of fabrication and usage, easy miniaturization, low-cost and versatility. The present thesis focuses on the development of nanobiosensing platforms with both optical and electrochemical mechanisms, while seeking for alternatives to natural bioreceptors and by employing low-cost and versatile micro- and nanofabrication tools. As optical biosensors, cellulose-based Surface-Enhanced Raman Spectroscopy (SERS) platforms were produced following both physical and chemical routes for the synthesis of Raman enhancement nanostructures. Particularly, following the chemical route, the superiority of nanocellulose substrates, as support for Raman active layers, over other types of cellulosic materials is demonstrated with the enhanced Raman signals. The resultant SERS platforms were used for the label-free screening of the antibiotic tetracycline (TET), exosomes from breast cancer tumoral cell lines and spike protein from SARS-CoV-2 virus. The potential for quantification and/or qualification of complex samples through Raman spectroscopy combined with multivariate analytical tools was successfully demonstrated. As electrochemical biosensors, laser-induced graphene (LIG) electrodes were generated onto polyimide substrates, in a mask-less approach, and used as the platform for the electropolymerization of biomimetic materials using molecular imprinting technology. Firstly, the LIG electrodes were fully optimized and characterized and their electrochemical performance was compared favourably with commercial screen-printed electrodes. The prepared molecularly imprinted polymers (MIPs) were used for the detection and quantification of the antibiotic chloramphenicol (CAP), attaining a limit of detection down to the nanomolar level. Finally, to showcase the freedom-of-design enable by the chosen method for electrode's patterning, a dual sensing system was fabricated and effectively used for the simultaneous detection of two different chemical compounds (ascorbic acid and amoxicillin). The biosensing concepts explored herein paves the way towards the development of robust analytical devices without relying on natural bioreceptors, with potential to be integrated in stand-alone multifunctional platforms to be used in point-of-care (POC) settings.

Keywords: biosensors; optical detection; electrochemical detection; surface-enhanced Raman spectroscopy; molecularly imprinted polymers; laser-induced graphene

Table of contents

Chapter 1. Motivation and aim of the thesis 2

1.1 Scientific context 2

1.2 Objectives 4

1.3 Thesis outline 5

Chapter 2. Introduction 9

2.1 Nanobiosensing platforms 9

2.1.1 Nanotechnology and nanomaterials 9

2.1.2 Biosensors 11

2.2 Optical detection 13

2.2.1 Surface-Enhanced Raman Spectroscopy 14

2.3 Electrochemical detection 31

2.3.1 Molecularly imprinted polymer's technology for biomimetic material's fabrication 31

2.3.2 Electrochemical readout 35

2.3.3 Laser-induced graphene as an alternative for electrode's patterning 41

Chapter 3. Materials and devices: fabrication and characterization 57

3.1 Cellulose-based SERS platforms 57

3.1.1 Cellulose-based substrates preparation 57

3.1.2 SERS platforms produced by physical processes 59

3.1.3 SERS platforms produced by chemical processes 59

3.1.4 SERS performance evaluation: Enhancement factor calculation 62

3.1.5 Applications of the prepared cellulose-based SERS platforms 62

3.2 LIG-based MIP platforms 65

3.2.1 Electrode's fabrication – LIG optimization 65

3.2.2 Biosensing element: fabrication and evaluation 66

Chapter 4. Cellulose-based platforms for SERS applications 73

4.1 SERS platforms produced through physical processes 73

4.1.1 Thermal evaporation of AgNPs on Tetra Pak® substrate for tetracycline screening on milk 74
4.2 SERS platforms produced through chemical processes 81
4.2.1 Nanocellulose membranes: preparation and characterization 83
4.2.2 Microwave-assisted synthesized AgNPs on nanocellulose substrates for breast cancer diagnosis 85
4.2.3 Microwave-assisted synthesized AuNPs on nanocellulose substrates for SARS-CoV-2 diagnosis 91
Chapter 5. LIG-based platforms for MIP applications 111
5.1 LIG electrodes: optimization and fabrication 111
5.2 Implementation of LIG electrodes for MIP-based electrochemical biosensors 120
5.2.1 MIPs for chloramphenicol screening 120
5.2.2 MIPs for dual-detection of amoxicillin and ascorbic acid 131
Chapter 6. Conclusions and future perspectives 147
6.1 Conclusions 147
6.1.1 SERS-based nanobiosensing platforms 147
6.1.2 MIP-based nanobiosensing platforms 150
6.1.3 Comparison of the developed nanobiosensing platforms with commercially available devices 151
6.2 Future work and perspectives 152
Chapter 7. Scientific outputs 157
7.1 Publications 157
7.1.1 Peer-reviewed publications: 157
7.1.2 Invited chapter books: 158
7.2 Oral and poster presentations 161
7.2.1 Oral presentations 161
7.2.2 Poster presentations 161
7.3 Participation in international and national research projects 162
7.4 Courses 162

7.5 Awards 162

7.6 Master thesis guidance 162

7.7 Tutoring of Master practical/lab classes 164

Annex section 165

References 181

List of figures

Figure 1.1 North America biosensors market growth by application. Values in USD million. Adopted from Grand View Research – biosensors market, 2020.[6] 2

Figure 1.2 Results from Web of Science Core Collection for the keywords 'biosensor' AND 'transduction method' (electrochemical, optical, thermal, acoustic, and gravimetric) showing the distribution of publications in the period of 2011 to 2021. Total number of articles: 22,325; Total number of reviews: 2,500. Data retrieved from Web of Science database (September 2021). 3

Figure 2.1 Timeline of some of the nanoscience and nanotechnology findings and achievements. 9

Figure 2.2 Top-down and bottom-up approaches for nanomaterial's production: most common fabrication methods employed in each approach. Adapted from Bayda, S., et al, 2020.[14] 10

Figure 2.3 Schematic representation of the components of a generic biosensor: the bioanalytes present in the sample react with the bioreceptor layer (e.g. enzyme, nucleic acids, antibody, microorganism, tissue, MIPs, etc.) directly attached to a transducer mechanism that transforms the physico-chemical interaction of the bioreceptor with the bioanalyte into a measurable signal. Adopted from Águas, H., et al, 2021.[24] 11

Figure 2.4 Sir Chandrasekhara Venkata Raman photograph, front page of his Inaugural Address detailing the Raman effect and relevant figures. Adapted from Raman, C.V., 1928.[60] 15

Figure 2.5 Schematic representation of the experiment that led to the finding of the Raman effect. 15

Figure 2.6 Energy level diagram for Rayleigh and Raman scattering, where $\Delta E = h\nu_{vib}$ represents the difference in vibration energy levels. Adopted from Kumar, S., et al, 2020.[64] 16

Figure 2.7 Number of publications per year since the first report of Raman enhancement. Insets of Martin Fleischmann photograph and the figure relative to the electrochemical cell used for Raman experiments, in 1974.[69] Data retrieved from Web of Science database (September 2021), with the keyword 'SERS'. 17

Figure 2.8 Mechanisms of chemical enhancement in SERS. *E* represents the local electromagnetic field, ω is the excitation frequency and E_f is the Fermi level for metal. HOMO is the highest occupied molecular orbital and LUMO is the lowest occupied molecular orbital. Adopted from Fateixa, S. et al, 2015.[57] 18

Figure 2.9 Schematic representation of Localized Surface Plasmon Resonance: The excitation of a LSPR in nanoparticles confines the light energy into sub-wavelength volume, leading to strongly enhanced local electromagnetic field. Adopted from Cecchet, F., et al, 2014.[77] 18

Figure 2.10 Historical timeline of important landmarks that contributed to the evolution of Raman and Surface-Enhanced Raman spectroscopy. 19

Figure 2.11 Number of publications per year of cellulose-based SERS devices. Inset of percentage distribution of the type of enhancement nanostructure utilized on paper and cellulose-based SERS devices in the last 10 years. Data retrieve from Web of Science database (September 2021), with the keywords: 'SERS' AND 'Paper' and 'SERS' AND 'Cellulose'. 21

Figure 2.12 Infographic with some of the most common production and transference techniques employed on the production of cellulose-based SERS substrates. 22

Figure 2.13 Healthcare applications – diagnostic and therapeutic: a) AuNR-paper for the detection of cancer cell trough an immunomagnetic assay and resultant SERS spectra of HT-29 cells, fibroblast and RBCs; b) Schematic workflow for the preparation of SERS probe for cardiac biomarkers detection and PCA-kNN prediction; c) Schematic procedure of a vertical-flow paper SERS device for screening of an anti-cancer drug and calibrations curve in water and serum. Adapted from Reokrungruang, P. et al, 2019,[117] Lim, W. et al, 2020[122] and Berger, A. et al, 2017.[123] 24

Figure 2.14 Environmental applications: a) Schematic illustration of the CNF-AuNR SERS platform, its photograph and respective SEM image and SERS spectra for the simultaneous detection of pesticides; b) Schematic workflow to produce the paper-based Au/AgNPs, SEM image and representative concentration-dependent SERS spectra with correspondent calibration curve. Adapted from Kwon, G. et al, 2019[144] and Yang, G. et al, 2020.[145] 27

Figure 2.15 Number of MIP-based sensors publications per year since the first repot on imprinted polymers in sensors, in 1992. Data retrieved from Web of Science database (September 2021) with the keywords: 'molecular* imprint*' AND 'sensor'. 32

Figure 2.16 Basic mechanism of thiophene electropolymerization. Adapted from Sharma, 2012.[180] 34

Figure 2.17 General procedure for molecular imprinting and non-imprinting processes: the chosen monomer and desired template are mixed in solution at a specified ratio. Electropolymerization is then performed, forming a layer comprised of the polymer with the trapped target on the surface of the transducer. The template is subsequently removed from the polymeric matrix. When the target is re-

introduced into the system, it binds to the cavities present in the MIP film, producing a measurable change. The non-imprinted polymer, is used as negative control and it is produced with the same approach but without adding the template, thus the imprinted cavities are not created not allowing target identification (represented with an X). 35

Figure 2.18 Healthcare applications – diagnostic and therapeutic: a) dual biorecognition MIP-SERS sensor for CEA screening; b) myoglobin and c) cTnT detection for cardiovascular disease's diagnosis; d) paper-based MIP sensor for 3-nitrotyrosine oxidative stress biomarker detection. Adapted from Carneiro, M. C. C. G. et al, 2019,[192] Ribeiro, J. A. et al, 2017,[193] Phonklam, K., et al, 2020[194] and Martins, G. V. et al, 2020.[195] 37

Figure 2.19 Environmental applications – food, dairy products, and water safety: a) lactose screening on milk samples; b) detection of estradiol hormone in eel serum samples. Adapted from da Silva, J. L. et al, 2021,[205] and Lee, M.-, H. et al, 2020.[206] 40

Figure 2.20 Materials and equipment for LIG fabrication from PI substrates by LDW: a) Schematic of the synthesis process of LIG from PI; b) photographs of the polyimide sheet, commercially known as Kapton, and the laser cutting system used by the authors; c) photographs of LIG as an owl and the letter R patterned on PI substrates. The black features are LIG, and the orange background is polyimide. Scale bar, 5 mm. Adapted from Lin, J., et al, 2014.[217] 43

Figure 2.21 Chemical structure of polyimide. 44

Figure 2.22 LIG characterization: a) Atomic percentages of carbon, oxygen and nitrogen as a function of laser power obtained with high-resolution XPS; b) SEM image of the LIG film; c) TEM image of LIG showing the heptagon with two pentagons, as well as a hexagon; d) Representative Raman spectrum of a LIG film and the starting PI film; e) XRD of powdered LIG scraped from the PI film and PI; f) Correlations of the sheet resistance and LIG film thicknesses with laser powers. Adapted from Lin, J. et al, 2014.[217] 45

Figure 2.23 Proposed scheme for roll-to-roll production of LIG films and functional LIG-based devices. Adopted from Ye, R., et al, 2018.[212] 46

Figure 2.24 Schematic representation of workflows to produce PI-derived LIG applications fabricated with an IR laser: a) electrochemical glucose sensor; b) pseudocapacitive microsupercapacitor; c) stackable supercapacitor; d) UV sensor with ZnO nanoparticles as the sensitive layer. Adapted from Tehrani, F., et al, 2016[224], Li, L, et al, 2016[225], Peng, Z., et al, 2015[227] and Samouco, A, et al, 2018[232]..... 47

Figure 2.25 LIG-based biosensors for glucose levels assessment: a) Schematic illustration of the produced of the Co_3O_4NPs-LIG biosensor, from a PI substrate coated with a $CoCl_2$/poly(amic acid) ink, and respective amperometric response of Co_3O_4NPs-LIG biosensors to various concentrations of glucose at an applied potential of +0.55 V with the correspondent calibration curve; b) Schematic procedures for the fabrication of LIG from Whatman paper for glucose quantification by chronoamperometry with the correspondent calibration curve. Adapted from Zhao, J., et al, 2021[245] and Pinheiro, T., et al, 2021.[236] 49

Figure 2.26 LIG-based biosensors for pathogen detection: a) Schematic illustration of the fabrication process of the AuNPs-LIG interdigitated array for the detection of *E. coli* O157:H7, with the respective photograph of the prepared the AuNPs-LIG biosensor, and the Nyquist plots obtained with AuNPs-LIG electrode (black line), antibody modification (red line), BSA blocking (blue line), and bacteria capture (purple line); b) Schematic illustration of the workflow for the fabrication of the LIG-based immunosensor for *S. enterica* detection. Adopted from You, Z., et al, 2020[250] and Soares, R., et al, 2020.[251] 51

Figure 2.27 Schematic representation of the fabrication process of LIG onto PI and transference to PDMS, and respective functionalization, and photographs and electrochemical results of in-situ analysis of methyl parathion on the surface of different agricultural products (spinach and apple). Adapted from Zhao, F., 2020.[255] 52

Figure 2.28 Schematic representation of the procedures for the fabrication and utilization of a MIP-based biosensor with LIG electrodes patterned onto a PI film, for the electrochemical detection of a cancer biomarker (Her-2). Adopted from Lahcen, A., 2021.[265] 53

Figure 3.1 a) Illustration of the composition of the cardboard substrates used. Adopted from Pimentel, A., et al, 2017[266]; b) Photographs of the cardboard substrate used. 58

Figure 3.2 Schematic representation of the workflow to obtain nanocellulose membranes and photograph of the resulting membrane. 58

Figure 3.3 Schematic representation of the optimized procedure to prepare NC@AgNPs SERS platforms. 60

Figure 3.4 Schematic representation of the optimized procedure to prepare NC_{inc}@AuNPs SERS platforms. 61

Figure 3.5 a) CO_2 laser cutting machine available at CENIMAT|i3N; b) Schematic representation of the laser setup. Adopted from Samouco, A., et al, 2017.[269] 65

Figure 3.6 Schematic representation of the architecture of the produced devices for both single and dual detection. 66

Figure 3.7 Switch box fabricated at CENIMAT|i3N to interface the dual detection LIG devices with the potentiostat. 67

Figure 4.1 Morphological characterization of the TP@AgNPs SERS platform: a) SEM image. The histogram for the size particle distribution is presented in the inset image; b) AFM imaging. 75

Figure 4.2 SERS measurements of TET: a) Optical photograph of the platform with milk spiked TET measurement set up. The zoom in shows a schematic representation of a single measurement; b) SERS spectra of 500 ppm TET aqueous solution showing TET characteristic peaks. The inset shows the TET hydrochloride molecule with positional number of carbon atoms; c) SERS spectra of milk (bottom) and 500 ppm TET spiked milk (top) showing its characteristic peaks. 76

Figure 4.3 TET spiked milk statistical analysis: Principal component analysis of TET detection and quantification in TP@AgNPs substrate. The two eigenvectors PC1 & PC2 accounting for 96.17% of total variance in the data set. 78

Figure 4.4 TET spiked milk statistical analysis: a) Correlation between the eigenvector PC1 variance and TET concentration. A linear correlation between the variance of the vector PC1 and TET concentration is observed for concentration values above 100 ppm; b) Correlation between the eigenvector PC2 variance and TET concentration. A linear correlation ($R^2 = 0.9153$) between the variance of the vector PC2 and TET concentration is observed for lower concentrations (0-100 ppm). Each point corresponds to the mean value and error bars to the standard deviation of three independent measurements. 78

Figure 4.5 Combinations of peak ratios and their correlation to the concentration of the analyte. **Grey (■)**: No correlation between ratio intensity and analyte concentration was found; **Red (■)**: Correlation between ratio intensity and analyte concentration was found above 100 ppm; **Yellow (■):** Correlation between ratio intensity and analyte concentration was found above 1 ppm; **Green (■):** Correlation between ratio intensity and analyte concentration was found above 0.01 ppm. 79

Figure 4.6 Dependence of SERS signal intensity ratio and TET concentration: a) Correlation between ratio 455 cm^{-1}/1280 cm^{-1} versus analyte concentration in logarithmic scale; b) Correlation between ratio

1322 cm^{-1}/1669 cm^{-1} versus analyte concentration in logarithmic scale; c) Correlation between ratio 874 cm^{-1}/1397 cm^{-1} versus analyte concentration in logarithmic scale. Diamond marker shows the ratio values obtained for milk samples without TET and grey shade the error (standard deviation). Each point in the final calibration curve corresponded to the mean value and the error bars to the standard deviation of three independent measurements. 80

Figure 4.7 NC membranes characterization: a) FTIR spectra comparison between reference BNC and washed *nata de coco* membrane; b) XRD diffractogram of washed *nata de coco* membranes. Diffraction peaks are identified with the respective crystallographic plane; c) Chemical structure of cellulose. 83

Figure 4.8 SEM and AFM morphological characterization of NC and BNC membranes: SEM imaging of a) NC and b) BNC membranes; c) and d) AFM scanning of NC membrane: 2D 5 μm^2 and 1.5 μm^2 scan. 84

Figure 4.9 SEM and AFM imaging of NC@AgNPs membranes synthesized with ammonium citrate, with different synthesis' parameters: a) 10 mM 10 min 100 °C; b) 10 mM 30 min 100 °C; c) 10 mM 10 min 120 °C. d) 10 mM 30min 120 °C; e) 100 mM 10 min 120 °C; f) AFM imaging of the NC@AgNPs membrane produced with 100 mM 10 min 120 °C; Insets: respective AgNPs size distribution and calculated average diameter. 86

Figure 4.10 EDS mapping of NC@AgNPs membranes synthesized with ammonium citrate, with different synthesis' parameters: a) 10 mM 10 min 100 °C; b) 10 mM 30 min 100 °C; c) 10 mM 10 min 120 °C. d) 10 mM 30min 120 °C; e) 100 mM 10 min 120 °C; f) EDS spectrum of the NC@AgNPs membrane produced with 100 mM 10 min 120 °C. All EDS images were treated equally in terms of contrast and brightness adjustment. 87

Figure 4.11 Diffractogram of the optimized NC@AgNPs membrane showing the characteristic AgNPs diffraction peaks. 88

Figure 4.12 SERS spectra of R6G deposited on the NC@AgNPs membranes: a) average of R6G SERS spectra (n=3) with different concentrations: from 10^{-6} M to 10^{-10} M with 633 nm laser and 10^{-11} M to 10^{-12} M with 532 nm laser; b) R6G 10^{-6} M SERS spectra displaying SERS platform reproducibility (n=20). 88

Figure 4.13 Nanoparticle tracking analysis, performed with NanoSight® NS300, of exosomes originated from cell lineages: a) MCF-10A (non-tumoral mammary gland) and b) MDA-MB-231 (breast cancer). The curves represent the average of 5 independent measurements and the respective standard

deviation. Insets show the concentration in particles/ml and the exosome's average size; c) AFM and d) SEM images of exosomes from cell line MCF-10A..... 89

Figure 4.14 Exosomes profiling using MCF-10A (non-tumoral, n=18) and MDA-MB-231 (tumoral, n=20) exosomes through SERS data analysis using PCA: a) PCA resultant score plot using PC1 and PC2 as the analysed principal components, with 95% confidence ellipses; b) Average PBS, MCF-10A exosomes and MDA-MB-231 exosomes SERS spectra: spectra peaks with most variance between groups highlighted..... 90

Figure 4.15 UV-Vis optical properties of synthesized AuNPs through D-glucose reduction, at room temperature, activated with an alkaline medium. The syntheses were repeated two times and the corresponding UV-Vis curves are represented separately..... 92

Figure 4.16 Optical properties of the synthesized gold nanoparticles at different concentrations of precursor and reducing agents: a) UV-Vis average spectra (n=3) of citrate-based gold nanoparticles; b) UV-Vis average spectra (n=3) of glucose-based gold nanoparticles; c) Representative TEM image of citrate-based gold nanoparticles; d) Representative TEM image of glucose-based gold nanoparticles.92

Figure 4.17 Analytical features calculated from the UV-Vis spectra of the synthesized AuNPs, by microwave irradiation, with citrate and glucose as reducing agents: a) SPR values as dependent of reactant's concentration; b) Bubble graph representation of AuNPs' diameter calculated by DLS. Absolute values for the present graph representation are presented in Table 4.2. 94

Figure 4.18 Stability evaluation of the synthesized AuNPs after 3 months of storage at 4 ºC: a) citrate-based AuNPs colloidal solutions photographs and calculated maximum absorbances; b) glucose-based AuNPs colloidal solutions photographs and calculated maximum absorbances. The percentage values represent the drop in the maximum absorbance value after 3 months of storage. 96

Figure 4.19 In-situ synthesis of gold nanoparticles onto nanocellulose membranes via seed and seedless-mediated growth methods: SEM images and photographs of the resultant membranes. Direct comparison of the membranes with and without the 30 min incubation step. 97

Figure 4.20 a) XRD diffractogram for the NC membrane with and without grown AuNPs on its fibres after each reaction cycle without and with the incubation step; b) and c) XPS analysis of the optimized NC_{inc}@AuNPs SERS platform..... 99

Figure 4.21 SEM image and optical photograph of glucose-based NC membrane with grown AuNPs with the optimized conditions for citrate-based synthesis. 100

Figure 4.22 Pictures of resulting membranes produced with the optimized method: right (office paper) and left (cardboard substrate). 101

Figure 4.23 In-situ synthesis of gold nanoparticles onto Whatman paper via a seed-mediated growth method, with a 30 min incubation step: SEM images and photographs of the resultant WP_{inc}@AuNPs. 101

Figure 4.24 Histograms of size distribution of AuNPs after 1st and 2nd cycle of microwave irradiation for nanocellulose and Whatman paper. 102

Figure 4.25 SERS performance evaluation of the prepared membranes: a) R6G SERS spectra obtained with SERS substrates after each reaction cycle, with and without the incubation step; b) R6G SERS spectra obtained with the SERS substrates by the seed and seedless-mediated growth methods; c) R6G SERS spectra obtained with the optimized SERS membranes with nanocellulose and Whatman paper substrate produced after each reaction cycle. 103

Figure 4.26 As-optimized SERS membrane performance: a) Comparison between R6G average SERS spectra (n=5) recorded on SERS membranes prepared with the optimized method and with a 24 h immersion method; b) Comparison between R6G average SERS spectra (n=5) recorded on SERS membranes prepared with the optimized method and on a glass substrate; c) R6G average SERS spectra (n = 5) obtained in the optimized NC_{inc}@AuNPs membrane after production, 3 and 7 months. 105

Figure 4.27 SEM images of NC membrane prepared with AuNPs via a 24h immersion method (NC_{24h}@AuNPs) and glass substrate with drop-casted AuNPs (Glass@AuNPs). 106

Figure 4.28 SERS spectra of S protein on the optimized SERS membranes. The grey area represents the average spectra (n=3). 107

Figure 5.1 Schematic of the LIG formation: the topmost layers of the substrate turn into LIG whereas the bottom part remains pristine and can act as mechanical support. 111

Figure 5.2 Optimization matrix for LIG formation by laser irradiation of PI substrates, with representative pictures. 112

Figure 5.3 SEM images of LIG produced by laser-induced conversion of PI at 25 W and 1.14 m/s: profile view (left panel) and top view (right panel). 112

Figure 5.4 Profile SEM images of LIG produced with increasing laser powers at 1.14 m/s scanning rate. 113

Figure 5.5 Chemical and structural characterization of PI and LIG produced at 25 W and 1.14 m/s: a) Raman spectra of LIG and PI; b) Diffractograms of LIG and PI. 113

Figure 5.6 Sheet resistance calculated, by Hall effect, for the LIG samples produced with a CO_2 infrared laser. 115

Figure 5.7 LIG patterned in polyimide substrates: a) optical photographs showing detail on the horizontal scribing of LIG; b) optical photograph showcasing the flexibility of the technique to pattern different architectures with high resolution. 116

Figure 5.8 Plot of the three different outcomes observed for different laser power and speed regions. 117

Figure 5.9 Characterization of LIG in PI: a) Sheet resistance as a function of the laser power for different laser speeds; b) Raman spectra of LIG in PI as a function of the laser power; c) I_D/I_G ratio calculated from Raman spectra for LIG produced at different laser powers and with a laser speed of 0.14 m/s; d) Evolution of carbon and oxygen content (wt%), calculated by EDS quantification, for LIG produced at different laser powers and with a laser speed of 0.14 m/s. 118

Figure 5.10 Schematic representation of the workflow employed on the production of the LIG electrodes (top) and the MIP fabrication (bottom) for the electrochemical CAP biosensor: Electrodeposition of EDOT with subsequent formation of poly(EDOT) followed by amination, electropolymerization of EBT, in the presence of CAP (MIP) or without CAP (NIP) and finally template removal. 121

Figure 5.11 Eriochrome black T chemical structure: nitro, sulfonic and hydroxyl functional groups. 121

Figure 5.12 Electrochemical characterization of commercial SPEs (C-SPE and G-SPE) and LIG-based device after cleaning, PEDOT electropolymerization and MIP formation: a) Cyclic voltammograms from -0.3 to 0.7 V at a scan rate of 50 mV/s; b) Nyquist plots obtained from EIS measurements at an open circuit potential. Indirect readings performed with the redox probe 5.0×10^{-3} M $[Fe(CN)_6]^{3-/4-}$ prepared in ACN buffer. 123

Figure 5.13 Direct comparison of the pre-treated C-SPE, G-SPE and LIG electrodes after the pre-treatment: a) Voltammograms and b) Nyquist plots. Indirect readings performed with the redox probe 5.0×10^{-3} M $[Fe(CN)_6]^{3-/4-}$ prepared in ACN buffer. 123

Figure 5.14 Comparison of the analytical features of C-SPE, G-SPE and LIG electrodes, followed by cyclic voltammetry (scan window from -0.3 to +0.7 V at 50 mV/s), after MIP and NIP fabrication and respective template removal. Indirect readings performed with the redox probe 5.0 x 10^{-3} M $[Fe(CN)_6]^{3-/4-}$ prepared in ACN buffer. 125

Figure 5.15 Analytical performance of the MIP-based C-SPE, G-SPE and LIG electrodes with increasing concentrations of CAP: a) Nyquist plots and b) respective calibration curve. Indirect readings performed with the redox probe 5.0 x 10^{-3} M $[Fe(CN)_6]^{3-/4-}$ prepared in ACN buffer. 127

Figure 5.16 Analytical performance of the NIP-based C-SPE, G-SPE and LIG electrodes with increasing concentrations of CAP: a) Nyquist plots and b) respective calibration curve. Indirect readings were performed with the redox pair 5.0 × 10^{-3} M $[Fe(CN)_6]^{3-}$ and 5.0 × 10^{-3} M $[Fe(CN)_6]^{4-}$ 128

Figure 5.17 Selectivity studies of the biosensor LIG-CAP against OTC, AMC and SDZ: a) Nyquist plots and b) respective *Rct* values and calculated RSD values. All solutions were prepared with equal concentrations of 1.00×10^{-6} M and incubated 20 min in the sensing surface. 129

Figure 5.18 Optimization of the dual-LIG devices architectures, to find the one with the required features as: small size, equal distance of the WE to the CE and with a CE with high surface area. The colour black represents the LIG material and colour grey represents silver ink. A picture of final device is presented on the right side. 131

Figure 5.19 Schematic representation the dual-LIG device and MIPs fabrication workflow: AMOX MIP fabrication comprises PEDOT electrodeposition and amination steps followed by electropolymerization around AMOX molecules and template removal; AA MIP fabrication comprises the electropolymerization step around AA molecules and template removal. 132

Figure 5.20 CV measurements of the as-produced LIG devices (8.5 W at 0.14 m/s), after pre-treatment and EDOT electropolymerization. Indirect readings performed with the redox probe 5.0 x 10^{-3} M $[Fe(CN)_6]^{3-/4-}$ prepared in ACN buffer, performed from -0.3 to +0.4 V, at 50 mV/s 133

Figure 5.21 Fabrication workflow for the AMOX MIP fabrication followed by cyclic voltammetry: a) comparison between MIP and NIP; b after template removal from MIP; c) after template removal from NIP. Indirect readings performed with the redox probe 5.0 x 10^{-3} M $[Fe(CN)_6]^{3-/4-}$ prepared in ACN buffer, performed from -0.3 to +0.4 V, at 50 mV/s. 135

Figure 5.22 Raman spectroscopy analysis of the electrode surface following each chemical modification for the fabrication of the AMOX MIP. The MIP and template removal spectra are multiplied by 10-fold to better highlight the peak's intensity changes. 136

Figure 5.23 AMOX MIP analytical performance: a) SWV measurements in MIP devices with the b) corresponding calibration curves, of standard solutions of AMOX with increasing concentrations, prepared in $LiClO_4$ electrolyte; c) SWV measurements in NIP devices with the b) corresponding calibration curves, of standard solutions of AMOX with increasing concentrations, prepared in $LiClO_4$ electrolyte. Indirect readings performed with the redox probe 5.0×10^{-3} M $[Fe(CN)_6]^{3-/4-}$ prepared in ACN buffer. 137

Figure 5.24 Pyrrole electropolymerization by cyclic voltammetry: a) AA MIP fabrication; b) AA NIP. 139

Figure 5.25 AA MIP analytical performance: a) SWV measurements in AA MIP film with increasing concentrations of AA and b) corresponding calibration curve. 140

Figure 5.26 Cyclic voltammograms showing the peak separation of both molecules in a) single and b) binary solutions..... 141

Figure 5.27 Analytical performance of the developed dual-LIG device for the simultaneously quantification of AMOX and AA: a) SWV direct readings of AA spiked in real samples and b) corresponding calibration curve; c) SWV direct readings of AMOX spiked in real samples and d) corresponding calibration curve. The SWV meausrements were carried out at 2 mV/s. 142

Figure 6.1 Preliminary results on LIG production onto nanocellulose membranes: a) representative photograph of the output of a optimization matrix (variation of laser power and speed); b) SEM image showing the localized LIG formation onto nanocellulose; c) output of the variation of laser conditions where □ represents the region of no laser effect, □ represents the region of LIG formation and, □ represents the region where the substrate is perforated or too fragile; d) sheet resistance measurements through hall effect (□ represents the laser conditions that yielded LIG in c) but, when patterning larger areas the substrate is perforated/fragile). 153

Figure 7.1 Number of citations achieved by the candidate until December 2021. Data retrieved from Google Scholar. 157

List of tables

Table 4.1 Assignment of TET characteristic Raman peaks. 77

Table 4.2 Analytical features calculated from the average UV-Vis spectra (n=3) of the synthesized AuNPs, by microwave irradiation, with citrate and glucose as reducing agents. AuNPs' diameter calculated by DLS. 93

Table 5.1 Revision of proposed electrochemical MIP devices for CAP sensing. 130

Table 5.2 Revision of proposed electrochemical MIP devices for AMOX sensing. 138

Abbreviations

2019-nCoV - Novel Coronavirus

3D - Three-dimensional

2D - Two-dimensional

4-AMP - 4-Aminothiophenol

4-MBA - 4-mercaptobenzoic acid

ACE2 - Angiotensin-converting Enzyme 2

ACN - Acetonitrile

AFM - Atomic Force Microscopy

AgNFs - Silver Nanoflowers

AgNPls- Silver Nanoplates

AMOX - Amoxicillin

ASSURED - Affordable, Sensitive, Specific, User-friendly, Rapid and Robust, Equipment-free and Delivered to those in need

AuNFs - Gold Nanoflowers

AuNPs - Gold Nanoparticles

AuNRs - Gold Nanorods

AuNSs - Gold Nanostars

Au-SPE - Gold-based Screen-Printed Electrodes

AuSph - Gold Nanospheres

BNC - Bacterial Nanocellulose

BPA - Bisphenol A

CAP - Chloramphenicol

CCD - Charge-Coupled Devices

CE - Counter Electrode

CEA - Carcinoembryonic Antigen

Co_3O_4NPs – Cobalt oxide nanoparticles

COVID-19 - 2019 Novel Coronavirus

C-SPE - Carbon-based Scree-Printed Electrodes

cTnT - Cardiac Troponin T

CuNPs - Copper nanoparticles

CV - Cyclic Voltammetry

DLS - Dynamic Light Scattering

DNA - Deoxyribonucleic Acid

DPV - Differential Pulse Voltammetry

EBT - Eriochrome Black T

EDOT - 3,4-Ethylenedioxythiophene

EDS - Energy-dispersive X-ray spectroscopy

EF - Enhancement Factor

EIS - Electrochemical Impedance Spectroscopy

EVs – Extracellular Vesicles

ELISA - Enzyme-linked Immunosorbent Assay

FTIR-ATR - Fourier-transform Infrared Spectroscopy – Attenuated Total Reflectance

FWHM - Full Width at Half Maximum

GC - Gas Chromatography

GLOBOCAN - Global Cancer Observatory

GO - Graphene Oxide

G-SPE - Graphene-based Screen-Printed Electrodes

HPLC - High-Performance Liquid Chromatography

IUPAC - International of Pure and Applied Chemistry

LASER - Light Amplification by Stimulated Emission of Radiation

LDW - Laser-Direct Writing

LIG - Laser-Induced Graphene

LOD - Limit of Detection

LOQ - Limit of Quantification

LSPR - Localized Surface Plasmon Resonance

MFC - Microfibrillated Cellulose

MIP - Molecularly Imprinting Polymer

MS - Mass Spectroscopy

MWCNTs - Multi-Walled Carbon Nanotubes

Na_3Ct - Sodium citrate

NC - Nanocellulose

NC@AgNPs - Nanocellulose substrate decorated with AgNPs

NC@AuNPs - Nanocellulose substrate decorated with gold nanoparticles

NCC - Nanocrystalline Cellulose

NC_{inc}@AuNPs - Nanocellulose substrate decorated with gold nanoparticles, with a pre-incubation step

$NC_{inc\text{-}20min}$@AuNPs - Nanocellulose substrate decorated with gold nanoparticles, with pre-incubation and a seedless method

NIP - Non-Imprinted Polymer

NPs - Nanoparticles

NTA - Nanoparticles Tracking Analysis

OTC - Oxytetracycline

PANI - Polyaniline

PCA - Principal Component Analysis

PDMS - Polydimethylsiloxane

PEDOT - Poly(3,4-ethylenedioxythiophene)

Phe - Phenylalanine

PI - Polyimide

POC - Point-of-Care

RA - Reducing Agent

RE - Reference Electrode

rGO - Reduced Graphene Oxide

RSD - Relative Standard Deviation

RT - Room Temperature

SARS-CoV-2 - Severe Acute Respiratory Syndrome Coronavirus 2

SDZ - Sulfadiazine

SEM - Scanning Electron Microscopy

SERS - Surface-Enhanced Raman Spectroscopy

SILAR – Successive Ionic Layer Absorption and Reaction

SPEs - Screen-Printed Electrodes

SPR - Surface Plasmon Resonance

STEM - Scanning Transmission Electron Microscopy

SWV - Square-Wave Voltammetry

TDM - Therapeutic Drug Monitoring

TET - Tetracycline

TP@AgNPs - Tetra Pak® substrate decorated with AgNPs

Trp - Tryptophan

Tyr - Tyrosine

UV - Ultraviolet

Vis - Visible

WE - Working Electrode

WHO - World Health Organization

WP_{inc}@AuNPs - Whatman paper substrate decorated with gold nanoparticles, with a pre-incubation step

XPS - X-ray Photoelectron Spectroscopy

XRD - X-ray Diffraction

Symbols

A_{SPR} - Absorbance at SPR

C - concentration

E - energy

E° - Standard reduction potential

h - Planck's constant (4.135×10^{-15} eV·s)

I - Current

I_{2D} - Raman intensity of graphene 2D band

I_D - Raman intensity of graphene D band

I_G - Raman intensity of graphene G band

m - Slope of calibration curve

Rct - Charge transfer resistance

ν - Frequency

X - Average value of blank signal

Z' - Imaginary component of impedance

Z" - Real component of impedance

σ - Standard deviation

CHAPTER 1

Motivation and aim of the thesis

Chapter 1. Motivation and aim of the thesis

1.1 Scientific context

The need for inexpensive, fast, reliable, and accurate sensing platforms is a constant demand in modern society. In fact, this aspect was reinforced recently with the outbreak of the Novel Coronavirus (2019-nCoV) which due to its rapid spreading was declared as a pandemic by the World Health Organization (WHO).[1]

Biosensor's platforms have demonstrated to be of utmost relevance as they improve the life quality in a wide range of areas, from healthcare to water and food control and environmental monitoring.[2–4] The biosensors research field began in 1962 with the designing of a glucose oxidase biosensor, which was introduced by Clark and Lyons.[5] Since then, the advent of nanotechnology and the development of nanofabrication tools has sparked further developments on the biosensing area. The global biosensors market was valued at USD 21.2 billion, in 2020, and it is expected to reach a value of USD 41.8 billion by 2028.[6] Figure 1.1 shows the evolution and predicted growth of North America biosensor's market, by application.

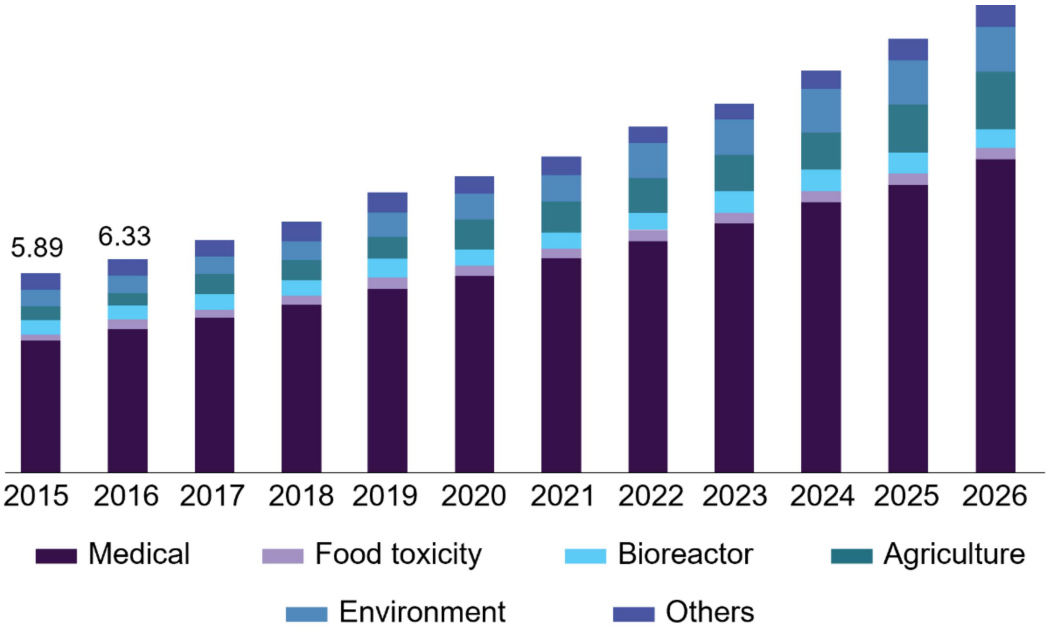

Figure 1.1 North America biosensors market growth by application. Values in USD million. Adopted from Grand View Research – biosensors market, 2020.[6]

Biosensors are defined by IUPAC (International of Pure and Applied Chemistry) as integrated receptor-transducer devices, which are able to provide selective quantitative, semiquantitative or qualitative analytical information using a biological recognition element. Among the past years, biosensor's definition has been evolving, due, for instance, to the development of novel biosensors that utilize inorganic and/or synthetic receptors. One can consider, a broader definition where biosensors are devices that utilizes a receptor of biological nature and/or the analysed sample is of a biological nature.[7]

The recognition element is a critical component of the biosensor, and it is conventionally of biological nature. Examples of the most used recognition elements are proteins, antibodies, enzymes, and nucleic acids. Early biosensors used naturally occurring recognition elements that were purified from biological or environmental systems. With advances in technology and synthetic chemistry, many biosensor recognition elements used today are synthesized in the laboratory to allow for improved stability and reproducibility of the biosensor function. For instance, molecular imprinting technology allows to create polymeric recognition elements, with biomimetic capabilities, to be used as an alternative to natural bioreceptors.

According to biosensor's operating principle, transducers can be of different natures, such as electrochemical, optical, thermal, acoustic, gravimetric among others.[2,8,9] Amongst the transduction techniques used in biosensors, electrochemical methods are by far the primarily employed followed by optical methods (Figure 1.2).[2,8]

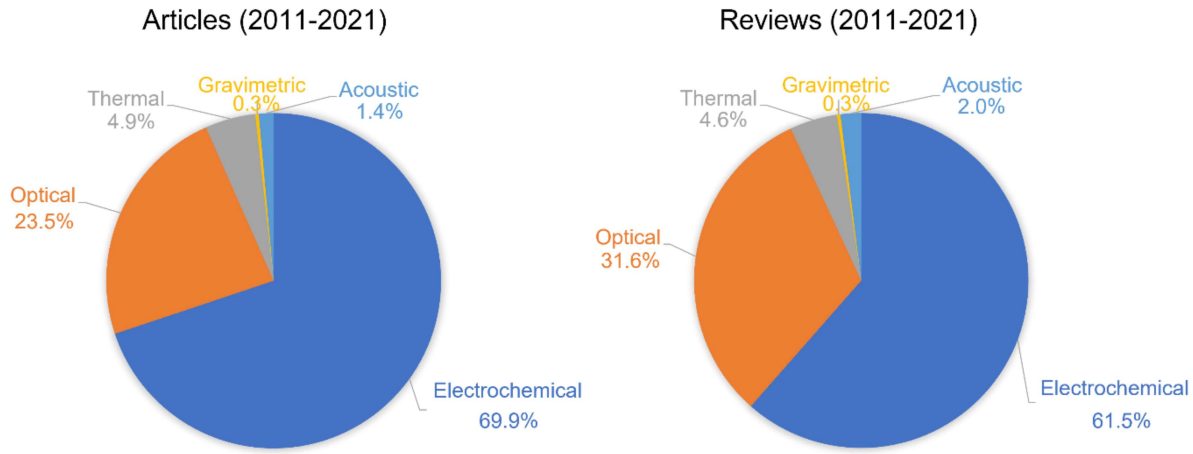

Figure 1.2 Results from Web of Science Core Collection for the keywords 'biosensor' AND 'transduction method' (electrochemical, optical, thermal, acoustic, and gravimetric) showing the distribution of publications in the period of 2011 to 2021. Total number of articles: 22,325; Total number of reviews: 2,500. Data retrieved from Web of Science database (September 2021).

The ubiquity of electrochemical methods in biosensors, as well as optical methods, owns to their relevant characteristics, such as high sensitivity, fast responses, ease of use and ease of miniaturization.

These types of biosensors are thus feasible to be used as point-of-care (POC) devices allowing for on-site testing.[2,8,9]

Nanotechnology has enabled advances in both electrochemical and optical biosensor technology. For instance, nanostructured electrodes provide high surface-to-volume ratio surfaces and also improve the electron transfer rate for electrochemical applications[10] and nano-active layers for Surface-Enhanced Raman Spectroscopy (SERS), lead to enhancement on sensing performance.[9]

Some of the challenges involved in the biosensor progress are (i) the efficient capturing of biorecognition signals and the transformation of these signals into measurable signals, using stable and inexpensive recognition elements, (ii) enhancing transducer performance i.e., increasing sensitivity, shortening response times, improving reproducibility, and attaining low detection limits, (iii) miniaturization of the biosensing devices using micro- and nanofabrication technologies, and (iv) the use of novel materials to introduce significant features, such as decrease in cost and flexibility. These challenges can be met through the integration of sensing technology with nano-based processes and nanomaterials, offering, for instance, high surface-to-volume ratio, good conductivities, and ease of tailoring.

1.2 Objectives

Due to the relevance and ubiquity of electrochemical and optical transduction mechanisms on biosensing this thesis seeks to explore novel technologies and substrates, aligned with the European Green Deal and the United Nation's Sustainable Development Goals, for the fabrication of such devices.

The main goals of this work are:

- to find solutions that do not require the use of natural bioreceptors, by using label-free approaches combined with SERS biosensing and molecularly imprinted recognition elements combined with electrochemical sensing;
- to use naturally occurring substrates, of renewable origin, such as cellulosic-based materials as biosensor's platforms to take advantage of their low-cost and inherent properties;
- to use simple, inexpensive, and scalable electrode's fabrication methods for electrochemical biosensors;

- to prove the feasibility and reliability of the developed sensing platforms by applying them to the detection of relevant molecules and biostructures, for both clinical and environmental applications.

1.3 Thesis outline

- **Chapter 1** presents the motivation and main goals of this thesis;
- **Chapter 2** provides some fundamental background on optical and electrochemical transduction methods, particularly regarding the inherent concepts of Raman spectroscopy and SERS for optical sensing and of molecular imprinting technology and laser-induced graphene (LIG) electrodes for electrochemical sensing;
- **Chapter 3** details the experimental methods used during this research work;
- **Chapter 4** focuses on the development and application of cellulose-based SERS platforms fabricated with both physical and chemical-based methods. The chapter starts with the use of a cardboard SERS platform, with silver nanoparticles produced through a physical process, for tetracycline quantification. Afterwards, chemical-based processes for the in-situ growth of Raman active nanoparticles onto nanocellulose is demonstrated. Microwave irradiation is used for the synthesis of both silver and gold nanoparticles for Raman enhancement and the resultant platforms are applied, respectively, for exosome's profiling with clinical relevance on cancer diagnosis and for the screening of the spike protein of the SARS-CoV-2 virus;
- **Chapter 5** demonstrates the use of biomimetic elements for electrochemical sensing combined with LIG electrodes. Firstly, a three-electrode architecture was fabricated with LIG electrodes, and its electrochemical features were directly compared with conventional screen-printed electrodes, as well as the analytical performance attained with a molecularly imprinting polymer (MIP)-based sensing element for chloramphenicol antibiotic detection. Finally, to demonstrate the versatility of the LIG technique for electrode's patterning a dual-detection system was constructed for antibiotic's monitoring;
- **Chapter 6** presents the main conclusions of this dissertation and provides possible further applications of the results and concepts developed.
- **Chapter 7** shows the scientific outputs of the candidate during the PhD period.

CHAPTER 2

Introduction

In this chapter a broad coverage of topics related with this thesis is presented. A brief overview about nanobiosensing platforms is given, followed by a background on Raman spectroscopy and SERS concepts and the current state-of-art of cellulose-based SERS substrates. Afterwards, some theoretical explanations about molecular imprinting technology are given as well as a coverage about the method used for electrode's patterning with LIG and the current state-of-art of LIG based biosensors.

Some of the contents present in this chapter were adapted from:

Marques, A. C., Águas, H., Martins, R., Silva, B. C., Sales, M. G. F., Fortunato, E. Surface-Enhanced Raman Scattering Paper-based analytical devices. In Paper-based Analytical Devices for Chemical Analysis and Diagnostics, Elsevier, **2021**, 1, 117-168.

Marques, A. C., Pinheiro, T.; Martins, G. V., Cardoso, A. R.; Martins, R., Sales, M. G., Fortunato, E. Non-Enzymatic Lab-on-Paper Devices for Biosensing Applications. In Comprehensive Analytical Chemistry, Elsevier, **2020**, 89, 189–237.

Chapter 2. Introduction

2.1 Nanobiosensing platforms

2.1.1 Nanotechnology and nanomaterials

Back in 1959, Nobel Prize laureate Richard Feynman introduced the concept of nanotechnology with his landmark lecture "*There's plenty of room at the bottom*" describing his vision to fabricate machines to manufacture smaller machines, down to the molecular level.[11] Later, in 1974, scientist Norio Taniguchi was the first to use and define the term "Nanotechnology" as the " (…) processing of separation, consolidation and deformation of materials by one atom or one molecule."[12]

Since then, the advent of nanotechnology and the development of nanofabrication tools has influenced every field of science and thus our everyday life (Figure 2.1).

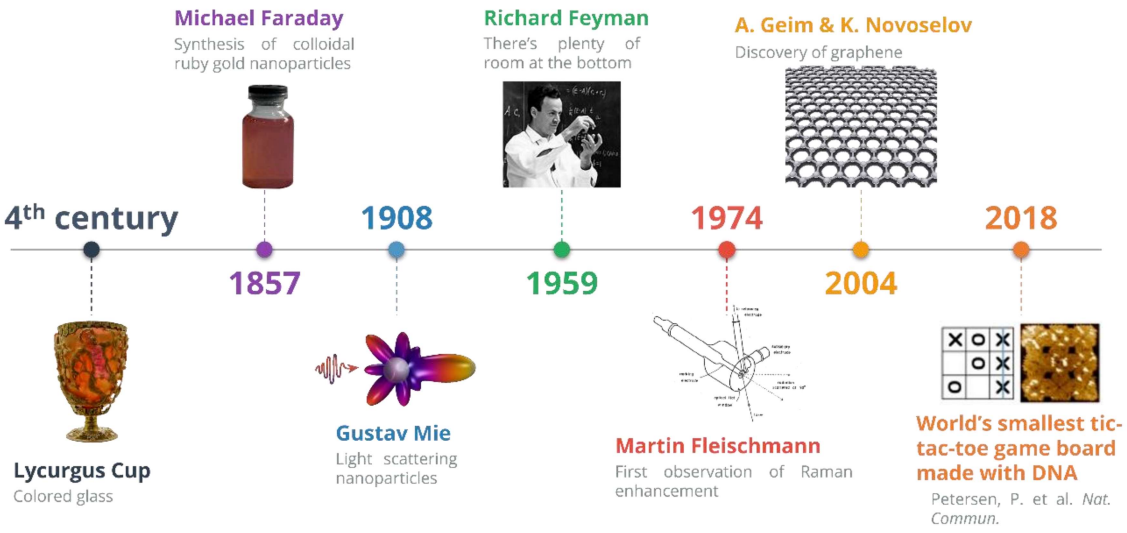

Figure 2.1 Timeline of some of the nanoscience and nanotechnology findings and achievements.

The National Nanotechnology Initiative in the United States of America defines Nanotechnology as "a science, engineering, and technology conducted at the nanoscale (1 to 100 nm), where unique phenomena enable novel applications in a wide range of fields, from chemistry, physics and biology, to medicine, engineering and electronics".[13]

So, nanotechnology deals with materials in the nanoscale called nanomaterials that can be found in nature or can be engineered. For the manufacture of nanomaterials, two approaches have been

established, through physical or chemical processes: top-down and bottom-up, with differences in degrees of quality, time of production and cost (Figure 2.2).

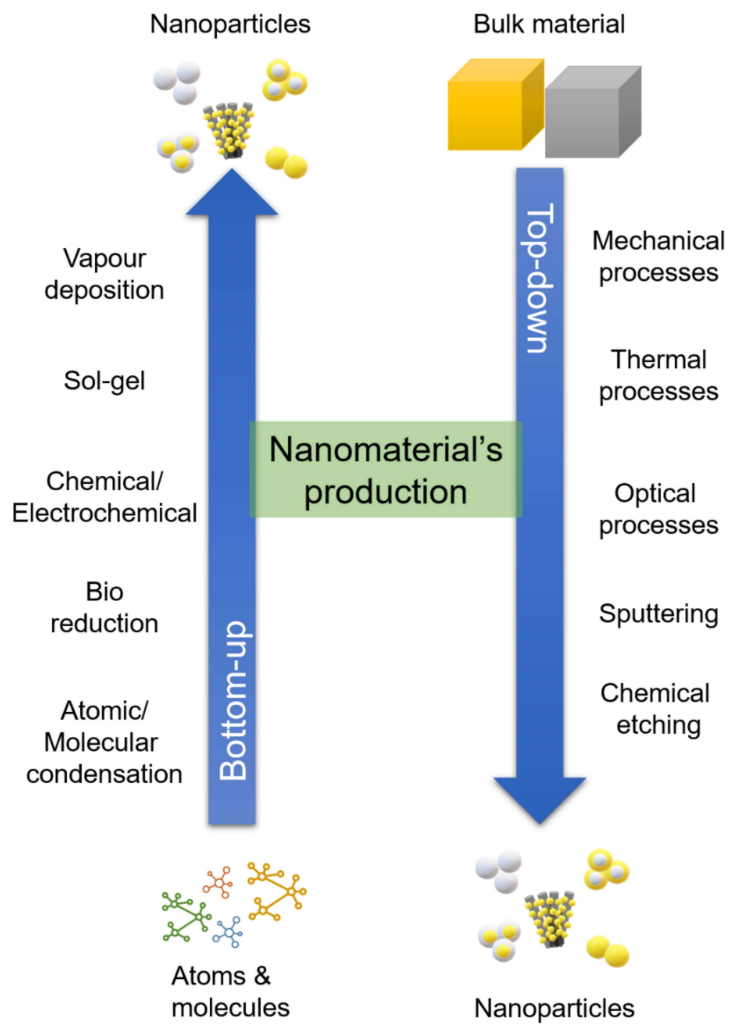

Figure 2.2 Top-down and bottom-up approaches for nanomaterial's production: most common fabrication methods employed in each approach. Adapted from Bayda, S., et al, 2020.[14]

The top-down approach is based on the breakdown of a bulk material to obtain nanostructures,[14] whereas the bottom-up approach is based on the build-up of nanomaterials from the bottom, atom-by-atom or molecule-by-molecule.[14]

In the past decades, the ubiquity of nanotechnology in the world has exponentially increased, with countless examples of applications in diverse fields, such as in energy, cosmetics, textile, defence and security, agriculture and food, biomedical, drug delivery and sensors.[15] This technology has revolutionized several industries and its impact and relevance was also demonstrated in the ongoing Coronavirus disease 2019 (COVID-19) pandemic situation in the development of diagnostic assays and vaccines. Nanomaterials are used in a multitude of products and applications, such as, in paints,

insulating layers, electrochromic windows, sunscreens and toothpastes, UV sensors, solar cells, biosensors, bioimaging, drug delivery, computer science, among others.[14,16–21]

Within the plethora of nanotechnology and nanomaterial's applications the enormous potential of the use of nanomaterials and nanofabrication tools in biosensor's devices has been recognized.[8,10,22] Following, a brief coverage of biosensors devices inherent concepts and the importance of nanotechnology on their remarkable evolution is given.

2.1.2 Biosensors

Biosensors are conventionally defined as devices able to convert the interaction of a recognition element with a target analyte to a measurable signal. These devices combine the selectivity of interaction of an analyte of interest with the recognition element, called bioreceptor, with the sensitivity of a transducer to convert such interaction into a measurable signal (Figure 2.3).[23]

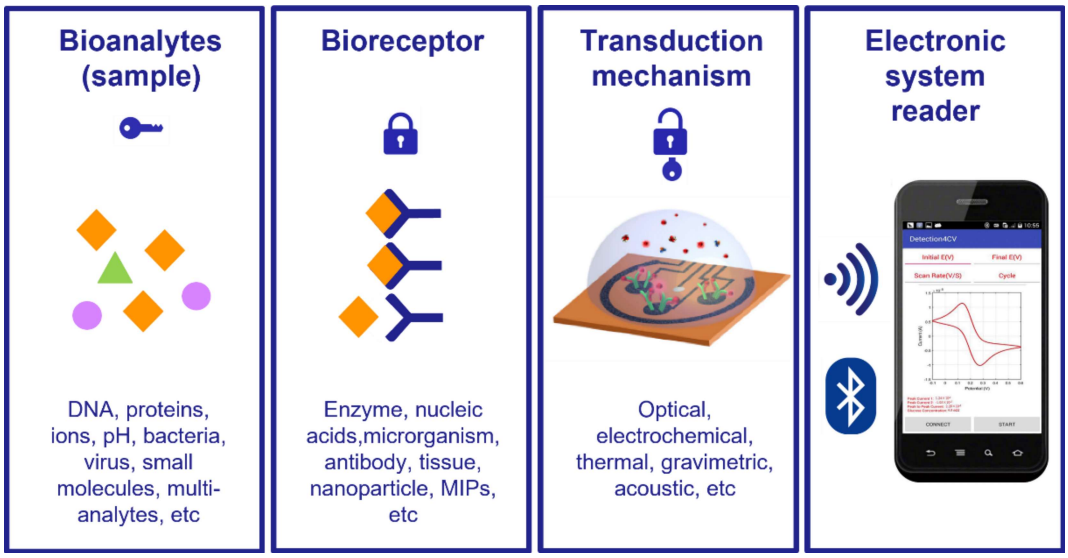

Figure 2.3 Schematic representation of the components of a generic biosensor: the bioanalytes present in the sample react with the bioreceptor layer (e.g. enzyme, nucleic acids, antibody, microorganism, tissue, MIPs, etc.) directly attached to a transducer mechanism that transforms the physico-chemical interaction of the bioreceptor with the bioanalyte into a measurable signal. Adopted from Águas, H., et al, 2021.[24]

In its core, a typical biosensor comprises an analyte, a recognition element, a transducer and a system reader:[8]

- *Analyte*: substance of interest whose presence is detected and, in some cases, quantified;
- *Recognition element*: also known as bioreceptor, is generally a biological element or a biomimetic material that can selectively recognize the analyte of interest;
- *Transducer*: element that converts the recognition event into a measurable signal that connects with the presence and quantity of a chemical or biological target. According to the operating

principle, transducers can be broadly categorized as electrochemical, optical, thermal, acoustic, and gravimetric transducers;

- *System reader*: the above elements can then be integrated with electronics, or not, depending on the type of biosensor and/or nature of signal output, to allow for analyte qualification and/or quantification.

The performance of the biosensor method can be evaluated by the following attributes:[25,26]

- *Selectivity*: measures the ability of the recognition element to discriminate a specific analyte in a complex sample;
- *Reproducibility*: is the ability of the device to give identical responses in independent measurements;
- *Stability*: shows the degree of susceptibility to factors such as pH, buffer composition, sample matrix composition, temperature, humidity, among others. It helps determine the optimal working conditions and the storage and operational lifetime of the biosensor;
- *Linearity and sensitivity*: the linear range defines the range of analyte concentrations for which the biosensor response changes linearly with the concentration. These can be represented mathematically as $y = mc$, where c is analyte' concentration, y is the output signal and m is the straight line' slope that represents the sensitivity of the device. The higher the slope, the better is the discrimination between concentrations and therefore the better is the sensitivity of the biosensor;
- *Limit of detection (LOD)*: expresses the smallest concentration or quantity that can be detected with reasonable certainty.

As mentioned, nanotechnology has revolutionized the conventional laboratory detection routes by igniting the biosensor's research area.[4,27] Some of the main impacts of nanotechnology on biosensors is visible on the improvement of their sensitivity and selectivity, due to physical, chemical, mechanical, magnetic and/or optical properties of nanomaterials incorporated in the devices.[28] Additionally, it facilitated the device's miniaturization, allowing for POC analysis, with the use of low sample volumes and simple detection procedures.[25] These devices are currently behind many successful monitoring procedures, with great implications in the food industry,[29–31] healthcare,[9,32–34] and environment,[17,35–37] reducing complexity, cost and time of analysis of conventional methods.[2,27,38]

Biosensors can be tailored to measure several target molecules, with different transduction principles, where a multitude of nanomaterials and biomimetic structures can be used. They enable rapid detection of several analytes in a simple and expedite way and have become relatively common in developed

countries, the best examples being the rapid pregnancy test and the glucometer. They are also highly relevant in developing countries because they show the potential to complement or even replace standard laboratorial testing, are easy to transport due to its lightweight, and easy to use and interpret its results. As such, in 2003, WHO established guidelines for the development of diagnosis for use in economically disadvantaged regions, known under the acronym ASSURED (**A**ffordable, **S**ensitive, **S**pecific, **U**ser-friendly, **R**apid and **R**obust, **E**quipment-free and **D**elivered to those in need).[39] More recently, in 2019, due to the advances in digital technology and mobile health and in order to provide real-time quality control for testing and treatment and facilitate sample collection, while using environmental friendly materials and processes, a redefinition of this acronym was proposed to REASSURED by adding: **R** – Real-time connectivity and **E** – Ease of specimen collection and environmental friendliness.[40]

As aforementioned, the selectivity of a biosensor is directly dependent on the interaction of the bioreceptor with the target compound, which constitutes a crucial part of the biosensors' performance and reliability.[41] Typically, these bioreceptors are enzymes, biomolecules, organelles, cells, proteins, among others. However, the use of these natural bioreceptors can present disadvantages such as, high cost, complex production routes and sensitivity to external factors (e.g. pH, temperature, humidity, etc.).[42,43] Moreover, in some cases, the analyte of interest may be too complex and/or not having yet a well-defined and stable bioreceptor for its detection. Approaches that do not rely on natural bioreceptors have been employed as a way to tackle these drawbacks.[19,20,44–46] Several strategies have been reported in the literature, such as following changes in the intrinsic properties of certain nanomaterials when interacting with the target analyte[17,47–50] or, for instance, by directly measuring the signal of the analyte with highly specific and sensitive spectroscopy methods.[51,52] Additionally, synthetic recognition elements have been used as biomimetic materials to mimic a specific biological property, offering higher stability and reproducibility than their natural counterparts.[9]

Biosensors can be classified by their transduction method where the most employed, and used in this work, are the optical and electrochemical mechanisms, which will be covered in the next section.

2.2 Optical detection

Optical detection has exhibited worthwhile performance in sensing biological systems and promoting significant advances in clinical diagnostics, drug discovery, food process control, and environmental monitoring.[53,54] One of the most excellent examples of optical detection is Surface-Enhanced Raman Spectroscopy (SERS), that is able to provide high selectivity and sensitivity, without relying on the use of natural bioreceptors.

2.2.1 Surface-Enhanced Raman Spectroscopy

Raman spectroscopy: a historical perspective

Raman spectroscopy is a spectroscopic technique based on molecular vibrations and is dependent on the inelastic scattering of a monochromatic light, usually from a laser, in the visible, near-infrared, or near-ultraviolet range of the electromagnetic spectra.[55–57] This effect was predicted theoretically, in 1923 by A. Smekal[58] and experimentally demonstrated by C.V. Raman in 1928.[59]

"*I propose this evening to speak to you on a new kind of radiation or light emission from atoms and molecules*."[60] These were the words, from Sir Chandrasekhara Venkata Raman, that anticipated one of the most impacting announcements on analytical methods. C.V. Raman, born in 1888, was an Indian physicist and the 1930' Nobel laureate "*for his work on the scattering of light and for the discovery of the effect named after him*."[61]

After finding a new phenomenon on the scattering of light, C.V. Raman made the announcement to the press in the same day, 28th of February in 1928. The Associated Press of India declared in the next day: "*Prof. C. V. Raman, F.R.S., of the Calcutta University, has made a discovery which promises to be of fundamental significance to physics... The new phenomenon exhibits features even more startling than those discovered by Prof. Compton with X-rays. The principal feature observed is that when matter is excited by light of one colour, the atoms contained in it emit light of two colours, one of which is different from the exciting colour and is lower down the spectrum. The astonishing thing is that the altered colour is quite independent of the nature of the substance used*."[62]

The events that led to his findings, together with his co-worker Kariamanickam Srinivasa Krishnan, were first detailed in an Inaugural Address delivered to the South Indian Science Association, at 16th of March in 1928 (Figure 2.4).[60] Later a paper was published in Nature at 31st of March, entitled "A new type of secondary radiation".[59]

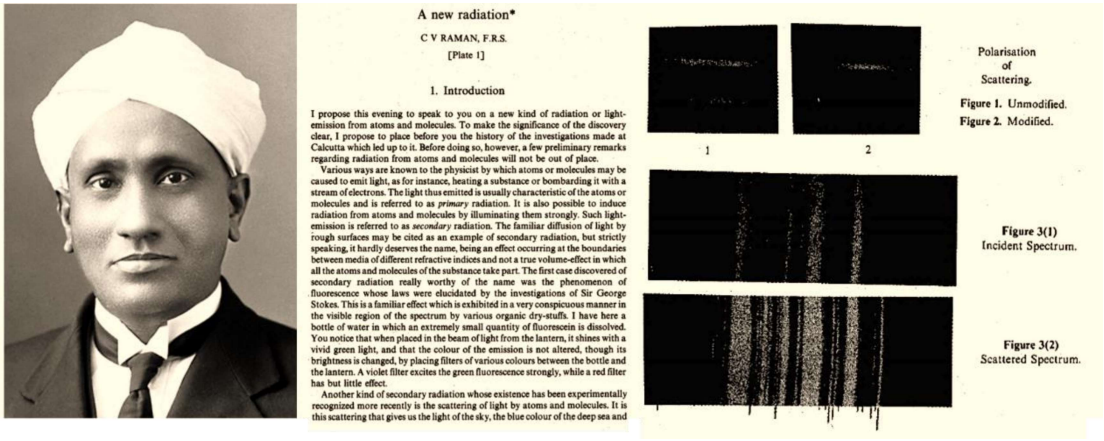

A new radiation*

C V RAMAN, F.R.S.

[Plate 1]

1. Introduction

I propose this evening to speak to you on a new kind of radiation or light-emission from atoms and molecules. To make the significance of the discovery clear, I propose to place before you the history of the investigations made at Calcutta which led up to it. Before doing so, however, a few preliminary remarks regarding radiation from atoms and molecules will not be out of place.

Various ways are known to the physicist by which atoms or molecules may be caused to emit light, as for instance, heating a substance or bombarding it with a stream of electrons. The light thus emitted is usually characteristic of the atoms or molecules and is referred to as *primary* radiation. It is also possible to induce radiation from atoms and molecules by illuminating them strongly. Such light-emission is referred to as *secondary* radiation. The familiar diffusion of light by rough surfaces may be cited as an example of secondary radiation, but strictly speaking, it hardly deserves the name, being an effect occurring at the boundaries between media of different refractive indices and not a true volume-effect in which all the atoms and molecules of the substance take part. The first case discovered of secondary radiation really worthy of the name was the phenomenon of fluorescence whose laws were elucidated by the investigations of Sir George Stokes. This is a familiar effect which is exhibited in a very conspicuous manner in the visible region of the spectrum by various organic dry-stuffs. I have here a bottle of water in which an extremely small quantity of fluorescein is dissolved. You notice that when placed in the beam of light from the lantern, it shines with a vivid green light, and that the colour of the emission is not altered, though its brightness is changed, by placing filters of various colours between the bottle and the lantern. A violet filter excites the green fluorescence strongly, while a red filter has but little effect.

Another kind of secondary radiation whose existence has been experimentally recognized more recently is the scattering of light by atoms and molecules. It is this scattering that gives us the light of the sky, the blue colour of the deep sea and

Polarisation of Scattering.

Figure 1. Unmodified.
Figure 2. Modified.

1 2

Figure 3(1) Incident Spectrum.

Figure 3(2) Scattered Spectrum.

Figure 2.4 Sir Chandrasekhara Venkata Raman photograph, front page of his Inaugural Address detailing the Raman effect and relevant figures. Adapted from Raman, C.V., 1928.[60]

The experiment that allowed C.V. Raman to find the new phenomenon on the scattering of light was based on the passage of sun's violet light, isolated with a violet filter, through a liquid sample and, by placing a green filter between the sample and the observer (Figure 2.5).

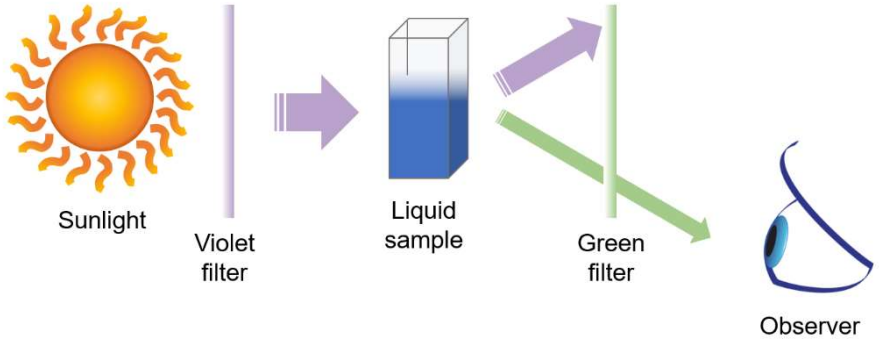

Figure 2.5 Schematic representation of the experiment that led to the finding of the Raman effect.

C.V. Raman observed that although most of the emerging scattered light had the same wavelength as the incident violet beam – known as, elastic or Rayleigh scattering – a small portion of the emitted light had a different wavelength – inelastic or Raman scattering. This phenomenon was observed, at the time, by C.V. Raman and his co-worker K. S. Krishnan, in more than 60 different liquid samples.[59,60]

From 1928 forward, more than 370,000 contributions (Web of science database search in October 2021) have used the Raman effect. The further improvement on instrumentation, especially the invention of Charge-Coupled Devices (CCD) detectors and Light Amplification by Stimulated Emission of Radiation (LASER) devices, has sparked an exponential increase on Raman spectroscopy associated experiments. For its high significance as analytical technique, it was designated, in 1998, as an International Historic Chemical Landmark, by the American Chemical Society.[63]

Raman spectroscopy and SERS: theoretical fundaments

The Raman effect describes the phenomenon of the inelastic scattering of light and is divided into two processes: anti-Stokes and Stokes scattering (Figure 2.6).

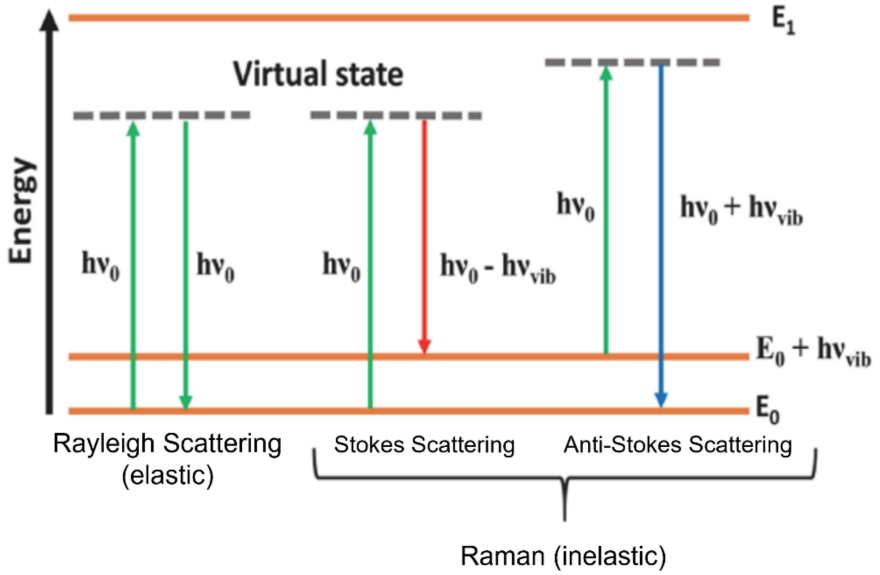

Figure 2.6 Energy level diagram for Rayleigh and Raman scattering, where $\Delta E = h\nu_{vib}$ represents the difference in vibration energy levels. Adopted from Kumar, S., et al, 2020.[64]

In an anti-Stokes scattering process, the scattered photon has a higher energy than the incident photon, which only happens if the molecule is already in an excited vibrational state. This event is very unlikely to succeed leading to the weakest signals. The Stokes scattering is the energy transference from light to a vibration of a molecule where the scattered photon has a lower energy, thus a higher wavelength than the incident photon. [65,66] Each photon spectral shift corresponds to the frequency of a specific vibrational mode of the molecule. These Raman shifts can be measured in a resultant Raman spectrum and serve as a 'molecular fingerprint' that enables the identification of chemicals and materials. Raman shift is expressed in relative wavenumbers (cm^{-1}) and is itself an expression of the difference between the absolute wavenumber of the laser wavelength ($1 / \lambda_L$) and the absolute wavenumber of the Raman emitted photon ($1 / \lambda_R$). Since Raman shift is directly proportional to the energy change of photons upon Raman scattering, is therefore independent of the excitation wavelength, making the comparison of acquired Raman spectra with those from reference libraries straightforward.[67]

Among the years, Raman spectroscopy has proven to be a powerful analytical technique, owing to its versatility and specificity on the identification of analytes, through the distinctive vibration of molecules, based on their structure and conformation.[56] Despite its specificity, Raman scattering is an

event with a very low probability, in 10^6-10^8 scattered photons only one is inelastically scattered, leading to extremely low Raman cross-sections.[56,57]

To surpass this drawback, SERS has emerged as a valuable solution to enhance the highly specific but weak signal intensities.[56,65,68] The implementation of SERS has been exponentially increasing in the past decades (Figure 2.7) since the first report on Raman effect enhancement observed in an aqueous solution of pyridine adsorbed on a rough silver electrode, by Martin Fleischmann and co-workers, in 1974.[69]

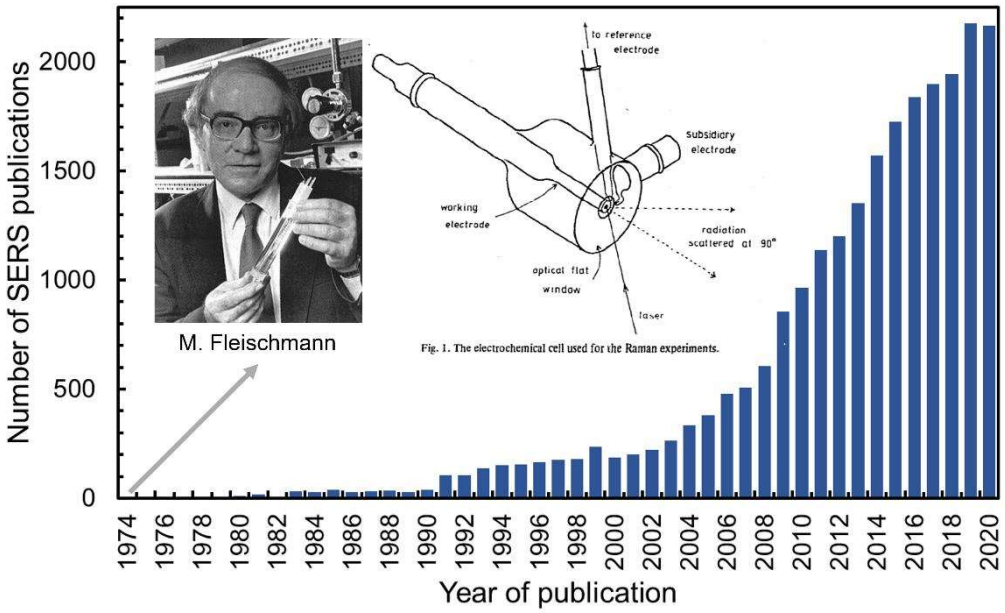

Figure 2.7 Number of publications per year since the first report of Raman enhancement. Insets of Martin Fleischmann photograph and the figure relative to the electrochemical cell used for Raman experiments, in 1974.[69] Data retrieved from Web of Science database (September 2021), with the keyword 'SERS'.

Three years later it was suggested that the signal enhancement could not be only explained by the presence of rough surfaces rendering increased surface areas. Jeanmaire and Van Duyne suggested that it was also due to an increase in the electromagnetic field due to the presence of silver,[70] while Albrecht and Creighton suggested that it was due to charge transferences between the analyte and silver.[71] Currently, these are the two accepted mechanisms to explain the phenomenon of Raman scattering signal enhancement, that can often occur at the same time – known as, electromagnetic and chemical enhancement, respectively.[55–57,68,72,73]

Chemical enhancement is associated with molecular orbital interactions between the analyte and the metallic surface.[57,66,74] This type of enhancement can lead to the intensification of Raman signals, in approximately 10-10^3 orders of magnitude.[56,72,75] Jensen, L. et al,[76] described the chemical enhancement as consisting in three distinct aspects, that may happen separately, as shown in Figure 2.8.

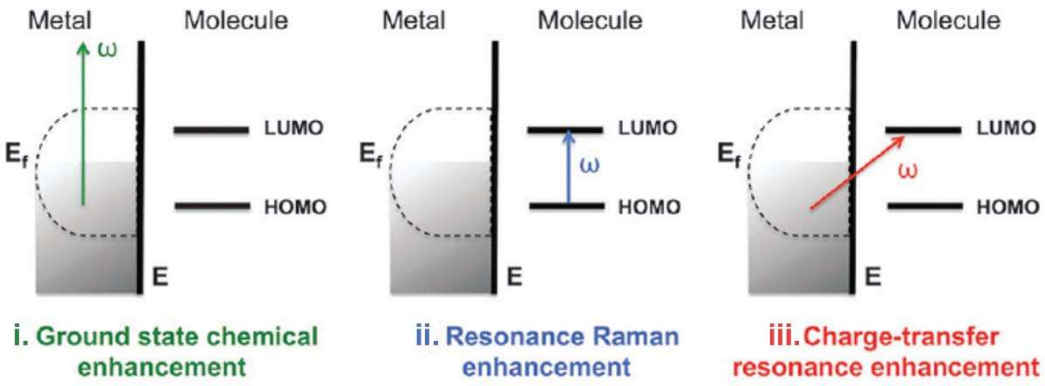

Figure 2.8 Mechanisms of chemical enhancement in SERS. *E* represents the local electromagnetic field, ω is the excitation frequency and E_f is the Fermi level for metal. HOMO is the highest occupied molecular orbital and LUMO is the lowest occupied molecular orbital. Adopted from Fateixa, S. et al, 2015.[57]

i. non-resonance Raman caused by ground-state chemical interactions between an analyte and the metal surface;
ii. resonance conditions of an adsorbate molecule and irradiation wavelength prompting resonance Raman enhancement;
iii. laser illumination being in resonance with photoinduced electron transfer transitions from the Fermi level of a metal surface to vacant states of the adsorbate.

Electromagnetic enhancement – the main contributor for the enhancement in SERS – is caused by plasmon resonances in the metal, which induces the scattering of photons by the delocalized electrons present on the metallic nanoparticle surface, providing the largest enhancements, for up to 10^4-10^{12}.[56,68] Among all metallic nanostructures, Ag, Au and Cu nanostructures are responsible to induce the highest Raman enhancements due to their Localized Surface Plasmon Resonance (LSPR) (Figure 2.9) in the visible and near infrared regions, which is strongly dependent on their size and morphology.[56]

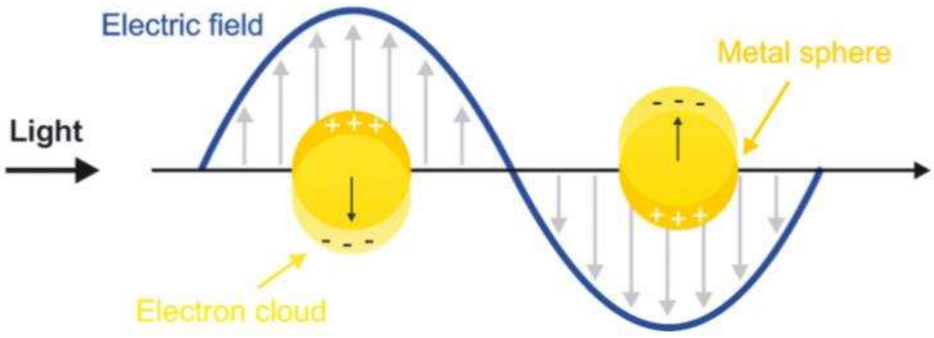

Figure 2.9 Schematic representation of Localized Surface Plasmon Resonance: The excitation of a LSPR in nanoparticles confines the light energy into sub-wavelength volume, leading to strongly enhanced local electromagnetic field. Adopted from Cecchet, F., et al, 2014.[77]

Moreover, when two metallic nanoparticles are at a certain close distance, it is generated a so called hot spot that can enhance even further Raman intensities, which can be particularly helpful for single-molecule detection.[56,65,68]

The magnitude of SERS effect can be calculated and, it is named enhancement factor (EF), which is one of the most important figures of merit to which SERS is concerned. This factor corresponds to the enhancement in Raman intensities of the molecules adsorbed on SERS surfaces, when compared to the same number of molecules in non-SERS surfaces.[65] Several factors can influence the SERS effect, such as: characteristics of the excitation source, detection setup, type of SERS substrate, intrinsic properties of the analyte, among others.[65]

The increase on the number of publications related with SERS was sparked with the boom of nanotechnology and nanofabrication techniques in the 1980s, specially due to the use of metallic nanoparticles.[78–81] Figure 2.10 shows a timeline of the evolution of Raman spectroscopy and SERS in the early years of development, which contributed to the exponential growth of the use of this technique on a multitude of applications.

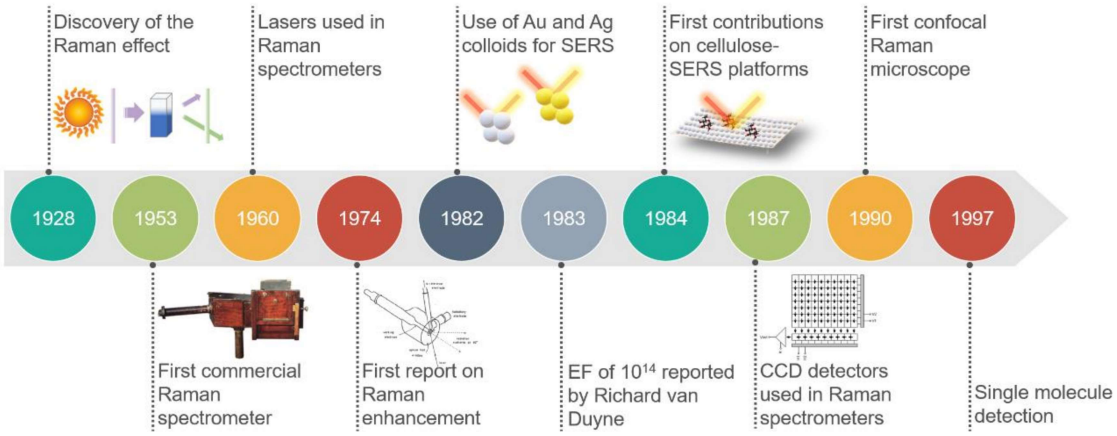

Figure 2.10 Historical timeline of important landmarks that contributed to the evolution of Raman and Surface-Enhanced Raman spectroscopy.

Raman enhancement nanostructures onto cellulosic substrates: characteristics and fabrication methods

One can consider that there are three main types of SERS platforms to produce suitable Raman enhancement:[65]

- rough metallic electrodes;
- metallic nanostructures in colloidal solutions;

- 'planar' metallic structures such as arrays of metallic nanostructures supported on planar substrates, such as glass, silicon, or cellulosic materials.

Although, the use of metallic electrodes for Raman enhancement can be viewed as the beginning of SERS, its use decreased in the past years due to the relatively low enhancement factors typically attainable. Colloidal metallic solutions, predominantly of Ag or Au nanostructures, are extensively used, and the SERS signal arises from a three-dimensional volume that is known as the scattering volume. In addition to the Raman enhancement of individual nanostructures, other factors such as the nanostructures concentration and its Brownian motion, play a major role in SERS experiments. Moreover, these colloidal solutions can be transferred to or grown in planar substrates, giving origin to the latter type of SERS platforms. In this case, the SERS signal arises from a two-dimensional (2D) plane, although with some three-dimensional (3D) structure, and can offer a higher practicability for SERS measurements, and it is the focus of this thesis.

In fact, the recent advances on SERS research have shown an increasing focus on the development of novel SERS platforms that can offer high sensitivities, uniformity, reproducibility, easiness of fabrication and an inherent low-cost. Cellulose-based materials in the form of paper substrates and other native or modified forms of cellulose have shown their relevance as a vehicle or support of SERS active layers due to their fundamental characteristics such as flexibility, which can facilitate sample collection, lightweight, biocompatibility, biodegradability and availability.[4,49,82–85] Moreover, cellulosic substrates can be easily tailored for different SERS purposes, offering advantageous properties, such as hydrophilicity or hydrophobicity, high surface area and easy adaptation to micro and nanofabrication purposes and printing technologies.[56,68,86] Ultimately, the aforementioned characteristics of cellulose make it an important candidate for POC applications based on SERS transduction mechanisms.

The first contributions using cellulose as SERS platform dates back to 1984.[87,88] Since then, a significant increase on the number of publications reporting cellulose and paper-based substrates on the fabrication of SERS devices has been observed (Figure 2.11).

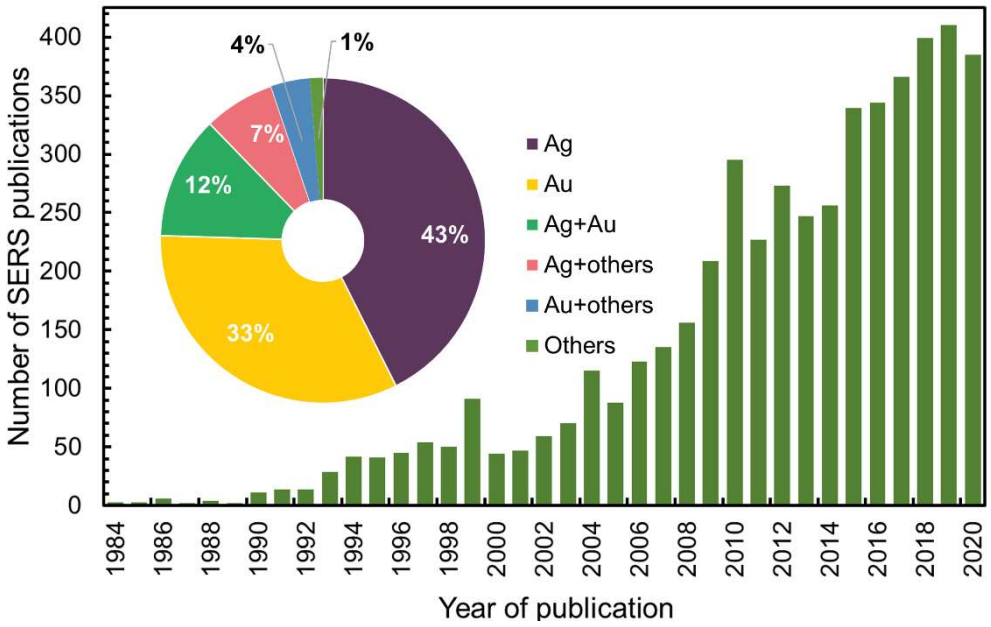

Figure 2.11 Number of publications per year of cellulose-based SERS devices. Inset of percentage distribution of the type of enhancement nanostructure utilized on paper and cellulose-based SERS devices in the last 10 years. Data retrieve from Web of Science database (September 2021), with the keywords: 'SERS' AND 'Paper' and 'SERS' AND 'Cellulose'.

Concerning the last 10 years, a Web of Science database search shows that the type of enhancement structures that are commonly applied to cellulose (Figure 2.11, inset) are Ag and Au nanostructures, due to their strong plasmon resonance. Among these, Ag accounts for the highest percentage, since it is the one that provides the larger signal enhancements.[65,89–93] Moreover, about 24% of cellulose-based SERS contributions has reported the use of composites of Ag and Au nanostructures,[94–96] Ag and Au with others nanostructures such as metal oxides[97–100] or graphene-based materials[101–104] and even other type of nanostructures as ZnO[105] or MoO_{3-x} nanosheets.[106]

Annex Table A1 resumes the main characteristics of representative cellulose-based SERS platforms with Au and Ag nanostructures.

Different strategies for enhancement nanostructure's synthesis and their deposition methods onto cellulose substrates achieving different analytical features have been reported.[89,92,97,107–109] Figure 2.12 shows an infographic with some of the most used techniques, employed with cellulose substrates, to produce Raman enhancement nanostructures and transference methods.

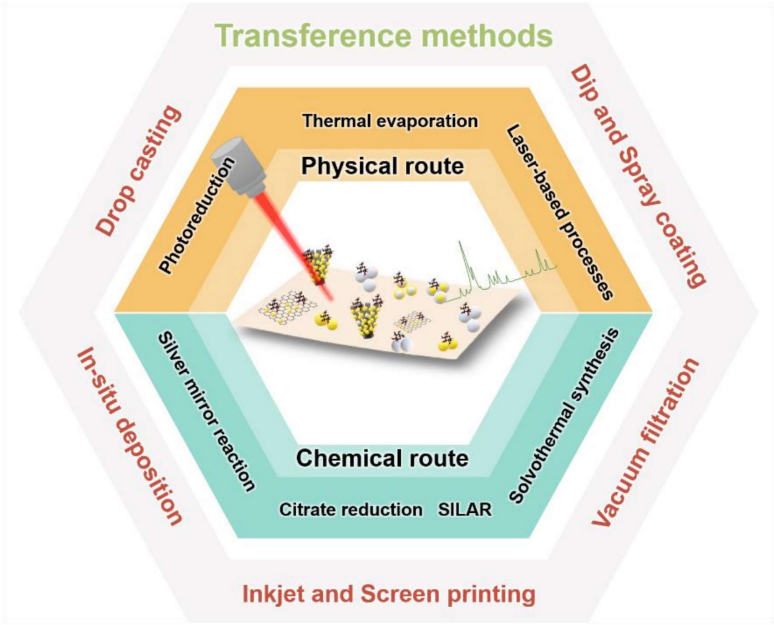

Figure 2.12 Infographic with some of the most common production and transference techniques employed on the production of cellulose-based SERS substrates.

Applications of cellulose-based SERS platforms

The high selectivity provided by Raman spectroscopy coupled with the high sensitivity enabled by SERS substrates has prompted its use on a multitude of applications in different fields, such as in healthcare – for diagnostic and therapeutic studies and follow-up – and in environmental settings – for pesticides detection, antibiotics control, pathogen agents and heavy metals screening, among others. Herein, a revision of the state-of-art on applications with cellulose-based SERS substrates is presented.

Healthcare applications: diagnostic and therapeutics

Cancer constitutes the second leading cause of mortality worldwide, only surpassed by cardiovascular disease.[110] The diagnosis of cancer in the current scenario is made by detection techniques that are usually expensive, invasive and time-consuming.[111] Thus, the development of simple, reliable, cost-effective and non-invasive detection methods for early cancer screening/diagnosis and posterior follow-up is particularly important, due to the disease's prevalence and potential lethality.

For the quantitative detection of Mucin-1 in whole blood, a cancer biomarker, Hu, S.-H. et al[112] developed a platform based on the in-situ synthesis of gold nanoparticles (AuNPs) onto filter paper. The performance of the SERS strip was evaluated with 4-mercaptobenzoic acid showing a relative standard deviation (RSD) lower than 8% thus demonstrating a high uniformity of the platform. Their detection strategy relied on the conjugation of AuNPs with aptamer of Mucin-1, which was then hybridized with a complementary DNA labelled with a Raman reporter. In the case of target's presence,

a replacement of complementary DNA occurs causing a decrease on the intensity of the SERS signal. This method rendered a log linear correlation from 50 ng/ml to 50 μg/ml and was successfully tested against other common proteins, with no significant signal loss.

AuNPs where also used as enhancement layer on a filter paper substrate for the label-free detection of adenosine in urine.[113] The presence of this nucleoside in urine samples has been correlated to several types of cancer[113,114] and its screening might be used for the non-invasive early diagnosis and follow-up of cancer. The preparation of the AuNPs followed a chemical route through the well-known citrate-based reduction method[115] resulting in 45 nm-average diameter spherical particles with an SPR centred at 532 nm. The deposition of the plasmonic nanostructures was achieved with a ring-oven pre-concentration system, thus improving sampling efficiency. Due to the complex nature of urine matrix samples, the authors proposed a SERS-chemometric method based on multivariate curve resolution-alternating least squares, combined with the standard addition method which allowed to achieve a sensitive, reproducible, and selective method for adenosine detection in urine samples.

As it is known, the anisotropy of the plasmonic structures can enhance even further the Raman signal.[116–120] In particular, gold nanoflowers (AuNFs) deposited on hydrophobic paper were used for cervical cancer diagnosis[121] through an immunoassay combined with Au-Ag nanoshuttles as SERS tags. This sandwich was able to quantitatively detect two common cervical cancers biomarkers, squamous cell carcinoma antigen and osteopontin in serum samples, with a LOD of 8.6 pg/ml and 4.4 pg/ml, respectively.

Gold nanorods (AuNRs) have also been successfully employed on cancer diagnosis through immersion onto filter papers, rendering EFs in the range of 10^6-10^8.[117,119] The intrinsic SERS spectra of HT-29 cell line from colorectal cancer was used in combination with principal component analysis and k-nearest-neighbour algorithm, to differentiate it from the negative controls, achieving sensitivities, specificities and accuracies above 80% (Figure 2.13a).[117]

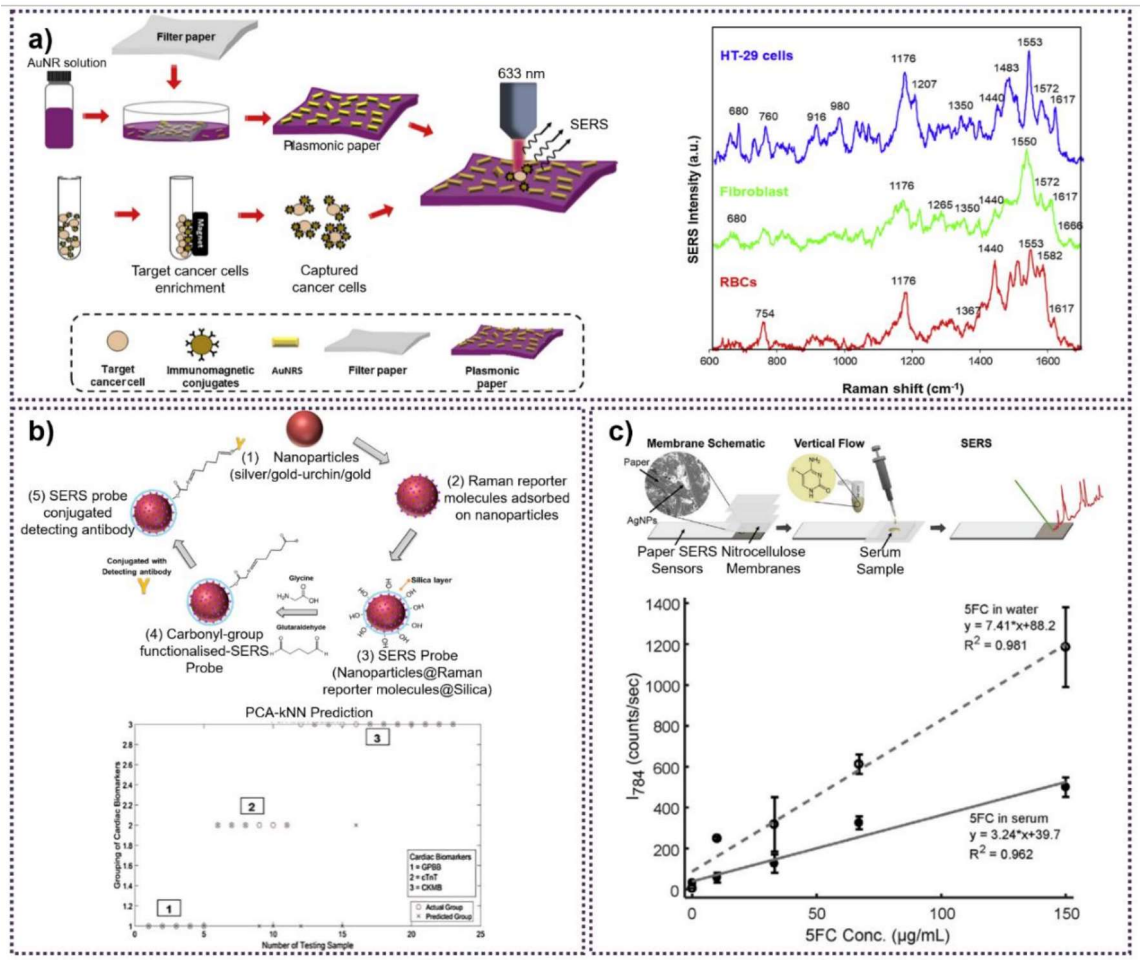

Figure 2.13 Healthcare applications – diagnostic and therapeutic: a) AuNR-paper for the detection of cancer cell trough an immunomagnetic assay and resultant SERS spectra of HT-29 cells, fibroblast and RBCs; b) Schematic workflow for the preparation of SERS probe for cardiac biomarkers detection and PCA-kNN prediction; c) Schematic procedure of a vertical-flow paper SERS device for screening of an anti-cancer drug and calibrations curve in water and serum. Adapted from Reokrungruang, P. et al, 2019,[117] Lim, W. et al, 2020[122] and Berger, A. et al, 2017.[123]

Liu, Q. and co-workers[119] established a method also based on AuNRs for the distinction between normal and cancerous cells through a peak ratio algorithm, achieving high sensitivity and selectivity.

Although Au nanostructures are the most used amongst biosensing applications, due to its inherent biocompatibility and easy conjugation with bioreceptors, Ag-based nanostructures or Au-Ag alloys have also been used. Ahn, Y. J. et al[124] developed a dual optical system (SERS and colorimetric) based on silver nanoplates (AgNPls) for the detection of hydrogen sulphide gas, released from live prostate cancer cells. The AgNPls that were chemically synthesized through a seed-mediated growth method were drop casted in PDMS-patterned filter paper detection zones. The SERS detection allowed monitoring quantitatively H_2S with a linear range of 82-330 nM.

The implementation of plasmonic bimetallic nanoparticles for SERS sensing was proven advantageous, due to the combination of features which allowed tailoring LSPR.[125,126] Reports on these nanostructures showed their use on cancer diagnosis either for folic acid detection with picomolar sensitivity[95] or also for exosomes profiling.[4,127] Through a statistical principal components analysis method, a platform based on Ag@Au core-shell nanostructures was fabricated[4,127], following a two-stage Successive Ionic Layer Absorption and Reaction (SILAR) method published by Kim et al.[79], for breast cancer screening.

Cardiovascular diseases are the leading cause of death worldwide[128] and efforts on the development of cellulose-based SERS platform for its screening and early detection have been recently reported. Mabbott, S. and co-workers[129] reported the detection of miR-29a, a microRNA associated with myocardial infarction, achieving a LOD down to 47 pg/µl. AuNPs, obtained through a citrate-based reduction method, were used as the Raman enhancement structures, and conjugated with complementary DNA to miR-29a and with a Raman reporter (malachite green isothiocyanate) for SERS readout. This system was applied in a three-dimensional paper-based microfluidic device comprising layers for sample loading, conjugation, incubation, capture and washing steps. The developed device also allowed the colorimetric discrimination between positive and negative results, offering a simple and easy-to-interpret solution to untrained personnel. Also, for myocardial infarction early diagnosis, Lim, W.Y et al[122] established a method based on the simultaneous detection of multiple cardiac biomarkers – GPBB, CK-MB and CTnT (Figure 2.13b). Antibodies against each of these biomarkers were conjugated with Ag, Au urchin and AuNPs and three different Raman reporters – 4-nitroaniline, *tert*-butylhydroquinone and methyl red, respectively. The characteristic Raman spectral signatures of each reporter were further processed with partial least squares models allowing the quantification of each biomarker. The obtained LOD of the developed paper-based SERS device was calculated as 8, 10 and 1 pg/ml for GPBB, CK-MB and cTnT, respectively.

Therapeutic drug monitoring (TDM) allows optimizing prescriptions and monitoring the safety and effectiveness use of life-saving drugs. A few SERS devices for on-site TDM have been reported in the literature. Berger, A.G., et al.[123] built a system with a vertical-flow architecture to monitor the antifungal flucytosine levels in undiluted serum, avoiding the need for complex and time-consuming sample preparation (Figure 2.13c). The developed solution comprises a filtering membrane, made of nitrocellulose, for sample pre-treatment, placed on top of an inkjet printed paper-based SERS sensor. This device combined with a portable Raman spectrometer allowed on-site detection. For the Raman signal enhancement, chemically synthesized AgNPs were printed in an array pattern allowing the identification of flucytosine characteristic Raman peaks. The most intense peak, at 784 cm^{-1}, was used for the quantification of the target levels achieving and LOD of 10 µg/ml. For even less invasive TDM

applications, Yokoyama, M. et al[130,131] has shown preliminary results of the use of tear samples, using the intrinsic capillary forces of cellulose. AuNRs absorbed on filter paper were used for screening anti-epileptic and anti-convulsant agents, sodium valproic acid[130] and sodium phenobarbital,[131] respectively.

Ponlamuangdee, K. and co-workers combined graphene oxide and AuNRs with a layer-by-layer immersion method on filter paper, for the fabrication of paper-based SERS devices.[101] Using R6G as the probe molecule, the authors were able to achieve an EF of 4.56 x 10^7, due to the electromagnetic and chemical enhancement effects arising from the AuNRs and graphene oxide, respectively. As proof-of-concept, the developed SERS substrate was tested in the detection of an anti-cancer drug, mitoxantrone, attaining a LOD of 5 μM. For the determination of ketoprofen in aqueous solutions and human saliva, Díaz-Liñán, M.C., et al immobilized silver nanoflowers (AgNFs) on nylon-coated paper[116] achieving a dual detection system based on SERS and ambient pressure mass spectrometry analysis, with a LOD and limit of quantification (LOQ) of 0.023 and 0.076 mg/L, respectively.

Besides the aforementioned methods, several other types of cellulose-based SERS substrates combining different types of papers and plasmonic structures have been reported in the biosensing field. For instance, the use of AuNPs onto hydrophilic or hydrophobic papers has been reported for the detection of L-citrulline,[132] uric acid[133] and virus-infected tears.[134] For SERS-based immunoassays, Oliveira, M.J. and co-workers, prepared a reusable SERS platform utilizing gold nanostars (AuNSs) and cellulose hydrogel.[109] For the detection of free bilirubin, graphene-isolated-Au-nanocrystals[135] and graphene oxide-AuNSs[102] were used. ZnO decorated with AuNPs has been reported for the diagnostic of prenatal diseases in women through the analysis of human amniotic fluids.[97] Ag was used in the form of nanoparticles deposited on regular office paper for glucose sensing[136], and for procalcitonin detection, in the form of nanowires combined with Au hollow nanocages.[137] Additionally, nanoshells combining Au and Ag where reported as Raman enhancement structures, for the detection of Myxovirus protein A through an immunoassay.[138]

Environmental applications: food, dairy products, beverages, and water safety

Inexpensive, accurate and simple-use sensing devices, such as cellulose-based SERS platforms, are of paramount relevance for environmental applications. Although there is regulation of governmental and non-governmental organizations around the world, reports on the presence of pesticides, dyes, antibiotics feed to livestock and/or in the aquaculture industry and other environmental pollutants are still recurrent.[139–142]

Thiram is a very well-known pesticide that is use as fungicide for the preservation of fruits, that can cause several health issues, such as lethargy and limited motor activity. Several groups have reported

the use of cellulose-based SERS devices for detecting and monitoring this compound. Based on Au nanostructures, different strategies can be found in the literature. For instance, Xiong, Z. and colleagues[143] optimized a composite based on cellulose nanofibers and chemically synthesized AuNPs, via electrostatic interactions. The direct comparison between this composite and a filter paper/AuNPs substrate, using 4-aminothiophenol as probe molecule, showed an enhancement of 20 times on the SERS spectra intensities. The application of the developed three-dimensional SERS platform on apple juice allowed detecting the presence of thiram with a limit of detection of 52 ppb. For the simultaneous detection of thiram and other pesticides,[144] such as tricyclazole and carbaryl, nanoporous cellulose was used as a matrix for AuNRs, rendering a uniform and well-distribution of the nanostructures throughout the substrate (Figure 2.14a).

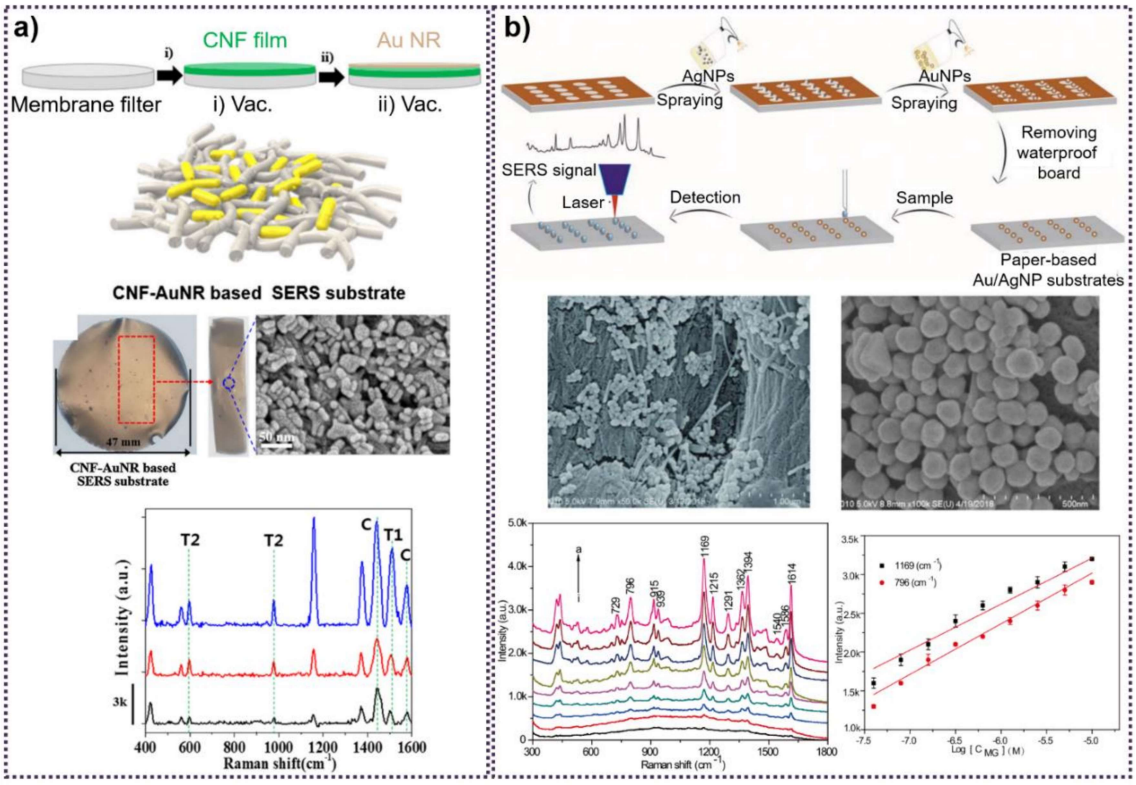

Figure 2.14 Environmental applications: a) Schematic illustration of the CNF-AuNR SERS platform, its photograph and respective SEM image and SERS spectra for the simultaneous detection of pesticides; b) Schematic workflow to produce the paper-based Au/AgNPs, SEM image and representative concentration-dependent SERS spectra with correspondent calibration curve. Adapted from Kwon, G. et al, 2019[144] and Yang, G. et al, 2020.[145]

An EF of 1.4 x 10^7 was obtained for R6G as probe molecule and LODs of 1 nM, 100 nM and 1 μM were calculated for thiram, tricyclazole and carbaryl, respectively. Additionally, the authors performed a real-scenario swab test to trace residues on apple peels, accomplishing limits of detection for thiram, tricyclazole and carbaryl of 6, 60 and 600 ng/cm^2, respectively. These values were well below the permitted maximum residual level on apple peels, of 2000 ng/cm^2. Luo, W. and colleagues[146] reported

a method for the simultaneous detection of thiram, parathion methyl and malachite green on apple peels, based on in-situ synthesized AuNPs on pseudo-paper films composed of polyethylenimine and microcrystalline cellulose. The platform achieved an EF of 3.02 x 10^6 and limits of detection of 1.1 ng/cm^2 for thiram, well below the maximum residue limit. More recently, Godoy, N.V., et al[147] used inkjet printing to deposit 77 nm-diameter sized gold nanospheres (AuSph) onto hydrophobic paper to enhance the device's sensing performance, due to the confinement of the analyte in the AuSph platform. A full optimization of the printing process tuning the number of nanoparticles in the sensing areas, allowed obtaining an EF up to 2.0 x 10^6, using 4-nitrophenol as model analyte, and a quantification region threshold of 10^{-11} M for thiram and for crystal violet. Hydrophobic paper was also used by Lee, D.J. et al[148] as substrate for the deposition of UV reduced AuNPs@GO flakes. A LOD of 10 nM and 1 μM was calculated for R6G and thiram, respectively.

Based on Ag nanostructures, Zhu, Y. et al[149] reported an AgNPs-decorated filter paper combined with dynamic SERS by collecting Raman spectra during the drying up process after sample loading onto the SERS substrate, for increased sensitivity. Crystal violet was used as probe molecule, demonstrating stronger signals with dynamic SERS than with after absolute evaporation of analyte. The produced SERS membranes, based on a simple silver mirror reaction, were swabbed on different fruit's peels – apples, bananas, and tomatoes – detecting thiram with LODs of 24, 7.2, and 36 ng/cm^2, respectively. The use of hydrophobic nanostructured paper substrates for thiram detection was reported by Martins, N.C.T. and colleagues,[91] using inkjet printing to deposit aqueous emulsions of Ag and polystyrene (PS) colloidal NPs. Crystal violet was used as the Raman probe to optimize the SERS performance of the proposed platform by varying the amounts of Ag/PS colloidal NPs, the number of printing layers and the degree of hydrophobicity of the office paper substrate. The authors shown that the strongest Raman enhancement of crystal violet was observed for the highest water contact angle (146°) attained, thus proving the improved features of using hydrophobic coatings. The SERS platform rendered a LOD of 0.024 ppm of thiram spiked in mineral water and apple juice, while in apple peal, the detection limit obtained was 600 ng/cm^2.

A AgNPs/GO paper was prepared by a screen printing method[150] for the detection of thiram and also thiabendazole and methyl parathion with LODs of 0.26, 28 and 7.4 ng/cm^2, respectively, in aqueous solutions and 1.2, 56 and 30 ng/cm^2, respectively, on the surface of fruits and vegetables. Sun, M. and colleagues developed SERS substrates with filter paper and Ag@SiO_2 core-shell nanoparticles,[151] for shell-isolated NP-enhanced Raman spectroscopy, to avoid potential disturbing interactions between analytes and the metal core. Crystal violet was used as probe molecule to optimize the size of the Ag

core and SiO_2 thickness, reaching a LOD of 10^{-9} M with 3 nm shell thickness, for both crystal violet and thiram.

The combination of Ag and Au has also been reported in cellulose-based SERS platforms for thiram detection. As example, Lin, X. et al[152] assembled an Au@Ag nanocubes monolayer on a patterned paper through a liquid-liquid interface self-assembly technique, for the detection of pesticides in soil, without the need for sample preparation. The SERS performance was evaluated with 4-MBA as probe molecule with an EF of 5.6 x 10^4 and an RSD of 12.8%. For the quantitative detection of thiram in soil, the paper untreated areas allowed sample injection and filtration of impurities, achieving a LOD of 0.148 mg/kg using thiram' characteristic peak centred at 1386 cm^{-1}. Asgari, S. et al[126] fabricated a nanofibrillar cellulose/Au@Ag core-shell nanoparticles composite for detection of thiram and also paraquat in lettuce. EF of ~10^4 was obtained for 4-MBA and an increase on Raman intensities of about 8 times was observed comparing the bimetallic nanoparticles with the AuNPs on the nanofibrillar cellulose. The nanocomposite achieved limits of detection of 71 and 46 μg/L for thiram and paraquat, respectively.

Synthetic dyes such as malachite green, methylene blue and metalin yellow, among others, used in the textile, paper, aquaculture and food industries can have harmful effects on human health.[153] The need for regular on-site monitoring of these dyes can be aided by paper-based SERS devices. Regenerated cellulose fibres, from wastepaper, were decorated with citrate-stabilized AuNPs and used on the detection of malachite green in water samples.[154] The composite achieved a LOD lower than 10 ppb, using malachite green' characteristic peak located at 1173 cm^{-1}. For the simultaneous detection of malachite green, methylene blue and crystal violet in fish, Yang, G. et al fabricated a filter paper-based SERS platform with sprayed AgNPs and AuNPs attaining an EF of 9.0 x 10^7 (Figure 2.14b)).[145] The combination of the high enhancement from AgNPs with the chemical stability of AuNPs rendered an RSD, among peak intensities, lower than 3% after 4 weeks of storage under ambient conditions with limits of detection of 4.3 x 10^{-9}, 2.0 x 10^{-8} and 8.1 x 10^{-8} M for malachite green, methylene blue and crystal violet, respectively. Zhu, Y. et al built a poly(4-styrenesulfonate) (PSS)-functionalized filter paper SERS platform for the simultaneous separation, pre-concentration and detection of samples, achieved due to the capillary forces of cellulose and the surface chemical gradient and electrostatic interaction generated by PSS.[155] As enhancement layer, AgNPs were prepared through the silver mirror reaction. As proof-of-concept, the authors applied the developed SERS substrate for screening the colorants sunset yellow and lemon yellow in drinks, with limits of detection of 10^{-5} M. Nanocomposites of nanocrystalline cellulose, AgNPs and SiO_2 were prepared by Ogundare, S.A. and co-workers for the detection of malachite green.[153] The addition of SiO_2 resulted in the clustering of AgNPs, increasing the hot-spots, which decreased the LOD from 5.2 to 0.9 nM. The integration of Ag on graphene nano-mesh-Ag-ZnO

hybrid papers was carried out by Bharadwaj, S. et al, for the detection of methyl orange, R6G and also paraquat.[103] The developed nanohybrid was deposited on filter paper by suction filtration and rendered a high amount of hot-spots, attaining an high EF of 1.97 x 10^{11} for paraquat molecules and, allowed detecting low levels of pollutants, down to 10^{-11}, 10^{-13} and 10^{-14} M, for methyl orange, R6G and paraquat, respectively. For the detection of crystal violet and malachite green on fish, a hydrophobic paper-based semiconducting substrate was fabricated with two-dimensional MoO_{3-x} nanosheets through a regular printing process, achieving limits of detection as low as 10^{-6} M for both molecules.[106]

Other examples of cellulose-based SERS platforms for dye's monitoring includes drop casted AgNPs on high-pressure homogenized nanocellulose from *nata de coco* to measure methylene blue in water,[156] in-situ grown AgNPs onto polydopamine templated filter paper for malachite green,[157] faceted AgNPs with cellulose nanofibrils for common dyes in water,[158] AgNPs grown in filter paper through silver mirror reaction,[159] inkjet Ag nanostructures on filter paper for metalin yellow and malachite green,[160] AgNPs in-situ synthesized on glass fibre paper for malachite green in fish,[161] AgNPs produced with the SILAR method for malachite green detection in aquaculture settings[80] and brush painted AgNPs on paper for malachite green.[162]

Additional reports of cellulose-based SERS platforms for environmental applications shows the detection of melamine in milk samples. These include nanofibrillated cellulose with AuNPs, which combined with partial least squares statistical analysis rendered a limit of detection of 1 ppm.[163] Other works include $Ag@SiO_2$ nanocubes on filter paper with 0.17 mg/L as limit of detection[99] and AgNPs with commercially available filter paper, made hydrophobic and achieving 1 ppm as limit of detection.[164] For the quality monitoring of wine, AuNRs-rGO deposited on paper through vacuum filtration were used for sulphur dioxide detection[165] and semiconductor ZnO was used for sulphites quantification.[105] Black phosphorus Au deposited on filter paper was reported for foodborne bacteria *Staphylococcus aureus*, *Listeria monocytogenes* and *Escherichia coli* screening[166] and Au thin films deposited onto filter paper by sputtering were applied on heavy metals detection.[167]

Other applications

Cellulose-based SERS devices have also demonstrated their many advantages in several other applications, due to its simplicity, low-cost, easy tailoring, high selectivity and sensitivity and on-site detection.

For instance, Au@Ag core-shell NPs self-assembled on filter paper was used for screening the drug estazolam in beverages.[96] AuNPs deposited on office paper, with an EF of 10^6, was applied for cocaine detection to fight drugs trafficking, with a dual-detection device combining SERS with electrochemical

measurements.[168] For explosives monitoring, AuNPs and AuNSs, deposited on filter paper, was used for picric acid detection.[169] In other works, Ag/AuNPs produced through laser ablation and soaked on filter paper were used in the detection of picric acid, 2,4-dinitrotoluene and 3-nitro-1,2,4-triazol-5-one[170], whereas Ag nanotriangles, also deposited on filter paper, were used for picric acid detection.[171] For cosmetics applications, filter paper with AgNPs was used for nicotinamide detection[172] and AgNPs, produced by a green synthesis method with glucose and combined with methylcellulose, were used for artwork analysis.[173]

2.3 Electrochemical detection

The modern era has accelerate the development of portable, low-cost and effective devices for analytical purposes.[174] Among the different analytical techniques, electrochemical biosensors have received large interest due to their high sensitivity and selectivity, easy miniaturization, low instrumentation cost and rapid and simple results.[174–177] As mentioned, there is a high demand of research and from the market for alternatives to the use of natural bioreceptors in applications in which selectivity is needed, such as electrochemical biosensing.[178] In particular, MIPs have evolved in the last decades to answer to the needs for robust biorecognition schemes.

2.3.1 Molecularly imprinted polymer's technology for biomimetic material's fabrication

Biomimetic materials are tailor-made artificial receptors that have the ability to interact with target analytes similarly to natural bioreceptors. Molecular imprinting technology is currently one of the most versatile, scalable, and cost-effective approach to produce the aforementioned materials. The resulting biomimetic materials are known as MIPs or plastic antibodies and incorporate binding sites bearing steric and chemical functionality that are complementary to the intended target. MIPs have thus been used as biorecognition elements for a broad selection of analytes, from small molecules to larger biomacromolecules, such as cells and bacteria.[179,180] The analogy between MIPs and bioreceptors as affinity reagents is straightforward: MIPs are able to mimic the receptor–ligand, antibody–antigen, or enzyme– substrate biorecognition and as a result, the recognition ability of the polymeric matrix to the target molecule occurs with a very high selectivity.[179–182]

The concept of molecular imprinting can be traced back to the 1930s when a soviet chemist, Polyakov, observed unusual adsorption properties of silica particles prepared in the presence of soluble additives. A few decades after, from the 1970s to the 1990s, scientists Günter Wulff in Germany and Klaus Mosbach in Sweden are known to have been the great drivers of the modern-day approaches to imprinting.[181,182] In fact, the growth in popularity of MIP technology, in the 1990s was due to the

introduction of a non-covalent imprinting approach, by Mosbach and colleagues, which enabled the choice of a wider range of monomers and easier removal of the template from the polymeric matrix.[182]

Mechanical, thermal and chemical stability, ease of preparation, versatility and their relatively low cost make MIP materials attractive for analytical applications. Additionally, MIP technology allows to a receptor for an analyte of interest to be available far faster than if relying on antibody generation. MIPs are used not only as recognition units in chemical and biosensors but also as column packings in chromatographic separations and sorbents for solid phase microextraction.[180,182]

The majority of MIP-based sensors published so far rely either on the generation of an optical or electrochemical response when MIPs bind to a specific target, with the latter being the most employed technique.[179] Since the first attempts, in 1992, to use bulk imprinted polymers in sensors, by Kukhar, V.P.' research group,[183] more than 4450 publications were made on sensor-related MIP applications, with a fairly exponential growth over the years (Figure 2.15).

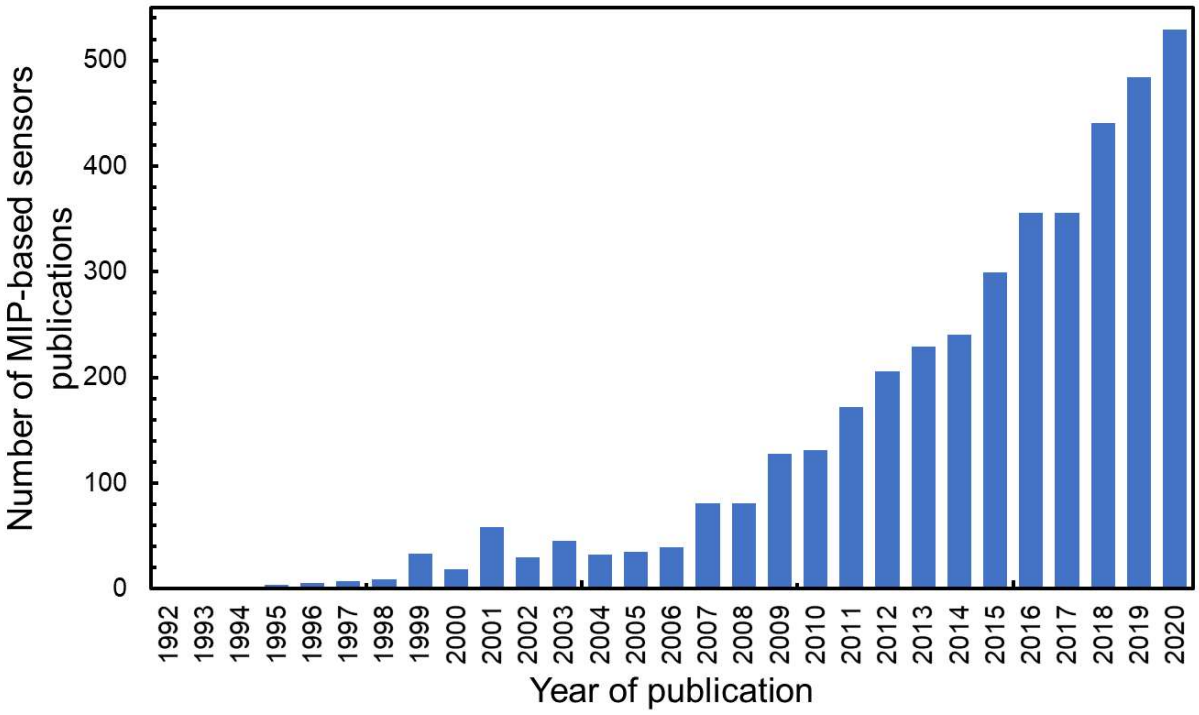

Figure 2.15 Number of MIP-based sensors publications per year since the first repot on imprinted polymers in sensors, in 1992. Data retrieved from Web of Science database (September 2021) with the keywords: 'molecular* imprint*' AND 'sensor'.

Synthesis of molecularly imprinted polymers

Generally, the molecular imprinting process involves the polymerization of a functional monomer in the presence of the target molecule, also known as template. Usually, the template can be either the

molecule of interest itself or a molecule of similar size and chemical functionality. The monomer is able to interact with the molecule and after polymerization its functional groups are kept in the same position by the highly cross-linked polymeric structure. After polymerization is complete, the extraction of the molecule from this polymeric network is performed, creating imprinted cavities that are complementary in size, shape, and orientation of their binding sites to those of the template. These cavities are then capable of selectively binding to the analyte even in the presence of similarly structured interfering analogues.[179,182]

Imprinted polymers can in theory be prepared for any analyte of interest. More than 10,000 molecules and biological structures have been successful imprinted, with templates as diverse as inorganic ions, drugs, nucleic acids, proteins, viruses, and even cells.[179] Methods to fabricate MIPs are either done in-situ or ex-situ and transferred afterwards to the sensor's surface. The latter, can represent some constrains on the transference process, resulting in limitations in mass transfer and diffusion kinetics.[178] Several procedures are used to prepare MIP films directly on transducer surfaces, such as electropolymerization, spin-coating, layer-by-layer deposition and, grafting, among others.[178,180] From these methods, electropolymerization is a more frequently followed approach, since it does not require neither a polymerization initiator nor UV light or heat and the method shows superior properties with respect to adherence to the transducer surface as well as simplicity, tunability and speed of preparation.[180,182]

Electropolymerization

Electropolymerization is a deposition procedure in which a polymeric layer is formed or coated upon an electrode/supporting substrate material. In the case of MIP production, this is done in the presence of the intended template. Usually, these electrochemical coatings are carried out utilizing a typical three-electrode setup, where a working electrode (i.e., where the coating occurs), reference electrode, and a counter electrode are used within a solution containing a monomer, solvent, and a supporting electrolyte – all of which are vital to the surface morphology of the polymeric film.[182]

Among the different available polymerization methods, electropolymerization stands out because it allows to control: [180,182]

- the rate of polymer nucleation and growth by proper selection of the electropolymerization parameters;
- the film thickness by the amount of charge passed during film deposition;
- the film morphology by suitable selection of an appropriate solvent and supporting electrolyte.

A proposed mechanism for the electropolymerization of an electroactive monomer process is said to involve alternate chemical [C] and electrode [E] reaction steps. This proposed mechanism can be explained using as example an electroactive monomer (commonly used with this end) – thiophene (Figure 2.16).

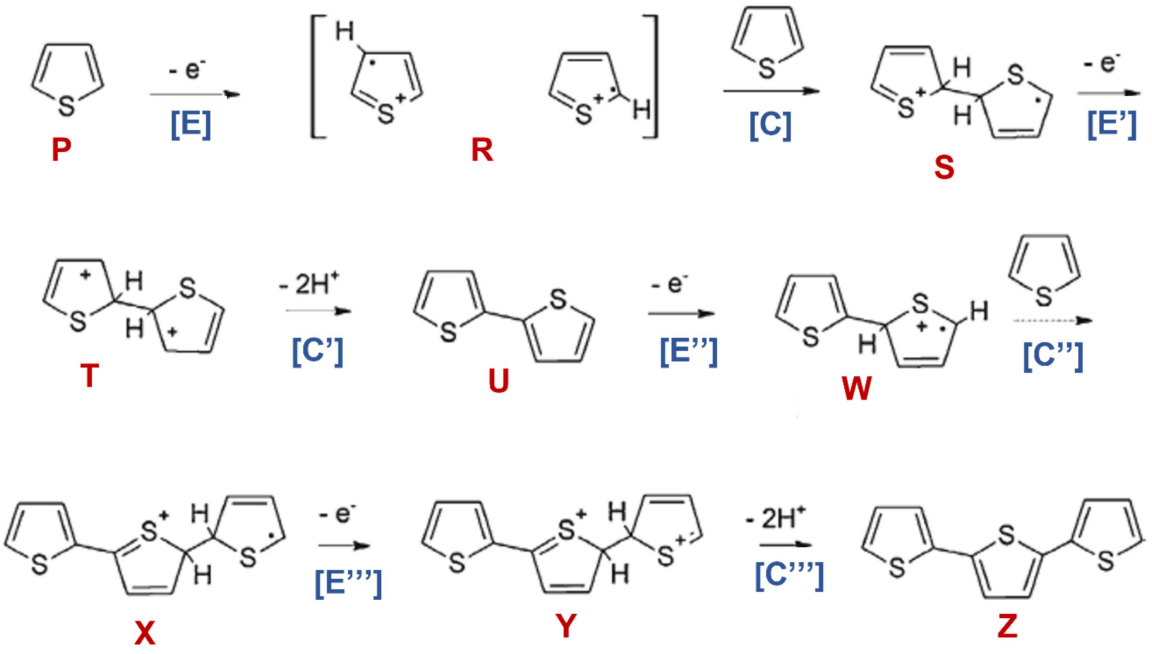

Figure 2.16 Basic mechanism of thiophene electropolymerization. Adapted from Sharma, 2012.[180]

Considering the potentiodynamic electropolymerization of thiophene, a radical cation R is most likely formed in the first [E] step of thiophene electrooxidation, manifested by an anodic peak of high positive potential. At the second [C] step, R reacts with the monomer P and the protonated dimer of a radical cation S is formed. Next, S is electrooxidized to dication T (so-called doubly charged σ-dimer) at the [E'] step. A neutral dimer U is the product of elimination of two protons [C']. Then, this dimer is oxidized in the second [E''] step, forming a radical cation W. In turn, W reacts with P in the [C''] step. These steps follow one another in accordance with the ECE'C'. mechanism to form a trimer, Z. Advantageously, the dimer R is electrooxidized at a potential lower than that of electrooxidation of the monomer P.

After the polymerization around the target molecules is terminated, the template is removed leaving behind imprinted cavities with affinity for the target (Figure 2.17).

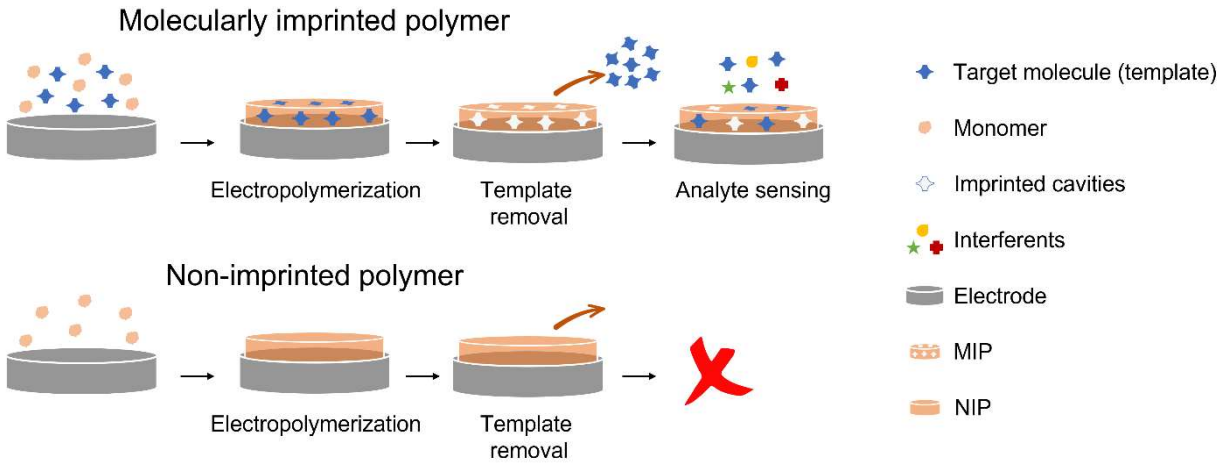

Figure 2.17 General procedure for molecular imprinting and non-imprinting processes: the chosen monomer and desired template are mixed in solution at a specified ratio. Electropolymerization is then performed, forming a layer comprised of the polymer with the trapped target on the surface of the transducer. The template is subsequently removed from the polymeric matrix. When the target is re-introduced into the system, it binds to the cavities present in the MIP film, producing a measurable change. The non-imprinted polymer, is used as negative control and it is produced with the same approach but without adding the template, thus the imprinted cavities are not created not allowing target identification (represented with an X).

Usually, for chemical and biosensing purposes a non-imprinted polymer (NIP) is also produced in the same way but without adding the template. It is used as negative control, to ensure that the analyte has specific affinity to the produced MIP and the changes observed in the transduction element are not due to non-specific binding events.

2.3.2 Electrochemical readout

Electrochemical sensors employ different electroanalytical techniques as transduction scheme. Commonly measured properties are: the current as the potential is varied – voltammetry, the current at a fixed voltage – amperometry, the voltage at zero current – potentiometry, conductivity, and capacitance or impedance changes.[179] Generally, electrochemical detection methods, such as electrochemical impedance spectroscopy (EIS), square-wave voltammetry (SWV), and differential pulse voltammetry (DPV), are among the most popular methods used in conjunction with MIPs.[182]

Applications of miniaturized electrochemical-based MIP devices

Although the early reports on electrochemical sensors with MIP elements are generally based on glassy carbon electrodes with a bulk configuration, the trend from the last decades is to use miniaturized electrodes to render lower costs and higher practicability on electrochemical measurements.

The highest icon of electrochemical devices is the glucose meter, including glucose strips that combine in the same spot (small size) two or three electrodes and allow glucose monitoring with a small drop

of blood.[184,185] The great advances generated by the glucose meters are an outcome of miniaturization, in which the multiple electrode-system is small, standing in a close and fixed position. This configuration offers many analytical advantages, such as the ability to measure small currents in the range of pico- to nanoamperes, rapid response to changes in applied potential, low Ohmic reduction in electric potential, efficient diffusional mass transport, and steady-state response at diffusion controlled potential, while requiring very low sample volumes.[186]

Generally, the commercial versions of combined electrode systems are typically based on carbon, an easily available and low-cost material, with good electrical properties. These carbon-based electrochemical devices available in the market are normally fabricated by lithography or screen-printing techniques, on top of ceramic substrates. The latter are the most common, known as screen-printed electrodes (SPEs), and their compatibility with MIP films has already been extensively demonstrated.[187–190]

A review on some of MIP applications developed by in-situ electropolymerization of MIP films on miniaturized planar electrodes, such as SPEs, using electrochemical readouts for the sensing response is presented next.

Healthcare applications: diagnostic and therapeutics

As mentioned before, cancer is responsible for millions of deaths annually and significantly constrains the quality of life from those who battle the disease and their relatives. So, the development of MIP-based strategies for cancer diagnosis and follow-up has been reported in the literature.

Ribeiro, J. A. and colleagues reported a method for the screening of the carbohydrate antigen 15-3 with the protein imprinted in a poly(Toluidine Blue) film on a gold-based SPEs (Au-SPE) platform.[191] To enhance the stability of the device a toluidine blue terminated monolayer was attached to the electrode's surface from which the polymer was then grown. The produced MIP displayed a binding affinity ~12-fold higher than the corresponding NIP and the analytical performance of the device was followed by DPV using a standard iron redox probe. The device revealed a linear response from 0.10 to 100 U/ml with a LOD below 0.10 U/ml, obtained from calibration curves with buffer and artificial serum. For the detection of the carcinoembryonic antigen (CEA), a strategy combining MIP with a natural antibody for SERS identification was reported (Figure 2.18a).[192]

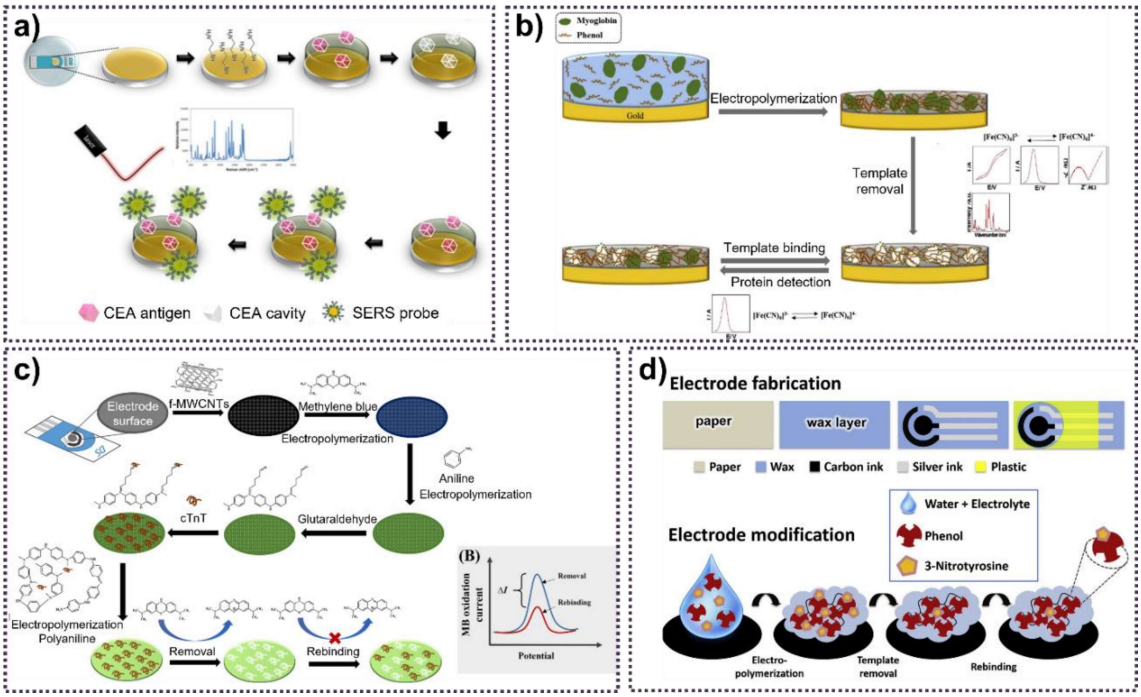

Figure 2.18 Healthcare applications – diagnostic and therapeutic: a) dual biorecognition MIP-SERS sensor for CEA screening; b) myoglobin and c) cTnT detection for cardiovascular disease's diagnosis; d) paper-based MIP sensor for 3-nitrotyrosine oxidative stress biomarker detection. Adapted from Carneiro, M. C. C. G. et al, 2019,[192] Ribeiro, J. A. et al, 2017,[193] Phonklam, K., et al, 2020[194] and Martins, G. V. et al, 2020.[195]

This strategy aimed to have a pre-concentration system, provided by the MIP film, while using the antibody combined with AuNSs and a Raman reporter to signal the presence of CEA on the MIP platform. Au-SPE electrodes were used and the use of gallic acid as monomer for MIP assembly, through electropolymerization was reported for the first time. The MIP film was assembled on the WE surface, in a self-assembled monolayer of cysteamine through bulk polymerization, by mixing the monomer and the target template (CEA) followed by cyclic voltammetry (CV) scans from -0.2 to 0.8 V at 0.025 V/s. The proposed workflow for MIP fabrication and CEA sensing offered a sensitive response down to 1.0 ng/ml, with a linear range from 1.0 up to 1000 ng/ml. This linear range had clinical relevance since CEA serum concentrations in healthy people stay below 10 ng/ml whereas levels higher than 20 ng/ml are usually indicative of malignant tumours.

Through the electropolymerization of *o*-phenylenediamine a MIP was produced by Bozal-Palabiyik, B., et al, for the electrochemical detection of vascular endothelial growth factor, which can be used as cancer biomarker.[196] The MIP layer was produced by CV on the surface of graphite SPEs and the optimized experimental conditions showed a linear detection range from 20 to 200 pg/ml and a LOD of 0.08 pg/ml.

Cardiovascular diseases are the leading cause of mortality worldwide and a few MIP-based SPEs have been reported so far. Ribeiro, J.A., and co-workers published in 2017 a platform based on the electropolymerization of phenol on Au-SPEs surface for the screening of myoglobin (Figure 2.18b).[193] The analytical performance of the sensor was investigated through SWV with an iron redox probe – calibration of the sensor with increasing concentrations of myoglobin showed sensitivities in the same order of magnitude for buffer (-6.14 x 10^{-7} A/decade) and diluted artificial serum (-6.69 x 10^{-7} A/decade) solutions, demonstrating that the serum matrix had no relevant impact on the analytical signal. More recently, Phonklam, K., et al[194] developed a MIP-based SPE biosensor based on the biomarker cardiac troponin T (cTnT) (Figure 2.18c). Aniline was electropolymerized around cTnT templates and a polymethylene blue redox probe was electrodeposited on multi-walled carbon nanotubes (MWCNTs) on carbon-based screen-printed electrodes (C-SPE). The decrease in the polymethylene blue current correlated with an increase of cTnT was followed by DPV and linearity was achieved between 0.10 to 8.0 pg/ml with a detection limit of 0.040 pg/ml.

Besides cancer and cardiovascular diseases diagnosis, the potential of MIP technology, combined with miniaturized electrodes has been demonstrated for other clinical conditions. Diouf, A., et al used electropolymerized poly(acrylamide) on the surface of Au-SPE for the detection of creatinine,[187] a marker for chronic nephritis and renal dysfunction, and salivary glucose[197] for diabetes monitoring. Pyrrole is used as monomer for several MIP-based biosensors, due to its easiness on electropolymerization, from kidney disease monitoring, using cystatin C as template and C-SPE modified with MWCNTs,[198] to Alzheimer diagnosis with interleukin-6 as the biomarker and template and C-SPE,[199] among others.[200–202]

In addition to the conventional ceramic-based SPE, paper can also be used as substrate for planar electrode's patterning. For instance, Martins, G.V., and colleagues prepared a C-SPE on regular office paper for the detection of the oxidative stress biomarker 3-nitrotyrosine, in human urine samples (Figure 2.18d).[195] The biomimetic material was produced through electropolymerization of phenol around 3-nitrotyrosine molecules with CV. After template removal, rebinding of the molecule revealed a wide linear range from 500 nM to 1 mM and a LOD of 22.3 nM. Later, Pereira, M. V., et al used a similar strategy to produce paper-based C-SPE for the screening of amyloid β-42, an Alzheimer' disease biomarker.[203] After PEDOT electropolymerization to enhance the electrode's electrical features, *o*-phenylenediamine was used as the monomer to fabricate the MIP layer around the target molecules. The vacant sites so obtained allowed for the specific rebinding of the target molecules rendering a limit of detection of 0.1 ng/ml.

Annex Table A2 shows the main characteristics of examples of MIP-based sensors developed for clinical applications, using electrochemical techniques on planar electrodes.

Environmental applications: food, dairy products, drugs, and water safety

Examples of MIP-based biosensors for environmental applications, produced through electropolymerization on planar electrodes include the screening of the antibiotic chloramphenicol (CAP) using eriochrome black T as the monomer to produce the imprinted sensing material. Herein, Cardoso, A. R. and colleagues prepared the MIP layer on top of C-SPE by chronoamperometry at +0.95 V for 250 sec.[204] Calibration curves were performed using EIS and SWV and a standard iron redox probe was used to follow the changes in the electrical properties of the sensing surface. In EIS calibrations a linear response was observed from 1 nM to 100 μM with a LOD of 0.26 nM whereas by SWV the linear behaviour was found in the same range, although with a slightly higher LOD of 0.65 nM. Selectivity studies were also performed with common interferents showing no relevant changes in the electrochemical response.

For the control of lactose in dairy products, da Silva, J. L. and co-workers prepared a MIP film by electropolymerizing pyrrole, in the presence of lactose, on a graphite paper electrode (Figure 2.19a).[205] The analytical performance of the optimized sensing device was analysed by DPV using a standard iron redox probe revealing two dynamic linear ranges of 1.0 to 10 nM and 25 to 125 nM with a detection limit of 0.88 nM.

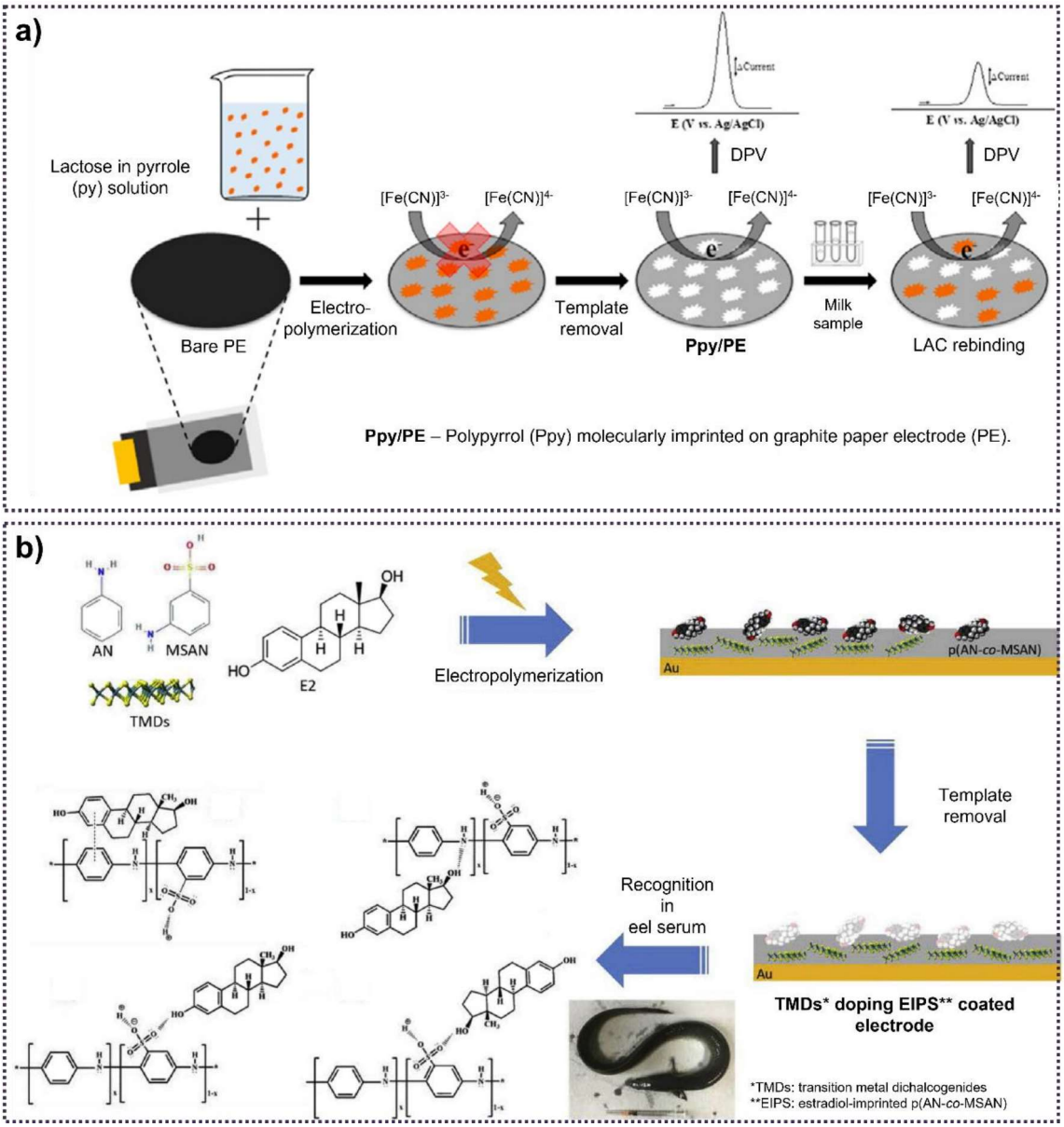

Figure 2.19 Environmental applications – food, dairy products, and water safety: a) lactose screening on milk samples; b) detection of estradiol hormone in eel serum samples. Adapted from da Silva, J. L. et al, 2021,[205] and Lee, M.-, H. et al, 2020.[206]

For the screening of a steroid hormone, 17 β-estradiol – used for instance in aquaculture – Lee, M.-, H. et al[206] and Truong, T. N. L., et al[207] found strategies to improve sensor sensitivity. Lee used modified SPE with transition metal dichalcogenides (Figure 2.19b) whereas Truong used C-SPE decorated with AuNPs. The latter stated that the harmonic distribution of AuNPs on the electrode's surface aids in the formation of a single oriented monomer layer onto the electrode, which in turn renders highly homogeneous polymeric matrices with low thickness, facilitating template removal. The developed sensing strategy rendered an LOD down to 2 fM with a linear detection response from 10 fM to 100 nM. Lee's approach consisted of doping the electrode's surface with tungsten disulphide (WS_2) and co-polymerized aniline and metanilic acid – poly(AN-*co*-MSAN) – around the template molecules of

the steroid hormone. This device was used to screen the hormone in eel serum samples with an accuracy of 94.4% when compared with a commercial sensing kit.

MIP-based planar electrochemical platforms have also been used in other applications such as in the profiling of cocaine samples, as reported by Grothe, R.A., and colleagues.[190] Benzocaine was used as the template molecule and 3-amino-4-hydroxybenzoic acid as the functional monomer onto SPEs with carbon ink as working electrode. The molecular recognition of benzocaine was achieved, in artificial urine samples, with a LOD down to 2.9 nM, by SWV. The method was successfully used to profile genuine cocaine samples, assisted by principal component analysis.

Annex Table A3 shows the main characteristics of examples of MIP-based sensors developed for environmental applications, using electrochemical techniques on planar electrodes.

2.3.3 Laser-induced graphene as an alternative for electrode's patterning

Although SPEs have been widely used for electrochemical sensing approaches, the fabrication of these devices require sometimes complex processes rendering expensive and time-consuming production procedures.[208] Besides, the use of these fabrication routes can significantly restrict the advances of electrochemical biosensor's academic research due to the difficulties on easily testing different architectures that can provide enhanced results or even the development of multifunctional and multimodal platforms. Overall, the development and application of one-step, scalable and versatile approaches for carbon-based electrodes patterning is essential.

Moreover, the sensitivity of MIP devices is related to the number of imprinted sites formed on the sensor surface. In conventional planar electrodes, such as SPEs, imprinting can face some obstacles, including restricted mobility and agglomeration of the cavities, compromising selectivity due to poor accessibility to the imprinted sites. The formation of nanostructured surfaces seems to be a promising way to overcome these problems. Compared to planar surfaces, nanostructured surfaces can offer high surface-to-volume ratio, thereby increase the number and proportion of sites available after electropolymerization. Based on this, some researchers have focused on the preparation of MIPs using matrices that can further increase the number of printable sites.[194,206,207]

Laser-Induced Graphene (LIG) is a nanostructured 3D carbon-based material, that can be used as electrode substrates, and it is produced by laser irradiation of substrates, in a mask-less approach offering low-cost and freedom of design for the electrode's architecture patterning.

This method LIG was used in this thesis for the fabrication of MIP-based electrochemical sensors.

Graphene: characteristics and production methods

Since its discovery in 2004, graphene-based nanomaterials have been broadly used due to their inimitable set of physical and chemical properties.[209] Owing to its distinctive and exceptional characteristics, graphene has proven to be broadly applicable in several fields, such as energy storage, electronics, catalysis, remediation and biotechnology.[210,211] Moreover, in many applications graphene, can be engineered into 3D porous structures to render higher surface areas while maintaining its high mobility and mechanical stability.[212]

Graphene is a one-atom thick sheet of sp^2-hybridized carbon atoms arranged in an honeycomb lattice where each atom shares with neighbours three in-plane σ-bonds and an out-of-plane π-bond, with an average interatomic distance of 1.42 Å. Due to its unique combination of crystallographic and electronic structures, this material exhibits high surface area (2630 $m^2 \cdot g^{-1}$), carrier mobility (~250,000 $cm^2 \cdot V^{-1} \cdot s^{-1}$), thermal conductivity (around 2000 - 4000 $W \cdot m^{-1} \cdot K^{-1}$) and transmittance (visible light and near infrared (IR) absorption ~2-3%) with excellent mechanical properties (Young's modulus: 1 x 10^{12} Pa), flexibility, good chemical stability and biocompatibility.[211,213,214]

However, despite intensive research efforts, chemical-free, low temperature and cost-effective processing of high quality graphene onto substrates remains a massive challenge.[213] Conventionally, graphene can be produced with different physical and chemical-based techniques. This includes mechanical exfoliation of graphite, chemical vapor deposition onto metallic substrates from gaseous hydrocarbon precursors and thermal decomposition and reduction of graphene oxide.[214,215] Nevertheless, these methods require either high processing temperatures, multi-step synthesis routes and/or the use of expensive precursors which significantly limits the scale-up of the current production methods, dropping their wide-spread commercial potential. Therefore, straightforward production methods that allow for simple, cost-effective, and scalable graphene-based material's production and patterning are absolutely needed.

Laser-induced graphene: conversion mechanism, characteristics, and applications

Laser-assisted processing techniques have emerged as powerful tools in a multitude of applications from materials manufacturing to medical treatment.[216] Specifically, Laser-Direct Writing (LDW) enables direct surface treatment and processing of materials in a mask-less, catalyst free, non-toxic, controllable and non-contact approach whilst allowing flexible, rapid and efficient processing of complex structures for laser macro, micro and nano manufacturing.[213]

In 2014, Tour, J. research group from Rice University in Houston, Texas published the paper: "Laser-induced porous graphene films from commercial polymers", reporting a method to induce 3D porous graphene in polymeric substrates using LDW which was termed as Laser-Induced Graphene – LIG.[217]

As the group stated in a subsequent paper, the discovery of LIG was a fluke: *"This was a serendipitous discovery when J. Lin of our group was attempting to lase GO dispersed upon a PI film. The laser missed the GO target and the PI was lased, becoming black. Upon checking the Raman spectrum, Lin noticed that the PI-bound black material was graphene!"*[216]

The conversion of commercially available polymers to LIG, such as polyimide (PI), was achieved by Tour's, group, using a common CO_2 laser system – with a wavelength of 10.6 μm – often found in machine shops for cutting and engraving purposes (Figure 2.20).

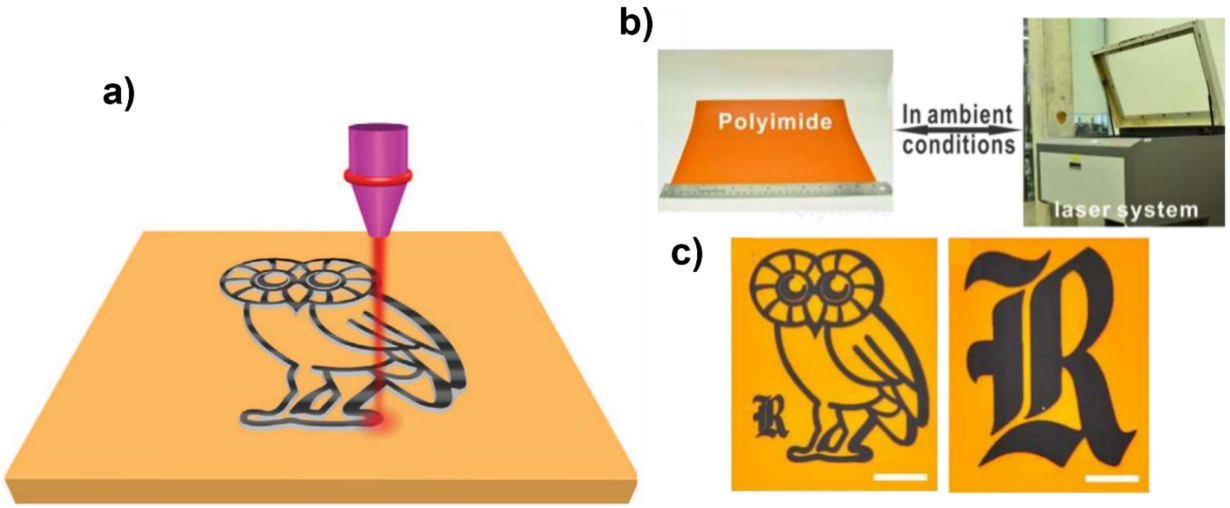

Figure 2.20 Materials and equipment for LIG fabrication from PI substrates by LDW: a) Schematic of the synthesis process of LIG from PI; b) photographs of the polyimide sheet, commercially known as Kapton, and the laser cutting system used by the authors; c) photographs of LIG as an owl and the letter R patterned on PI substrates. The black features are LIG, and the orange background is polyimide. Scale bar, 5 mm. Adapted from Lin, J., et al, 2014.[217]

The chemical structure of PI is particularly suitable for the generation of LIG, because of the presence of aromatic sp^2 carbons that are more prone to form the hexagonal graphene structure than other precursors, which just generate amorphous carbon (Figure 2.21).[214]

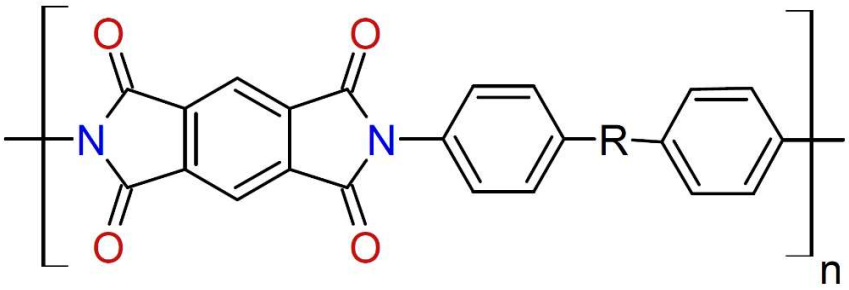

Figure 2.21 Chemical structure of polyimide.

Although the exact mechanism of PI conversion into LIG with infrared lasers is not fully detailed yet, it is believed that it is most likely due to a photothermal effect. Generally, photothermal effects occur in lasers with long wavelengths with relatively long pulses, such as the CO_2-InfraRed laser, whereas photochemical processes tend to occur in lasers with short wavelengths and pulse widths. The created energy upon laser irradiation onto the substrate generates lattice vibrations which leads to high localized temperatures (~2500 °C) able to break the C – O, C = O and N – C bonds of PI. Furthermore, small molecules are released as gases, while the aromatic compounds rearranged themselves into a graphenic structure.[217] The proposed mechanism, of PI conversion into LIG, was confirmed by the dramatic decrease in oxygen and nitrogen contents in LIG observed by high resolution X-ray photoelectron spectroscopy (XPS) showing the dissociation of the C – O, C = O and N – C bonds of PI (Figure 2.22a).[214,217]

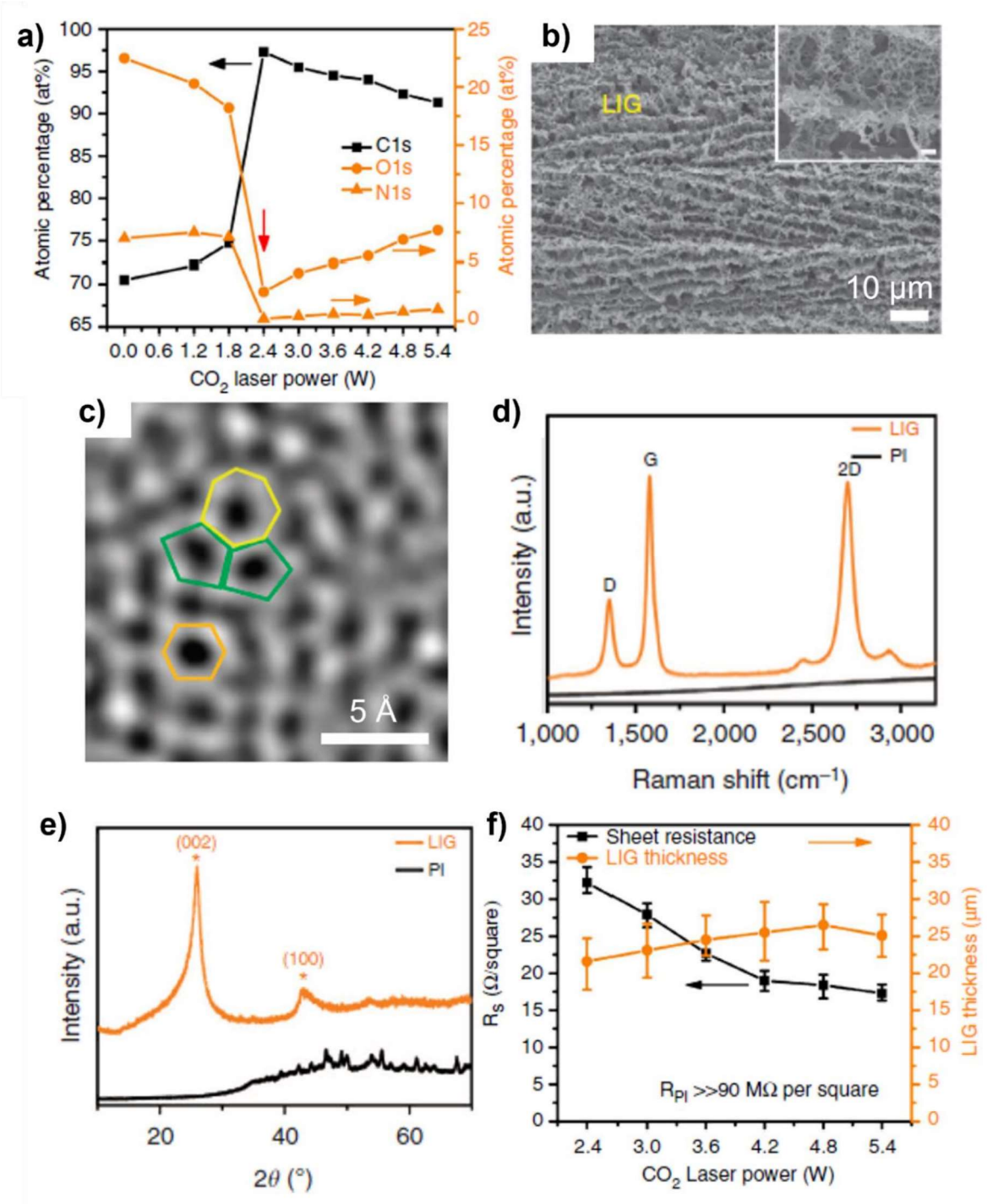

Figure 2.22 LIG characterization: a) Atomic percentages of carbon, oxygen and nitrogen as a function of laser power obtained with high-resolution XPS; b) SEM image of the LIG film; c) TEM image of LIG showing the heptagon with two pentagons, as well as a hexagon; d) Representative Raman spectrum of a LIG film and the starting PI film; e) XRD of powdered LIG scraped from the PI film and PI; f) Correlations of the sheet resistance and LIG film thicknesses with laser powers. Adapted from Lin, J. et al, 2014.[217]

The resulting material presents an hierarchical structure with abundant wrinkles on the graphene surface, with a surface area of ~340 $m^2 \cdot g^{-1}$ – comparable to the 3D graphene obtained by wet-chemistry – high thermal stability (>900 °C) and excellent conductivity (5 - 25 $S \cdot cm^{-1}$).[212,215] LIG surface morphology

is foamy-like and it is characterized by a complex and inhomogeneous porous pattern resultant from the rapid generation of gases during irradiation, as shown by scanning electron microscopy (SEM) (Figure 2.22b). Moreover, contrary to the ordinary hexagonal lattice of graphene, scanning transmission electron microscopy (STEM) imaging of LIG revealed a hexagon and pentagon-heptagon hybrid lattice (Figure 2.22c). This is termed as "kinetic graphene" due to the rapid cooling upon laser irradiation leaving no time to equilibration to the fully hexagonal lattice.[212,214] Additionally, Raman spectroscopy and X-ray diffraction (XRD) further confirm the graphenic nature of LIG. Raman analysis shows the typical 2D band centred at 2700 cm^{-1} associated with randomly stacked graphene layers and the D-band resultant from the presence of defects (Figure 2.22d). The low I_D/I_G ratio is characteristic of a highly crystalline graphene structure – also corroborated with the sharp (002) XRD peak (Figure 2.22e) and the calculated I_{2D}/I_G ratio of ≈1 indicates the graphene is few-layered, which is consistent with the structure observed by STEM.[215–217] Additionally, the authors investigated the influence of laser parameters, such as power and scan rate on the sheet resistance of the resultant LIG (Figure 2.22f) – in the tested range, as the laser power increased up to 5.4 W the sheet resistance decreases up to a minimum value of < 15 Ω/square.

Advantages of the established method include: selective and localized reduction with flexibility in patterning the desired device's architectures with fully customizable geometries, combined with the need of minimal infrastructure (computer-controlled laser rastering system operating in air), low-cost and high-throughput makes this technology suitable for roll-to-roll manufacturing, critical for future commercial applications of LIG-based devices.[214,215,217] In fact, the discovering authors proposed a strategy for the roll-to-roll production of LIG with subsequent development of hybrid materials, serving different applications (Figure 2.23).[212]

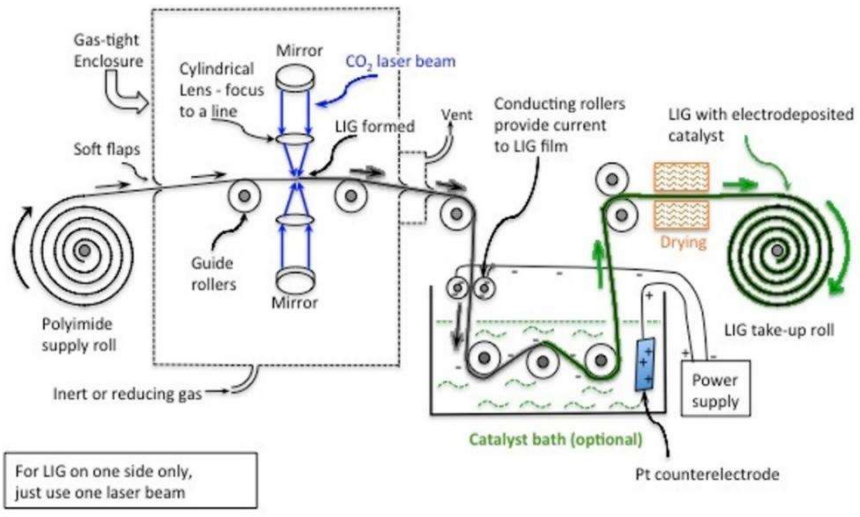

Figure 2.23 Proposed scheme for roll-to-roll production of LIG films and functional LIG-based devices. Adopted from Ye, R., et al, 2018.[212]

The strategy includes a LIG forming chamber and an optional catalyst electrodeposition bath. The PI sheet is then fed continuously into the lasing chamber by a supply roll and the in-plane 3D LIG film will form on two-sided irradiation. After that, the LIG film can be immersed into a catalyst electrodeposition bath for the formation of hybrid materials. The film is then collected by a take-up roll upon drying.

Since the discovery of PI conversion to LIG by CO_2 laser irradiation, the method has been employed in a number of devices and applications, as in biosensors,[35,218–224] supercapacitors,[225–227] water-splitting electrodes for energy storage,[228] as adsorbent for water treatment,[229] antimicrobial devices[211,230] and UV sensors[231] (Figure 2.24).

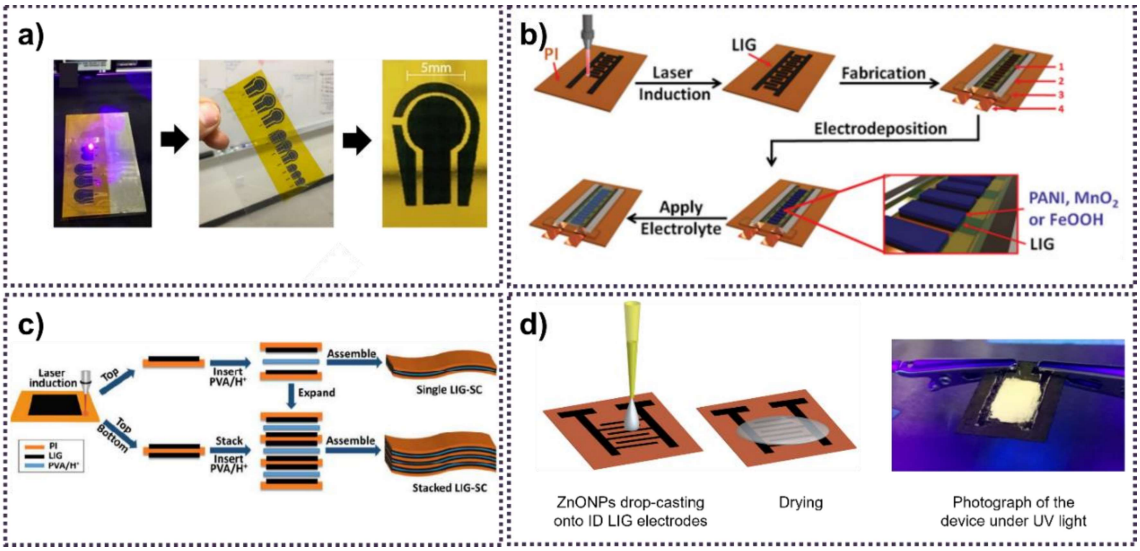

Figure 2.24 Schematic representation of workflows to produce PI-derived LIG applications fabricated with an IR laser: a) electrochemical glucose sensor; b) pseudocapacitive microsupercapacitor; c) stackable supercapacitor; d) UV sensor with ZnO nanoparticles as the sensitive layer. Adapted from Tehrani, F., et al, 2016[224], Li, L, et al, 2016[225], Peng, Z., et al, 2015[227] and Samouco, A, et al, 2018[232].

Despite the successful implementation of PI-derived LIG in different applications, the reliance on PI as the polymer precursor for the formation of LIG is a limitation. Recent efforts have been made to produce LIG from other carbon-based substrates – LIG can now be obtained from a variety of materials, ranging from thermoplastic polymers, phenolic resins, biopolymers like lignin and even textiles, cellulose, wood, cork or even food (e.g., potato skins, bread and coconut shells).[214,233–236]

Initially, a way to create LIG from wood was attained by using controlled inert environments, as reported by Ye, R. and colleagues in 2017.[234] Later, a multiple lasing strategy was established which enabled the conversion of an even larger variety of carbon-containing materials in ambient atmosphere, thus simplifying the production procedure for LIG. In this case, the LIG precursor is first converted to amorphous carbon by a first laser scribing, then the amorphous carbon turns to crystalline graphene

by further lasing. This two-step LIG conversion mechanism was explained by the fact that amorphous carbon is a heterogeneous material consisting of sp^2 carbon clusters embedded within a sp^3 carbon matrix and it has a strong IR absorption in a range from ~700 to 1200 cm^{-1}. CO_2 lasers output a band centred at 10.6 μm (943.40 cm^{-1}) but ranges between 927 and 951 cm^{-1}. These frequencies are absorbed by the C–C bonds present in the precursor substrate materials that are not present in LIG. As such, it is likely that these substrates are first photothermally converted to amorphous carbon. Subsequent exposures of the amorphous carbon then effect the transformation to graphene.[233]

In general, multiple lasing allows almost any carbon precursor that does not ablate when exposed to a CO_2 laser beam to be converted into LIG. High-temperature engineering plastics such as PI, Kevlar, polysulfones, poly(ether imide), and polyphenylene sulphide are readily converted into LIG, without any pre-treatment required. Cross-linked polymers such as phenolic resin and cross-linked polystyrene are also suitable substrates for LIG formation. While lignin is the only natural polymer that was found that can be converted directly to LIG, polysaccharides such as cellulose and starch can be readily activated for conversion into LIG with the application of fire-retardant agents. Another approach is the use of UV lasers, which enable the conversion of even more precursors like PDMS with increased resolution.[214,233]

Finally, the modification of LIG with heteroatom doping or the formation of composites has been employed as an effective approach for the engineering of the material's properties, increasing the potential of LIG for other applications.[215]

Laser-induced graphene for biosensors

In the biosensor's field LIG has been implemented as carbon-based electrodes for electrochemical sensing.[215,223,235,237,238] Compared to graphene fabricated with conventional methods, LIG generates defects, which is not always a disadvantage, as it has been demonstrated that electron transfer kinetics can be enhanced at graphene edge sites due to its abundance in corrugations and defect densities.[215] Although the research on LIG-based biosensors field is still in the early stages it has been steadily growing, and some reports have already shown LIG potential for practical applications. Reported LIG-derived biosensors include strategies for ionic species,[239,240] small molecules[219,241] and nucleic acids[242] detection, either by using natural bioreceptors[241,243] and/or catalytic nanostructures, such as platinum[219] or copper nanoparticles[224].

Glucose levels quantification, with clinical relevance for diabetes monitoring, was attained with LIG electrodes, following both enzymatic and non-enzymatic assays. Pereira, S.O., et al used a CO_2-IR laser,

with 10.6 μm wavelength, for the enzymatic quantification of glucose levels. Settu, K., and colleagues used a 405 nm laser for the photoconversion of PI tape to LIG and an enzymatic assay with glucose oxidase (GOx) with chitosan, to facilitate immobilization of GOx onto LIG surface.[244] This workflow allow the authors to obtain a LIG-based glucose biosensors with a sensitivity of 43.15 $\mu A \cdot mM^{-1} \cdot cm^{-2}$ and an LOD of 0.431 mM.

Following enzyme-free approaches, a PI film was doped with a salt-based cobalt ink to directly and simultaneously pattern LIG electrodes decorated with Co_3O_4NPs (Figure 2.25a), for the catalytic action over glucose molecules, yielding a sensitivity of 214 $\mu A \cdot mM^{-1} \cdot cm^{-2}$, a LOD of 0.41 μM and a response time of 0.49 sec.[245] Moreover, Zahed, M.A. and co-workers, fabricated LIG electrodes on PI films, with a 10.6 μm laser, that were modified with PEDOT:PSS and Pt@Pd NPs for glucose quantification and with polyaniline (PANI) for pH assessment.[246] The analytical features obtained with the developed sensing device were a linear range from 10 μM to 9.2 mM with a sensitivity of 247 $\mu A \cdot mM^{-1} \cdot cm^{-2}$ and a LOD of 3 μM for glucose and, a linear range of pH 4 – 7 and a sensitivity of 75.06 mV/pH, for pH assessment.

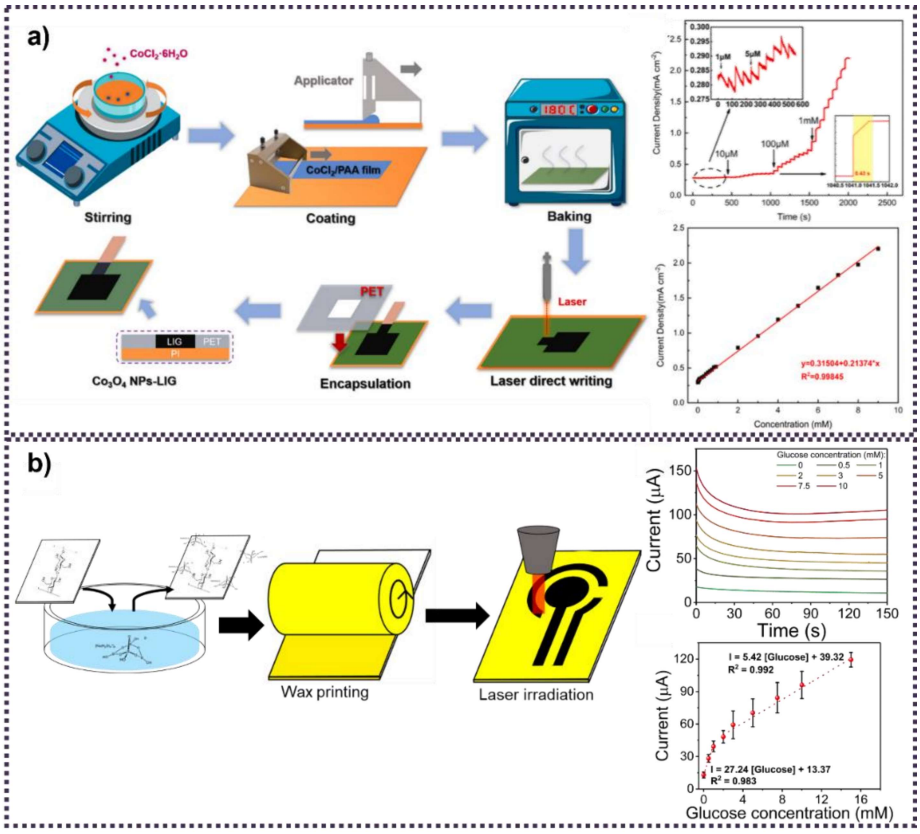

Figure 2.25 LIG-based biosensors for glucose levels assessment: a) Schematic illustration of the produced of the Co_3O_4NPs-LIG biosensor, from a PI substrate coated with a $CoCl_2$/poly(amic acid) ink, and respective amperometric response of Co_3O_4NPs-LIG biosensors to various concentrations of glucose at an applied potential of +0.55 V with the correspondent calibration curve; b) Schematic procedures for the fabrication of LIG from Whatman paper for glucose quantification by chronoamperometry with the correspondent calibration curve. Adapted from Zhao, J., et al, 2021[245] and Pinheiro, T., et al, 2021.[236]

Based on an electrochemiluminescence assay, Bhaiyya, M., et al[247] prepared LIG electrodes from a PI film, with a 10.6 μm laser, for the detection of not only glucose but also H_2O_2, lactate and choline. The method allowed to achieve linear ranges from 0.1-50, 0.1-70, 1-100 and 1-100 μM with respective LODs of 4.36, 2.51, 5.32, 4.01 μM for H_2O_2, glucose, lactate and choline, respectively.

Finally, for glucose levels quantification, alternative substrates, coming from sustainable sources, were also reported for LIG photoconversion. With a phenolic resin and a 405 nm laser a three-electrode architecture was patterned for the enzymatic electrochemical determination of glucose levels attaining a linear range from 0.1 to 10 mM.[248] Other examples of alternative carbon sources for LIG preparation, with a 10.6 μm laser, include lignin for the enzymatic multidetection of glucose, lactate and alcohol in sweat matrix, with a LIG doped with N and decorated with MXene/Prussian Blue[249] and Whatman paper, pre-treated with a fire-retardant agent, for the enzymatic quantification of glucose levels, with a detection limit of 0.13 mM (Figure 2.25b).[236]

Besides glucose quantification, other LIG-based biosensors were already reported in the literature. Impedimetric or capacitive immunosensors were developed onto LIG surfaces for pathogen detection,[250,251] cancer diagnosis[252] or thrombin monitoring.[253] For *Escherichia coli* O157:H7 detection, a PI film was coated with metal precursors for the simultaneous conversion to interdigitated LIG electrodes decorated with metallic nanoparticles (Figure 2.26a), achieving an LOD of 10^2 CFU/ml within a linear range from 10^2 to 10^8 CFU/ml.[250] *Salmonella enterica* was detected in chicken broth with an electrochemical impedimetric assay based on LIG electrodes, prepared with a 10.6 μm laser in a PI film, with a LOD of 13 ± 7 CFU/ml (Figure 2.26b).[251] A label-free electrochemical immunosensor assay was designed for the monitoring of cancer biomarker, CEA, with LIG prepared from a PI film with a 405 nm laser and decorated with AuNPs. A linear range from 0.01 to 100 ng/ml with a LOD of 5.0 pg/ml was achieved.[252]

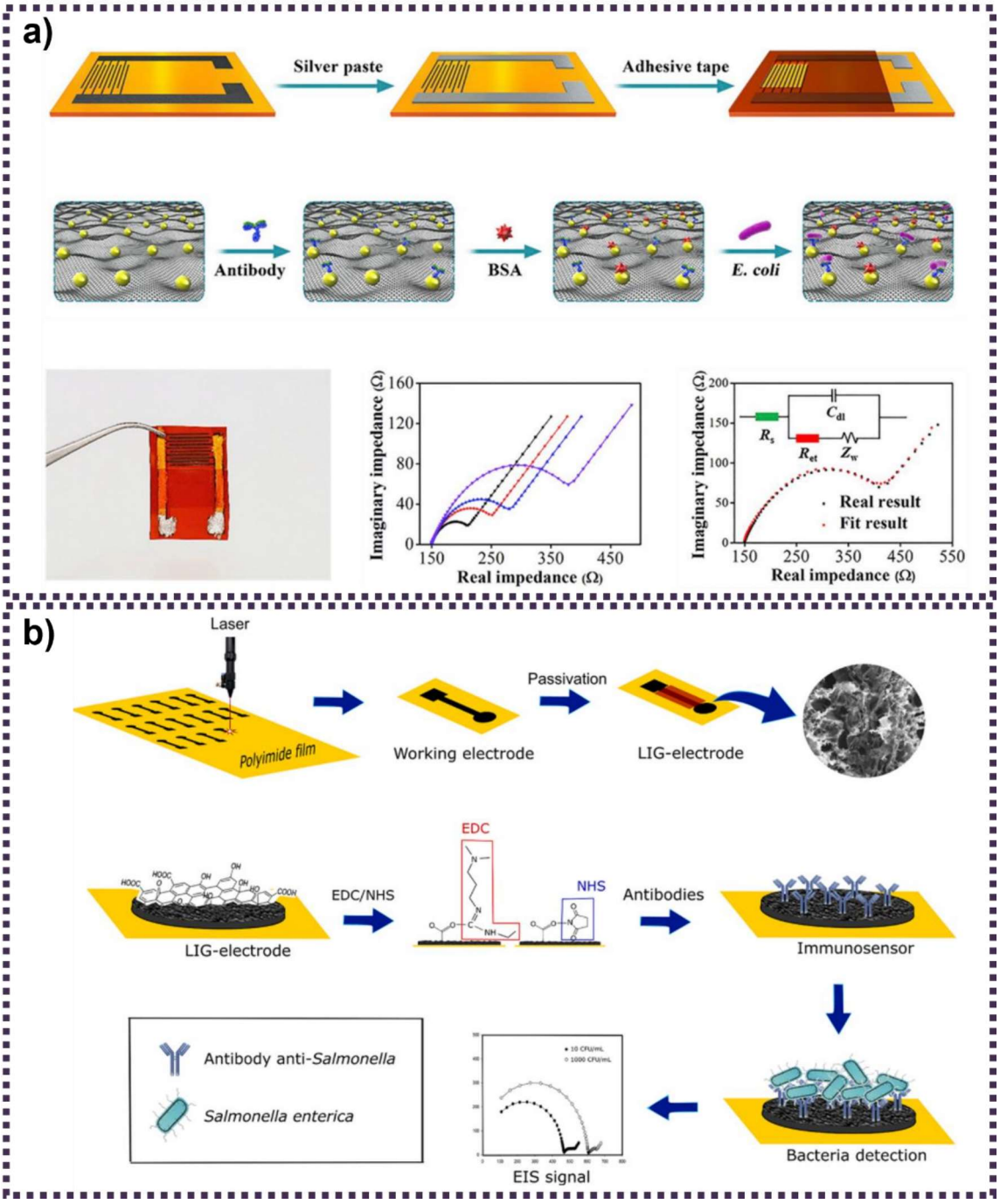

Figure 2.26 LIG-based biosensors for pathogen detection: a) Schematic illustration of the fabrication process of the AuNPs-LIG interdigitated array for the detection of *E. coli* O157:H7, with the respective photograph of the prepared the AuNPs-LIG biosensor, and the Nyquist plots obtained with AuNPs-LIG electrode (black line), antibody modification (red line), BSA blocking (blue line), and bacteria capture (purple line); b) Schematic illustration of the workflow for the fabrication of the LIG-based immunosensor for *S. enterica* detection. Adopted from You, Z., et al, 2020[250] and Soares, R., et al, 2020.[251]

Pesticides monitoring LIG-based biosensors prepared in PI substrates converted to LIG, with a 10.6 μm laser, were developed for atrazine quantification, with an enzymatic electrochemical assay, attaining a sensitivity of 28.9 nA·μM^{-1}.[254] A wearable pesticide monitoring device for plants and crops was

developed by Zhao, F. and colleagues, using methyl parathion as model molecule to demonstrate the concept (Figure 2.27).[255]

Figure 2.27 Schematic representation of the fabrication process of LIG onto PI and transference to PDMS, and respective functionalization, and photographs and electrochemical results of in-situ analysis of methyl parathion on the surface of different agricultural products (spinach and apple). Adapted from Zhao, F., 2020.[255]

LIG conductive surfaces were induced in PI substrates and transferred to flexible and conformable PDMS. Upon transferring, the LIG sensing area was modified with AuNPs and an electrochemical assay, based on organophosphorus hydrolase, was carried out yielding a LOD of 0.01 μM in a linear range from 20 to 500 μM.

A visible 405 nm laser was used to convert PI substrates to LIG that were applied to nitrogen sensing in soil[256] and nitride detection.[257] Also, using a 405 nm laser, Vanegas, D.C. and co-workers developed an electrochemical assay with LIG modified with copper nanoparticles (CuNPs) and diamine oxidase for biogenic amines detection in food. The authors achieved with this method a sensitivity of 23.3 $\mu A \cdot mM^{-1}$ and a LOD of 11.6 μM, with a response time of 7.3 sec.[258]

Araujo, W.R., and colleagues developed a paperboard-based LIG electrochemical device, prepared with a 10.6 μm laser, with a successful implementation for different analytical applications in the clinical, pharmaceutical, food, and forensic fields.[235] Following, Martins, A.B., et al and Tasić, N., et al developed electrochemical assays for sulphites detection in commercial beverages[259] and lead monitoring,[260] respectively, with LIG electrodes prepared with a 10.6 μm laser, onto a paperboard substrate, thus demonstrating the feasibility of low-cost substrates, as paperboard, for LIG patterning, and implementation on environmental and food control applications.

Annex Table A4 shows the characteristic and analytical features of some of the reported LIG-based biosensors.

Additionally, the capability of LIG electrodes to be integrated in multimodal sensors, to gather signals from both chemical and physical sensors has also been demonstrated. Examples of sweat-based wearable hybrid sensors, with integrated temperature, strain and chemical (uric acid and tyrosine) sensing has been reported by Yang, Y. and co-workers,[261] whereas Xuan, X., et al developed a stretchable and flexible device to monitor glucose levels, pH and electrocardiogram.[262] Moreover, Yu, Y., et al reported a multiflavor sensing system, which consisted on PI-derived LIG functionalized with AuNPs, rGO, and PANI for sensing NaCl, sugar, and vinegar.[263]

As mentioned before, LIG-based electrodes can be beneficial for MIP-derived sensing strategies. So, in this PhD work it is demonstrated the use of such electrodes as platform for MIP procedures for both single and dual detection of molecules. Following the work presented herein in this subject, which was the first to report the combination of LIG with MIP technologies, and resulted in two peer-reviewed publications,[35,222] other works have been reported in the literature using the same approach. For instance, Salama, K.N., research group prepared LIG electrodes, with a 10.6 μm laser, onto PI substrates, with a three-electrode architecture, for the fabrication of MIPs to be used as sensing layer for the detection of bisphenol A (BPA)[264] and the cancer marker Her-2[265] (Figure 2.28).

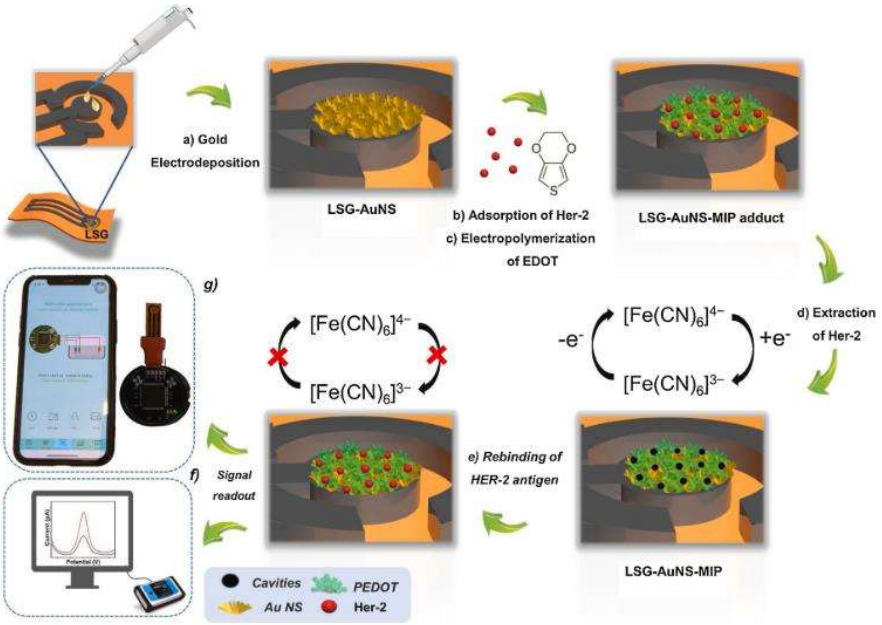

Figure 2.28 Schematic representation of the procedures for the fabrication and utilization of a MIP-based biosensor with LIG electrodes patterned onto a PI film, for the electrochemical detection of a cancer biomarker (Her-2). Adopted from Lahcen, A., 2021.[265]

For BPA detection, pyrrole was used as the monomer and BPA as the template, achieving a high selective biosensing assay, with a linear range between 0.05 and 20 μM and a LOD of 8 nM. For Her-2

monitoring, EDOT was used as the monomer, and the developed sensing strategy showed an excellent ability to detect Her-2 in the concentration range from 1 to 200 ng/ml, with a LOD of 0.43 ng/ml.

CHAPTER 3

Materials and devices: fabrication and characterization techniques

Chapter 3. Materials and devices: fabrication and characterization

This chapter summarizes the experimental procedures followed for the fabrication and application of the cellulose-based SERS and LIG-based MIP platforms during this thesis. Additionally, the characterization techniques used for the developed nanobiosensing platforms studies are also described.

3.1 Cellulose-based SERS platforms

Herein, optical nanobiosensing platforms based on SERS were fabricated using cellulosic materials as substrates. The fabrication of the SERS platforms was carried out following both physical and chemical routes to produce AgNPs and AuNPs. Three types of SERS platforms were developed, optimized, and used for the screening of both simple molecules and complex biostructures:

(i) AgNPs produced by a physical process onto a cardboard substrate were used for the quantification of the antibiotic tetracycline spiked in milk samples;
(ii) AgNPs produced by a chemical process onto a nanocellulose substrate were used for the profiling of exosomes for breast cancer diagnosis;
(iii) AuNPs produced by a chemical process onto a nanocellulose substrate were used for the screening of the SARS-CoV-2 spike protein.

3.1.1 Cellulose-based substrates preparation

Cardboard substrate

The cardboard substrate, commercially known as Tetra Pak®, was used as received, supplied by StoraEnso (Helsinki, Finland), and used for the growth of AgNPs, by a physical route. The substrate is composed by pressed cellulose fibres, polymeric coatings, and evaporated aluminium, with a thin native oxide (Al_xO_y) layer present on top of the aluminium layer (Figure 3.1).

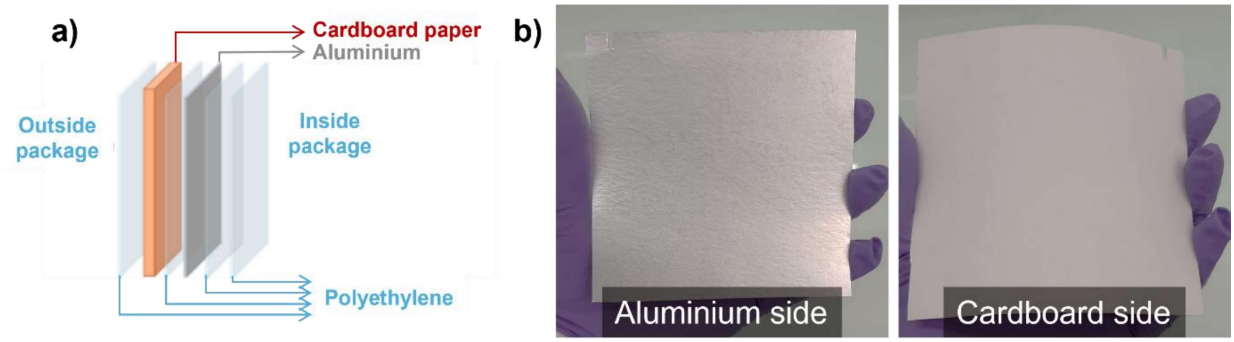

Figure 3.1 a) Illustration of the composition of the cardboard substrates used. Adopted from Pimentel, A., et al, 2017[266]; b) Photographs of the cardboard substrate used.

Nanocellulose membrane

Nanocellulose (NC) membranes were used as the substrate for the growth of plasmonic nanoparticles (AgNPs and AuNPs) by a chemical route. The workflow employed to obtain NC membranes is depicted in Figure 3.2. Raw *nata de coco* cubes obtained from the bacterial fermentation of coconut water or milk were purchased from Zhen Xin Canned Food. Since the cubes are sold in a preservation syrup, sugar was removed from the *nata de coco* cubes by water/ethanol washing cycles (4 hours each for 48 hours) under constant stirring. Afterwards, while still wet, the cubes were pre-pressed using a manual press (HeatPressUK, Swing-a-way) for 15 minutes. After fully dried (desiccator vacuum at room temperature), the membranes were submitted to 10 ton pressing for 2 minutes, using a Manual Hydraulic Press (Specac, 15-ton max.), to ensure thickness homogeneity (between 40-50 μm, measured with Mitutoyo digital micrometer).

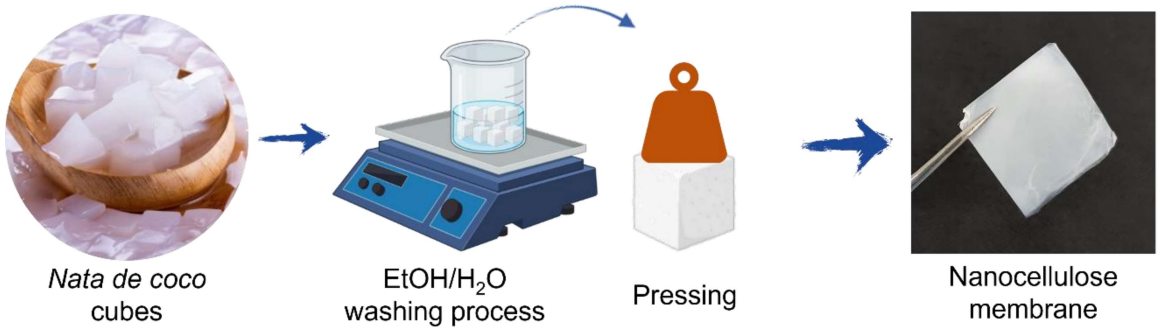

Figure 3.2 Schematic representation of the workflow to obtain nanocellulose membranes and photograph of the resulting membrane.

Characterization

The chemical structure of the obtained NC membranes was assessed by Fourier Transform Infrared Attenuated Total Reflectance (FTIR-ATR) spectroscopy (Nicolet iS10 FT-IR Spectrometer, Thermo electron corporation, Massachusetts, USA) with a 600 to 4000 cm^{-1} wavenumber scan. X-Ray diffraction

(XRD, Malvern Panalytical, X'Pert Pro, Surrey, UK), equipped with a CuKα target with a wavelength of 1.5406 Å was used to study cellulose diffraction peaks. The membranes were morphologically analysed through Scanning Electron Microscopy (SEM, Carl Zeiss AURIGA FIB-SEM Crossbeam, Oberkochen, Germany). In addition to SEM analysis, Atomic Force Microscope (AFM, Olympus AC160TS, Tokyo, Japan) imaging was also performed for further morphological surface analysis as well as the determination of sample rugosity, using the *Gwyddion* software.

3.1.2 SERS platforms produced by physical processes

Thermal evaporation was used to fabricate a SERS platform based on AgNPs deposited onto the carboard substrate. This SERS platform was produced by our group (CENIMAT|i3N), as shown by Araújo, A., et al, 2014, and it is fully described and characterized elsewhere.[267] From hereafter this platform will be named as: **TP@AgNPs**.

Briefly, AgNPs were obtained by the deposition of metal layers (silver metal pieces with 99,99% purity, supplied by CERAC, Inc. (Milwaukee, Wisconsin, USA)) directly on the cardboard substrate (10×10 cm^2) using an electron gun-assisted thermal evaporation approach, while the substrate was kept at 150 °C during the thermal evaporation. The deposition was conducted under a working pressure of 10^{-5} mbar and a deposition rate of 0.07 $nm \cdot s^{-1}$ until the thickness of the Ag film reached 6 nm. The thicknesses and growth rates of the films were inferred by a calibrated quartz crystal detector.

Characterization

The cardboard substrate surface after the NPs deposition was imaged by SEM and the average height of the AgNPs was measured by AFM in ac mode.

3.1.3 SERS platforms produced by chemical processes

Microwave-assisted irradiation was used for the in-situ hydrothermal growth of plasmonic nanoparticles onto NC membranes. The syntheses were performed in a Discover SP microwave reactor from CEM Corporation (NC, USA). Prior to use, all glassware was soaked in aqua regia (HCl/HNO_3 3:1, v/v) for 24 hours and rinsed with Millipore water. All chemicals were used as received without further purification. Distilled water passed through a Millipore water system was used in all experiments.

Herein two types of SERS platforms were produced using silver nanoparticles (from hereafter named as **NC@AgNPs**) and using gold nanoparticles (from hereafter named as **NC_{inc}@AuNPs**).

NC@AgNPs platform fabrication

The synthesis protocol followed a previously published method with few modifications by Ajmal, M.C., et al, 2016.[268] Briefly, a volume of 10 ml of $AgNO_3$ solution (silver nitrate, 99.0%, Sigma-Aldrich) was prepared (0.01 M and 0.1 M) and mixed with 10 ml of ammonium citrate dibasic solutions (99.0%, Fluka) at 0.005 M and 0.05 M, respectively, resulting in a whitish solution. Ammonia solution (NH_3, 25.0%, Merck) was added dropwise until the solution became clear (about 2-3 drops). All solutions were prepared under constant stirring on a heating plate at a constant temperature of 50 °C. The prepared reaction mixtures were transferred to a microwave vessel and the syntheses were carried out at 100 W, with a set safe maximum pressure of 280 psi, in the presence of the NC membrane. A synthesis parameter's optimization was carried out by varying the temperature (100 °C and 120 °C) and synthesis time (10 min and 30 min). The obtained NC@AgNPs membranes were dried at room temperature in a desiccator with vacuum for about 1 day, until fully dried. The optimized conditions that rendered a fully covered NC membrane with the in-situ synthesized AgNPs were 0.1 M $AgNO_3$ with 0.05 M ammonium citrate with microwave parameters of 120 °C, 10 min at 100 W (Figure 3.3).

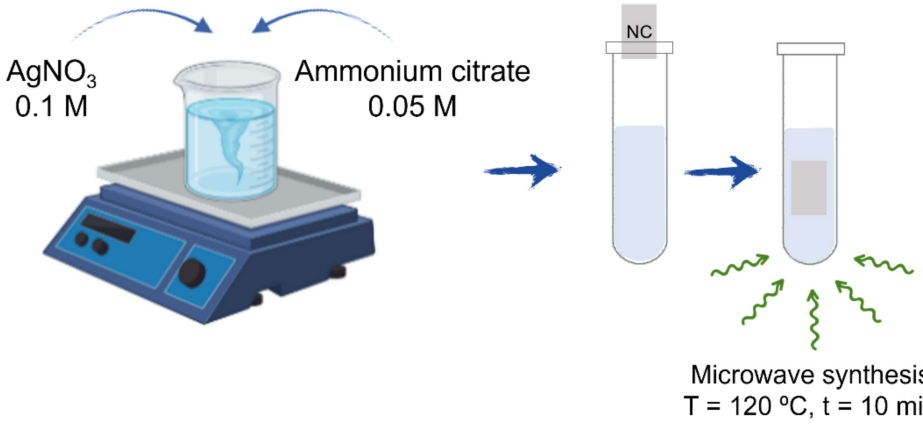

Figure 3.3 Schematic representation of the optimized procedure to prepare NC@AgNPs SERS platforms.

Characterization

The obtained NC@AgNPs membranes were characterized by XRD, Energy Dispersive X-ray spectroscopy (EDS) coupled with SEM imaging for chemical identification and AFM.

NC_{inc}@AuNPs platform' fabrication

Initially, a systematic study on AuNPs synthesis was performed prior to in-situ synthesis onto NC membranes. For that, a volume of 0.5 ml of a $HAuCl_4$ solution (tetrachloroauric (III) acid ($HAuCl_4{\cdot}3H_2O$, ≥ 99.9%, Sigma Aldrich)) was transferred to a microwave vessel followed by 0.5 ml of a reducing agent

(RA) solution and 4.0 ml of distilled water. Two different final concentrations of $HAuCl_4$ were tested, 0.5 and 1.0 mM, and two different RAs were used, Na_3Ct (trisodium citrate, 99.9%, Carl Roth)) and glucose (β-D-glucose, ≥ 99.9%, Sigma Aldrich)), at the final concentrations of 2.5 and 5.0 mM. When glucose was used as RA, 60 µl of 1 M NaOH (sodium hydroxide, LABKEM), were added to the mixture. The prepared vessels were then transferred to the microwave reactor, and subject to 100 W, for 10 min at 120 °C, with a maximum pressure of 280 psi.

The in-situ AuNPs synthesis onto NC membranes was achieved through a seed-mediated growth method, with the previously optimized concentrations (1.0 mM $HAuCl_4$ and 5.0 mM Na_3Ct) and the same microwave parameters, while resorting to two reaction cycles (Figure 3.4).

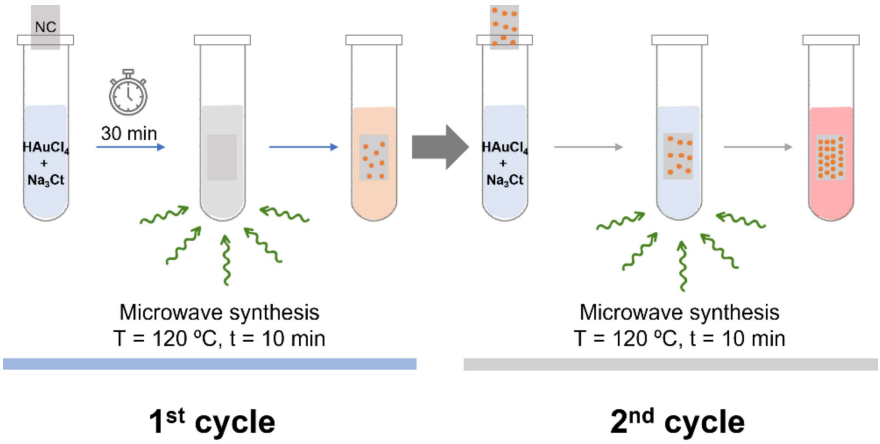

Figure 3.4 Schematic representation of the optimized procedure to prepare NC_{inc}@AuNPs SERS platforms.

The first microwave reaction cycle, was preceded by the incubation of the NC membrane into the reaction mixture, for 30 min. Next, this membrane was transferred to a freshly prepared reaction mixture and subjected to a second microwave irradiation cycle (NC_{inc}@AuNPs). After each cycle, the membranes were thoroughly washed under a gentle stream of distilled water to remove unreacted species. The NC_{inc}@AuNPs obtained after the second cycle were allowed to dry at room temperature in a desiccated environment. For SERS performance comparison purposes other SERS substrates were also produced, using NC membranes without the incubation step (NC@AuNPs) and with and without the incubation step with a seedless method and a reaction time of 20 min ($NC_{inc\text{-}20min}$@AuNPs and NC_{20min}@AuNPs, respectively). Other cellulosic substrates were also used with the optimized conditions: Whatman paper (WP_{inc}@AuNPs), office paper (OP_{inc}@AuNPs) and cardboard substrate (CB_{inc}@AuNPs).

Characterization

The optical characteristics of the synthesized AuNPs colloidal solutions were assessed through UV-Vis spectroscopy (Spark® multimode microplate reader, TECAN, Switzerland). Imaging of AuNPs was carried out by transmission electron microscopy (TEM, ThermoFisher Scientific Inc, TITAN C-Twin) operated at 300 kV. The size of the AuNPs was determined by Dynamic Light Scattering (DLS, AvidNano W130i, USA). The SERS membranes were chemically, structurally, and morphologically characterized through X-ray photoelectron spectroscopy (XPS, Kratos Axis Supra, UK) equipped with a monochromate Al Kα radiation (1486.6 eV), XRD and SEM, respectively.

3.1.4 SERS performance evaluation: Enhancement factor calculation

The SERS EF was calculated using R6G (Rhodamine 6G, Sigma-Aldrich 95.0%) as probe molecule and determined using equation 2.1:[93,118]

$$EF = \frac{I_{SERS}}{I_{Raman}} \times \frac{N_{Raman}}{N_{SERS}} \qquad \text{eq. 3.1}$$

where I_{SERS} and I_{Raman} are the integrated signal intensities of R6G and N_{SERS} and N_{Raman} are the number of R6G molecules deposited on SERS and Raman substrate, calculated by equation 2.2:

$$N_{SERS/Raman} = N_A \times V \times C_{SERS/Raman} \times \frac{A_{laser}}{A_{SERS/Raman}} \qquad \text{eq. 3.2}$$

where N_A is the Avogadro number, V represents the sample' droplet volume, C_{SERS} and C_{Raman} are the R6G molar concentration used in SERS and Raman measurements, respectively, A_{laser} is the laser spot area and A_{SERS} and A_{Raman} are the substrate area.

3.1.5 Applications of the prepared cellulose-based SERS platforms

Raman measurements were carried out with a Renishaw® inVia™ Qontor® confocal Raman microscope (Gloucestershire, UK) equipped with a Renishaw Centrus 2957T3 detector and with 633 and 532 nm laser lines. The laser beam was focused with a 50× Olympus objective lens (N10.6 LMPLAN FL N). The 521 cm^{-1} peak of a silicon wafer was used between the different Raman sessions to calibrate the spectrograph for possible fluctuations of the Raman system.

Tetracycline screening on milk samples with TP@AgNPs

The developed TP@AgNPs SERS platform was used herein for the screening of the antibiotic tetracycline (TET, tetracycline hydrochloride, Sigma-Aldrich) spiked in milk samples. The SERS platforms were prepared for measurements by dropping 2 μl of whole milk, onto the SERS platform,

with added concentrations of TET with concentrations ranging from 0.01 to 1000 ppm. Samples were allowed to dry at room temperature.

Raman measurements were conducted with a 633 nm laser operating at 50 mW, with 5 accumulations of 10 seconds laser exposure. The spectra were recorded as an extended scan. Data is expressed as mean ± standard deviation from at least three independent experiments. Statistical analysis was performed using GraphPad Prism version 6.00 software. Principal Component Analysis was performed using XLStats 2014 software, to highlight the similarities and differences in the data.

Breast cancer exosomes profiling with NC@AgNPs

The developed NC@AgNPs SERS platform was used herein for exosomes profiling for breast cancer diagnosis. The membranes were individualized into 4 mm^2 squares, for single measurements, and to each square a 2 μl drop of analyte was deposited. Prior to exosome's profiling, the performance of the prepared NC@AgNPs SERS platform was evaluated, with R6G as model molecule, and using 633 nm laser at 16 mW with 5 accumulations of 5 seconds laser exposure, and 532 nm laser with the same parameters but with a lower laser power of 5 mW.

The latter were used for Raman measurements of exosomes coming from mammalian cells: breast tumorous cells MDA-MB-231 and non-tumorous breast epithelial cells MCF-10A. The procedure for the cell culture and exosomes purification was conducted at Champalimaud Foundation with the Systems Oncology research group and is described below:

Cell culture, exosomes purification and respective characterization

Breast tumorous cells MDA-MB-231 (ATCC) were cultivated using 500 ml of Lonza™ BioWhittaker™ DMEM high glucose with UltraGlutamine medium, with 10% Foetal Bovine Serum (FBS, 50 ml, Biowest FBS) and 1% Penicillin/Streptomycin antibiotic solution (P/S, 5 ml). Exosomes-free medium was prepared by ultra-centrifuging (Beckman Coultier, Optima XPN-100 Ultracentrifuge) normal FBS and discarding the obtained pellet, to remove exosomes (100 000 × g, 2 h 20 min, 10 min), making sure that the exosomes present in the final samples are all secreted by the desired cell lineages. For preparation of exosomes-enriched conditioned media, cells were incubated for 2 days at 37 °C and 5% CO_2 in the media described above containing exosomes-depleted FBS.

Non-tumorous breast epithelial cells MCF-10A (ATCC) were cultivated analogy to the above described. DMEM/F12 medium was used, with 5% exosomes-depleted Horse Serum and Epidermal Growth Factor (EGF, 20 ng/ml), hydrocortisone (0.5 mg/ml) and finally cholera toxin (100 ng/ml).

Exosome's isolation/purification procedure was the same for both cellular lineages. The procedure started by collecting the conditioned medium with two initial centrifugations (10 min, 500 × g, 10 °C and 20 min, 3000×g, 10 °C) to remove any suspended or dead cells in the medium. To remove large extracellular vesicles, media was centrifuged (20 min, 12 000×g, 10 °C), being the supernatant collected. To obtain an exosome's enriched medium, conditioned media was centrifuged (2 h 20 min, 100 000×g, 10 °C), being the exosomes-enriched pellet collected. Sucrose cushion purification followed, diluting the previously obtained pellet in 14 ml phosphate buffered saline (PBS) and adding it to 4 ml sucrose solution (D2O containing 2.4 g of protease-free sucrose, 0.192 g of Tris base adjusted to pH 7.4). Ultra-centrifugation of the prepared was preformed (1 h 10 min, 100 000×g, 10 °C), where 5 ml of the centrifugation resultant sucrose fraction (away from the pellet) is collected using a 18G needle placed at the bottom. Finally, 16 ml of PBS is added to the previously collected sucrose/exosomes solution and a last ultra-centrifugation was made over night (16 h, 100 000×g, 10 °C), where the purified and isolated exosomes are collected as a pellet and resuspended in 100 μl of PBS.

The obtained exosomes were re-suspended in a PBS solution (pH) and all measurements were made using 10^9 particles/mL dilutions. Exosome's size and concentration characterization was made using NanoSight®, NS300 (Malvern Panalytical, Surrey, UK).

Upon SERS measurements, for reliable results regarding the analysed biological samples, statistical analysis was used to compensate for the sample and substrate variability, allowing for exosome profiling using a Principal Component Analysis (PCA) method. All obtained data was analysed and treated using OriginLab (Northampton, MA, USA) and the respective PCA application for spectroscopy was used for exosomes classification.

SARS-CoV-2 spike protein screening with NC_{inc}@AuNPs

The developed NC_{inc}@AuNPs SERS platform was used herein for SARS-CoV-2 spike protein screening. The membranes were individualized into 4 mm^2 squares, for single measurements. Prior to SARS-CoV-2 spike protein screening, the performance of the prepared NC_{inc}@AgNPs SERS platform was evaluated, using 2 μl of R6G as model molecule, and using 633 nm laser at 3.2 mW with 10 accumulations of 10 seconds laser exposure.

SARS-CoV-2 spike protein (Recombinant SARS-CoV-2 spike protein, S1 subunit (230-01101), RayBiotech) screening was performed by measuring its intrinsic spectra (with the previous measurement conditions), in triplicates, at two different concentrations: 2000 and 5 ng/ml, prepared in

phosphate buffered saline pH 7.2 (PBS, BioUltra). The conditions used for SERS measurement were the same used for R6G' measurements.

3.2 LIG-based MIP platforms

Herein, electrochemical nanobiosensing platforms were fabricated based on electrode's patterning with the LIG technique and combined with biomimetic materials produced with MIP technology. The developed and optimized electrochemical devices were used for the screening of antibiotics:

(i) chloramphenicol (CAP) on a single detection approach;

(ii) amoxicillin (AMOX) and ascorbic acid (AA) with a simultaneous dual detection approach.

3.2.1 Electrode's fabrication – LIG optimization

For the electrode's patterning a computer-controlled CO_2 laser cutting machine (VLS 3.50, Universal laser systems, Scottsdale, AZ, USA) was used to selectively irradiate polyimide substrates (Dupont, Wilmington, DE, USA - with a thickness of 0.075 mm). The laser equipment (Figure 3.5) has a wavelength of 10.6 μm, with a focal length of 50.8 mm, a spot size of 0.127 mm and maximum power output of 50 W.

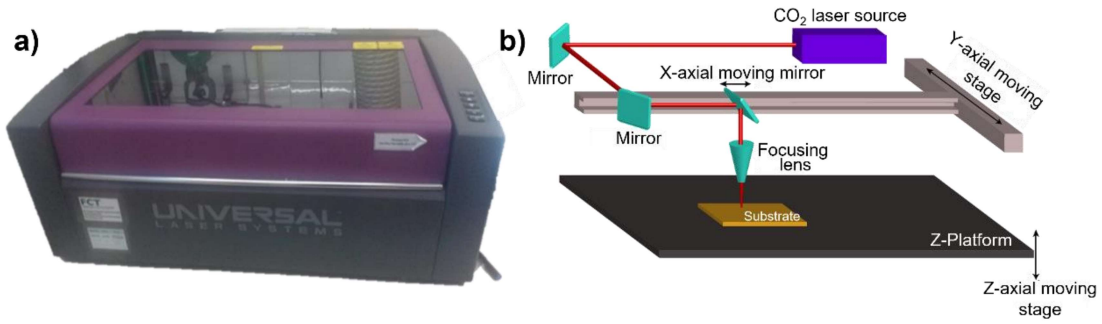

Figure 3.5 a) CO_2 laser cutting machine available at CENIMAT|i3N; b) Schematic representation of the laser setup. Adopted from Samouco, A., et al, 2017.[269]

A study on laser parameters (namely, laser power and speed) was conducted to evaluate which laser conditions would lead to the formation of LIG. Laser settings of 25 W at 1.1 m/s were used to fabricate the electrodes for the single detection biosensor. Further optimization of the laser parameters allowed to find a set of settings yielding a lower sheet resistance (8.5 W at 0.14 m/s) and were used in the electrode's fabrication of the dual detection biosensor.

Two different architectures were designed to fabricate the single and dual detection devices as depicted in Figure 3.6.

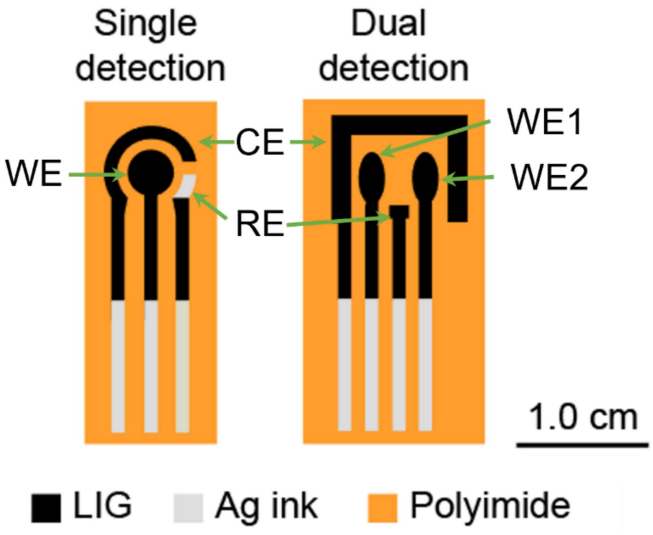

Figure 3.6 Schematic representation of the architecture of the produced devices for both single and dual detection.

In the case of the single detection biosensor, the LIG-based device architecture was designed with a 3-electrode configuration (counter, working and reference electrode, named CE, WE, RE, respectively). CE and WE were patterned with LIG and silver conductive ink (AG-510 silver ink, surface resistivity: <0.015 Ω/square/mil, Conductive compounds, Inc., New Hampshire, USA) was used to define the RE. In the case of the dual detection biosensor, the dual-LIG device was designed with a dual WEs architecture, sharing the same CE and RE.

In both devices, silver conductive ink was also used to define the conductivity tracks to be interfaced with a potentiostat. Upon printing a curing process of the silver ink was conducted, by placing the devices in a hot plate at 120 °C for 10 min. The devices were then encapsulated on plastic sheets using a home version laminator. These plastic sheets were previously patterned in the CO_2 laser cutting machine, to define the electrodes area and the conductive tracks, leaving them exposed.

Characterization

The synthesized carbonaceous material was further characterized by SEM, Raman Spectroscopy and XRD. Lastly, sheet resistance (Ω/square), was determined by Hall effect measurements in Van der Pauw geometry in a Biorad HL 5500 equipment using a constant magnetic field of 0.5 T at room temperature.

3.2.2 Biosensing element: fabrication and evaluation

The biosensing elements for both single and dual detection devices were fabricated at BioMark – Sensor Research, through molecular imprinting polymer technology.

All electrochemical procedures, for both MIP fabrication and analytical performance evaluation, were performed with a potentiostat/galvanostat from Metrohm Autolab (Utrecht, Netherlands), model PGSTAT320N, controlled by NOVA 1.11 software. The single detection devices were interfaced with the potentiostat with a switch box from BioTID Electronic while the switch box for the dual detection devices (Figure 3.7) was developed and fabricated in-house, at CENIMAT|i3N, to accommodate electrical connections with the dual-WE architecture.

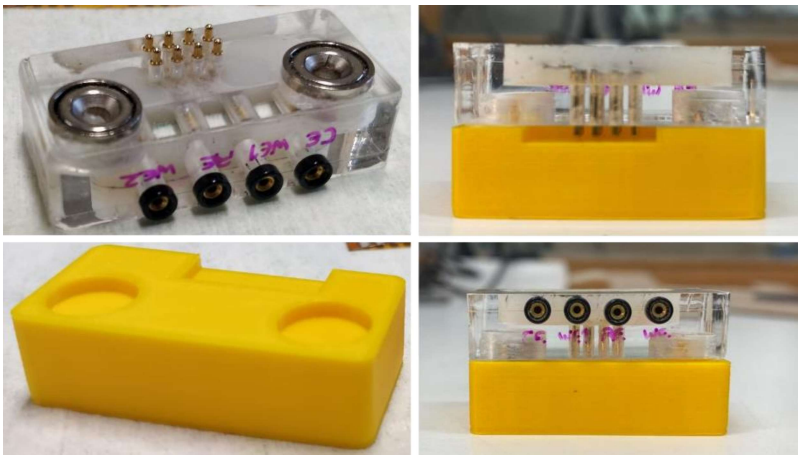

Figure 3.7 Switch box fabricated at CENIMAT|i3N to interface the dual detection LIG devices with the potentiostat.

Single detection: MIP fabrication for CAP sensing and evaluation of analytical performance

The biosensing layer was fabricated following a previous work from Cardoso, A.R., et al, 2018.[204] For comparison purposes, the fabrication of the MIP sensing element was done not only on the LIG device but also in commercial SPEs, purchased from Orion High Technologies, Madrid, Spain. Two types of SPEs were used: C-SPE (with carbon ink as the WE and CE and silver ink as RE) and G-SPE (similar to C-SPE but with a thin layer of graphene deposited on the WE). The assembling architecture of the LIG device (shown in Figure 3.6) was the same as the commercial SPEs, with a WE diameter of 4 mm.

The assembly process was similar for all devices, except for an initial step that was only performed for the LIG device. The as-produced LIG devices were incubated in 0.01 M EDOT in 0.10 M KCl (potassium chloride, Merck) for 180 s, to aid on fixing some loosen LIG particles, created during laser irradiation. Afterwards, all WEs devices were subjected to a pre-treatment by chronoamperometry, at +1.70 V for 180 sec, with 0.10 M KCl, followed by surface's rinsing with ultrapure water to eliminate residual chemical compounds. Then EDOT (3,4-ethylenedioxythiophene, 97%, Alfa Aesar) was electrochemically polymerized to PEDOT in the electrode sensing area by chronoamperometry, at +0.90 V for 10 sec, to aid on the stabilization and improved the reproducibility of the devices. Next, an incubation of the sensing area with 0.01 M 4-AMP (4-aminothiophenol, 96%, Acros Organics) (prepared

in Milli-Q water and ethanol 1:1) for 1 hour, was carried out to ensure a covalent bonding to the PEDOT structure and to firmly attach to the surface the MIP layer.

The MIP layer was produced by bulk electropolymerization using EBT (Eriochrome Black T, Biochem) as functional monomer in the presence of the template CAP (chloramphenicol, Fluka) prepared in ACN (acetonitrile, Carlo Erba): 0.10 M CAP in 0.20 M ACN with 1.0×10^{-3} M of EBT in 0.20 M ACN. The NIP layer was produced similarly but without adding CAP. EBT was electropolymerized to PEBT by chronoamperometry at +0.95 V for 250 sec. Finally, after assembling the MIP layer, the CAP template was removed by incubating the sensing layer in ACN and performing consecutive CV scanning from −0.2 to +0.8 V, with a scan-rate of 0.1 V/s for 20 cycles. This potential range was selected to maintain the integrity of the polymer while avoiding the electro-activity of CAP, which could irreversibly entrap the template within the PEBT film. The same procedure was followed for the NIP layer.

To follow each step of MIP and NIP assembly, the electrical properties of the modified surfaces were followed-up by CV and EIS, using a redox probe solution of 5.0×10^{-3} M $[Fe(CN)_6]^{3-}$ and 5.0×10^{-3} M $[Fe(CN)_6]^{4-}$ (potassium hexacyanoferrate III ($K_3[Fe(CN)_6]$) and potassium hexacyanoferrate II ($K_4[Fe(CN)_6]$) trihydrate, Riedel-de Häen). All electrochemical assays were carried out in duplicate. CV measurements were performed from −0.3 to +0.7 V, at a scan-rate of 50 mV/s. EIS measurements were performed at an open circuit potential, using a sinusoidal potential perturbation with an amplitude of 0.01 V, and 50 data points, logarithmically distributed over 10–0.01 Hz frequency range. The EIS data was fitted into a Randles equivalent circuit, using 1.11 Nova Software from Autolab.

Calibration curves were carried out by incubating for 20 min standard solutions of CAP prepared in lithium perchlorate buffer ($LiClO_4$, Sigma-Aldrich), with concentrations ranging from 1.0 nM to 10 mM, and the electrical response of each incubation was followed by EIS measurements.

The LOD was calculated as $X+3\sigma$, where X represents the average value of the EIS blank signals (obtained in the absence of CAP) and σ is the known standard deviation of EIS blank signal consecutive readings.[270]

Selectivity studies were made as previously reported, using possible interfering species: oxytetracycline (OTC), amoxicillin (AMOX) and sulfadiazine (SDZ), which are antibiotics commonly used in fish farming.[204] Solutions of CAP with each interfering species were prepared with a concentration of 1.0×10^{-6} M, in 1:1 volume ratio. The LIG devices were incubated with each solution for 20 min and electrical response was followed by EIS measurements.

Dual detection: MIP fabrication for AMOX and AA screening and evaluation of analytical performance

Initially, a 0.10 M KCl solution was used to clean the dual-LIG device's electrodes surface. Then, for the AMOX MIP layer assembly, a 0.010 M EDOT solution was prepared in 0.10 M KCl and electropolymerized by chronoamperometry, at +0.90 V for 10 sec. Next, a mixture of 4-AMP (prepared in ethanol and ultrapure water, 3:7) and EBT (prepared in 0.20 M ACN) with the same concentration (1.0×10^{-5}M), was electropolymerized at +0.95 V for 0.5 sec. Next, a mixture of 1.0×10^{-3} M AMOX and 1.0×10^{-3} M of EBT, prepared in 0.20 M ACN, was subject to electropolymerization by chronoamperometry at +0.45 V for 250 sec. As a negative control, a NIP film was also fabricated, which consisted in a similar procedure but without AMOX. The template removal was achieved by incubation of the electrodes in ACN that were then subject to consecutive CV scanning, from +0.5 to +0.8 V, with a scan-rate of 0.1 V/s for 40 cycles.

The electrical changes occurring at the electrode's surface were followed by indirect measurements with an iron redox probe (5.0×10^{-3} M $K_3[Fe(CN)_6]$ and 5.0×10^{-3} M $K_4[Fe(CN)_6]$, prepared in 0.20 M ACN). CV measurements were acquired by scanning potentials from −0.3 to +0.4 V, at a scan-rate of 50 mV/s, to follow each step of the AMOX film's assembly. Square Wave Voltammetry (SWV) was also used to follow-up all the chemical modifications in the MIP construction steps, by scanning from -0.3 to +0.4 V, at scan-rate of 20 mV/s.

The AA MIP film fabrication followed a previously published work by Özcan, L, et al.[271] Briefly, the film was prepared by electropolymerizing pyrrole (0.025 M) in the presence of AA (0.01 M), using $LiClO_4$ (0.1 M) as electrolyte. This was made by CV, swiping the potential from -0.60 to +0.80V, for 7 cycles. For the removal step, few modifications were made. The template was removed by covering the working electrode with a 0.05 M phosphate buffer solution, for a given time, without agitation.

For AMOX readings of the novel MIP film, the modified surfaces were followed-up by CV and SWV assays, of a redox probe solution of 5.0×10^{-3} M $[Fe(CN)_6]^{3-}$ and 5.0×10^{-3} M $[Fe(CN)_6]^{4-}$, prepared in 0.20 M ACN in buffer. Calibration curves were followed by SWV and involved the incubation of standard solutions of AMOX, with concentrations ranging from 100 nM to 50 μM, prepared in $LiClO_4$ buffer. For AA readings, the direct oxidation of the analyte was made, as AA is an electroactive species. Finally, for readings in binary samples, combining AMOX and AA, SWV measurements were conducted within different potential ranges for AMOX (scanning potentials from +0.50 to +1.0 V, at a scan-rate of 2 mV/s) and AA (scanning potentials from −0.2 to +0.5 V, at a scan-rate of 2 mV/s), and the electroactivity features displayed by each target analyte were monitored.

LOD for AMOX sensing was calculated as X+3σ, where X represents the average value of the SWV blank signals (obtained in the absence of AMOX) and σ is the known standard deviation of SWV blank signal consecutive readings.[270]

CHAPTER 4

Cellulose-based platforms for SERS applications

This chapter presents the exploitation of several strategies for the fabrication and optimization of SERS platforms using cellulose as substrate and both physical and chemical routes to produce nanostructures for Raman signal intensification, specifically, silver and gold nanoparticles. The produced platforms were successfully applied in the measurement of simple molecules, such as antibiotics, and more complex analytes, such as exosomes, for cancer diagnosis.

The chapter is divided in two main sub-chapters:

Chapter 4.1. SERS platforms produced through physical processes:

- application of a SERS platform composed by a substrate made of cardboard with a top layer of evaporated aluminium oxide (Al_xO_y), commercially known as Tetra Pak®. AgNPs were used for Raman enhancement and were produced by e-beam thermal evaporation. This platform was successfully used for the screening of tetracycline in milk.

Chapter 4.2. SERS platforms produced through chemical processes:

- production of a SERS platform comprising a nanocellulose substrate with in-situ synthesized AgNPs This platform was fully optimized in terms of Raman enhancement, and it was employed in a label-free approach for breast cancer' exosomes profiling;
- production of a SERS platform comprising a nanocellulose substrate with in-situ synthesized AuNPs. This platform was fully optimized in terms of Raman enhancement, and it was employed in a label-free approach for spike protein from SARS-CoV-2 virus detection.

Some of the results shown herein were adapted from:

- **Marques, A.C.**, Veigas, B., Araújo, A., Pagará, B., Baptista, P. V., Águas, H., Martins, R., Fortunato, E. Paper-Based SERS Platform for One-Step Screening of Tetracycline in Milk. Scientific Reports, **2019**, 9, 1–8.
- Ferreira, N.; **Marques, A.C.**, Águas, H.; Bandarenka, H., Martins, R.; Bodo, C., Costa-Silva, B., Fortunato, E. Label-Free Nanosensing Platform for Breast Cancer Exosome Profiling. ACS Sensors, **2019**, 4, 2073–2083.
- **Marques, A.C.**, Pinheiro, T., Morais, M., Martins, C., Andrade, A.F., Martins, R., Sales, M.G.F., Fortunato, E. Bottom-up microwave-assisted seed mediated synthesis of gold nanoparticles onto nanocellulose to boost stability and high performance for SERS applications. Applied Surface Science, **2021**, 561, 150060.

Chapter 4. Cellulose-based platforms for SERS applications

The use of supporting matrices for the Raman enhancement nanostructures offers a higher convenience and higher throughput for SERS measurements and, in some cases, can enhance the Raman signal even further. Many materials have been used as SERS substrates, from conventional glass, silicon wafers to cellulose-based substrates.[20,68,93,100,272–276] As mentioned in Chapter 2, cellulose is an outstanding polymeric material due to its inherent low-cost, lightweight, biocompatibility, recyclability and versatility. It exists in many formats, from the regular office paper to nanoscale formats, such as nanocellulose. Since the first reports on cellulose as SERS platform in 1984,[87,88] several cellulose-based SERS substrates have been proposed in the literature, with different cellulose formats, nanostructures fabrication strategies and deposition methods.[19,20,79,144,163,266]

4.1 SERS platforms produced through physical processes

Moving forward from the original substrates for SERS, that consisted in roughened metallic electrodes,[69] physical processes have been routinely used for SERS platform's fabrication. Namely, photolithography and nanolithography have the advantage of being able to fine control the geometric features of the Raman enhancement nanostructures, allowing for high reproducibility in SERS intensities.[277] However, these approaches have substantial drawbacks, such as high patterning times and high costs, which constrains their scale-up prospects.

A method for one-step deposition of metallic nanoparticles, onto cellulose-based substrates, by e-beam thermal evaporation was established by our group.[85,267] This method of metal deposition results in the direct arrangement of individual nanoparticles, with a good control of size and shape, without the need of any post-thermal treatment.[267,278] It consists on the formation of AgNPs in-situ during the thermal evaporation of thin films of Ag deposited on substrates that are heated up to 150 ^{o}C.[267] The considerable low temperatures required enables the method to be appropriate to a broad range of low-cost and flexible materials, such as cellulosic substrates, that are not compatible with the conventional annealing de-wetting methods carried out at higher temperatures (300-500 ^{o}C).[267,279–281] In general, this process allows for a simple and inexpensive production of SERS substrates that are highly stable, homogeneous in terms of morphology and exhibit prominent Raman enhancement effects throughout the substrate.[267]

Herein it is demonstrated the use of the aforementioned method combined with an inexpensive, recyclable and widely used cardboard substrate, commonly used as disposable packaging material,

and known as Tetra Pak®, for antibiotic residue's quantification. From hereafter, this platform will be named as – TP@AgNPs – Tetra Pak® substrate decorated with AgNPs.

4.1.1 Thermal evaporation of AgNPs on Tetra Pak® substrate for tetracycline screening on milk

Nowadays, antibiotics are extensively used in livestock for therapeutic purposes and, in some countries, for growth promotion. However, it's massive use may create problems for the food industry, for instance the milk transformation industry and consumers.[282,283] The residues of antibiotics in milk can cause several problems to the final consumer such as, allergic reactions and development of antibiotic-resistance microorganisms, as well as being responsible for disruption of Ca^{2+} metabolism which is harmful to the formation of teeth and bones in children.[282–286] When antibiotics are used, dairymen must follow specific protocols to prevent the prevalence of antibiotic residues in milk above the established legal limits. Despite that, reports show that there is still presence of antibiotics in milk above the recommended values.[282,287] This is more prevalent in developing countries – for instance, in Brazil a study showed the presence of antibiotic residues above the legal limits, within the class of tetracyclines (TET), in 8 out of 21 commercial brands tested.[288] So, the use of monitoring tests by regulatory authorities and dairy personnel are highly relevant and have shown to drastically decrease the occurrence of antibiotic-adulterated milk.[282,283]

Currently, the most common methods employed for TET residues monitoring include microbial inhibition tests,[289,290] immunoassays,[291,292] and chemical-physical methods such as high-performance liquid chromatography (HPLC)[293,294] and/or mass spectroscopy.[295,296] However, these methods have high operational costs, complex sample preparation, and normally require a high volume of reagents and specialized personnel.[283,287]

Herein, the TP@AgNPs platform was allied to a highly simplified sample handling and data analysis protocol, following a peak ratio analysis for a single-step detection and quantification of TET in milk matrix without the need for any sample's pre-treatment nor labelling protocols.

TP@AgNPs SERS platform: production and characterization

SERS platforms were produced on cardboard packaging by a one-step thermal transformation of a 6 nm Ag film to an array of AgNPs by a solid-state dewetting method.[267,297] The cardboard is composed by a paper-based layer coated with evaporated aluminium. In contact with air, a thin layer of Al_xO_y is formed which is important for the stability of AgNPs. An optimization of SERS response to the AgNPs of various shapes and sizes was systematically investigated elsewhere, in a previous work from our group.[267] A electromagnetic simulation using the Mie theory was performed and helped determine that

6 nm Ag thin film, that renders 60 nm-sized AgNPs gives the best SERS performance. This optimal local electric field enhancement is able to increase the Raman signal up to 10^6.[267]

Reproducibility and stability of the produced substrates were also assessed showing an SERS intensity variation lower than 5% along the substrate area, with a shelf life higher than 6 months without loss in SERS performance.[267,297] This high shelf life can be explained by the low oxidation rate of the AgNPs when in the presence of the aluminium layer in the cardboard structure. This metal layer acts as a sacrificial anode, providing cathodic protection and preventing the oxidation of the AgNPs, due to the higher standard reduction potential of silver (E^0 = +0.80 V) in comparison with aluminium (E^0 = -1.68 V).

SEM and AFM analyses of the used TP@AgNPs platform has been carried out and it is presented in Figure 4.1.

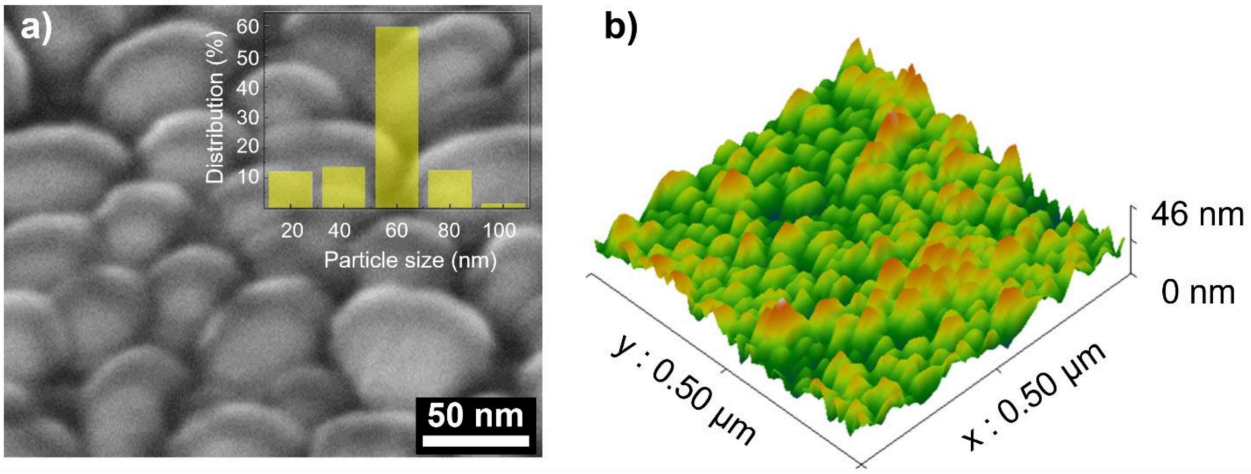

Figure 4.1 Morphological characterization of the TP@AgNPs SERS platform: a) SEM image. The histogram for the size particle distribution is presented in the inset image; b) AFM imaging.

The SEM image of the produced AgNPs (Figure 4.1a), on top of the Tetra Pak® substrate, reveals a highly dense and uniform distribution of the nanostructures with an elongated spherical shape and an average diameter of 60 nm. The uniformity and close proximity of the nanostructures, produced by thermal evaporation, contributes to the high reproducibility of SERS and to the Raman signal enhancement, due to the presence of hot spots (narrow gaps between neighbours NPs), that are excited by the surface plasmon coupling.[100] Additionally, AFM measurements of the NPs revealed an average height of ~46 nm, with typical in-plane ellipsoid features with ratios of ~1.3 (Figure 4.1b).

Implementation of TP@AgNPs as a platform for tetracycline screening

To test the ability of reproducible detection and quantification of TET with this platform, SERS spectra of whole milk spiked with different TET concentrations were acquired (Figure 4.2). Each milk spiked TET sample was deposited onto the SERS substrate and allowed to dry at RT (Figure 4.2a), after which three individual spectra were measured for each concentration. The measured SERS spectra of 500 ppm TET aqueous solution, milk, and milk spiked TET (500 ppm) are shown in Figure 4.2b and c, respectively.

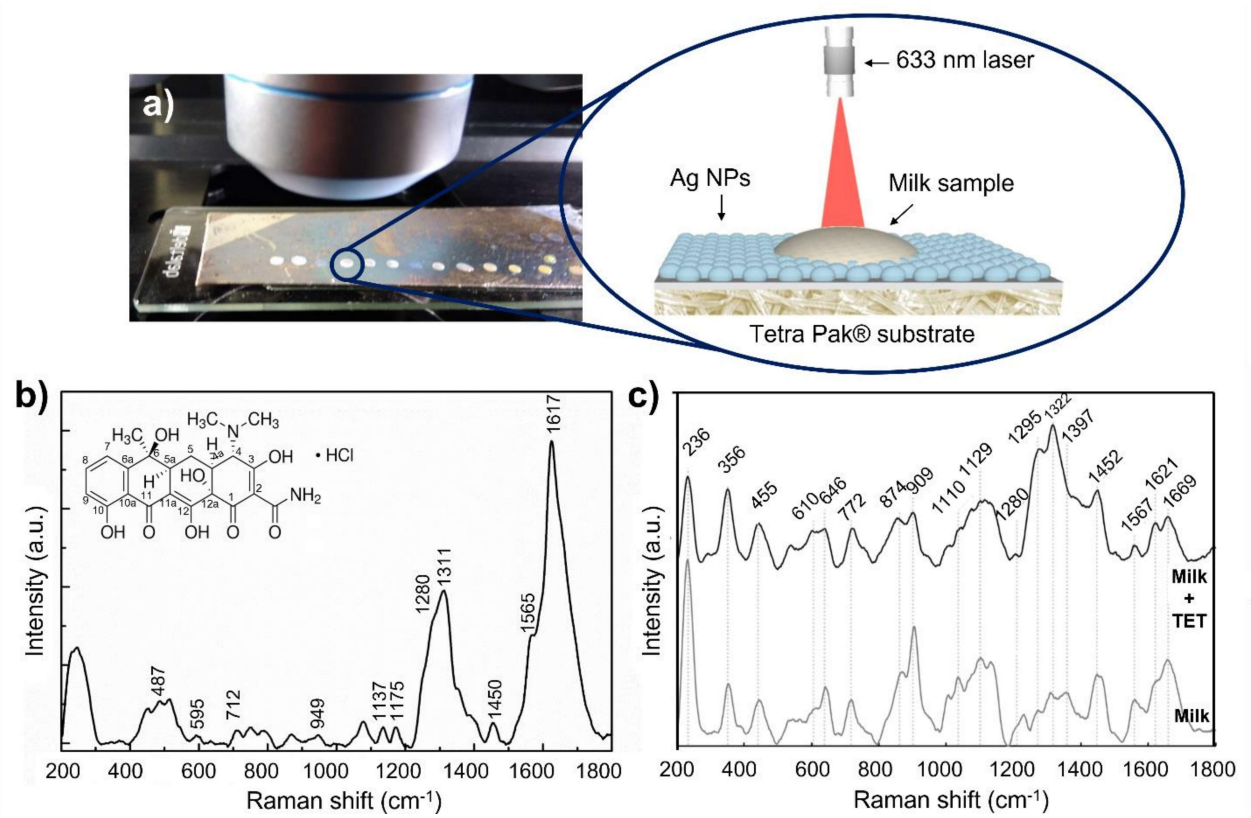

Figure 4.2 SERS measurements of TET: a) Optical photograph of the platform with milk spiked TET measurement set up. The zoom in shows a schematic representation of a single measurement; b) SERS spectra of 500 ppm TET aqueous solution showing TET characteristic peaks. The inset shows the TET hydrochloride molecule with positional number of carbon atoms; c) SERS spectra of milk (bottom) and 500 ppm TET spiked milk (top) showing its characteristic peaks.

The SERS spectra of TET in aqueous solution shows TET characteristic Raman shifts and their assignment is shown in Table 4.1.[287,298]

Table 4.1 Assignment of TET characteristic Raman peaks.

Raman shift (cm^{-1})	**Peak assignment**
487	Torsional and/or bending (ring)
595	δ(amid-ONH)
712	ω(amin-NH), υ(CO6,12), γ(OH3,6,10,12,12a)
949	υ(CO3)
1137	υ(CO6,12)
1175	υ(CO3)
1280	δ(CH4,4a,5a), δ(OH12), δ(amid-NH), υ(CO10), υ(CO3), υ(CH7,8.9), υ(amid-NC), υ(C4aC5), υ(D)
1311	δ(OH10,12), δ(CH4,4a,5,5a), υ(C5aC11a), υ(C1C2), υ(C9C10,C10C10a,C10a,C11), υ(CO11,12), υ(CO3), δ(CH7,8,9)
1450	δ(CH7,8,9), δ(OH12), υ(D), υ(CO10,CO11,CO12), δ(amin-CH3)
1565	δ(OH10,12), υ(D), υ(C11aC12)
1617	υ(CO1), υ(amid-CO), δ(amid-NH), υ(CO3), υ(C2C3), υ(OH10,12), υ(amid-CO2)

υ, stretching; **δ**, bending; **ω**, out-of-plane swing; **γ**, out-of-plane bending.

Additionally, to the characteristic milk peaks a set of more pronounced peaks appear in the TET spiked milk (Figure 4.2c) at 1280 cm^{-1}, 1322 cm^{-1} and 1621 cm^{-1}. This evidence is in accordance with the TET characteristic peaks reported in the literature[287,298] although with a small shift, due to the interaction of TET with the milk matrix, and possibly to the interaction of the metallic nanoparticles with TET.[299] The peak at 1280 cm^{-1} is correlated to bending modes of C-H in the positions 4, 4a, 5, 5a, O-H12 and amide-NH and to stretching modes of C10,3-O, C-H7,8,9, C4a-C5 and amide-NC. The peak at 1322 cm^{-1} is assigned to ring breathing of stretching modes C6a-C7, C9-C10 and bending modes of O-H10,12 and to

C-H4,4a,5,5a. Finally, the peak at 1621 cm^{-1} is attributed to the stretching modes of C1,3-O, C2-C3 and amide-CO and to the breathing modes of amide-CO and amide-NH.

A principal component analysis (PCA) was performed to the obtained spectra of milk spiked TET with increasing concentrations (Figure 4.3).

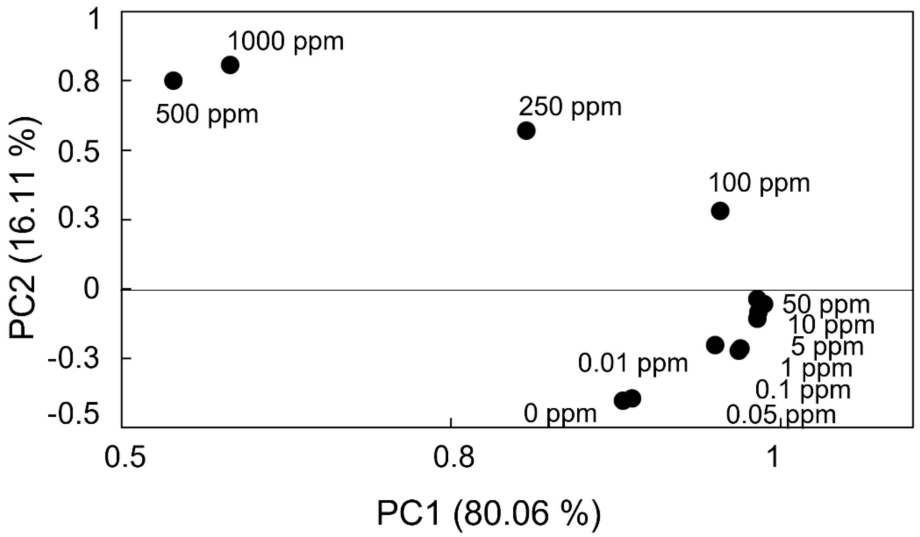

Figure 4.3 TET spiked milk statistical analysis: Principal component analysis of TET detection and quantification in TP@AgNPs substrate. The two eigenvectors PC1 & PC2 accounting for 96.17% of total variance in the data set.

The PCA showed that 96.17% of the variance was comprised in two eigenvectors. Most of the variance (80.06%) only showed a linear correlation to TET concentrations above 100 ppm (Figure 4.4a).

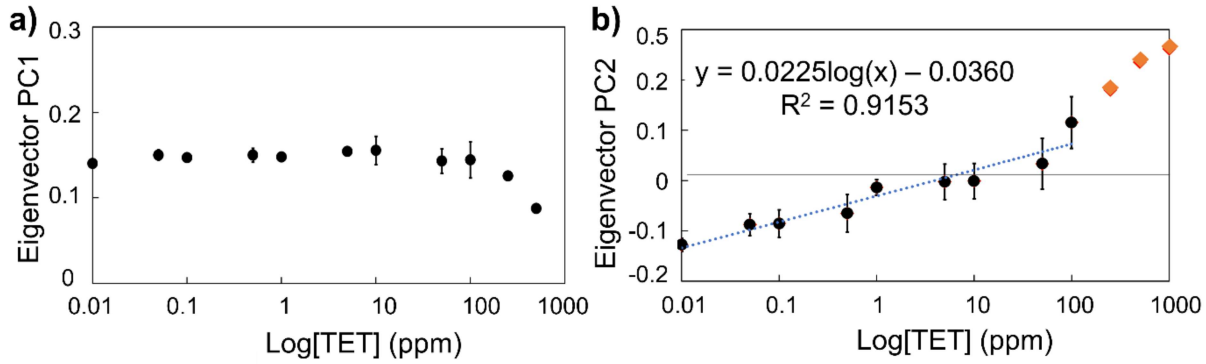

Figure 4.4 TET spiked milk statistical analysis: a) Correlation between the eigenvector PC1 variance and TET concentration. A linear correlation between the variance of the vector PC1 and TET concentration is observed for concentration values above 100 ppm; b) Correlation between the eigenvector PC2 variance and TET concentration. A linear correlation ($R^2 = 0.9153$) between the variance of the vector PC2 and TET concentration is observed for lower concentrations (0-100 ppm). Each point corresponds to the mean value and error bars to the standard deviation of three independent measurements.

However, the second eigenvector corresponding to 16.11% of total variance showed a fair correlation (R^2= 0.9153) for lower concentrations (< 100 ppm) (Figure 4.4b).

While PCA is extremely powerful to access the correlation between spectral changes and analyte concentrations a simplified measurement procedure was envisioned, to establish a method for TET quantification. As such, in this approach all the possible combinations of peak ratios and their correlation to the concentration of the analyte were analysed.

Figure 4.5 shows the resultant matrix with a colour code showing the peak ratio's combinations outcomes. The construction of the matrix made it easier to determine whether a correlation existed, and thus to narrow down the number of peak ratios that could be used to quantify TET.

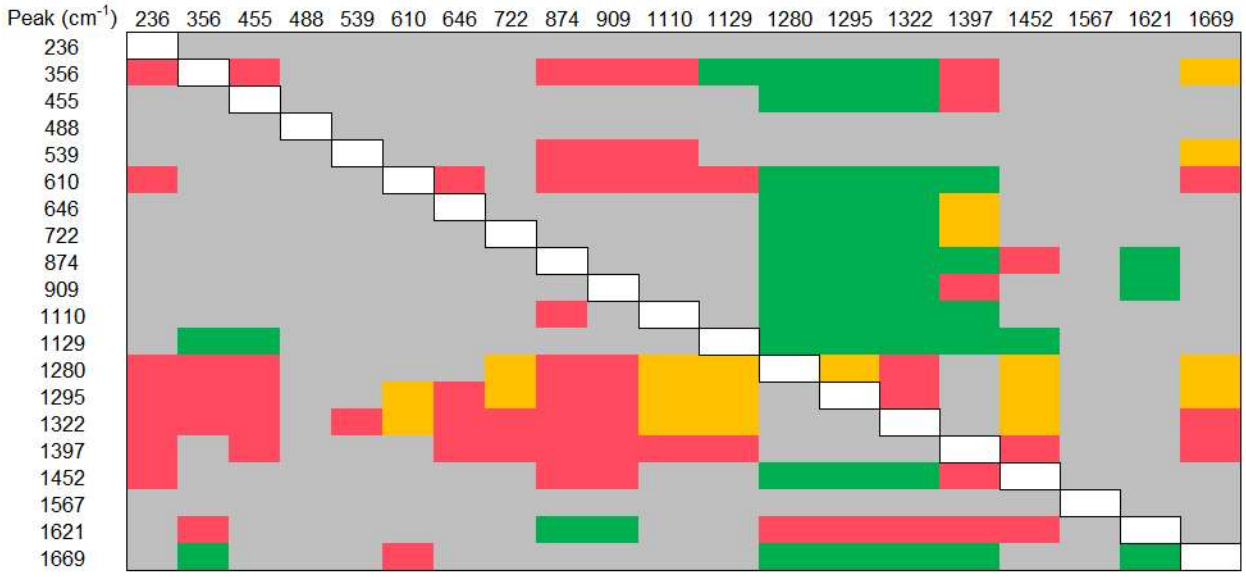

Figure 4.5 Combinations of peak ratios and their correlation to the concentration of the analyte. **Grey (■)**: No correlation between ratio intensity and analyte concentration was found; **Red (■)**: Correlation between ratio intensity and analyte concentration was found above 100 ppm; **Yellow (■):** Correlation between ratio intensity and analyte concentration was found above 1 ppm; **Green (■):** Correlation between ratio intensity and analyte concentration was found above 0.01 ppm.

By analysing the colour-coded matrix, three ratios were selected for further analysis: 455 cm^{-1}/1280 cm^{-1}, 1322 cm^{-1}/1669 cm^{-1} and 874cm^{-1}/1397 cm^{-1}.

The characteristic milk peaks selected for the peak ratio analysis, at 455, 1397 and 1669 cm^{-1}, although with small shifts, can be attribute to lactose, amino acids (such as glycine and l-valine) and to amide I, respectively.[300,301] The disappearance of the 1397 cm^{-1} peak in the milk spiked TET spectrum (Figure 4.2) it is possibly due to the interaction of TET with the protein fraction of milk. Evidence of this interaction has been previously shown elsewhere, where it is described the adsorption capability of TET to milk.[302]

From all peak and peak ratio intensities present in the full spectra the ratio 455 cm^{-1}/1280 cm^{-1} (Figure 4.6a) showed a linear correlation in a logarithmic scale (R^2 = 0.97) for the entire tested range (0-1000 ppm).

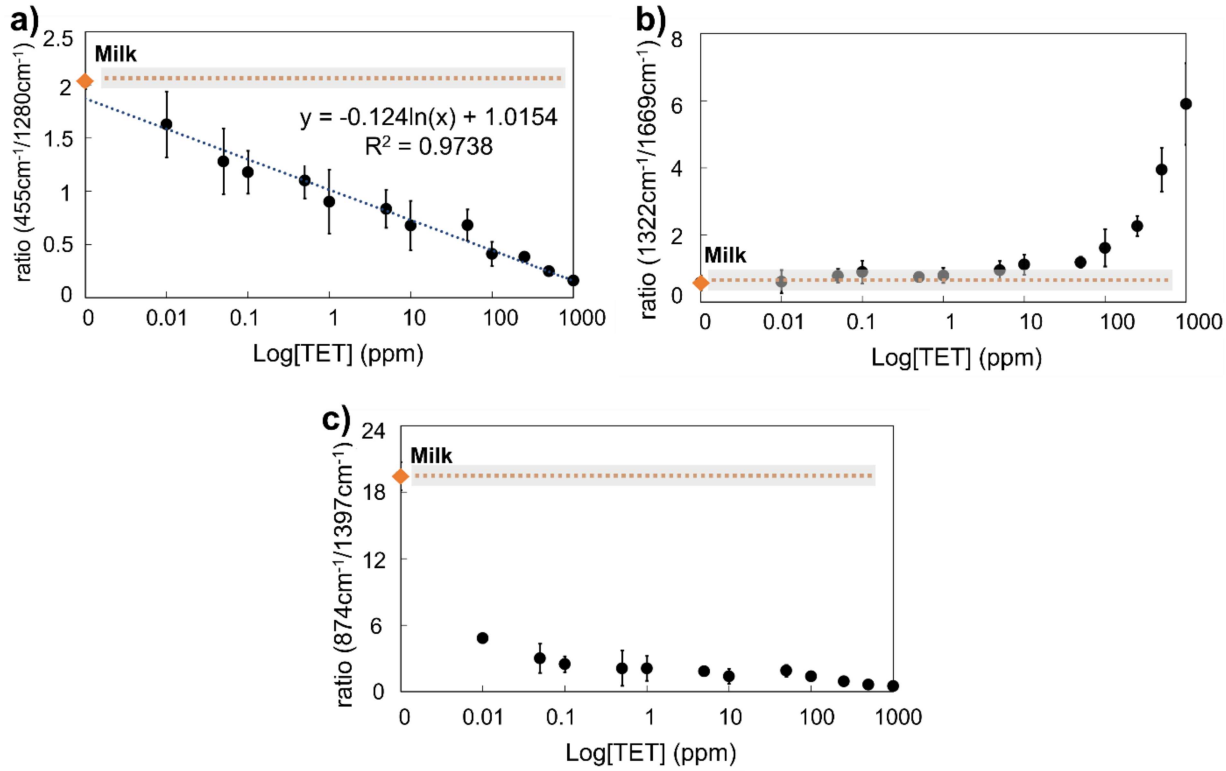

Figure 4.6 Dependence of SERS signal intensity ratio and TET concentration: a) Correlation between ratio 455 cm^{-1}/1280 cm^{-1} versus analyte concentration in logarithmic scale; b) Correlation between ratio 1322 cm^{-1}/1669 cm^{-1} versus analyte concentration in logarithmic scale; c) Correlation between ratio 874 cm^{-1}/1397 cm^{-1} versus analyte concentration in logarithmic scale. Diamond marker shows the ratio values obtained for milk samples without TET and grey shade the error (standard deviation). Each point in the final calibration curve corresponded to the mean value and the error bars to the standard deviation of three independent measurements.

For this ratio, the LOD was found to be 0.1 ppm. The other selected two peak combinations showed high correlation to analyte concentration. The ratio 1322 cm^{-1}/1669 cm^{-1} (Figure 4.6b) is a clear representation of the correlation found in the PCA F1 vector analysis, with an LOD above 100 ppm of TET, well above the desired sensitivity needed for this application. Moreover, the ratio 874 cm^{-1}/1397 cm^{-1} showed to have a LOD lower than 0.01 ppm of TET although with a shorter linear range (Figure 4.6c).

The present method follows a label-free approach for the simple detection and quantification of TET residues in milk with high-throughput, with a LOD within the maximum value defined by government associations. Although some reports, based on SERS[287,303] or fluorescence-based methods[304] report lower LOD for the screening of TET, they comprise complex procedures for the fabrication of the sensing

platforms and/or detection schemes. Nonetheless, the presented SERS platform and detection method is able to answer to the maximum value of TET residues in milk, as defined by the European Union[305] (0.1 ppm) and by the United States Food and Drug Administration[306] (0.3 ppm). Additionally, these results prove that a simple two peak measurement approach is reliable for the quantification of TET residue in milk while maintaining a low detection protocol' time.

4.2 SERS platforms produced through chemical processes

Traditionally, top-down techniques, such as physical-deposition processes, have been used to fabricate SERS platforms. However, these techniques can be cumbersome, expensive, difficult to scale up and time-consuming.[307,308] Chemical-based processes are affordable, simple, scalable, easily tailored and liable high-throughput. Among the wet chemistry methods, microwave-assisted synthesis uses volumetric dielectric heating, allowing for rapid and uniform heating of the reaction mixture yielding well-controlled and homogenous products - as compared with its counterpart conventional heating - resulting in a decrease on reaction time by more than one order of magnitude.[17,21,308,309]

Various SERS platforms have been reported using microwave-assisted synthesis to produce enhancement nanostructures and are mostly based on Ag nanostructures.[20,266,307–312] Although AgNPs are able to provide the highest Raman enhancements, due to their strong plasmon resonance effect, they are chemically unstable and prone to early oxidation, which can compromise the shelf life of SERS platforms.[79] On the contrary, AuNPs have high chemical stability, are biocompatible and offer easy functionalization with biomarkers. So, the development of microwave-based fabrication strategies for AuNPs-based SERS platforms is of high relevance. In 2014, Su, S. and colleagues used microwave irradiation to decorate MoS_2 nanosheets with AuNPs.[313] A RSD of around 20% was attained with an EF of 8.2×10^5 with 10^{-4} M R6G as probe molecule. Later, a method to prepare Au-graphene-Au dimers and its used for SERS was reported by Ghosh, P. et al., with an EF of around 10^7 with R6G.[314] The method combined microwave-assisted synthesis of a first layer of AuNPs grown in an amino-functionalized Si wafer, transfer of a graphene monolayer from a copper foil to the Au-SiO_2 substrate, followed by microwave growth of the second layer of AuNPs. More recently, Li, H. and co-workers described a method for the microwave synthesis of AuNPs prepared with a magnetic ionic liquid, used as a synergistic enhancer and stabilizing compound, for the detection of clopidol.[315] However, some of the works reported so far require multi-step approaches and/or rely on expensive substrates and materials.

Among the wet-based deposition methods, in-situ synthesis methods[146,161,316–318] shows benefits since the nanostructures' production and their deposition on the substrate can be done in a single step. This

generally leads to simple and fast SERS platform's fabrication, avoiding, for instance, long immersion times of the substrate onto plasmonic nanoparticles colloidal solutions.[319]

Herein, it is presented contributions on using microwave-assisted synthesis to produce plasmonic nanostructures – namely, AgNPs and AuNPs – directly grown on nanocellulose substrates, obtained from *nata de coco* cubes. As proof of concept, the as-produced SERS membranes were used for the label-free screening of breast cancer (sub-section 4.2.2) and SARS-CoV-2 S protein (sub-section 4.2.3), respectively.

From *nata de coco* cubes to nanocellulose membranes

Bacterial nanocellulose (BNC) — also called bacterial cellulose, microbial cellulose, or biocellulose — is produced by aerobic bacteria, such as *Gluconacetobacter,* an acetic acid bacteria, as a pure component of their excreted biofilms. These bacteria are widespread in nature where the fermentation of sugars and plant carbohydrates takes place. In contrast to microfibrillated cellulose (MFC) and nanocrystalline cellulose (NCC) that are obtained from vegetal sources, BNC is produced as a polymer by biotechnological assembly processes from low-molecular weight carbon sources, such as D-glucose. Generally, these bacteria are cultivated in aqueous nutrient media, and BNC is excreted as exopolysaccharide at the interface to the air. The resulting form-stable BNC hydrogel is composed of a nanofiber network, with fibres diameters ranging from 20 to 100 nm, with up to 99% water content. This nanomaterial is biocompatible, has a high weight-average molecular weight, high crystallinity, high chemical purity, high surface-to-volume ratio and good mechanical stability.[320] These characteristics make BNC an attractive candidate for numerous industries, such as food, paper, textile, medical devices, among others.[321,322]

Moreover, the attractiveness of BNC for bio and chemical sensing has also been demonstrate, particularly in SERS applications. Following, the first report on BNC-based SERS sensing,[92] utilizing AgNPs for Raman enhancement, where the superiority of BNC over conventional vegetable cellulose analogues was demonstrated, several SERS reports using BNC have been published. BNC has been combined with AgNPs,[156,323–325] AuNPs[326–328] and AuNRs,[329] bimetallic AuNRs@AgNCs[330] or with Au@magnetic nanoparticles.[98] The preparation of the Raman enhancement nanostructures incorporated with BNC are generally produced following solution-based processes, that are either directly grown onto the BNC fibres[98,324–326,328] or transferred afterwards following methods such as drop and drying,[156] filtration[323,329] or immersion.[330] So, the feasibility of bacterial cellulosic substrates has been successfully demonstrated over the years, targeting different applications from pesticides screening to

bacteria.[98,323,329] However, some of the reported fabrication workflows require either multi-step procedures[323,329,330] or lengthy in-situ synthesis using conventional heating processes.[98,328]

Currently, the main commercial exploitation of BNC is *nata de coco*. *Nata de coco* is a polymer naturally synthesised by *Acetobacter xylinum* bacteria strain in a coconut water medium. Generally, *nata de coco* is produced by inoculating bacteria directly in the culture medium, resulting in an inexpensive product, mass produced in Southeast Asia (originally from the Philippines).[331,332] *Nata de coco* is conventionally commercialized in the form of cubes, to be used in desserts, and it is sold in sugar-based preservation syrups.

4.2.1 Nanocellulose membranes: preparation and characterization

Nanocellulose (NC) membranes, to be used as support for the plasmonic nanoparticles, were prepared from the *nata de coco* cubes. To assure that the resultant NC membranes were free from its preservation syrup, the cubes were thoroughly washed, prior to the pressure-driven membranes processing. Afterwards the produced NC membranes were directly compared with a BNC membrane, produced by *Acetobacter xylinum*, with 99% purity[333], by FTIR-ATR spectroscopy (Figure 4.7).

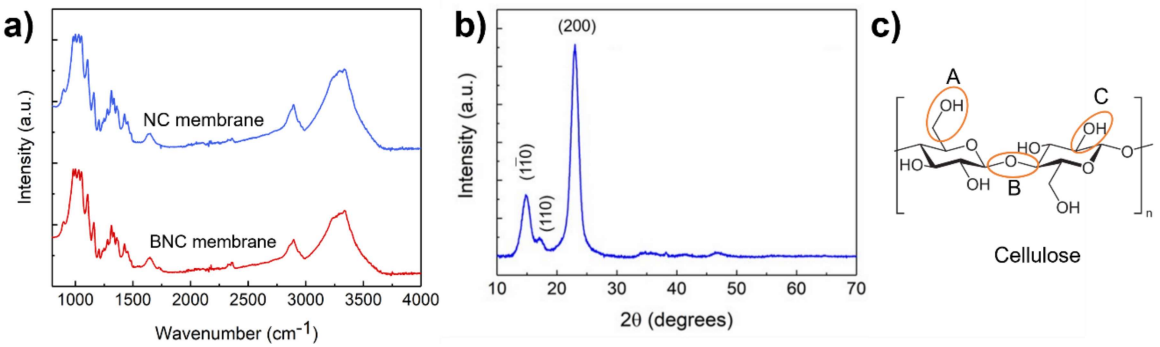

Figure 4.7 NC membranes characterization: a) FTIR spectra comparison between reference BNC and washed *nata de coco* membrane; b) XRD diffractogram of washed *nata de coco* membranes. Diffraction peaks are identified with the respective crystallographic plane; c) Chemical structure of cellulose.

A high similarity between the spectra of reference BNC membrane and the NC membrane (Figure 4.7a) is observed - in both FTIR spectra it is possible to identify cellulose characteristic peaks especially in the fingerprint region (900 – 1500 cm^{-1}). Characteristic peaks of the asymmetric deformation of CH_2-OH bonds of hydroxyl groups (Figure 4.7c - A), C-O-C bonds of β-glycosides (Figure 4.7c - B), as well as C-OH bonds (Figure 4.7c - C) are part of this region. In addition to this, it is also possible to identify the characteristic peak of C-H bonds at 2909 cm^{-1}, present in cellulose.[334,335]

Finally, XRD was used for structural characterization (Figure 4.7b). By analysing the obtained diffractogram, NC membranes show major diffraction peaks at 14.7°, 16.9° and 22.9°, corresponding to

the ($1\bar{1}0$), (110) and (200) crystallographic planes, respectively.[336] These peaks are characteristic of the two phases of the cellulose crystalline structure (I_α and I_β).[337] The fact that the two peaks at 2θ values of 14.7° and 16.9° are distinguishable from one another, corroborates the high crystallinity of nanocellulose, since if there were any amorphous components present there would be a peak convolution.[337]

The obtained NC membranes were imaged through SEM and AFM (Figure 4.8) and compared directly with the BNC reference.

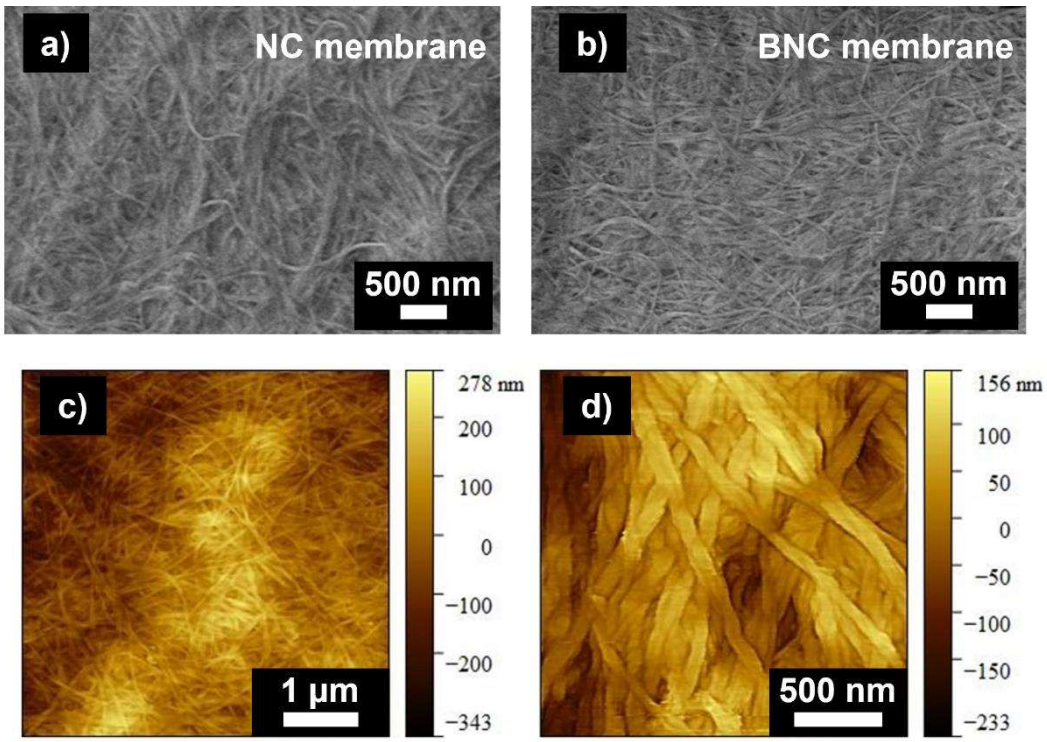

Figure 4.8 SEM and AFM morphological characterization of NC and BNC membranes: SEM imaging of a) NC and b) BNC membranes; c) and d) AFM scanning of NC membrane: 2D 5 μm^2 and 1.5 μm^2 scan.

Both membranes are composed by a three-dimensional network of intertwined cellulose fibres with a width on the nanoscale range. The fibre diameter was calculated with ImageJ software, showing similar values for both membranes, with values of 35.25 ± 12.16 nm for the NC membrane obtained from *nata de coco* cubes and, 54.26 ± 6.97 nm for the BNC reference. AFM images of NC membranes are presented in Figure 4.8c and d. The rugosity root mean square value was calculated from the 5 μm^2 scanning area image, using the *Gwyddion* software, with a value of 75 ± 10.78 nm.

4.2.2 Microwave-assisted synthesized AgNPs on nanocellulose substrates for breast cancer diagnosis

Based on the Global Cancer Observatory (GLOBOCAN) estimates, about 19.3 million new cancer cases and 9.9 million deaths occurred in 2020 worldwide.[338] Breast cancer is the most frequently diagnosed form of cancer and the leading cause of cancer death among females worldwide, with an estimated 2.3 million new cases and 684,996 deaths in 2020, for both sexes.[338] The diagnosis of breast cancer in the current scenario is made by mammography and its spectroscopy, and breast biopsy test. All these detection techniques are usually expensive, invasive and time-consuming.[111] Thus, the development of simple, reliable, cost-effective and non-invasive detection methods for early cancer diagnosis and posterior follow-up is particularly important, due to the disease's prevalence and potential lethality.

Exosomes are small (50–100 nm in diameter) extracellular vesicles (EVs) secreted from various mammalian cells into body fluids such as blood, saliva, and urine. These EVs show potential for cancer diagnostics, as they transport several molecular contents of the cells from which they are secreted.[110,339–341] Additionally, exosome analysis is minimally invasive and can afford relatively unbiased readouts of the entire tumour burden, less affected by the scarcity of the samples or intra-tumoral heterogeneity.[342] The essential first step of current exosome analysis is purification by ultracentrifugation. Afterwards, exosomes may be analysed using western blot, enzyme-linked immunosorbent assay or flow cytometry. Though non-invasive, robust and effective, these analytical methods are still expensive, time-consuming and rely heavily on the sample handling skills.[32] Thus, the development of sensor technologies for rapid, inexpensive, simple and on-site exosome screening is necessary. Some exosomes-based sensors have already been reported, such as label-free exosome assay utilizing transmission SPR,[343] mass-sensitive sensors,[344] aptamer-based sensors,[32] magneto-electrochemical sensors,[342] among others.[111,345]

Label-free exosome identification and differentiation trough SERS has already been studied and proven its feasibility, focusing on different proteins present in tumoral and non-tumoral exosomes, providing distinguishable Raman signal.[52,346] In fact, due to the intrinsic exosomal heterogeneity which restraints the identification of specific disease-related biomarkers for selective separation and labelling of clinically relevant exosome subpopulations, the number of reports on label-free approaches surpasses the labelled approaches.[347]

Herein, AgNPs were synthesized directly onto NC membranes (NC@AgNPs), assisted by microwave irradiation, for the label-free profiling of exosomes from MCF-10A (non-tumorigenic breast epithelium) and MDA-MB-231 (breast cancer) cell cultures lineages.

NC@AgNPs SERS platform: production and characterization

The AgNPs synthesis was achieved through a chemical route where silver nitrate ($AgNO_3$) was used as precursor and ammonium citrate ($C_6H_{17}N_3O_7$) as reducing agent. This agent has a preferential attachment on silver (111) crystallographic plane and works as a local growing inhibitor, thus favouring an anisotropic growth.[268,348] An optimization process was carried out by varying synthesis' parameters, such as temperature, time, and precursor concentration to obtain fully covered NC membranes with AgNPs thus favouring the creation of hot spots for SERS measurements.

The resulting NC@AgNPs membranes were analyse through SEM and AFM to observe the resulting nanoparticle morphology and size distribution (Figure 4.9).

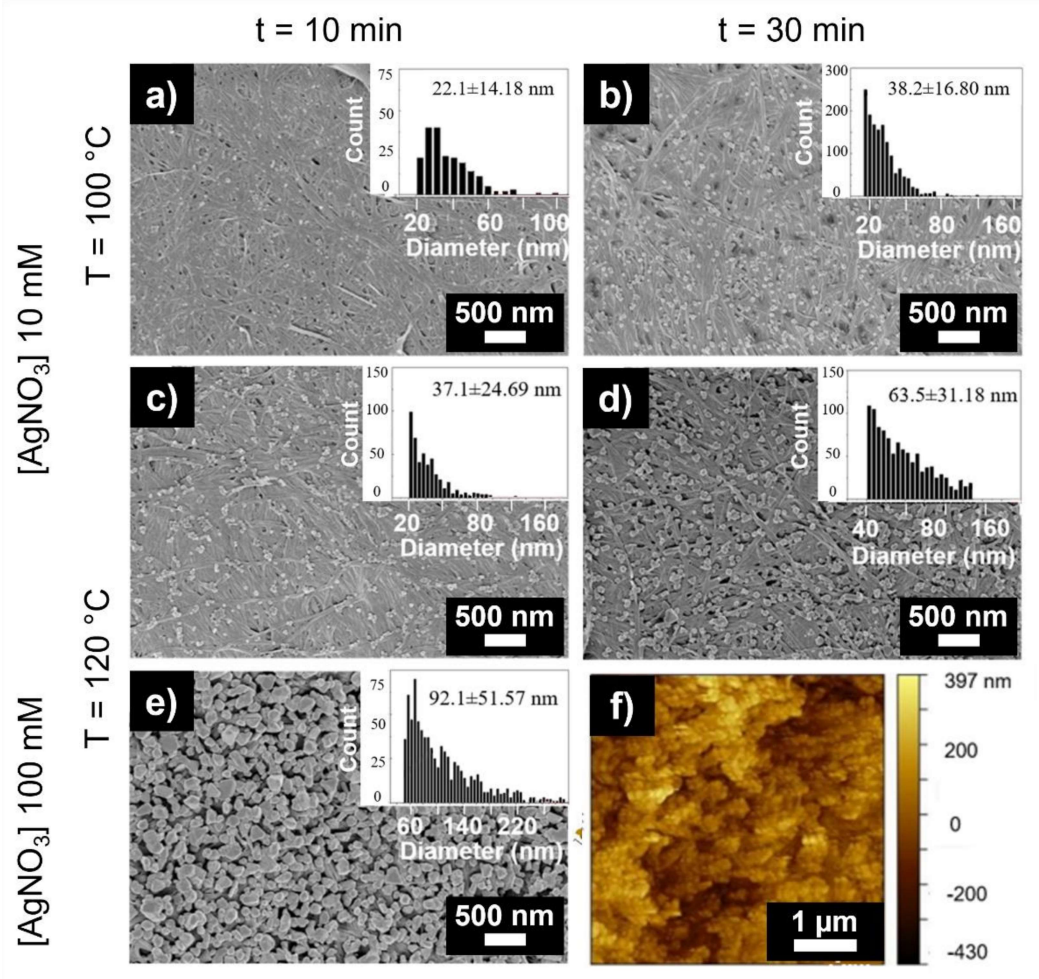

Figure 4.9 SEM and AFM imaging of NC@AgNPs membranes synthesized with ammonium citrate, with different synthesis' parameters: a) 10 mM 10 min 100 °C; b) 10 mM 30 min 100 °C; c) 10 mM 10 min 120 °C. d) 10 mM 30min 120 °C; e) 100 mM 10 min 120 °C; f) AFM imaging of the NC@AgNPs membrane produced with 100 mM 10 min 120 °C; Insets: respective AgNPs size distribution and calculated average diameter.

A clear nanoparticle size and distribution dependence on the synthesis parameters is observed. Optimal conditions were found to be 120 °C, 10 min synthesis time and 100 mM $AgNO_3$ concentration, with a

respective ammonium citrate dibasic concentration of 50 mM, since it produces anisotropic AgNPs, covering entirely the NC membrane (Figure 4.9e). The optimal substrate was also morphologically characterized by AFM (Figure 4.9f). A rugosity value of 139.4 ± 46.44 nm was obtained, calculated analogously to the presented before. As expected, compared to bare NC fibres, the rugosity increased due to the presence of AgNPs.

Energy-dispersive X-ray spectroscopy (EDS) (Figure 4.10) was used for chemical tracking of Ag further demonstrating the formation of AgNPs and proving the synthesis success in homogeneously covering the nanocellulose fibres.

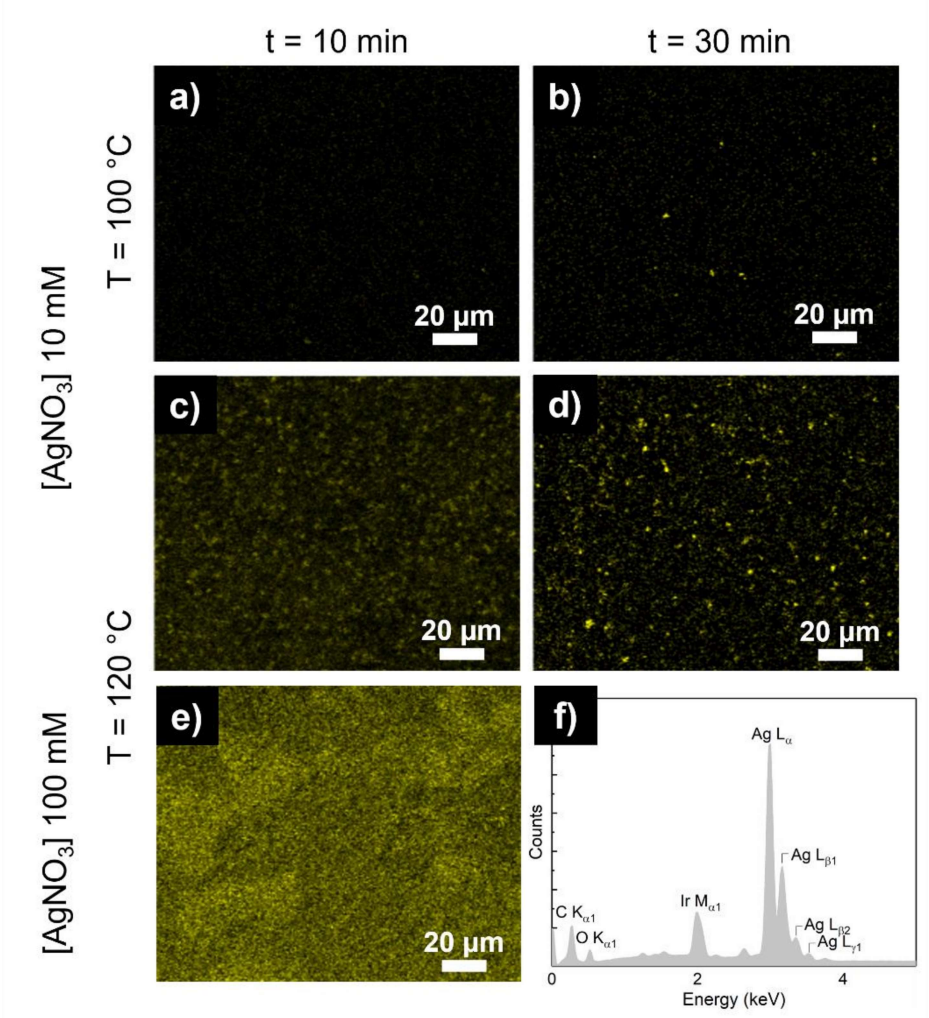

Figure 4.10 EDS mapping of NC@AgNPs membranes synthesized with ammonium citrate, with different synthesis' parameters: a) 10 mM 10 min 100 °C; b) 10 mM 30 min 100 °C; c) 10 mM 10 min 120 °C. d) 10 mM 30min 120 °C; e) 100 mM 10 min 120 °C; f) EDS spectrum of the NC@AgNPs membrane produced with 100 mM 10 min 120 °C. All EDS images were treated equally in terms of contrast and brightness adjustment.

Finally, the XRD analysis of the optimized NC@AgNPs membranes is presented in Figure 4.11.

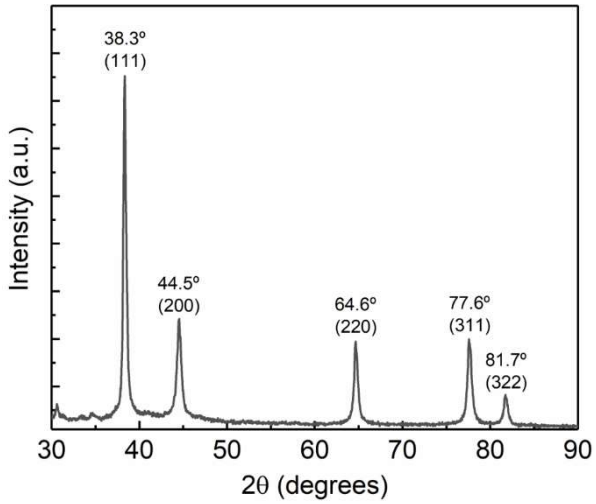

Figure 4.11 Diffractogram of the optimized NC@AgNPs membrane showing the characteristic AgNPs diffraction peaks.

As seen above, silver crystalline planes (111), (200), (220) and (311) can be identified in the diffractogram, confirming the presence of face-centred cubic structure of AgNPs, with well-defined peaks.[349]

Implementation of NC@AgNPs as a platform for breast cancer diagnosis

Firstly, the produced NC@AgNPs membrane was characterized in terms of LOD and reproducibility (Figure 4.12). R6G was used as a model molecule due to its well-defined Raman characteristic peaks.

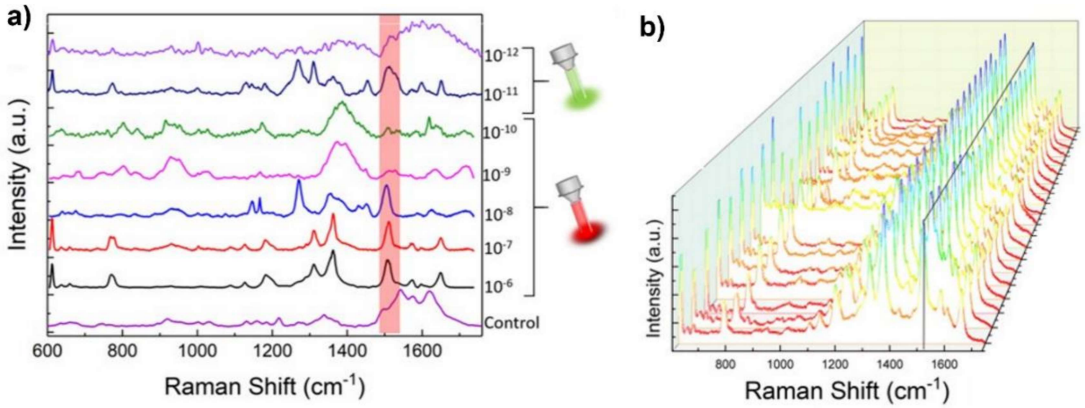

Figure 4.12 SERS spectra of R6G deposited on the NC@AgNPs membranes: a) average of R6G SERS spectra (n=3) with different concentrations: from 10^{-6} M to 10^{-10} M with 633 nm laser and 10^{-11} M to 10^{-12} M with 532 nm laser; b) R6G 10^{-6} M SERS spectra displaying SERS platform reproducibility (n=20).

The lowest concentration at which the R6G signature could be identified was experimentally tested to further characterize the membranes as SERS substrates: R6G concentrations from 10^{-6} M to 10^{-12} M were

used. The obtained average spectra of three measurements for each concentration are presented in Figure 4.12a**.** Following the peak at 1510 cm^{-1} the lowest detectable concentration, with a 633 nm laser, stays between 10^{-9} to 10^{-10} M. Moreover, with a 532 nm laser, it is possible to distinguish R6G signal, from the background, up until 10^{-11} M. In terms of reproducibility, 20 measurements on different substrate' batches were taken on random sample spots, to test inter and intra SERS substrate reproducibility, with 10^{-6} M R6G. Reproducibility was evaluated by tracking R6G characteristic peak at 1510 cm^{-1}. As seen in Figure 4.12b**,** R6G peak at 1510 cm^{-1} can be identified in all recorded spectra, with a good intensity homogeneity, demonstrating the high reproducibility of the NC@AgNPs membranes as SERS substrates, with an RSD lower than 6%.

Having demonstrated the ability of the prepared SERS platform for Raman signal amplification, with good analytical performances, SERS measurements were carried out with exosome samples coming from tumoral (MDA-MB-231) and non-tumoral (MCF-10A) cell lines, with a concentration of 10^{9} exosomes/ml, since the followed protocol for exosomes isolation, can provide no less than 10^{10} exosomes/ml (as shown in the Nanoparticles Tracking Analysis (NTA) Figure 4.13), even from patient-derived samples.

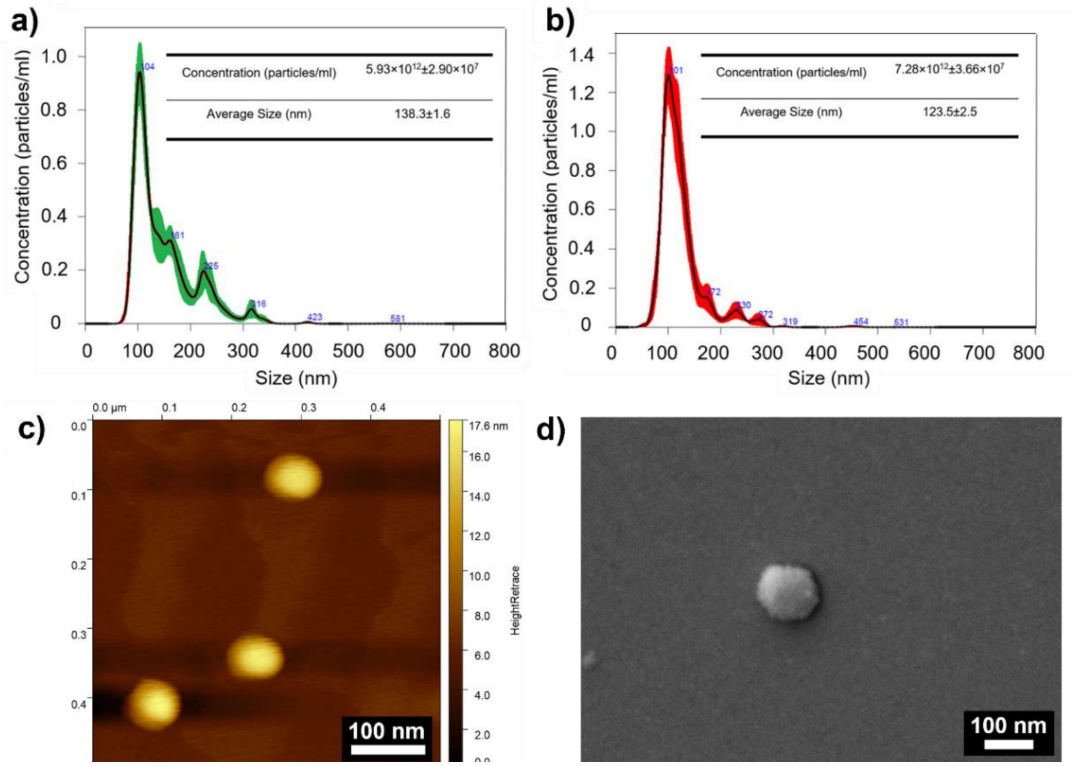

Figure 4.13 Nanoparticle tracking analysis, performed with NanoSight® NS300, of exosomes originated from cell lineages: a) MCF-10A (non-tumoral mammary gland) and b) MDA-MB-231 (breast cancer). The curves represent the average of 5 independent measurements and the respective standard deviation. Insets show the concentration in particles/ml and the exosome's average size; c) AFM and d) SEM images of exosomes from cell line MCF-10A.

The followed exosome's isolation and purification protocol rendered concentrations of $5.93 \times 10^{12} \pm 2.90 \times 10^{7}$ and $7.28 \times 10^{12} \pm 3.66 \times 10^{7}$ for exosomes obtained from the non-tumoral and tumoral cell lines, respectively. Moreover, NTA allows for the estimation of the particles size showing an average size of 138.3 ± 1.6 nm for the non-tumoral exosomes and 123.5 ± 2.5 nm for the tumoral exosomes. Additionally, AFM and SEM imaging of exosomes was performed (Figure 4.13) showing the globular morphology of these biostructures.[350]

Since spectral data of exosomes is highly complex due to the presence of several surface's proteins, the use of multivariate mathematic and statistic methods is commonly required for a more accurate spectral analysis.[347] So, here PCA was used to reduce the high multidimensionality of the large set of vibrational data by identifying a dominant, smaller group of variables while still retaining most of the key information of the initial large data set. PCA conducts a linear (orthogonal) transformation on the SERS data, compressing a multitude of correlated variables (i.e., Raman shift peaks) into linearly uncorrelated variables known as principal components (PCs). By decreasing the multidimensionality of the data set PCA can aid in separating valid diagnostic information from a statistically complex background and be used as a classification tool for cancer diagnosis.

A clear distinction between control (PBS buffer), tumoral and non-tumoral exosomes was observed in the score plot (Figure 4.14a), and the spectral features that more contribute for this differentiation can be visualized when analysing the stacked average spectra of the samples (Figure 4.14b).

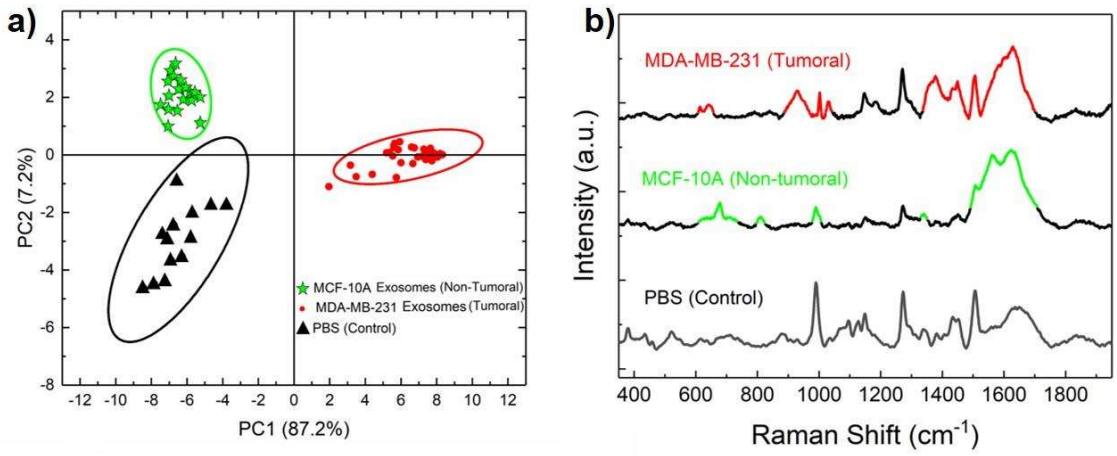

Figure 4.14 Exosomes profiling using MCF-10A (non-tumoral, n=18) and MDA-MB-231 (tumoral, n=20) exosomes through SERS data analysis using PCA: a) PCA resultant score plot using PC1 and PC2 as the analysed principal components, with 95% confidence ellipses; b) Average PBS, MCF-10A exosomes and MDA-MB-231 exosomes SERS spectra: spectra peaks with most variance between groups highlighted.

Additionally, it is possible to see that most of the variance is represented by PC1 and PC2, 87.2% and 7.2%, respectively, thus accounting for a total of 94.4% of the total variance. The results obtained with

NC@AgNPs combined with PCA analysis for exosome's profiling from mammalian cells show the potential of this approach to be used for breast cancer diagnosis and follow-up, as well as other forms of cancer and other diseases.

4.2.3 Microwave-assisted synthesized AuNPs on nanocellulose substrates for SARS-CoV-2 diagnosis

The ongoing pandemic of COVID-19 caused by the SARS-CoV-2 virus has caused to date more than 252 million cases and more than 5.09 million deaths (data accessed on 12nd November, 2021)[1]. Several diagnostic strategies and perspectives have been reported in the literature.[351,352] Spike (S) protein was identified as one of the potential biomarkers to diagnose this disease.[353–355] A few works on SERS-based S protein screening have been already reported. Zhang, D. et al has described a SERS platform, based on silver nanorods grown on a silicon substrate, for the recognition of S protein using the receptor angiotensin-converting enzyme 2 (ACE2) as biomarker.[356] Also, a work based on Ta_2C MXenes for Raman signal intensification was used for S protein recognition,[357] thus validating the SERS approach for COVID-19 diagnosis.

Herein, a protocol for the in-situ growth of AuNPs onto NC membranes was established (NC_{inc}@AuNPs) with which promising preliminary results of the label-free detection of the S protein of SARS-CoV-2 virus is shown, thus demonstrating the potentialities of the developed method for SERS membranes fabrication. The developed SERS platforms were directly compared with other cellulose formats and were fully characterized in terms of Raman enhancement, substrate reproducibility and shelf-life.

Solution-based AuNPs synthesis: production and characterization

Initially, a study on the dependence of AuNPs properties from reactant's concentration and type of chemical reducing agent (RA) was conducted to select proper parameters for the in-situ SERS membranes fabrication. $HAuCl_4$ was used as the precursor and tested at concentrations of 0.5 and 1.0 mM. As for the RAs, the nanoparticles were synthesized with sodium citrate (Na_3Ct), following a modified Turkevich method[115] and with glucose, at the concentrations of 2.5 and 5.0 mM. The syntheses were performed for 10 min at 120 °C, assisted by microwave irradiation. In addition, when glucose was used as RA, the syntheses were also performed at RT, without microwave irradiation, since it is reported in the literature, glucose-based AuNPs production promoted by an alkaline medium at RT.[50,358,359] However, the syntheses outcome showed poor reproducibility as optical properties is concerned, with variable surface plasmon resonance and absorbance values (Figure 4.15). For this reason, this approach was disregarded in further optimizations.

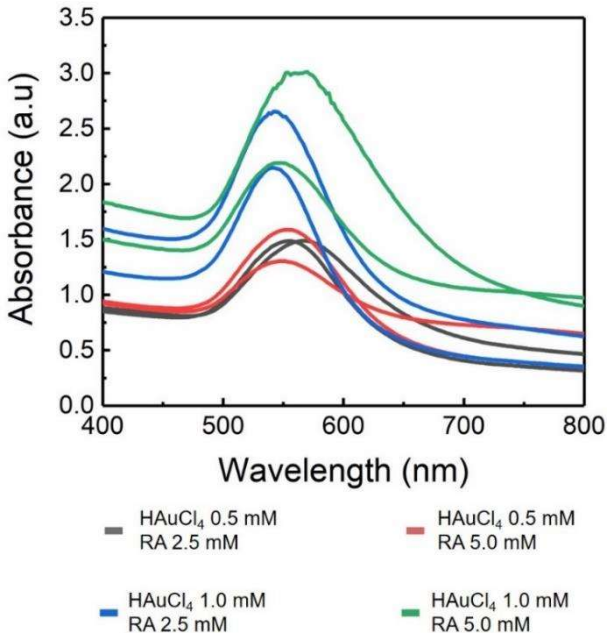

Figure 4.15 UV-Vis optical properties of synthesized AuNPs through D-glucose reduction, at room temperature, activated with an alkaline medium. The syntheses were repeated two times and the corresponding UV-Vis curves are represented separately.

The optical properties and morphology of AuNPs produced using both Na_3Ct and glucose through microwave irradiation were assessed by UV-Vis spectroscopy and TEM, respectively (Figure 4.16).

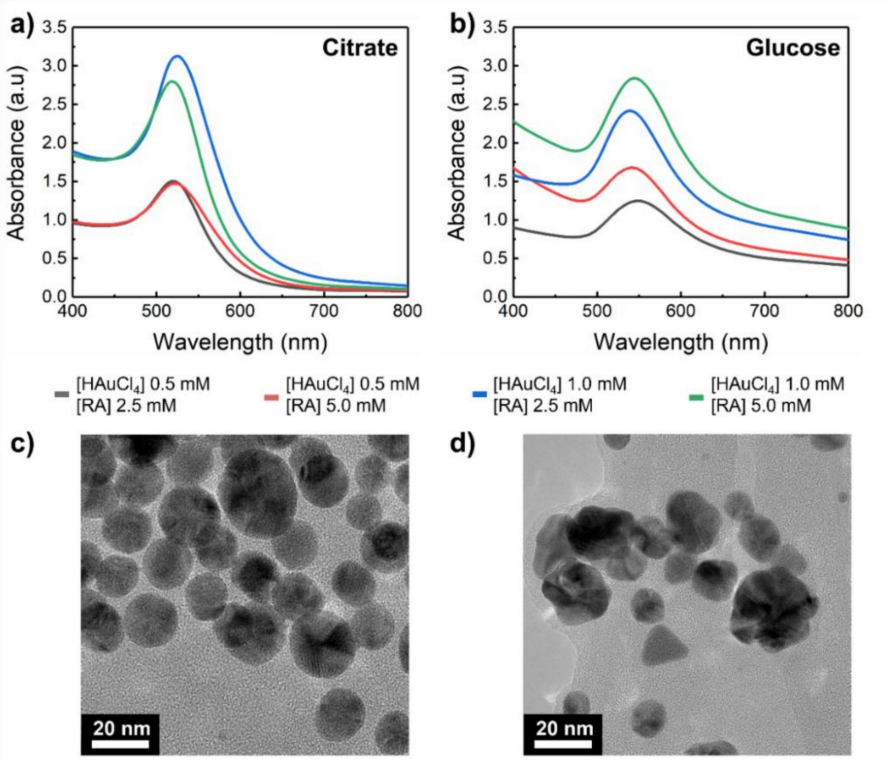

Figure 4.16 Optical properties of the synthesized gold nanoparticles at different concentrations of precursor and reducing agents: a) UV-Vis average spectra (n=3) of citrate-based gold nanoparticles; b) UV-Vis average spectra (n=3) of glucose-based gold nanoparticles; c) Representative TEM image of citrate-based gold nanoparticles; d) Representative TEM image of glucose-based gold nanoparticles.

As expected, a SPR band was observed in all the performed syntheses, thus confirming the successful growth of the AuNPs. Reproducibility was assessed by repeating each synthesis in triplicate and evaluating the resulting optical properties. In general, a good reproducibility was achieved for both citrate and glucose-based syntheses with microwave irradiation, evidenced by the calculated low standard deviations (Table 4.2).

Table 4.2 Analytical features calculated from the average UV-Vis spectra (n=3) of the synthesized AuNPs, by microwave irradiation, with citrate and glucose as reducing agents. AuNPs' diameter calculated by DLS.

[RA] (mM)		[$HAuCl_4$] (mM)	SPR (nm)	Diameter (nm)
Citrate	2.5	0.5	520 ± 0	15.37 ± 2.79
		1	526 ± 2	38.28 ± 4.07
	5.0	0.5	520 ± 2	14.68 ± 4.04
		1	518 ± 2	24.47 ± 3.42
Glucose	2.5	0.5	549 ± 3	45.91 ± 15.23
		1	538 ± 4	129.82 ± 23.15
	5.0	0.5	541 ± 1	60.68 ± 13.7
		1	546 ± 0	80.93 ± 21.96

The reaction for the synthesis of AuNPs by citrate and glucose reduction is based on the oxidation of the reducing agents to dicarboxy acetone and gluconic acid, respectively, with subsequent reduction of Au(III) to Au(0).[359,360] In the glucose-based AuNPs the reaction synthesis is performed in an alkaline medium since it facilitates de reduction of Au(III) by opening the glucose ring.[361] In both cases, the reducing agents act also as a capping agent, contributing to the formation of an outer shell of anionic charges, from the carboxylate groups in citrate or hydroxyl groups, from glucose.[362,363]

For both syntheses, the absorbance values obtained rose when higher concentrations of gold salt precursor were used (Figure 4.16a,b), which may be indicative of an increased number of AuNPs, when $HAuCl_4$ is used in a higher concentration. This observation can be correlated with Polte, J. et al.[364] growth mechanism, explaining that a higher concentration of gold salt precursor leads to a higher

amount of nuclei particles. The authors showed that the conventional LaMer model is unable to predict the evolution of nanoparticle's size distribution, only describing the process of nucleation followed by a growth of the stable nuclei. Polte, J. demonstrated experimentally that the AuNPs formation mechanisms follow four main steps: in a first step, due to the high reduction rate, a rapid formation of clusters of particles with 1-2 nm occurs; then, in a second step, the reduction rate decreases which leads to the coalescence of the freshly formed clusters, translating in a decrease in the number of particles, until stabilization. The number of particles remains then constant throughout the rest of the synthesis process, and their growth in size occurs during the following steps. In the third step, the AuNPs continue their growth through a diffusional process of the reduced gold atoms present in solution and an electrical double layer is created around the AuNPs. Lastly, in the final step, the growth rate increases leading to a rapid reduction of the remaining gold salt, the nanoparticles achieve their final size, and the appearance of a ruby/red colour is indicative of reaction completion.

Figure 4.17 shows the obtained SPR values and AuNPs' diameter obtained by DLS for the citrate and glucose-based AuNPs.

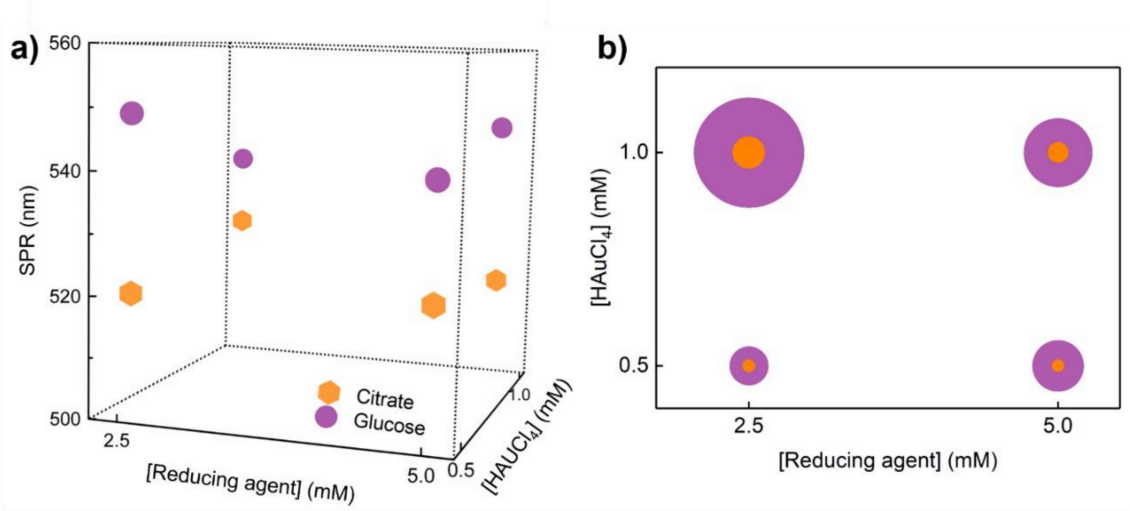

Figure 4.17 Analytical features calculated from the UV-Vis spectra of the synthesized AuNPs, by microwave irradiation, with citrate and glucose as reducing agents: a) SPR values as dependent of reactant's concentration; b) Bubble graph representation of AuNPs' diameter calculated by DLS. Absolute values for the present graph representation are presented in Table 4.2.

The obtained SPR values for citrate-based AuNPs, centred around 520 nm, and for glucose-based AuNPs, centred around 540 nm (Figure 4.17a), are in agreement with those reported in the literature.[362] Moreover, glucose-based AuNPs showed broader absorption bands than the citrate-based AuNPs, which can indicate a higher heterogeneity in size and/or shape of the glucose-based AuNPs.[359] This was confirmed by TEM imaging (Figure 4.16c,d) where spherical particles are visible on the citrate-based AuNPs, whereas the AuNPs prepared with glucose shows anisotropic shapes. Although this

anisotropy of glucose-based AuNPs shape is observed in the literature,[362,365,366] no detailed explanation for such behaviour is given. However, Ishizaka, T. et al relates this behaviour with the influence of the adding rate of NaOH: rapid NaOH supply leads to higher pH medium, which leads to instantaneous formation of small nanoparticles and rapid completion of reduction. On the contrary, slow NaOH adding rates renders lower alkalinity, and therefore a slower reduction process.[361] In fact, the pH environment has an appreciable influence, particularly on the nanoparticle formation rate and the size. The surface of AuNPs is equilibrated with Au–O^- and Au–OH, depending on the pH: at high pH, the surface will be more negative according to the increase in the number of Au–O^- and particles will repel each other, inhibiting further growth of particles and mutual coagulation. In contrast, when the concentration of NaOH is lower and/or close to neutrality, particle repulsion will be suppressed by the relative decrease of Au-O^- on the gold surface.[365,367] Although herein NaOH is added directly to the reaction mixture, prior to the reduction process, this explanation may be extrapolated to our case, since the final pH was close to 7.0, thus the anisotropic shape of the resultant glucose-based AuNPs.

As expected from the SPR values, citrate-based AuNPs have smaller particle' sizes than the glucose-based AuNPs (Figure 4.17b and Table 4.2). One possible explanation for the overall higher SPR and higher diameter of glucose-based AuNPs can be due to the possibility of adsorption of the hydroxyl groups present in the capping layer of these particles which leads to their agglutination. Moreover, a strong dependence of particles' diameter on the concentration of RA was observed, especially for citrate-based AuNPs: for constant $HAuCl_4$ concentrations, higher [RA] renders smaller AuNPs diameter, with higher influence in high $HAuCl_4$ concentrations. These results corroborate with literature data relating the quantity of reducing agent with the final particle size. A high amount of citrate ions strongly favours nucleation leading to a high quantity of nuclei which in turn results in smaller AuNPs, due to the rapid consumption of citrate for $HAuCl_4$ reduction.[364,368–370]

In the case of glucose, this correlation between RA concentration and final particle size was only observed for high concentrations of $HAuCl_4$. The SPR value and particle size can also be strongly influenced by the morphology and/or shape homogeneity of the NPs. In fact, these deviations are observed in the glucose-based AuNPs, since this reducing agent renders AuNPs with higher heterogeneity in terms of shape and size, as it was corroborated by TEM imaging (Figure 4.16d).[359]

The stability of the synthesized AuNPs was evaluated through visual inspection and direct comparison of the A_{SPR} value after 3 months of production (Figure 4.18).

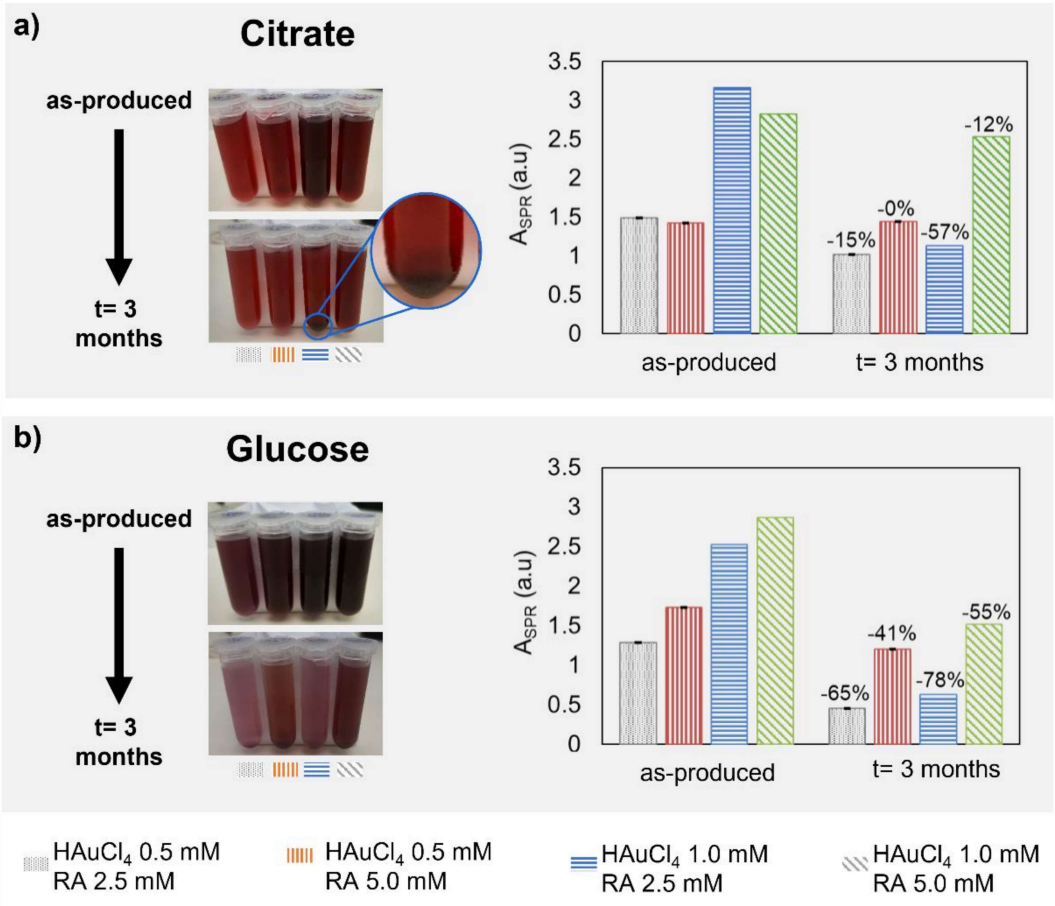

Figure 4.18 Stability evaluation of the synthesized AuNPs after 3 months of storage at 4 ºC: a) citrate-based AuNPs colloidal solutions photographs and calculated maximum absorbances; b) glucose-based AuNPs colloidal solutions photographs and calculated maximum absorbances. The percentage values represent the drop in the maximum absorbance value after 3 months of storage.

Exceptional high stability of the AuNPs produced through citrate-based synthesis is observed, which shows the higher stability efficiency of citrate when compared to glucose.[363] After 3 months of storage at 4 °C, the glucose-based AuNPs precipitated, which translates in drops of the SPR absorbances, of the supernatant, from 41% to 78%. In fact, as mentioned above, this can be explained by the aglutination of glucose-based AuNPs through adsorption which leads to their precipitation. The highest drops are observed for 2.5 mM glucose which can indicate that this concentration is limitant, and it is not enough to efficiently stabilize the produced nanoparticles through a capping process. Besides, the possible abundance of Au-OH groups, as mentioned before, may lead to weak hydrogen bonding interactions between glucose and the surface of AuNPs, which is not strong enough to stabilize the particles for longer storage times.[365] For the AuNPs produced through citrate reduction route, although lower than glucose-based nanoparticles, the highest decrease on A_{SPR} is also observed when 2.5 mM of reducing agent is used. In fact, a noticeable precipitate of AuNPs synthesized with 1.0 mM of $HAuCl_4$ and 2.5 mM of Na_3Ct is visible, with a 57% reduction of the A_{SPR}. A possible explanation could be that when

the reducing agent, which is responsible for both reduction and stabilization of the particles, is present in a low concentration, thus at a low reducing agent to gold ratio, it is not sufficient to efficiently cap the AuNPs, leading to their aggregation with consequent precipitation.[364]

For these reasons, Na_3Ct at 5.0 mM was chosen as the reducing agent and optimal concentration with 1.0 mM $HAuCl_4$ due to its highly stabilized AuNPs combined with a high maximum SPR absorbance, centered at 518 ± 2 nm, which is important to obtain a high loading of NPs onto cellulose-based SERS membranes, increasing the number of hot spots which can result in a more efficient Raman signal amplification.

NC_{inc}@AuNPs SERS platform: production and characterization

The prepared NC membranes from *nata de coco* cubes were subjected to an in-situ growth of AuNPs with the previously optimized conditions. Briefly, a NC membrane was placed inside the microwave vessel, with the reaction mixture, and subjected to microwave irradiation for AuNPs synthesis. The as-prepared membrane was then transferred to a new microwave vessel with a freshly prepared reaction mixture and subjected again to microwave irradiation.

Figure 4.19 shows the resulting SEM images and optical photographs of the prepared NC@AuNPs membranes.

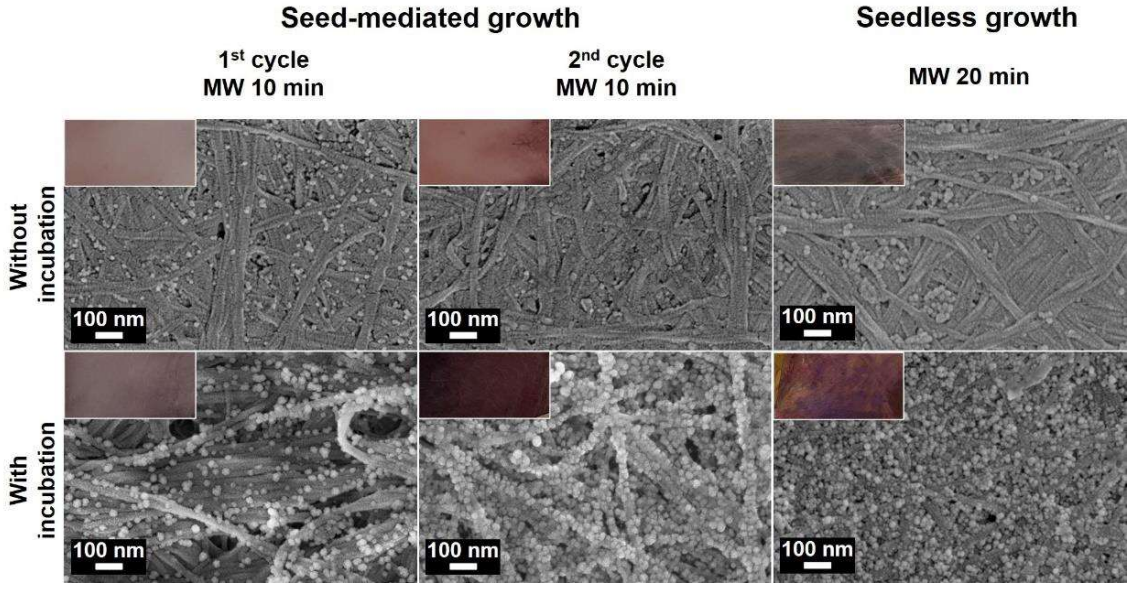

Figure 4.19 In-situ synthesis of gold nanoparticles onto nanocellulose membranes via seed and seedless-mediated growth methods: SEM images and photographs of the resultant membranes. Direct comparison of the membranes with and without the 30 min incubation step.

The growth of the AuNPs onto the NC membrane was performed, in a first stage, by immersing the substrate in the reaction mixture and subjecting it immediately to microwave irradiation. The successful growth of AuNPs onto the NC fibres was confirmed by SEM imaging and by the light purple colour of the obtained membrane. The as-prepared membrane was then used as a seed layer and subjected to a second cycle of synthesis (NC@AuNPs). An increase in the purple colour intensity was observed, which may indicate the formation of larger clusters of AuNPs, as observed in the SEM image. However, these large clusters are heterogeneously dispersed throughout the NC fibres and at a very low density.

As it is known, the dispersion of closely-packed AuNPs throughout the substrate is critical for SERS performance, where the main contributor for high EF is the electromagnetic effect that can be magnified when the plasmonic NPs are close to each other, creating hot-spots.[315] To increase the AuNPs' density onto the NC membranes, an incubation time of 30 min preceded the seed-mediated growth process. We believe that this incubation time, prior to microwave irradiation, allowed the formation of pre-colloidal nuclei, visible by the change of the reaction mixture to a greyish colour solution, and for an efficient nanocellulose' wicking of the reaction mixture. This led to an increase in the number of AuNPs loaded onto the NC membrane, compared to the same process without incubation (Figure 4.19). Additionally, the 2nd cycle of microwave synthesis revealed a full coverage of the NC fibres, visible in the SEM image and in the inset picture of NC_{inc}@AuNPs membrane that presents a dark purple colour.

The XRD analysis performed on the SERS membranes obtained by the seed-mediated growth method, with and without the incubation step (NC_{inc}@AuNPs and NC@AuNPs, respectively), revealed the presence of the characteristic AuNPs crystallographic peaks (Figure 4.20a).

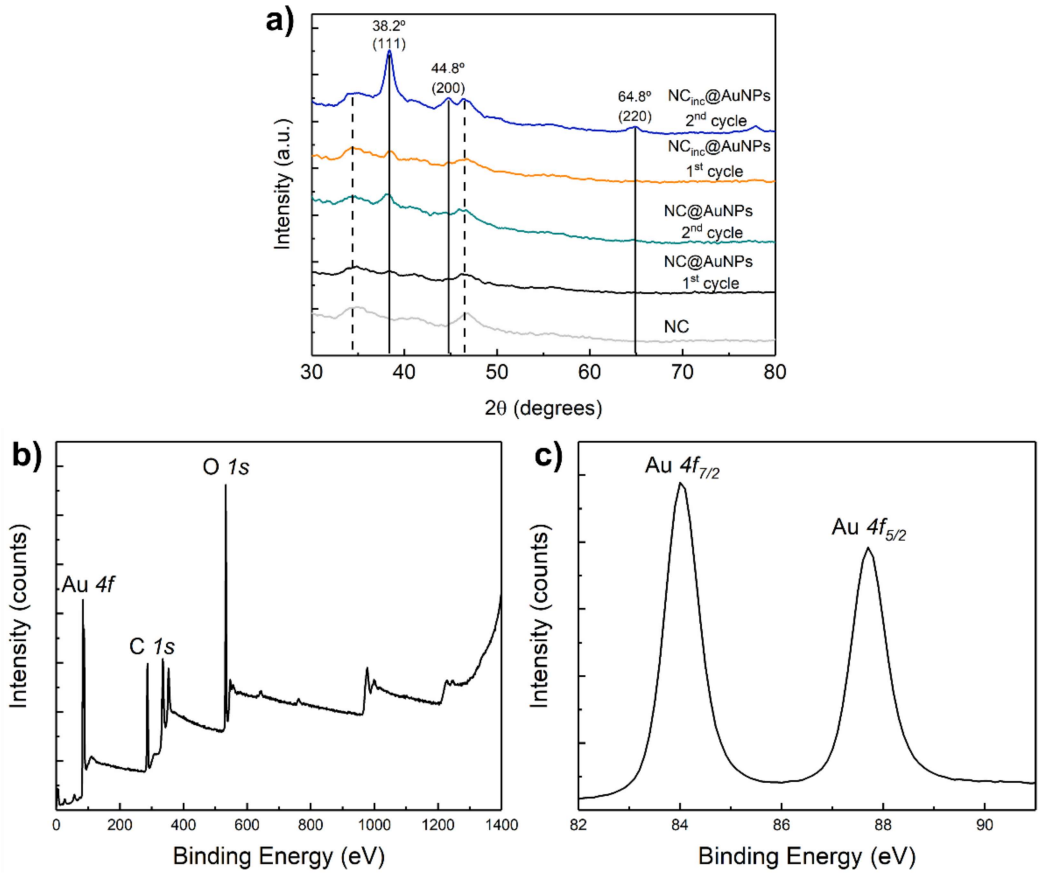

Figure 4.20 a) XRD diffractogram for the NC membrane with and without grown AuNPs on its fibres after each reaction cycle without and with the incubation step; b) and c) XPS analysis of the optimized NC_{inc}@AuNPs SERS platform.

In addition, is it observed, especially in the most prominent peak at 38.2°, assigned to the (111) crystallographic plane,[371] an increase in its intensity from the 1st to the 2nd cycles, indicative of the increase in the AuNPs number. A XPS analysis was also performed to the final and optimized NC_{inc}@AuNPs membrane, with the incubation step and the seed-mediated growth method (Figure 4.20b,c). As expected, the presence of the peaks from oxygen (O *1s*) and carbon (C *1s*), from the capping layer, respectively centred at 533 and 287 eV, are visible (Figure 4.20b). The peak at 84 eV, assigned to Au $4f_{7/2}$, and the peak at 88 eV, attributed to Au $4f_{5/2}$, with a peak separation of 3.7 eV and with $I4f_{7/2} > I4f_{5/2}$ (Figure 4.20c), confirms the complete reduction of Au^{3+} to Au^0, reinforcing the successful growth of AuNPs.[372–375]

Having established the need for an incubation step, the necessity of a seed-mediated growth method instead of a seedless AuNPs growth onto the NC membrane was also investigated. For that, the reaction time was increased to 20 min, to assure that the homogeneous growth of AuNPs was directly related to the seed and not to the total reaction time. These syntheses were performed by maintaining all the other microwave parameters and reactants concentration constant, without and with the incubation

step. Although both cases lead to AuNPs' growth, confirmed by SEM and by the membranes' purple colour, as expected, the synthesis carried out with the incubation step resulted in a NC membrane with a higher density of AuNPs. By directly comparing the SERS membranes obtained by the seed and seedless-mediated growth, with the incubation step (NC_{inc}@AuNPs and $NC_{inc\text{-}20min}$@AuNPs, respectively), it was possible to observe in both cases a good coverage of the NC fibres with the in-situ synthesized AuNPs. However, a lower coverage of the cellulose fibres by the AuNPs is observed when compared with the seed-mediated growth method. This reveals the importance of having a seed for the subsequent growth of AuNPs and the importance of renew the reaction mixture offering more citrate and gold ions for the synthesis of more AuNPs.

Despite the better outcomes displayed by the solution-based citrate reduction route for the AuNPs synthesis, the previously optimized conditions for the preparation of SERS membranes (incubation step followed by a seed-mediated growth method) were mimicked using glucose as the RA. However, this synthesis method showed a poorer coverage of the cellulose' nanofibers and a very low AuNPs' density with bigger particles' sizes than the citrate-based synthesis, which can be correlated with the results obtained in the solution-based synthesis (Figure 4.21).

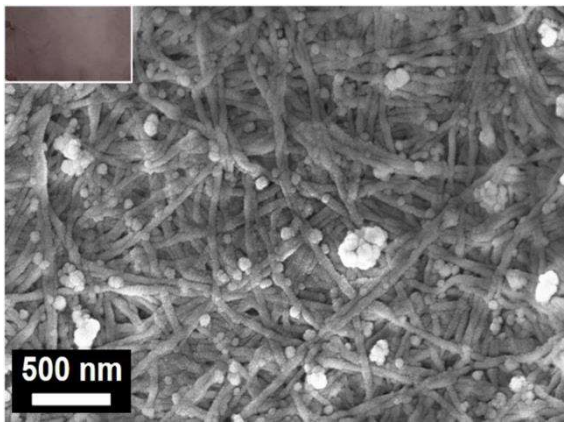

Figure 4.21 SEM image and optical photograph of glucose-based NC membrane with grown AuNPs with the optimized conditions for citrate-based synthesis.

A possible explanation for the poor coverage was given by Xia and co-workers,[309] stating that the carbonyl groups of reducing agents can effectively absorb microwaves, facilitating the reduction process. In opposition to citrate that is composed of several carbonyl groups, glucose has five hydroxyl groups that compete for microwave absorption.

Additionally, the optimized in-situ seed-mediated growth method for NC membranes was also performed with other cellulosic substrates: office paper, cardboard, Tetra Pak (data not shown) and Whatman paper grade 1. Due to the lower hydrophilic nature of both office paper and cardboard

substrates (Annex - Figure A1), the synthesis rendered an inhomogeneous distribution of the AuNPs (Figure 4.22).

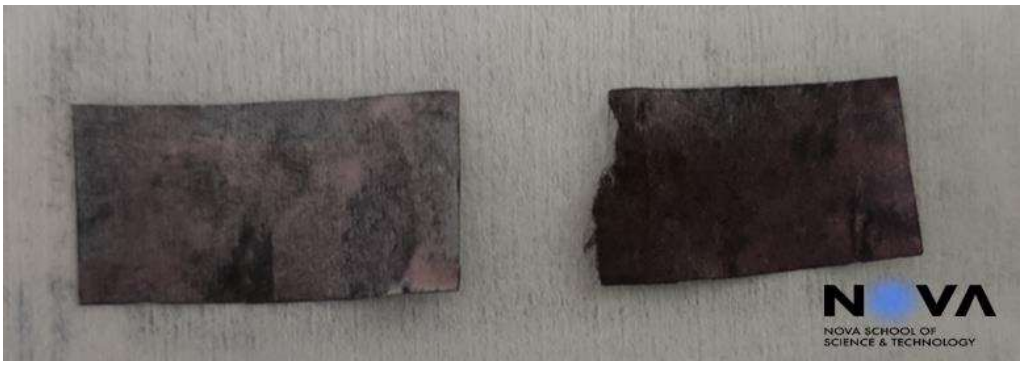

Figure 4.22 Pictures of resulting membranes produced with the optimized method: right (office paper) and left (cardboard substrate).

On the contrary, the Whatman paper's hydrophilic nature allowed to successfully wick the reaction mixture, showing a homogeneous distribution and coverage of the AuNPs on the cellulose fibres (WP_{inc}@AuNPs) (Figure 4.23).

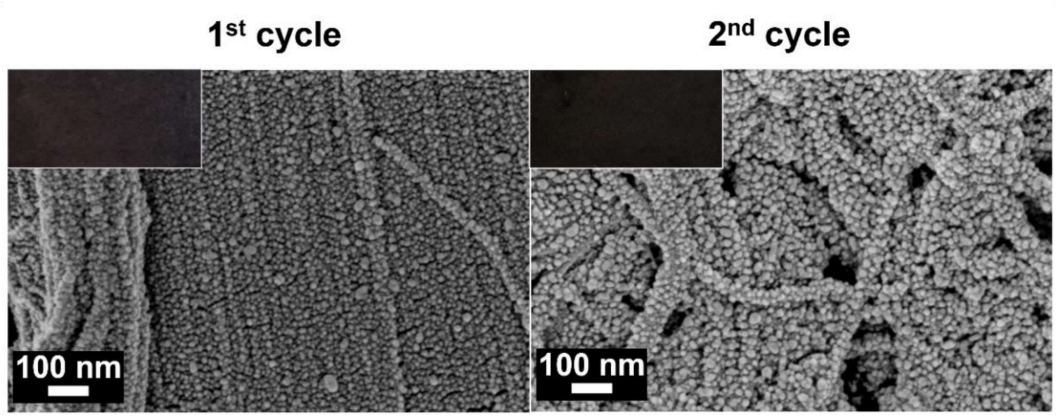

Figure 4.23 In-situ synthesis of gold nanoparticles onto Whatman paper via a seed-mediated growth method, with a 30 min incubation step: SEM images and photographs of the resultant WP_{inc}@AuNPs.

Like the NC membranes, an increase in the AuNPs density was visible from the 1st to 2nd cycle. However, comparing the outcome after 1st cycle of both substrates, the WP_{inc}@AuNPs seems to have a higher particle density. This feature can be due to a higher capillary action of Whatman paper and/or its higher grammage which can lead to the wicking of a superior amount of reaction mixture, resulting in a higher amount of in-situ grown AuNPs. Nevertheless, an increase on the number of AuNPs after the 2nd reaction cycle was visible, with AuNPs fully covering the papers fibres, demonstrated by the SEM image and the darker colour of the resulting WP_{inc}@AuNPs.

The average diameter size of the AuNPs obtained after each cycle was calculated for both NC and Whatman paper substrates, using the ImageJ software (Figure 4.24).

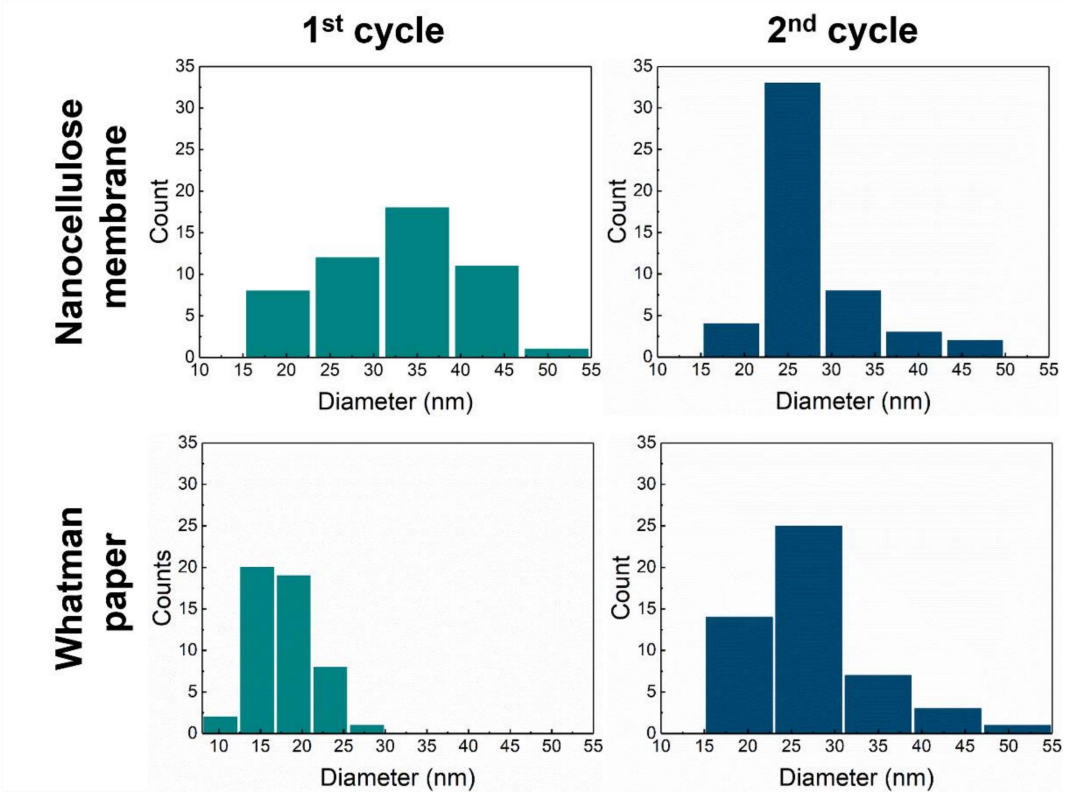

Figure 4.24 Histograms of size distribution of AuNPs after 1st and 2nd cycle of microwave irradiation for nanocellulose and Whatman paper.

Both substrates revealed AuNPs with similar sizes (27.6 ± 6 and 27.1 ± 7 nm for NC_{inc}@AuNPs and WP_{inc}@AuNPs, respectively), after the 2nd reaction cycle. However, after the 1st cycle, the NC_{inc}@AuNPs membrane had bigger sized particles (32.3 ± 8 nm) than the WP_{inc}@AuNPs membrane (17.8 ± 4 nm). This fact may be explained by the faster wicking of the reaction mixture by the Whatman paper substrate, which can result in a faster AuNPs growth and consequently in nanoparticles with smaller sizes.

The ability of the prepared membranes to be used as SERS substrates was evaluated, using R6G as the probe molecule (Figure 4.25).

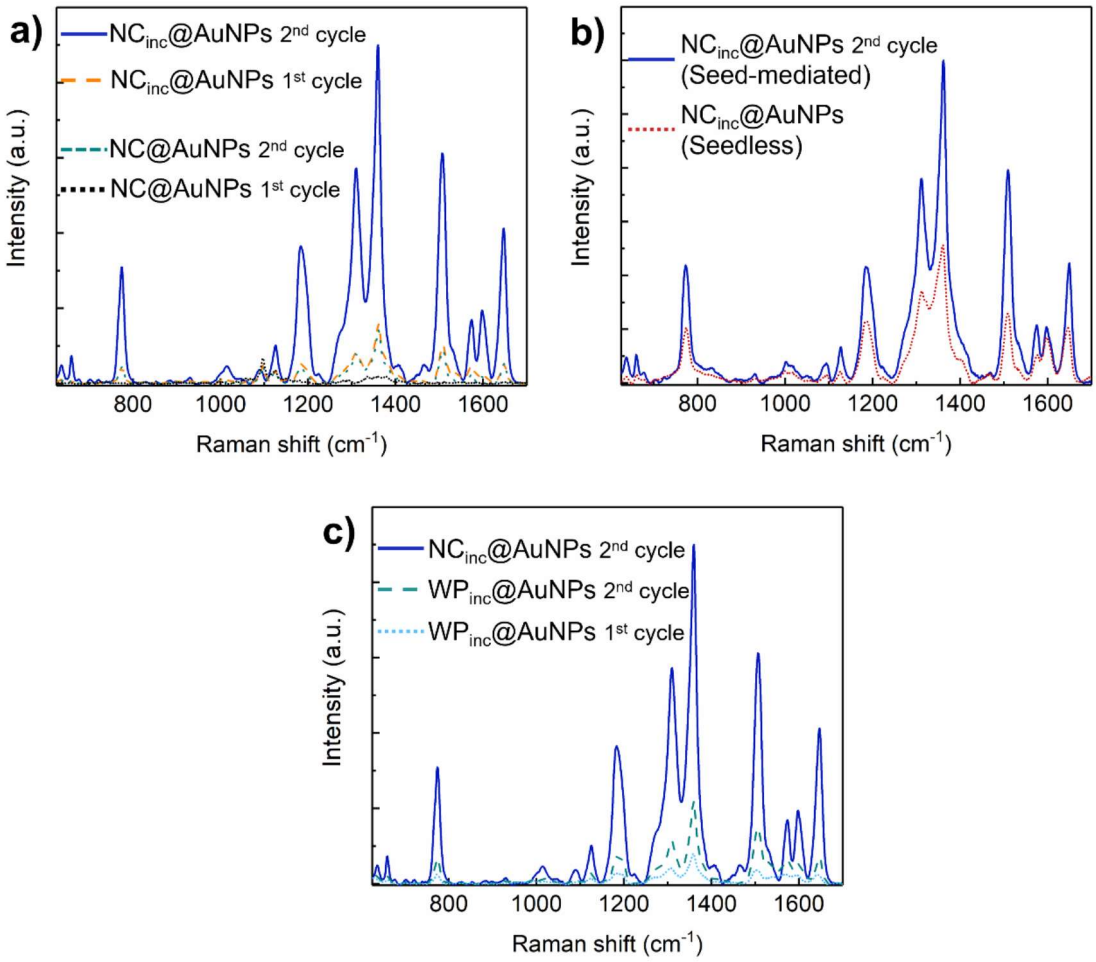

Figure 4.25 SERS performance evaluation of the prepared membranes: a) R6G SERS spectra obtained with SERS substrates after each reaction cycle, with and without the incubation step; b) R6G SERS spectra obtained with the SERS substrates by the seed and seedless-mediated growth methods; c) R6G SERS spectra obtained with the optimized SERS membranes with nanocellulose and Whatman paper substrate produced after each reaction cycle.

Figure 4.25a shows the R6G spectra obtained using the prepared NC@AuNPs and NC$_{inc}$@AuNPs membranes after the 1st and 2nd cycle of microwave irradiation. No R6G characteristic bands were observed with the NC@AuNPs membrane with one reaction cycle and without the incubation step. After the seed-mediated growth, it was possible to notice the R6G bands, although with low signal intensity. On the contrary, a high increase on R6G spectrum intensity was clearly visible, by 6-fold (using the intensity of the most intense band), for the NC$_{inc}$@AuNPs when compared with its counterpart NC@AuNPs, clearly showing the need for and importance of the incubation step. In these cases, the main R6G characteristic bands were clearly visible at 767 and 1184 cm^{-1} attributed to C-H out-of-plane bending and C-H in-plane bending vibrations, respectively. Additionally, the bands at 1360, 1508, 1570 and 1651 cm^{-1} were assigned to symmetric modes of in-plane C-C and C-O-C stretching vibrations.[315]

By comparing the membranes obtained with the incubation step followed by a seed-mediated and seedless growth (Figure 4.25b) it was evident that the membrane obtained by the seed-mediated growth had a better SERS performance. In fact, despite the NC_{inc}@AuNPs membranes obtained with the seedless growth showed well distributed AuNPs, with a good surface coverage, by directly comparing these membranes with the ones obtained through an optimized seed-mediated growth it was observed that the latter had a higher NPs' surface coverage around the cellulose nanofibers.

Finally, Figure 4.25c shows the comparison between the R6G SERS spectra of the optimized NC_{inc}@AuNPs membrane with the membranes produced using Whatman paper as substrate, after the 1st and 2nd cycle of synthesis. Regarding the WP_{inc}@AuNPs membranes, an increase in the SERS signal from the 1st to 2nd cycle of reaction is visible, due to a high amount of AuNPs distributed through the cellulose fibres. Additionally, a higher SERS intensity for the NC_{inc}@AuNPs membranes is observed. This can be explained by high surface area and surface-to-volume ratio of the NC substrate, and since SERS is a surface effect, it can benefit from having the analyte well dispersed in the surface of the SERS substrate. Despite the hydrophilic nature of both substrates and their three-dimensional morphology, which can lead to the absorption of the analyte throughout all the membranes' thickness, the NC substrate has a structure with low porous content and/or nanosized pores, which enables a higher availability of the analyte to the incident laser.

Additionally, the as-optimized SERS membranes were compared with a widely used immersion method to decorate supporting substrates with plasmonic nanostructures.[81,376–378] For that, an NC membrane was immersed in a AuNPs colloidal solution (prepared with the optimized parameters, $HAuCl_4$ 1.0 mM with Na_3Ct 5.0 mM) for 24 h, allowed to dry at RT and the R6G spectrum was recorded (Figure 4.26a).

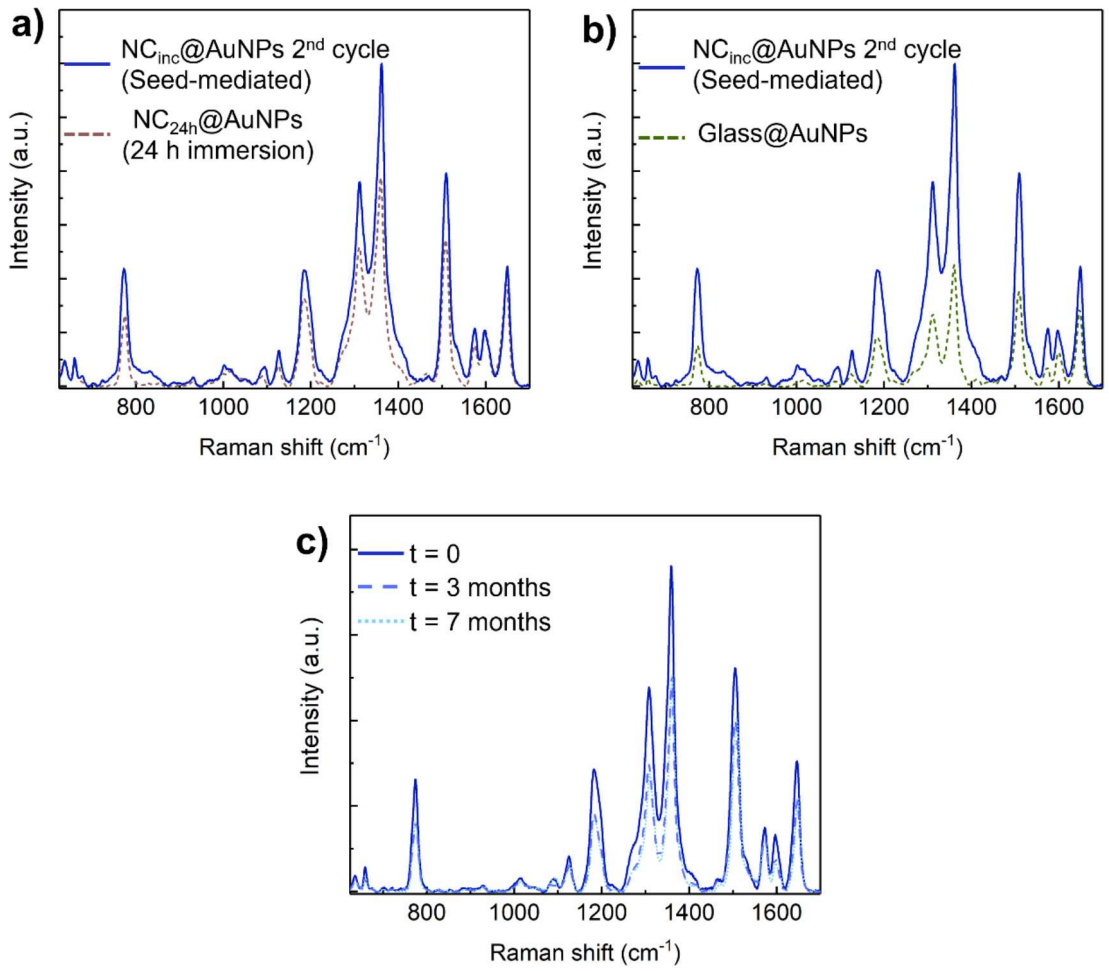

Figure 4.26 As-optimized SERS membrane performance: a) Comparison between R6G average SERS spectra (n=5) recorded on SERS membranes prepared with the optimized method and with a 24 h immersion method; b) Comparison between R6G average SERS spectra (n=5) recorded on SERS membranes prepared with the optimized method and on a glass substrate; c) R6G average SERS spectra (n = 5) obtained in the optimized NC$_{inc}$@AuNPs membrane after production, 3 and 7 months.

A direct comparison of the recorded R6G spectra on the NC$_{inc}$@AuNPs membranes with the ones prepared with the 24 hours immersion method reveals the enhanced performance of our approach, attaining overall higher SERS intensities with a much shorter preparation time. Moreover, to assess the importance of having a high surface area substrate for Raman signal amplification, a 2 µl volume of the AuNPs colloidal solution was deposited on a glass substrate and allowed to dry at RT. Figure 4.26b shows the obtained R6G spectra which reveals a lower SERS signal when compared with our substrate, evidencing the advantages of using cellulose-based substrates as supporting matrix for Raman enhancement nanostructures.

In fact, as seen in Figure 4.27, the AuNPs distribution through the substrates is too dispersed and with a low quantity of AuNPs per area, which explains their worst SERS performance, when compared with our optimized substrate.

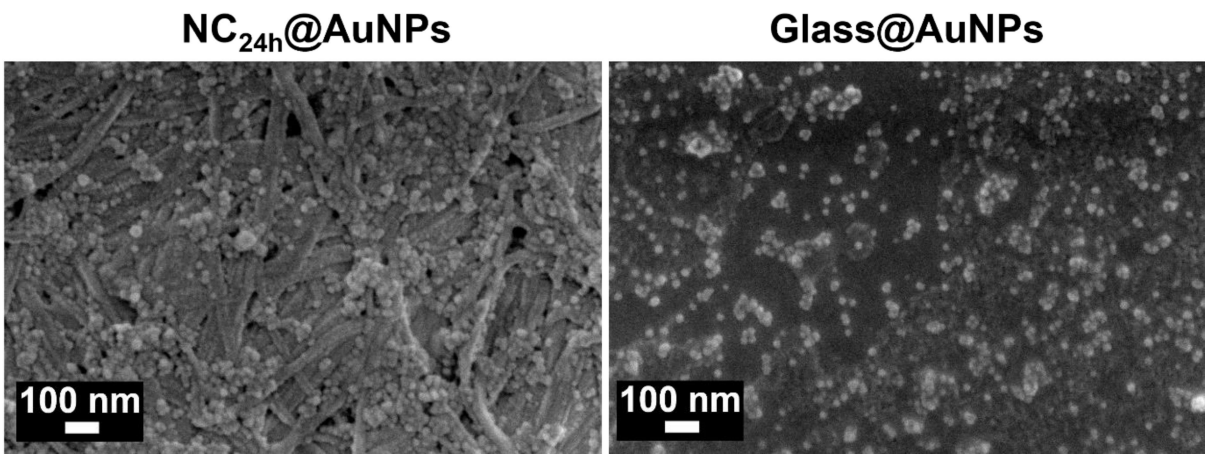

Figure 4.27 SEM images of NC membrane prepared with AuNPs via a 24h immersion method (NC_{24h}@AuNPs) and glass substrate with drop-casted AuNPs (Glass@AuNPs).

Within the most relevant figures of merit of SERS substrates are the EF, RSD, the cost, and the shelf life. The herein produced and optimized SERS platform achieved an EF up to ~10^6, with 10^{-6} M R6G, for both most intense peaks of 1360 and 1508 cm^{-1}, with an RSD lower than 8%, which confirms the good performance of our approach within the state of the art of AuNPs Raman enhancement.[146,147,168] In terms of cost, the use of a low-cost and commercially available substrate allied with a solution-based production method, with an energy-efficient synthesis method, reduces the final cost of the produced membranes significantly, within the cents range, well below the price of the substrates currently available in the market.

Finally, R6G SERS spectra were recorded over time to assess its shelf life (Figure 4.26c) showing a good performance even after 7 months of production. Accounting for the R6G most intense peak of 1360 cm^{-1} a 33% drop in its intensity was observed with the membrane after 3 months of production which remained stable after 7 months. Despite this intensity drop of R6G signal, its main characteristic peaks were still clearly identified, showing that the observed decrease does not have a significant impact upon SERS performance. This evidenced the long shelf life of the produced and optimized SERS membrane, even stored at room temperature without requiring special storage conditions.

Implementation of NC_{inc}@AuNPs as a platform for S protein screening

Herein, we show preliminary results for label-free S protein screening showing the feasibility of the developed SERS platform (Figure 4.28).

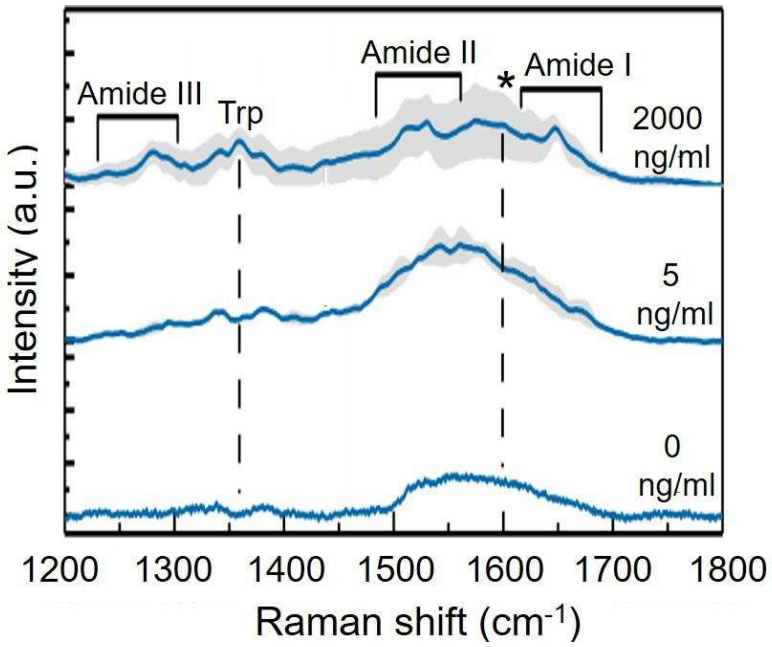

Figure 4.28 SERS spectra of S protein on the optimized SERS membranes. The grey area represents the average spectra (n=3).

The recorded average SERS spectra of S protein for 2000 and 5 ng/ml shows the characteristic bands of proteins. Amide I region is identified in 1600-1690 cm^{-1} associated with C=O stretching, Amide II in 1480-1575 cm^{-1} and Amide III in 1229-1301 cm^{-1} caused by CN stretching and NH bending. Additionally, the peak at 1361 cm^{-1} is attributed to Trp the zone marked with an * can be attributed to aminoacid Phenylalanine (Phe) or Tyrosine (Tyr) and Tryptophan (Trp) residues bands.[379,380]

These results can be seen as initial evidence of label-free COVID-19 diagnosis using a highly stable and low-cost platform. Moreover, for more complex samples, as for the detection of the S protein in biological samples (e.g., serum or saliva), PCA analysis can be also used to help discriminate the specific vibrations of the S protein chemical structure.

CHAPTER 5

LIG-based platforms for MIP fabrication

In this chapter it is presented the developments on the production of planar electrodes, following the method of laser-induced graphene established by the Tour, J. group, in 2014.[217] This method enables the laser-induced photoconversion of polyimide substrates into carbonaceous materials, in a one-step mask less approach. The fabricated LIG electrodes were used to produce MIP-based electrochemical biosensors, with different electrode's architecture, showcasing the versatility of laser-induced graphene technique.

The chapter is divided in two main sub-chapters:

Chapter 5.1. Laser-induced graphene electrodes optimization and fabrication:

- study of the laser parameters required to produced LIG and its chemical, morphological, structural, and electrical characterization.

Chapter 5.2. Implementation of LIG electrodes for MIP-based electrochemical biosensors:

- fabrication of LIG-based electrodes for single detection of chloramphenicol. Each chemical modification carried out for MIP fabrication was followed by cyclic voltammetry and electrochemical impedance spectroscopy and directly compared with commercial SPEs;
- fabrication of LIG-based electrodes for dual detection of amoxicillin and ascorbic acid. Each chemical modification for MIP fabrication was followed by cyclic voltammetry and a strategy for dual detection of molecules was established.

Some of the results shown herein were adapted from:

- Samouco, A., **Marques, A. C.**, Pimentel, A., Martins, R., Fortunato, E., Laser-Induced Electrodes towards Low-Cost Flexible UV ZnO Sensors. Flexible Printed Electronics, **2018**, 3(4), 044002.
- Cardoso, A. R., **Marques, A. C.**, Santos, L., Carvalho, A. F., Costa, F. M., Martins, R., Sales, M. G. F., Fortunato, E., Molecularly-Imprinted Chloramphenicol Sensor with Laser-Induced Graphene Electrodes. Biosensors&Bioelectronics, **2019**, 124–125, 167–175.
- **Marques, A. C.**, Cardoso, A. R., Martins, R., Sales, M. G. F., Fortunato, E., Laser-Induced Graphene-Based Platforms for Dual Biorecognition of Molecules. ACS Applied Nano Materials, **2020**, 3(3), 2795–2803.

Chapter 5. LIG-based platforms for MIP applications

5.1 LIG electrodes: optimization and fabrication

In this sub-chapter it is presented results on the optimization and fabrication of carbonaceous electrodes using the LIG technique onto flexible PI substrates. A CO_2 infrared laser, with a wavelength of 10.6 µm, was used to convert PI substrates into LIG. Although LIG production is wavelength independent and has been reported with other laser wavelengths and alternative carbon sources, the use of 10.6 µm laser dominates the number of publications reported so far. PI has a strong absorption at 10.6 µm,[381,382] and this wavelength provides higher quality LIG[383] and can yield higher sensitivities on electrochemical applications[384], than with other laser sources.

A schematic representation of the process is presented in Figure 5.1.

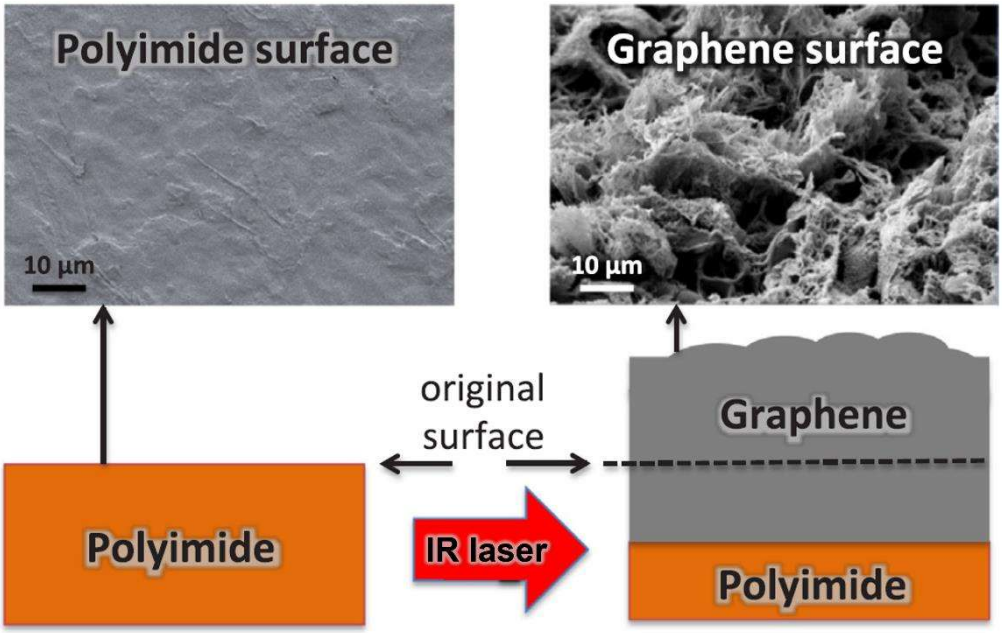

Figure 5.1 Schematic of the LIG formation: the topmost layers of the substrate turn into LIG whereas the bottom part remains pristine and can act as mechanical support.

A preliminary assessment on the laser' parameters (power and speed) required to induced LIG was carried out by patterning 4.0 cm^2 squares at laser powers of 5, 12.5, 25 and 37.5 W and laser speed of 0.38, 0.76 and 1.14 m/s. The outcome of this assessment is presented in the optimization matrix below (Figure 5.2)

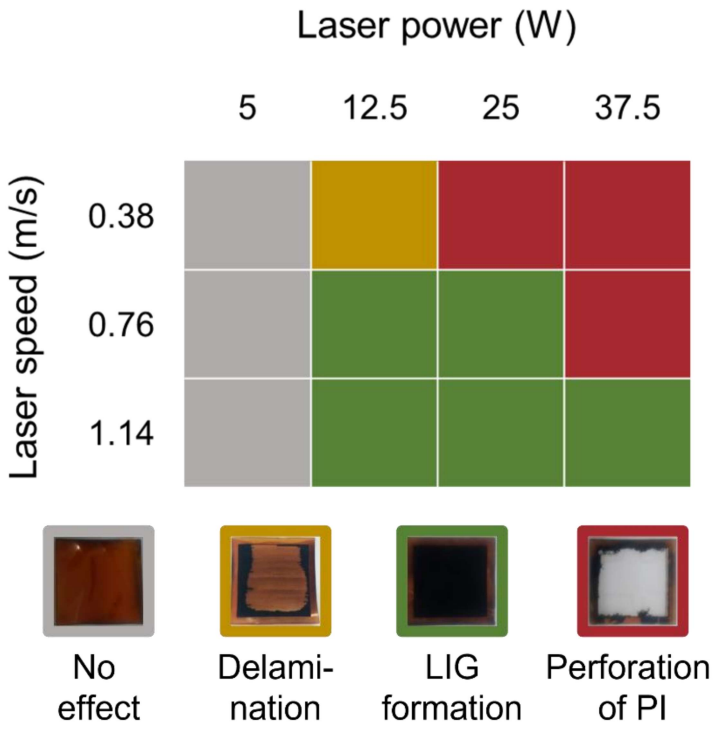

Figure 5.2 Optimization matrix for LIG formation by laser irradiation of PI substrates, with representative pictures.

In general, in the range of power and speed tested, it is possible to observe that at lower laser powers (5 W) no LIG photoconversion occurs, since the induced localized temperature is not enough to photothermally convert into graphemic structures.[35,214,217] With the increase of laser power, three different behaviours were observed: for higher speeds a successful photothermal conversion of PI into LIG occurs and, for lower speeds it is visible a delamination of LIG from PI (12.5 W) or the total perforation of PI in the treated area, due to very high localized temperatures.

Representative SEM images, at increasing magnifications, of the morphology of the produced LIG is presented in Figure 5.3.

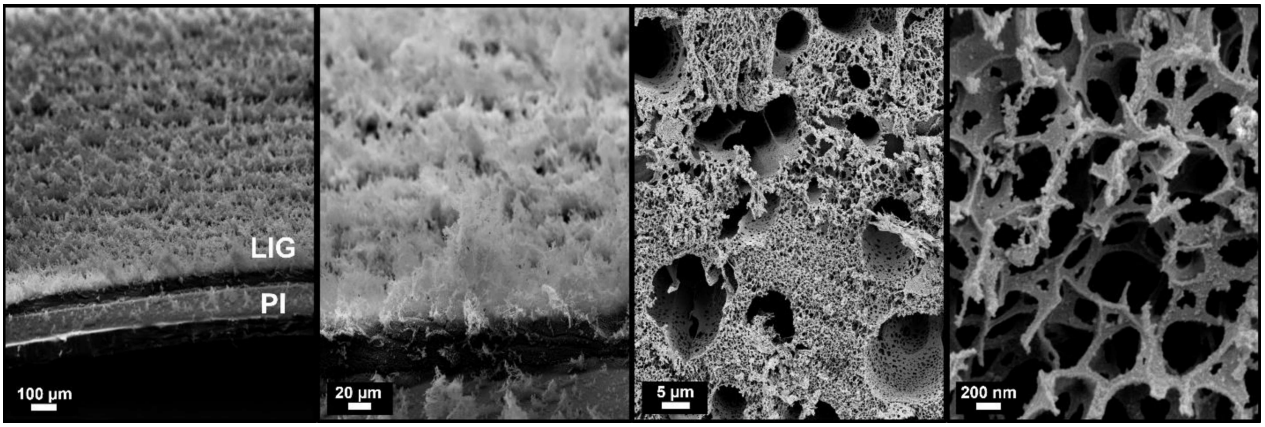

Figure 5.3 SEM images of LIG produced by laser-induced conversion of PI at 25 W and 1.14 m/s: profile view (left panel) and top view (right panel).

The SEM images show a foamy-like appearance, with a layer on top of the PI surface of approximately 100 µm of thickness, and a porous 3D network visible in the higher magnification images, resulting from the rapid liberation of gaseous products.[217] This porous structure renders high surface areas (reported values ~ 340 m^2/g)[217] which can enhance their performance as sensor devices, as well as other applications like wastewater remediation, supercapacitors, fuel cells, among others.[217,385–387]

Additionally, as visible in Figure 5.4 it was observed a strong dependence of the LIG morphologic profile on laser power, where higher laser powers yield thicker and rougher surfaces.

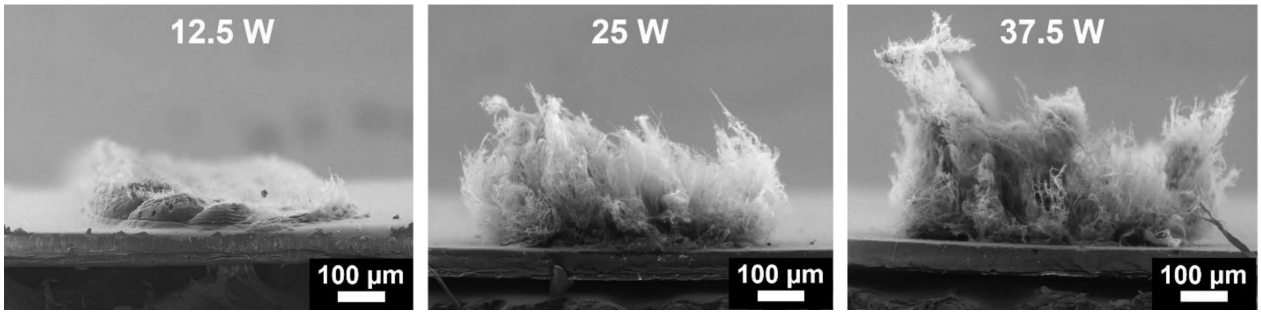

Figure 5.4 Profile SEM images of LIG produced with increasing laser powers at 1.14 m/s scanning rate.

A chemical and structural analysis was performed, respectively, by Raman spectroscopy and XRD (Figure 5.5).

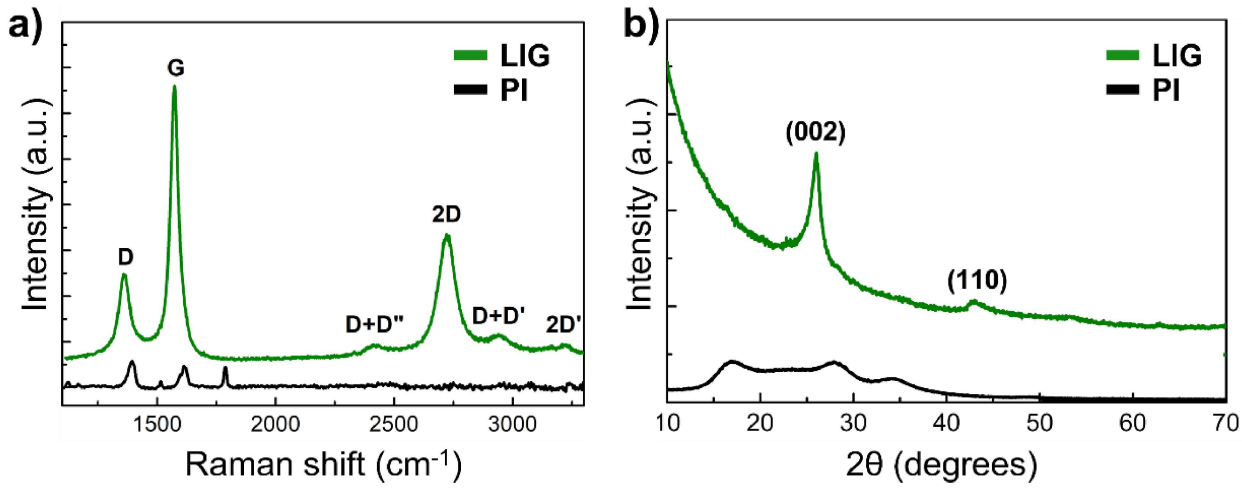

Figure 5.5 Chemical and structural characterization of PI and LIG produced at 25 W and 1.14 m/s: a) Raman spectra of LIG and PI; b) Diffractograms of LIG and PI.

The starting PI material characterised by Raman spectroscopy (Figure 5.5a) showed a set of features commonly found in the literature.[388] C-N-C transverse and axial vibrations occur at 1125 and 1395 cm^{-1}, respectively, C=C stretch at 1515 cm^{-1}, carboxylic acid at 1598 cm^{-1} (shoulder), aromatic imide at

1615 cm^{-1}, and C=O symmetric stretch at 1787 cm^{-1}. No PI Raman signal was found in LIG, suggesting a full conversion at the surface. The normalization of the Raman spectra to the G-band (1573 cm^{-1}) revealed that all samples that had a successful conversion into LIG, produced in the optimization matrix (Figure 5.2), were uniform and similar to each other. Figure 5.5a shows a representative spectrum of the sample processed at 25 W and 1.14 m/s, exhibiting the typical signature of a graphene foam sample, and featuring wide and intense D, G and 2D bands.[217] The presence of the defect-allowed D band at 1362 cm^{-1}, corresponding to the breathing mode of sp^2 coordinated 6 atom rings in defective graphitic phases, suggests a moderate density of lattice defects, activating the D band, forbidden in perfect graphene due to momentum conservation selection rules.[389] These defects are also present at the edges of graphene sheets, which appear in high quantities in graphene foams. Furthermore, the presence of covalently bonded oxygen, typical of LIG, provides local defects that induce the Raman D band.[217] The broadening of the D band to 51 cm^{-1} full width at half maximum (FWHM) is due to phonon scattering at defects. The prominent G band corresponds to the stretching mode of the sp^2 bonded carbon atoms. The 2D band (2722 cm^{-1}), a second-order two phonon process, sometimes referred to as an overtone of the D band, is the result of a two-phonon lattice vibrational process. Moreover, the I_{2D}/I_G ratio of 0.44 suggests that the graphene has a multi-layer structure of 4-5 layers characteristic of graphene foams.[382] However, the perfect fit with a single Lorentzian curve hints that there is weak coupling between graphene sheets.[390] The D+D'', D+D' and 2D' bands are also typical of graphene and graphene-based materials.[391] Out of those, the D+D' (often identified as D+G) band is also present in defective graphene structures.[217,391] The typical Raman spectra obtained is compatible with graphene foams produced by the interaction of a laser beam with PI films,[217] with a 2D band typically lower than the G band and an intense D band. The presence of defects can be beneficial for analytical purposes, since it has been demonstrated that electron transfer has higher rates on graphene edge-plane than in the basal plane.[215,392]

Figure 5.5b shows the diffractogram of PI, where a pattern of wide bands at low angles typical of this polymeric material is patent.[393] The diffractogram obtained for LIG in powder form shows an intense peak at 26.03°, attributed to the (002) plane, and a peak at 43.00° indexed to (110) reflections originated by an in-plane structure.[217]

Additionally, the LIG samples were characterized in terms of sheet resistance (Figure 5.6).

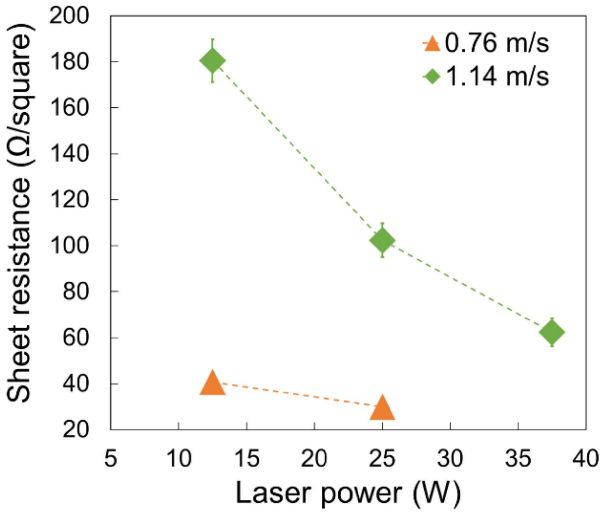

Figure 5.6 Sheet resistance calculated, by Hall effect, for the LIG samples produced with a CO_2 infrared laser.

The observed behaviour is in accordance with the reported in the literature[382] – higher laser power tends to increase porosity, LIG thickness (as observed in Figure 5.4) and decrease LIG sheet resistance. Moreover, the lower sheet resistances were obtained for lower laser speeds where the lowest LIG sheet resistance, of 30.0 ± 2.6 Ω/square, was obtained with 25 W at 0.76 m/s. However, with these parameters, when irradiating large areas, the heating of PI substrates causes deformations of the material, which ultimately causes nonuniform laser focal point in different areas of the substrate. This leads to holes in the substrate and/or overly loose graphene powder on the PI substrate, which delaminates from its surface. For this reason, to preserve the integrity of the substrate and induce homogeneous LIG the optimized power and speed of the CO_2 laser was considered 25 W at 1.14 m/s, yielding a relative low sheet resistance of 102.4 ± 7.3 Ω/square and larger patterned areas without defects on the electrodes.

These results hints on the feasibility of the method for electrode's patterning through consecutive scribing of horizontal lines (Figure 5.7a), with very low production times.

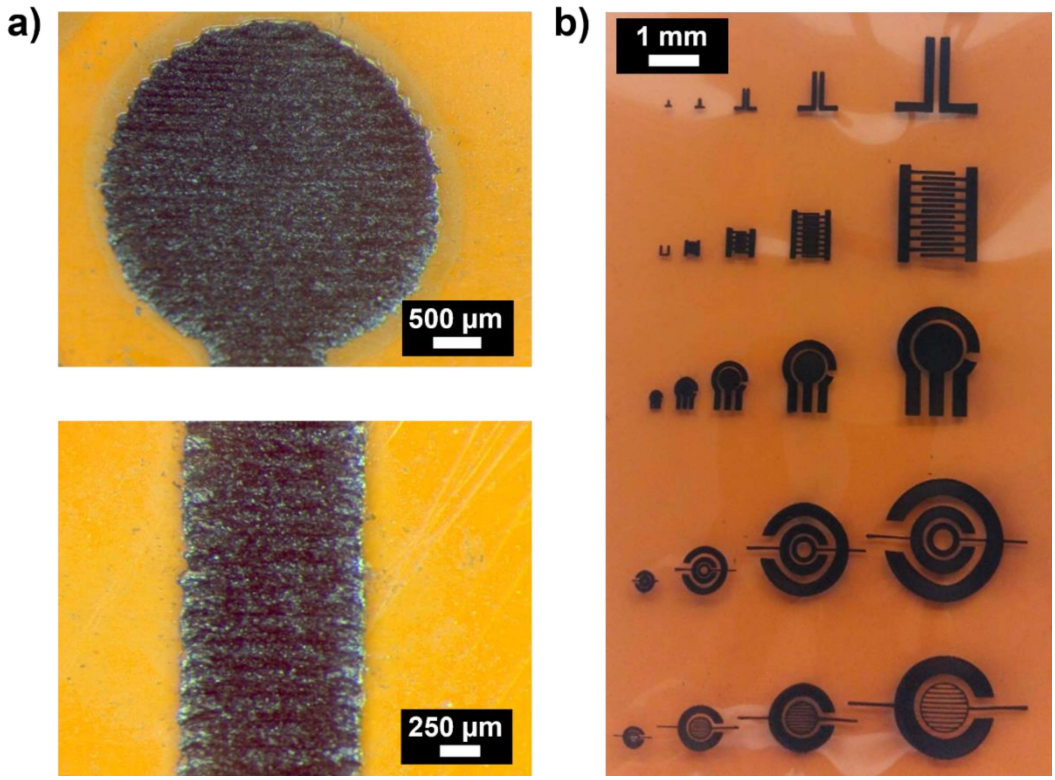

Figure 5.7 LIG patterned in polyimide substrates: a) optical photographs showing detail on the horizontal scribing of LIG; b) optical photograph showcasing the flexibility of the technique to pattern different architectures with high resolution.

This method can be easily integrated in roll-to-roll processes, for a large-scale production. The resolution of the method, with the selected parameters, was roughly calculated as 100 µm, thereby allowing patterning of electrodes with high resolution while offering freedom of design in the production of different device's geometries (Figure 5.7b), in an effective one-step approach.

These parameters (25 W at 1.14 m/s) were used to pattern carbon-based electrodes for electrochemical biosensors combined with molecular-imprinted technology, and applied for chloramphenicol quantification, a common antibiotic used for veterinary purposes. The results obtained are presented in section 5.2.1.

Additionally, a more comprehensive study about LIG properties dependence on laser parameter was performed, by widening the range of tested laser parameters. The laser power was varied from 40 W to 2 W and tested in a wider range of speeds (from 1.27 m/s to 0.05 m/s).

The plot presented in Figure 5.8 shows the outcome of laser power and speed on the PI substrate.

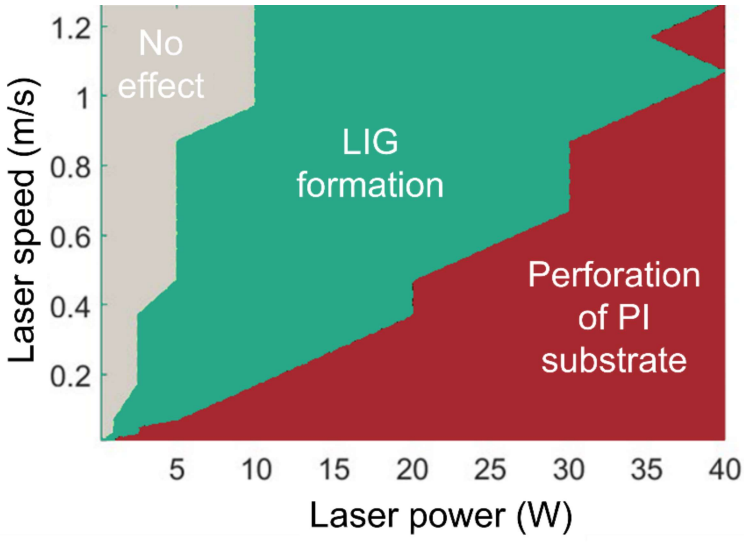

Figure 5.8 Plot of the three different outcomes observed for different laser power and speed regions.

As in Figure 5.2, three main aftereffects are observed on PI substrate upon laser irradiation: (i) no effect on the substrate, (ii) LIG formation and (iii) perforation of the substrate. For higher scanning speeds and lower laser powers the heating effect is not high enough to break the chemical bonds necessary for the conversion to LIG from PI. On the other hand, for higher laser powers and lower scanning speeds, the energy that is impinged on the polymer becomes high enough to break all chemical bonds without undergoing the recombination process that is required for the formation of LIG. Thus, the polymer is punctured and becomes permanently damaged, with occasional formation of LIG around the edges of the perforation, due to an uncontrolled thermal energy dispersion gradient. LIG can only be obtained with a combination of laser power and scanning speed, such that the amount of energy provided to the polymer is high enough to break the C-O, C=O and N-C bonds, but not so high that it causes the perforation of the polymer.

As it was visible by the preliminary sheet resistance measurements (Figure 5.6), lower speeds yield the lowest sheet resistance. So, since in the wider tested range (Figure 5.8) it was observed LIG formation in the low speed and low power range and, since the combination of these doesn't lead to nonuniform LIG formation and/or holes in the substrate and overly loose graphene powder on the PI substrate (as observed before for lower speeds 0.76 m/s and higher power 25 W), these region was investigated in more detail.

Figure 5.9 shows the analytical features obtained in these range of low power and speeds.

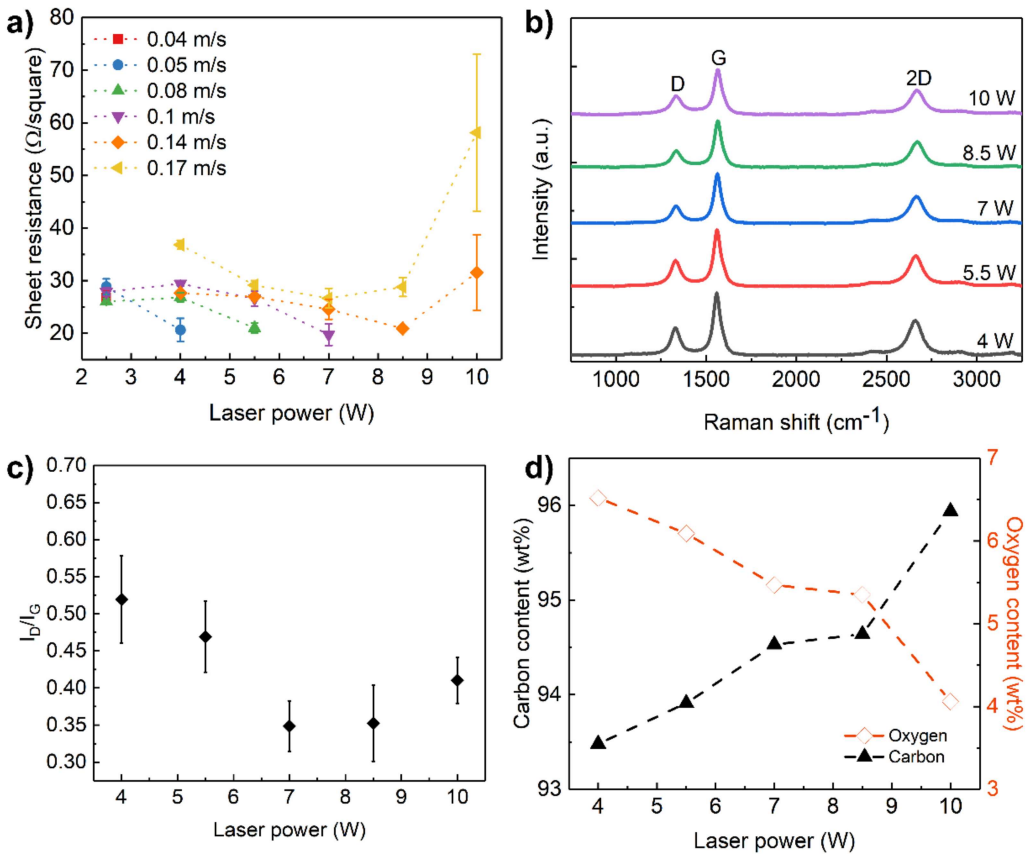

Figure 5.9 Characterization of LIG in PI: a) Sheet resistance as a function of the laser power for different laser speeds; b) Raman spectra of LIG in PI as a function of the laser power; c) I_D/I_G ratio calculated from Raman spectra for LIG produced at different laser powers and with a laser speed of 0.14 m/s; d) Evolution of carbon and oxygen content (wt%), calculated by EDS quantification, for LIG produced at different laser powers and with a laser speed of 0.14 m/s.

Figure 5.9a shows the sheet resistance in function of the laser power for different laser speeds. The lowest sheet resistance obtained was 19.75 ± 2.07 Ω/square for a laser power of 7 W and a scanning speed of 0.10 m/s. Furthermore, for some scan rates it is visible two different slopes in the sheet resistance. Lin, J. et al justifies this by the influence of the thermal power on the graphitization.[217] The higher the power, the higher the graphitization level, which leads to an increase of the quality of the film and a decrease on the sheet resistance. However, for highest laser powers the oxidation starts to play an increasingly deleterious role in the quality of the films, which rises the sheet resistance.

Laser scanning speeds of 0.14 and 0.17 m/s yielded the higher number of conditions of laser power where LIG photoconversion from PI occurred. In order to analyze the quality of LIG, a systematic study of Raman spectroscopy was performed, over the samples obtained with 0.14 m/s of laser speed and powers raging from 4 W to 10 W (Figure 5.9b). In all spectra, it is observed the three Raman bands characteristic of graphene and graphitic materials, the D, G and 2D bands. The intensity ratio of D and G bands (I_D/I_G) can be used to determine the quality of graphitization or defective disorders on the

crystalline graphite (Figure 5.9c) and hint on the electrical properties of the LIG material.[382] With the increasing of laser power from 4 W to 7 W, the ratio of I_D/I_G decreased to a minimum value of 0.35, with a plateau up to 8.5 W suggesting a higher degree of graphene could be obtained at higher laser powers up to 8.5 W paired with the lowest sheet resistance of 20.91 ± 0.45 Ω/square. Based on this comprehensive study of laser power's influence on LIG's electrical resistance and Raman spectrum, it can be concluded that a good set of laser power and speed to produce high-quality LIG can be 8.5 W at 0.14 m/s. Consistent with the trend of electric resistance's dependence on laser power, the ratio of I_D/I_G increased when laser power was further increased to 10 W. This change in the ratio of I_D/I_G could be attributed to the oxidation induced by the higher laser power of 10 W.

As mentioned, the intensity ratio of I_{2D}/I_G is commonly used as an indicator of the nature of the graphene layers, particularly, $I_{2D}/I_G > 2$ is a typical feature of monolayer graphene. For the LIG formed with 8.5 W at 0.14 m/s, a I_{2D}/I_G ratio of 0.86 was obtained, which suggests graphene stacked structures.[217]

Finally, EDS was performed to follow the LIG induction process. When looking at the concentration of carbon and oxygen for increasing laser powers (Figure 5.9d), it is visible a decrease of oxygen and an increase of carbon contents, proving that higher powers lead to higher graphitization.

These parameters (8.5 W at 0.14 m/s) were used to pattern carbon-based electrodes for electrochemical biosensors combined with molecular-imprinted technology and applied for the dual detection of ascorbic acid and amoxicillin screening and quantification, common antibiotics found in food products from animal sources. The results obtained are presented in section 5.2.2.

5.2 Implementation of LIG electrodes for MIP-based electrochemical biosensors

In this sub-chapter, the parameters optimized for LIG formation onto polyimide substrates, established in sub-chapter 5.1, were used for the patterning of planar electrodes, and applied to the production of electrochemical biosensors using molecularly-imprinted materials as biorecognition elements, for molecular single and dual detection.

5.2.1 MIPs for chloramphenicol screening

Chloramphenicol (CAP) is a broad-spectrum antibiotic, member of the amphenicol family, and effective against most Gram-positive and Gram-negative bacteria.[204,394] This antibiotic has been widely used in veterinary practice for both prophylactic and therapeutic purposes. However, CAP is hematotoxic for humans and can cause serious adverse consequences such as the loss of ability to produce blood cells, called bone marrow aplasia, which can lead to aplastic anaemia. Since, this can be fatal the presence of this antibiotic in food products of animal origin must be strictly screened. In fact, in some countries the use of this antibiotic is currently banned. However, due to its low price and effectiveness, illegal use of CAP persists, and it is still found in mammals, birds, bees, and aquaculture. It is also still being widely used in developing countries.[204,394]

The detection of CAP can be achieved by several methods, such as HPLC alone or combined with mass spectroscopy (HPLC-MS), gas chromatography (GC), and enzyme-linked immunosorbent assay (ELISA).[395,396] However, these methods can be complex, time-consuming, expensive and some of them are unable to attain an effective LOD.[396,397] So, the development of biosensors for point-of-care CAP screening can offer several advantages to the conventional methods, such as higher sensitivity, while offering fast, accurate and easy readings.[394,398]

Herein, for the first time, LIG technique was combined with MIP technology for CAP screening.[35] A three-electrodes architecture (working electrode – WE, counter electrode – CE, reference electrode – RE) was patterned by LIG technique and the biorecognition element was produced on-site, by direct electropolymerization of a suitable monomer (Figure 5.10).[35,204] The overall analytical features of the biosensor assembled on the LIG-based devices were compared to commercial SPEs, with carbon (C-SPE) and graphene (G-SPE) inks as working electrodes.

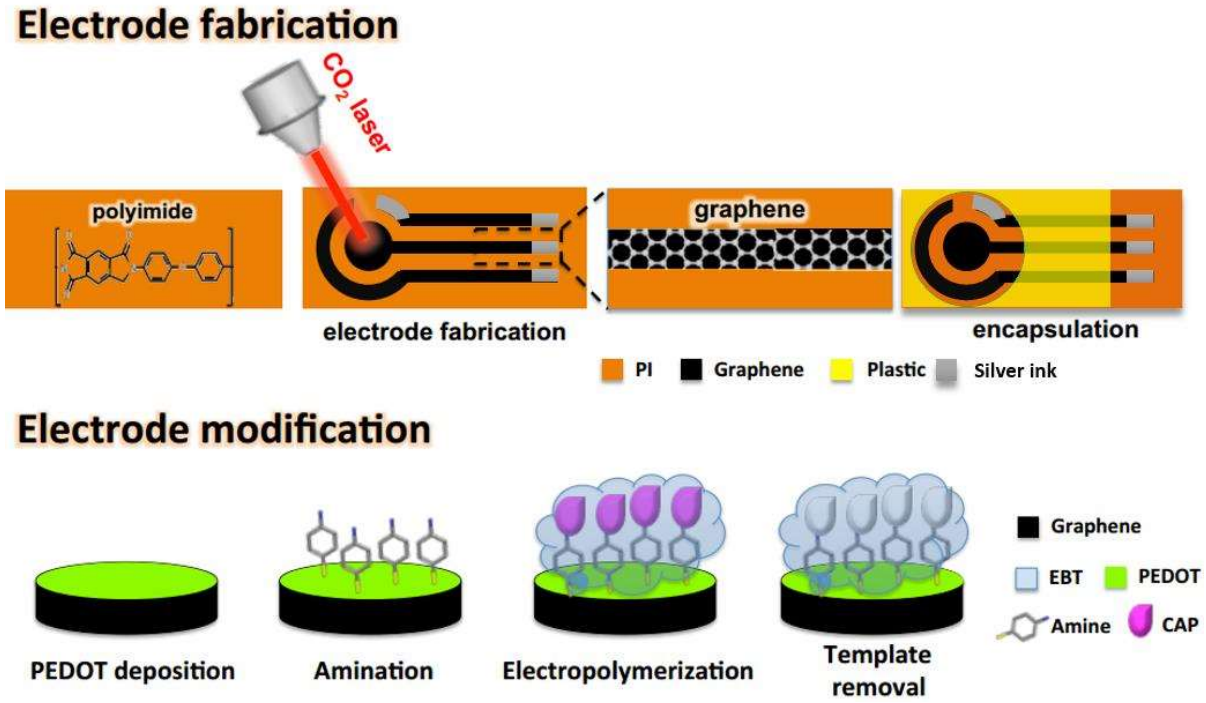

Figure 5.10 Schematic representation of the workflow employed on the production of the LIG electrodes (top) and the MIP fabrication (bottom) for the electrochemical CAP biosensor: Electrodeposition of EDOT with subsequent formation of poly(EDOT) followed by amination, electropolymerization of EBT, in the presence of CAP (MIP) or without CAP (NIP) and finally template removal.

Eriochrome Black T (EBT) was selected as the monomer for the growth of the MIP layer since it has several functional groups in its chemical structure (Figure 5.11), thus having the potential to generate excellent complementary rebinding sites, as it is reported in the literature.[204,399,400]

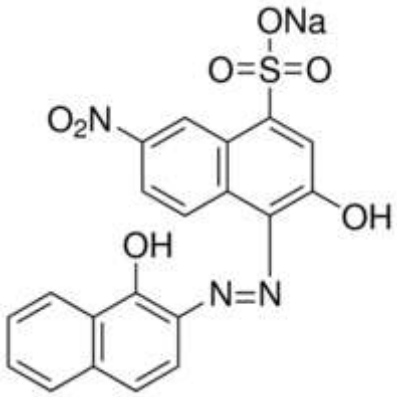

Figure 5.11 Eriochrome black T chemical structure: nitro, sulfonic and hydroxyl functional groups.

The electrode's modification for CAP sensing followed four main steps:

(1) electrode's pre-treatment with a saline solution followed by PEDOT deposition by electropolymerization, to enhance the electrical features and stability of the sensing surface.[204,401,402]

(2) amination to be used as a linker between the PEDOT structure and the MIP/NIP layer. An aminothiophenol compound was used since it contains a -SH functional group, which can bound to PEDOT through a disulphide bound and an aromatic amine that can also be involved in the polymerization of EBT.[204,402]

(3) electropolymerization of EBT to poly(EBT), around CAP molecules for MIP production and without CAP for NIP production (used as negative control). A bulk imprinting approach was followed since it is more suitable for small molecules, such as CAP, than surface imprinting.[181,204]

(4) template removal, where the MIP and NIP were incubated in an acetonitrile (ACN) solution, due to the high solubility of CAP in ACN, and CV cycles were performed in a potential range selected to not damage poly(EBT) while avoiding the electroactivity of CAP.[204]

The remaining matrix will have imprinted positions with complementary shape to the casted compound, in which the target analyte may therefore rebind, as a natural antibody binds to its target compound.

Electrochemical characterization and comparison to commercial electrodes

Each chemical modification performed on the sensing surface of C-SPE, G-SPE and LIG devices was monitored by CV and EIS measurements, following the changes in the electron transfer properties of a standard iron redox probe (Figure 5.12).

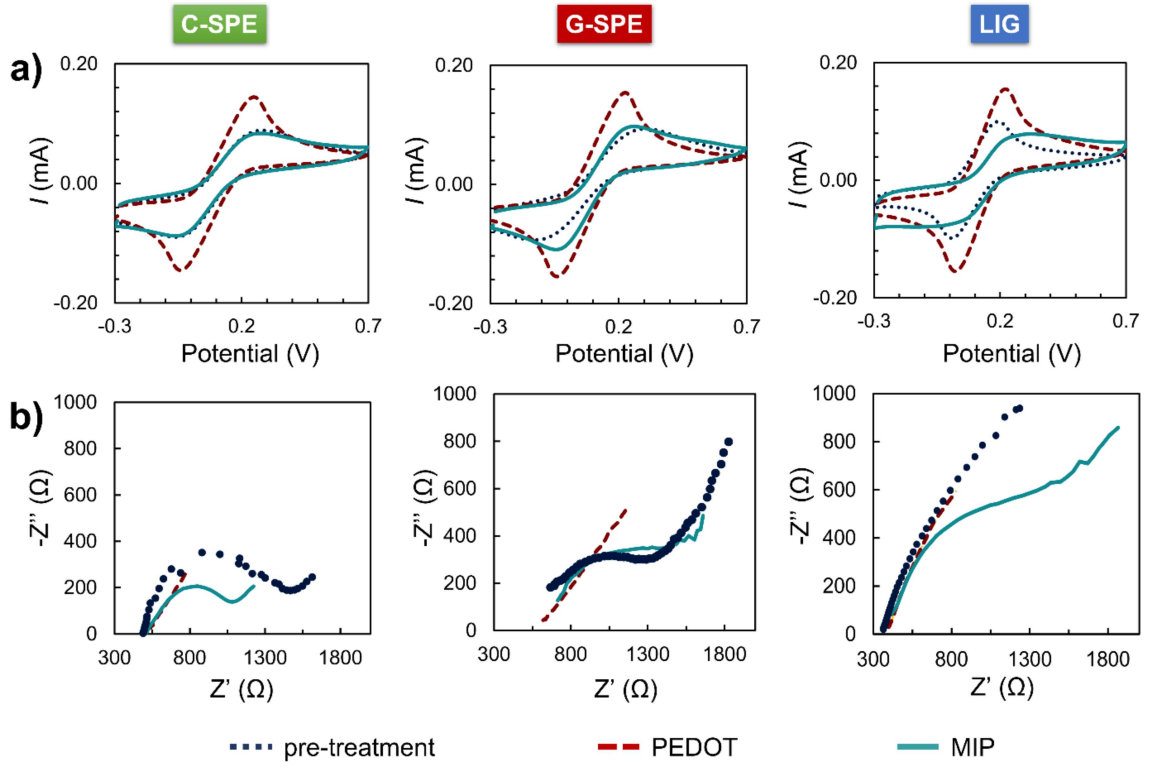

Figure 5.12 Electrochemical characterization of commercial SPEs (C-SPE and G-SPE) and LIG-based device after cleaning, PEDOT electropolymerization and MIP formation: a) Cyclic voltammograms from -0.3 to 0.7 V at a scan rate of 50 mV/s; b) Nyquist plots obtained from EIS measurements at an open circuit potential. Indirect readings performed with the redox probe 5.0 x 10^{-3} M $[Fe(CN)_6]^{3-/4-}$ prepared in ACN buffer.

Initially, the electrodes were pre-treated by chronoamperometry in a 0.10 M KCl solution to improve the stability of the as-received (C-SPE and G-SPE) and as-produced (LIG) electrodes.[204]

CV measurements (Figure 5.12a and Figure 5.13a), showed that the currents of the electrodes after the pre-treatment were slightly higher in the LIG-based devices, with a narrower peak-to-peak separation, than in the commercial SPEs (Annex Table A5).

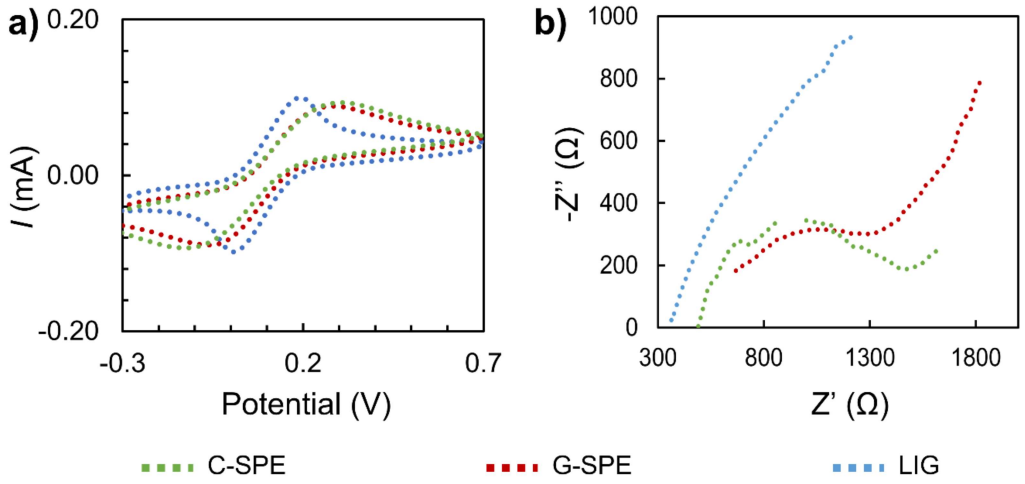

Figure 5.13 Direct comparison of the pre-treated C-SPE, G-SPE and LIG electrodes after the pre-treatment: a) Voltammograms and b) Nyquist plots. Indirect readings performed with the redox probe 5.0 x 10^{-3} M $[Fe(CN)_6]^{3-/4-}$ prepared in ACN buffer.

In addition, the typical peak shape of the iron redox probe is better defined in the LIG-based electrodes, thereby inferring the better electrical properties of these devices when compared to the commercial ones. This is correlated with EIS measurements (Figure 5.12b and Figure 5.13b) where the LIG-based electrodes showed lower *Rct* values after the pre-treatment and subsequent steps (Annex Table A6). This different behaviour, compared to the other devices, can also be due to the EDOT incubation prior to the biosensor assembly. Being EDOT a conducting monomer, it contributed to the absence of the typical semicircle in EIS (Figure 5.13b).

With better electrical features in the blank signal, the subsequent electrochemical stages were also different for the LIG-based devices (Annex Table A5 and Table A6). As expected, due to the conductive nature of PEDOT, the subsequent stage of EDOT polymerization enhanced the typical current of the iron redox probe and reduced the peak-to-peak separation (Figure 5.12a), for all devices. Although, all yielded similar current values after electropolymerization of EDOT, the LIG electrodes showed a lower peak-to-peak separation, and lower *Rct* values. In general, this distinct behaviour demonstrates that the LIG-based devices can be a serious alternative candidate to the current commercially available SPEs. Moreover, the growth of the PEDOT film on top of the electrodes helps to guarantee the reproducibility of the devices, due to the high stable nature of the polymer.

The formation of MIP enclosed two main steps: growth of the polymer poly(EBT) around CAP molecules followed by CAP removal to leave imprinted cavities with selectivity for CAP. A previous study has shown that CAP is electroactive, in aqueous solutions with pH values around 7.0, in the same potential range where EBT is electropolymerized which can lead to irreversibly bounding of CAP molecules to poly(EBT), hindering the subsequent template removing process which can result in the unsuccessful formation of imprinted rebinding sites. However, the same study shows that when ACN is used as solvent during the imprinting stage, CAP is no longer electroactive while EBT monomers maintain their electroactivity.[204] For this reason, the same approach was used in this work. The formation of the imprinted polymer layer was revealed by the decrease currents of the redox peaks, in comparison with PEDOT layer, and increase on *Rct*, due to the insulating and non-conductive nature of poly(EBT). The distinguished behaviour of LIG-based devices was also signalled by a higher amount of polymeric imprinted film formed, since the more the peak current decreases, the higher the amount of poly(EBT) formed on the surface. Considering that the PEDOT currents where higher in the LIG-based devices, the electrical stimulus generating the polymer was stronger in these, thereby yielding a higher amount of poly(EBT) formed. As expected, this higher amount of polymer was coupled with a higher peak-to-peak potential separation after MIP growth.[188,403]

As a negative control and to assess the selectivity of the produced MIP devices, NIP layers were also grown in all carbon-based devices, and were subjected to the same procedures, except for adding the template molecules. Figure 5.14 shows a comparison between MIP and NIP electrochemical features.

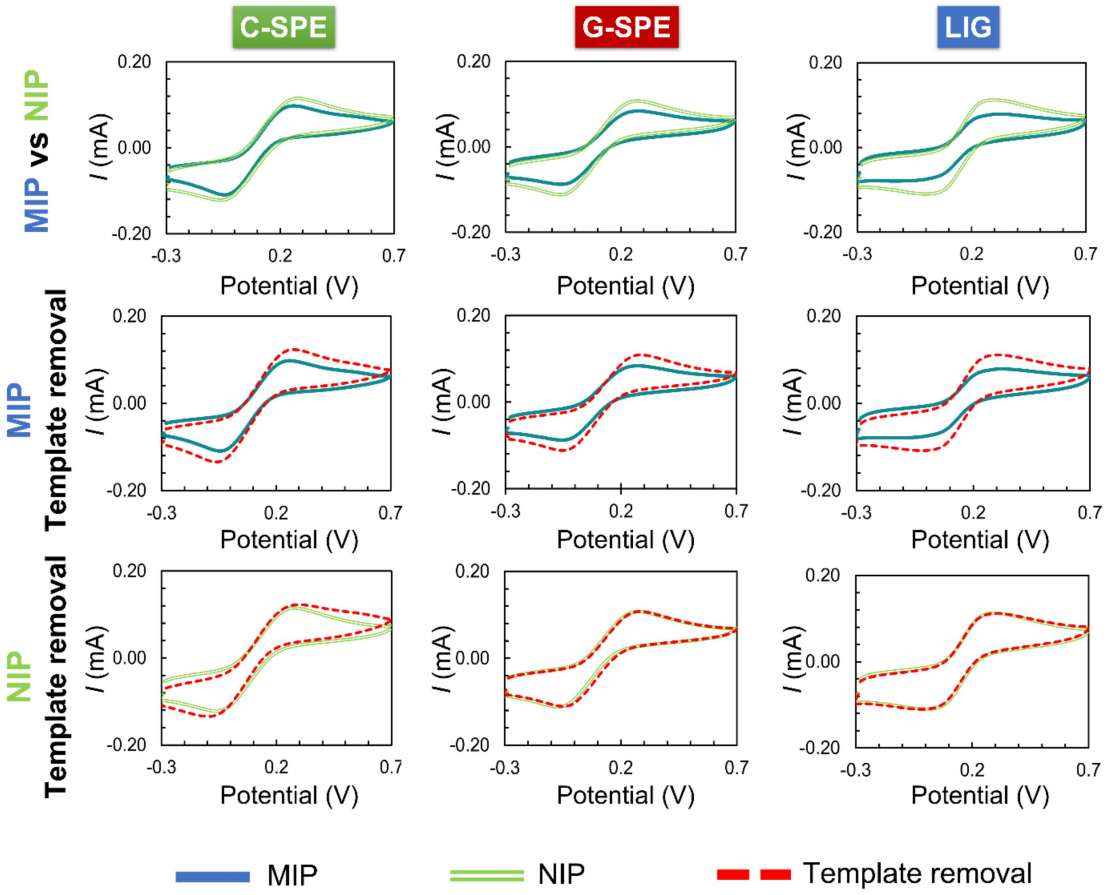

Figure 5.14 Comparison of the analytical features of C-SPE, G-SPE and LIG electrodes, followed by cyclic voltammetry (scan window from -0.3 to +0.7 V at 50 mV/s), after MIP and NIP fabrication and respective template removal. Indirect readings performed with the redox probe 5.0 x 10^{-3} M $[Fe(CN)_6]^{3-/4-}$ prepared in ACN buffer.

As it is observed the MIP layer has lower peak currents and a higher separation of cathodic and anodic peaks when compared to the NIP layer. These differences result from the presence of CAP in the MIP polymerization step, as this was the only experimental difference between MIP and NIP materials. As CAP is a non-conductive element, and MIP growth is achieved by applying an electrical potential to the electrode surface, the presence of CAP hindered the polymer growth.[204] Moreover, a bigger difference between MIP and NIP films was promoted by the LIG-based device, most probably due to the higher extent of film formed on its surface, compared to the SPEs.

For the template removal step, the MIP and NIP films were exposed to an aqueous ACN solution. As expected, in NIP template removal the peak separation of the iron redox probe remained unaltered, since nothing was being removed from the surface. In contrast, the extraction of CAP from the MIP

network was evidenced by increased currents, due to the facilitated current flow caused by the absence of the antibiotic, confirming the effective removal of CAP from the MIP films, without damaging the polymer. In addition, it was interesting to note that the LIG-based electrodes had a closer behaviour to the G-SPE in the imprinting stage. After electropolymerization, the current of the MIP films in these devices were similar, likely confirming the characterization of the material, where the presence of graphene dominated the carbon nanostructure generated by laser irradiation of PI.

The EIS measurements corroborated the behaviour observed by CV measurements for MIP/NIP growth and template removal. The MIP polymer had a higher *Rct* compared to the NIP, which was assigned to the presence of CAP in the MIP polymerization step, as previously explained. The larger difference before and after CAP removal was, once again, obtained with the LIG device. Finally, as expected, the *Rct* remained constant after the NIP removal stage but decreased in the MIP film.

Analytical Performance

The analytical performance of the different carbon-based devices (C-SPE, G-SPE and LIG device) as biosensors was evaluated by incubating the sensing area with increasing concentrations of CAP standard solutions. For this purpose, a certain volume of each CAP standard solution was incubated for 20 min, to allow CAP rebinding. After this, the electrode was washed and incubated with the standard iron redox probe, for electrical readings through EIS (Figure 5.15a). The resulting calibration data plotted *Rct* against logarithm CAP concentration (Figure 5.15b).

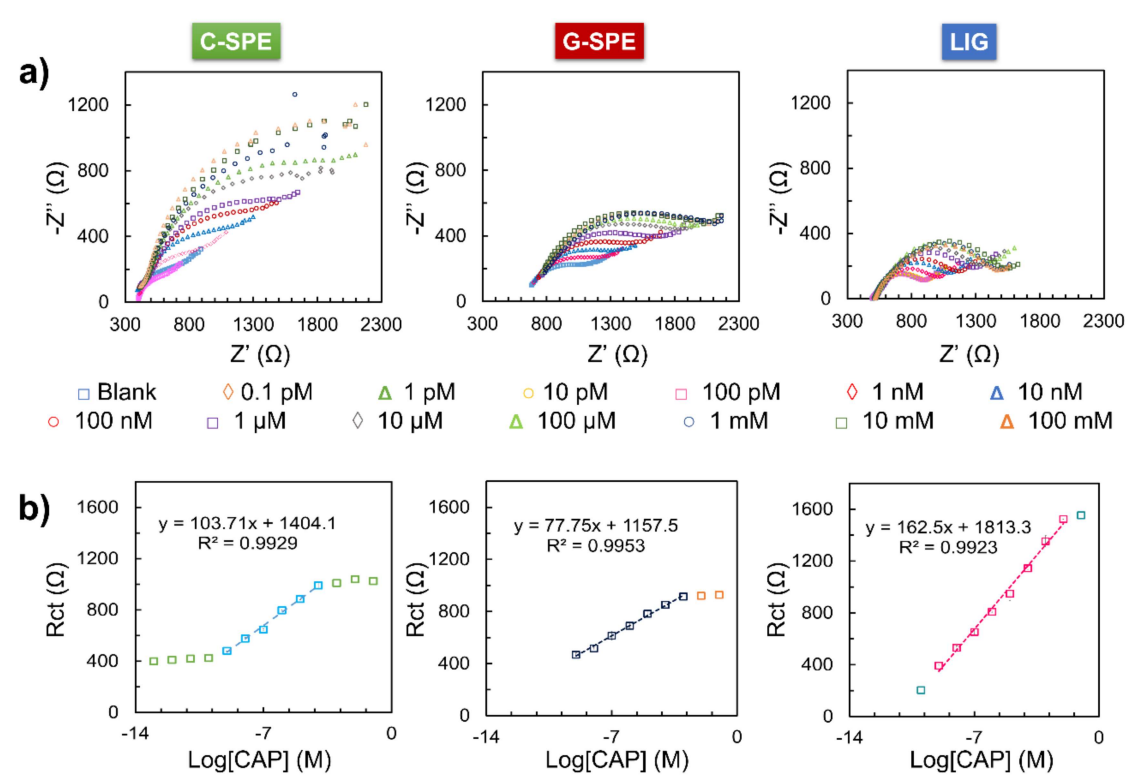

Figure 5.15 Analytical performance of the MIP-based C-SPE, G-SPE and LIG electrodes with increasing concentrations of CAP: a) Nyquist plots and b) respective calibration curve. Indirect readings performed with the redox probe 5.0 x 10^{-3} M $[Fe(CN)_6]^{3-/4-}$ prepared in ACN buffer.

In general, EIS measurements showed that increasing concentrations of CAP increased the electrical resistance of the surface, as the diameter of the semicircles in the Nyquist plots increased. This was a common trend between commercial and LIG-based electrodes. C-SPE showed a linear behaviour between 1 nM to 100 µM, with an average slope of 103.71 ± 2.80 Ω/decade. The G-SPE device calibration displayed a linear response in the range of 1 nM to 1 mM, with a slope value of 77.0 ± 1.09 Ω/decade. Finally, the LIG device showed the broadest linear behaviour from 1 nM to 10 mM with an average slope of 162.5 ± 5.17 Ω/decade (higher than the commercial SPEs), demonstrating the higher sensitivity of the device for CAP sensing.

This higher sensitivity of the LIG device can be correlated with the higher surface area provided by LIG electrodes, as mentioned before. The sensitivity of MIP biosensors is related to the number of imprinted sites generated onto the sensor's surface. The high surface-to-volume ratio can lead to an increase of the number and proportion of locals available to electropolymerization, which leads to an increase of the polymer imprinting capacity.[404]

Overall, these results showed that all three-electrode systems displayed a highly sensitive response for CAP determination. Yet, the LIG-based device described herein showed an increased

performance, when compared to G-SPE and C-SPE, considering sensitivity and extent of linear range. Finally, the LOD of the LIG-based MIP biosensor was calculated as 0.62 nM.

In parallel, the same measurements were performed with the corresponding NIP devices, which serve as a control of the imprinting process, monitoring the non-specific response of the sensing film (Figure 5.16).

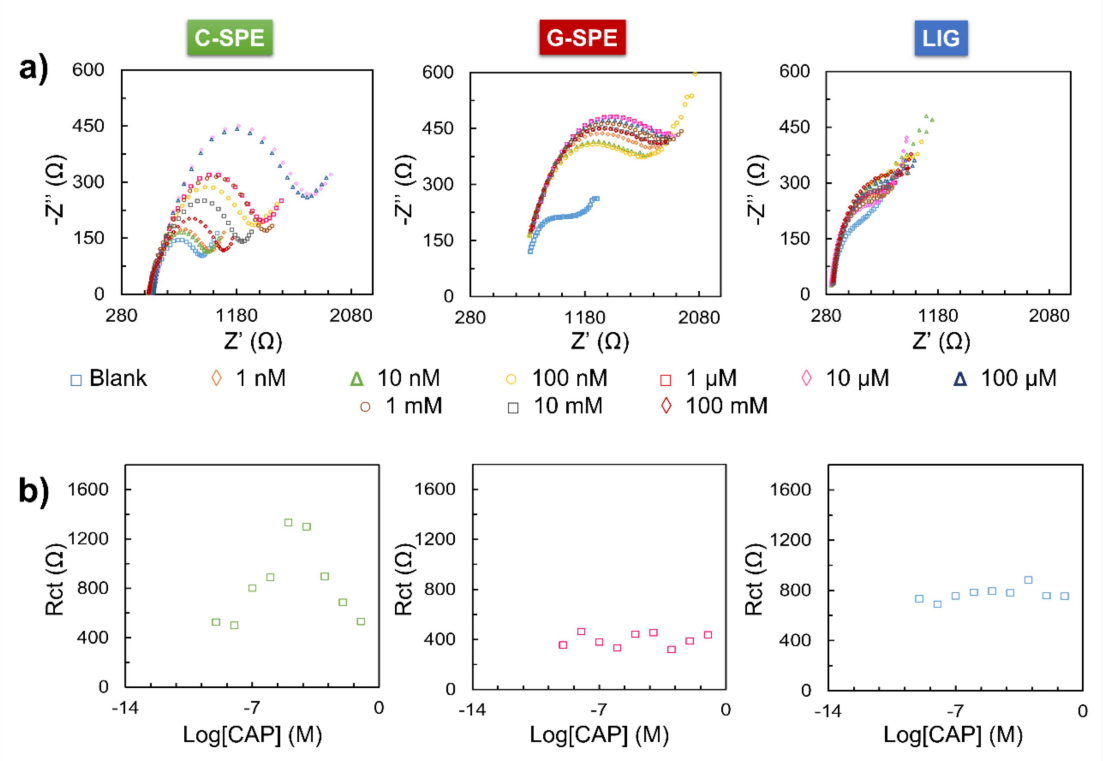

Figure 5.16 Analytical performance of the NIP-based C-SPE, G-SPE and LIG electrodes with increasing concentrations of CAP: a) Nyquist plots and b) respective calibration curve. Indirect readings were performed with the redox pair 5.0 × 10^{-3} M $[Fe(CN)_6]^{3-}$ and 5.0 × 10^{-3} M $[Fe(CN)_6]^{4-}$.

In general, the results presented a random behaviour against increasing CAP concentrations in all devices. Overall, these results showed that the NIP film was unable to detect CAP, independently of its concentration, thus suggesting negligible non-specific interactions between CAP and poly(EBT).

Finally, to further assess the selectivity of the developed LIG-based biosensors, competitive assays were carried out, as in Cardoso, A. R., et al.[204] As interfering species, other antibiotics used in aquaculture settings and/or in other animal industry, were selected: oxytetracycline (OTC), amoxicillin (AMOX) and sulfadiazine (SDZ). The results obtained are shown in Figure 5.17, evidencing the RSD induced by each interfering species.

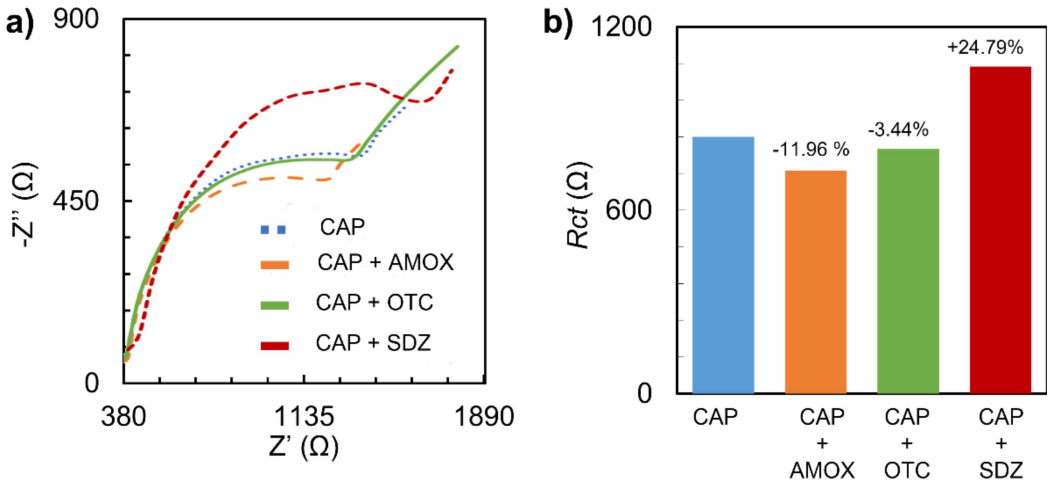

Figure 5.17 Selectivity studies of the biosensor LIG-CAP against OTC, AMC and SDZ: a) Nyquist plots and b) respective *Rct* values and calculated RSD values. All solutions were prepared with equal concentrations of 1.00×10^{-6} M and incubated 20 min in the sensing surface.

The RSD for OTC was -3.44%, for AMC -11.96%; and for sulfadiazine +24.79%. While OTC and AMOX had no significant interfering effect upon the CAP response, SDZ had a more significant impact on the MIP layer. However, as shown before,[204] this interference effect has nothing to do with the sensing surface, but reflected a chemical interaction between SDZ and CAP. Overall, this data confirms the good selectivity of the LIG devices.

A comparison of the analytical features attained with the developed LIG device and some of the reported electrochemical MIP devices, in the literature, for CAP sensing, was carried out, as seen bellow (Table 5.1).

Table 5.1 Revision of proposed electrochemical MIP devices for CAP sensing.

Preparation method	Monomer	EC readout	Linear range	Sensitivity	LOD	Author, year
Electropolymerization onto planar gold electrode	aniline	DPV	0.1 μM - 0.1 mM	-	0.1 μM	Vu, V.-P., 2019[405]
Electropolymerization onto GCE	resorcinol	EIS	1 pM – 1 nM	14.2 Ω/pM	0.3 pM	Roushani, M., 2019[406]
Precipitation polymerization and transference to a solid electrode	MAA	PTM	10^{-5} - 10^{-3} M	57.85 mV/dec	7.6 μM	Edañol, Y.D.G., 2016[407]
Coating of MWCNTs@MIP onto modified GCE	C16VimCl	DPV	5 nM - 0.5 μM and 0.5 - 4 μM	128.18 and 9.8 μA/μM	0.1 nM	Yang, G., 2015[408]
Electropolymerization onto C-SPE	EBT	EIS	1 nM - 100 μM	100.8 Ω/dec	0.26 nM	Cardoso, A.R., 2018[204]
Electropolymerization onto LIG surface	EBT	EIS	1 nM - 10 mM	162.5 Ω/dec	0.62 nM	**This work**

DPV: differential pulse voltammetry; GCE: glassy carbon electrode; EIS: electrochemical impedance spectroscopy; MAA: methacrylic acid; PTM: potentiometry; C16VimCl: 3-hexadecyl-1- vinylimidazolium chloride; C-SPE: carbon screen-printed electrode; EBT: eriochrome black T.

As seen, when comparing with the literature, the herein developed sensing device shows the widest linear range, with a high sensitivity due to the high surface area of LIG, that leads to the imprinting of a higher number of cavities. Moreover, the detection limit obtained is within the state of the art of those reported in literature.

As such, the induction of LIG from laser irradiation of polyimide substrates can be perceived as a valuable alternative to fabricate planar nanostructured carbon-based electrodes for electrochemical sensing.

5.2.2 MIPs for dual-detection of amoxicillin and ascorbic acid

To demonstrate the freedom of design and versatility enabled by the chosen technique (LIG) to pattern planar electrodes, a different architecture was exploited, with two WEs sharing the same CE and RE, for the simultaneous detection of AMOX and AA, using MIP technology.

AMOX belongs to the penicillin's class of antibiotics and acts against a broad spectrum of Gram-positive and Gram-negative microorganisms. It is considered the most important penicillin applied in aquaculture[409] and it is important to monitor its levels due to possible public health issues related to the development of antimicrobial-resistant bacteria, that can be transferred to humans.[282,410,411] Several studies have shown that AA, commonly known as vitamin C, plays an important role in the diet of fish. AA is an essential micronutrient for normal growth and physiological function of most aquatic animals. So, AA-deficient diets result in several deficiency signs, as retarded growth, impaired feed conversion, skeletal deformities in the operculum and cartilage of the gills, anaemia, delay or decrease in wound healing, reduction in reproductive performance and decrease in hatchability. The quantitative requirements for dietary vitamin C have been determined for several fish species and the recommended values range from 20 to 50 $mg \cdot kg^{-1}$.[412–414] Thus, both AMOX and AA may be found in aquaculture tanks, thus having the ability to reach environmental waters. Overall, it is important to have an analytical method capable of monitoring both analytes in water.

Electrode's system architectures

To allow for the simultaneous detection of AMOX and AA the electrode's system architecture was envisioned as having two WEs, sharing the same CE and RE. With this purpose, the devices produced herein were optimized in terms of architecture, electrochemical configuration, and electrode's sheet resistance (shown in sub-chapter 5.1). A few architectures were considered (Figure 5.18) to find the one with an overall smaller size, simplicity, good distance between electrodes and same distance of the WEs to the CE.

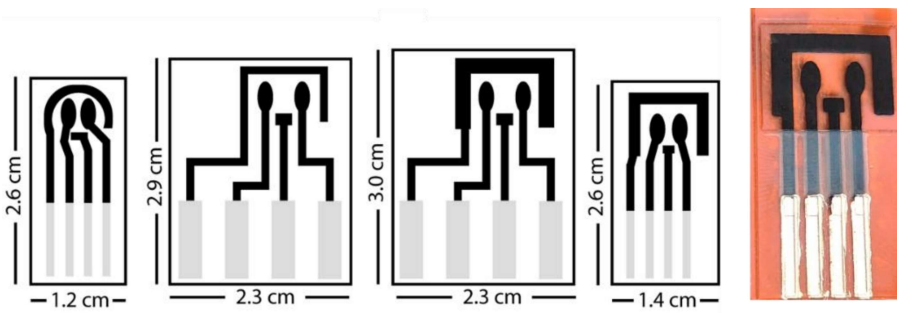

Figure 5.18 Optimization of the dual-LIG devices architectures, to find the one with the required features as: small size, equal distance of the WE to the CE and with a CE with high surface area. The colour black represents the LIG material and colour grey represents silver ink. A picture of final device is presented on the right side.

To assure an equal distance of both WEs to the shared CE, the electrodes were designed with a rectangular architecture, ensuring at the same time a good distance between all electrodes, thus avoiding short-circuits that could be caused by the increase on the width of the LIG features, upon laser irradiation, from the nominal LIG width. Additionally, the width of the CE was increased, to ensure an higher surface area, so that the half-reaction occurring at the CE could occur fast enough.[415,416] Also, in this case the RE was produced also by the LIG technique. This procedure was effective, being also quicker and less expensive than modifying it with a silver-based ink. Overall, this allowed an easier production of the dual-LIG device, with less human error contribution and good analytical features.[417]

Biomimetic material's production workflow

The biorecognition elements for AMOX and AA were assembled on their respective WE of the dual-LIG device. The strategy employed for the fabrication of the biomimetic materials was similar to the approach followed in the previous sub-section. A schematic representation of the fabrication workflow is depicted in Figure 5.19.

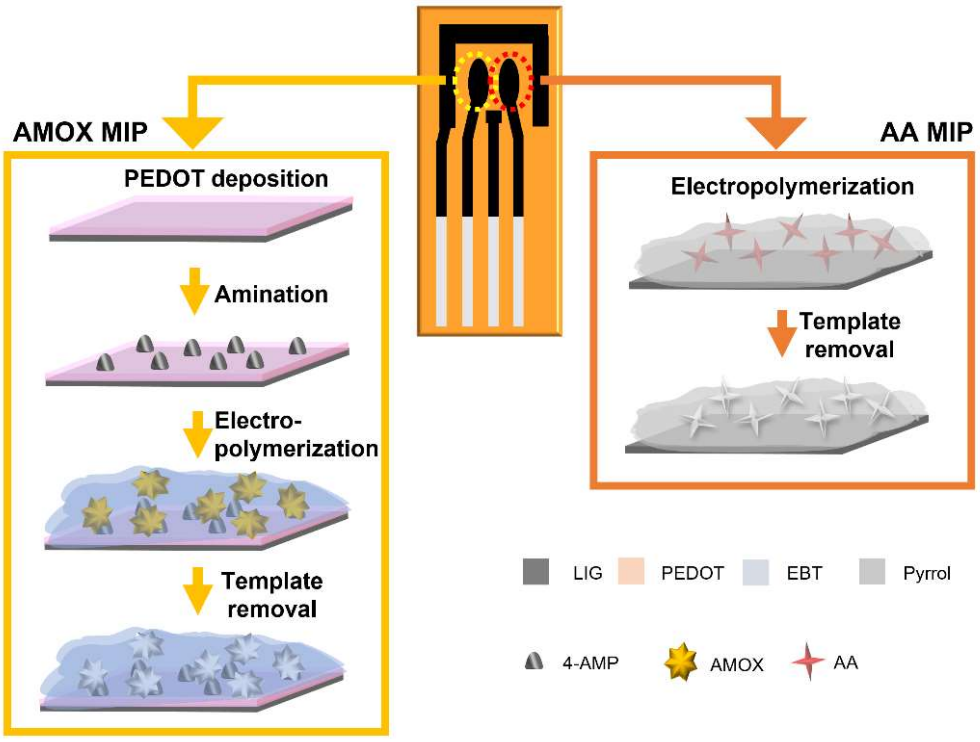

Figure 5.19 Schematic representation the dual-LIG device and MIPs fabrication workflow: AMOX MIP fabrication comprises PEDOT electrodeposition and amination steps followed by electropolymerization around AMOX molecules and template removal; AA MIP fabrication comprises the electropolymerization step around AA molecules and template removal.

Besides a few modifications, the MIP for AA was produced by following a previously published work by Özcan, L., et al.[271] On the contrary, the MIP for AMOX was fully optimized herein, since it was used

a different polymer and different strategies from the previous reported works for electrochemistry-based AMOX sensing.[418–422]

As in the workflow for the fabrication of MIP for CAP sensing, shown in sub-section 5.2.1, the WEs were pre-treated with a 0.1 M KCl solution followed by EDOT electropolymerization (Figure 5.20).

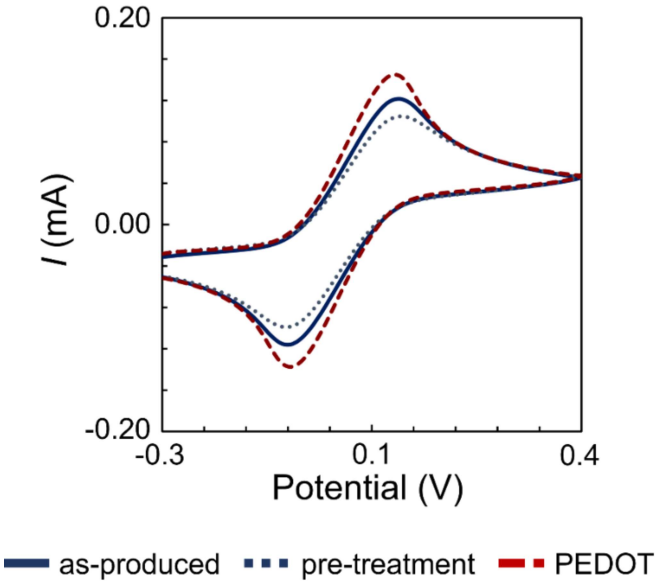

Figure 5.20 CV measurements of the as-produced LIG devices (8.5 W at 0.14 m/s), after pre-treatment and EDOT electropolymerization. Indirect readings performed with the redox probe 5.0 x 10^{-3} M $[Fe(CN)_6]^{3-/4-}$ prepared in ACN buffer, performed from -0.3 to +0.4 V, at 50 mV/s

As it is observed, this pre-treating step decreased the typical currents generated in CV, by the iron redox probe, when compared to as-produced electrodes, and increases slightly the potential separation between the CV oxidation and reduction peaks. This can be explained by the presence of some superficial particles of graphene that were not strongly bound to the electrode surface, in the as-produced electrodes. After the KCl-based cleaning stage, only the particles efficiently bound to the surface remained, thereby explaining the small decrease on the current values. Still, this pre-treatment is important to assure a stable electrochemical response before being used in the subsequent steps.

The subsequent steps were related to the assembly of the biomimetic materials for AMOX and AA, in agreement with the target analyte. The AMOX and AA sensing material's optimization and fabrication process, as well as the attained analytical performance are described next.

AMOX sensing material

The WE surface, for AMOX assembly, was then modified by EDOT electrochemical polymerization, through the application of +0.90 V, for 10 seconds. Overall, this procedure enhanced the electrical

features of the WEs (Figure 5.20), by increasing peak currents and narrowing the peak-to-peak separation. Moreover, this modification also contributed to the final and optimum stabilization of the graphene materials generated by laser irradiation. After this, a mixture of 4-AMP and EBT was electropolymerized, to assure an steady binding between the PEDOT film and the subsequent poly(EBT) layer, as it was previously shown.[35,204]

The first stage to assemble MIP and NIP films was to identify the experimental conditions that would allow the production of an effective AMOX imprinted layer by electropolymerizing EBT and ensuring that the template molecule remained unaffected. Several conditions were tested for this purpose, by checking the occurrence of redox peaks in CV assays for different electrochemical conditions and background solutions. It was found that an EBT solution of 1 mM, prepared in ACN, revealed an oxidation peak around +0.2 V and that under this condition AMOX was not electroactive (Annex Figure A2).

After this, the MIP film for AMOX was produced by electropolymerizing EBT by chronoamperometry in the presence of the template AMOX. The control NIP film was produced similarly, but in the absence of AMOX. Figure 5.21a shows the CVs of a standard iron redox probe upon MIP and NIP fabrication of AMOX.

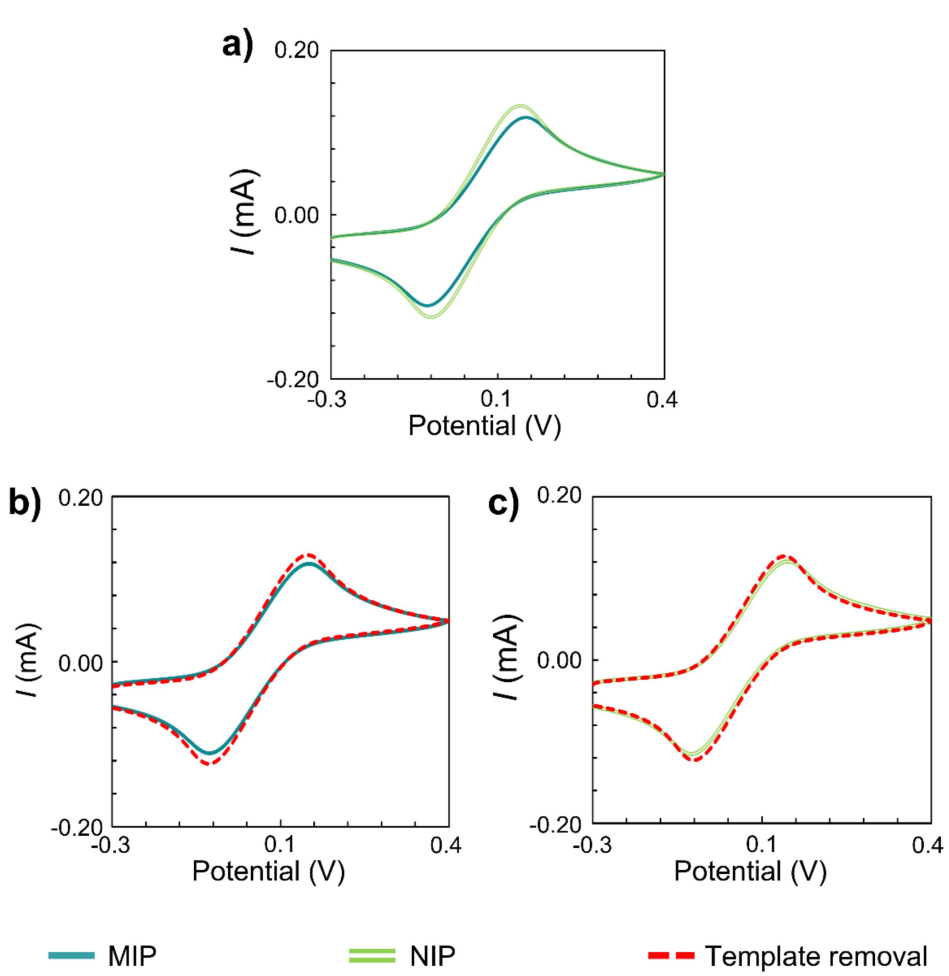

Figure 5.21 Fabrication workflow for the AMOX MIP fabrication followed by cyclic voltammetry: a) comparison between MIP and NIP; b after template removal from MIP; c) after template removal from NIP. Indirect readings performed with the redox probe 5.0 x 10^{-3} M $[Fe(CN)_6]^{3-/4-}$ prepared in ACN buffer, performed from -0.3 to +0.4 V, at 50 mV/s.

As expected, the presence of the polymeric layer decreased the peak currents observed in the CV assays, due to poly(EBT) being an insulating polymer. This current decrease was more intense in the MIP film, which signalled the presence of AMOX, a non-conductive element that blocks the current flow to the WE conductive surface and restricts the polymer growth.

After the polymerization stage, the electrodes for MIP and NIP were incubated in ACN and subject to consecutive CV sweepings, from +0.5 to +0.8 V, with a scanning-rate of 0.1 V/s, for 40 cycles, to remove AMOX from the polymeric matrix. These conditions ensured the integrity of the polymer, while avoiding the electroactivity of AMOX, which could be irreversibly entrapped within the poly(EBT) film. The iron redox probe readings indicated a substantial change in the MIP film, evidencing a significant current recovery, which confirmed the successful exit of AMOX from the polymeric network (Figure 5.21b). Consistently, the NIP film remained almost unchanged in terms of peak current because there was no template to be extracted from it (Figure 5.21c).

Raman spectroscopy was used to follow the chemical modifications performed in the construction of the MIP layer for AMOX. In detail, Raman spectra were recorded on WE surface as-produced and after PEDOT polymerization, AMOX MIP fabrication and template removal step (Figure 5.22).

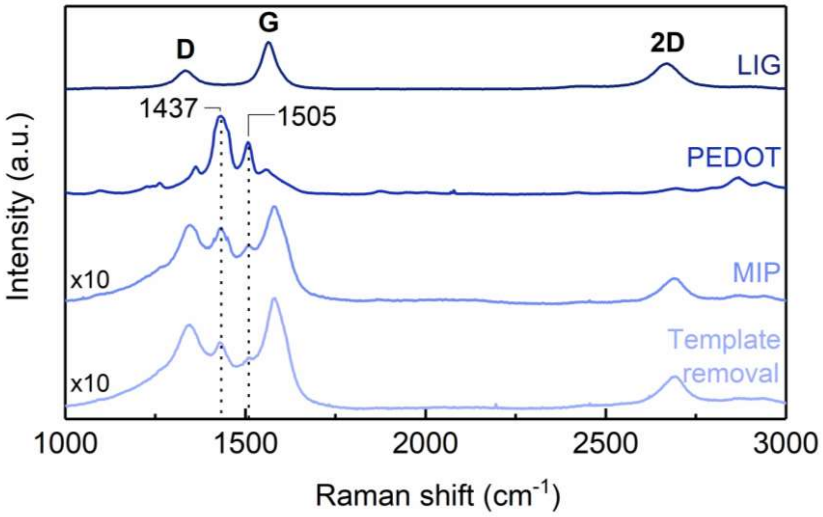

Figure 5.22 Raman spectroscopy analysis of the electrode surface following each chemical modification for the fabrication of the AMOX MIP. The MIP and template removal spectra are multiplied by 10-fold to better highlight the peak's intensity changes.

As expected, the characteristic D and G peaks of graphitic materials are present in all spectra. The presence of the D peak, at 1330 cm^{-1}, characteristic of carbon structural defects, is in accordance with the literature for LIG substrates.[35,217,231] Moreover, the G peak, at 1590 cm^{-1}, reflects the C-C stretching of the first order scattering of sp^2 carbon hybridization.[391,423,424] Thus, to follow the modifications of the LIG material along the MIP construction, the ratio of I_D/I_G can be used as a tool to evaluate the quality of the graphitic material and the ordered/disordered modifications.[391,423,424]

In general, when EDOT was added to the clean LIG surface, two very prominent peaks appeared around 1437 and 1505 cm^{-1}, between the G and D peaks (I_D/I_G of 0.82). These peaks are respectively characteristic of the $C_\alpha = C_\beta$ symmetric and asymmetric stretching vibrations of PEDOT[425] and, as expected, were still present in all subsequent steps, although with lower intensities due to the EBT polymeric layer. Although very small differences were observed between the MIP and template removal steps, it was possible to see a mild increase on the PEDOT peaks intensity after template removal, due to the presence of vacancies on the poly(EBT) layer, which is confirmed by the increase of the I_D/I_G ratio, from 0.76 to 0.79.

Finally, the analytical performance of the AMOX MIP was followed by incubating the LIG-devices with increasing concentrations of AMOX solutions, for 20 minutes, washing the solution out and measuring

the electrical performance by SWV assays with the iron standard redox probe. The typical data obtained is shown in Figure 5.23.

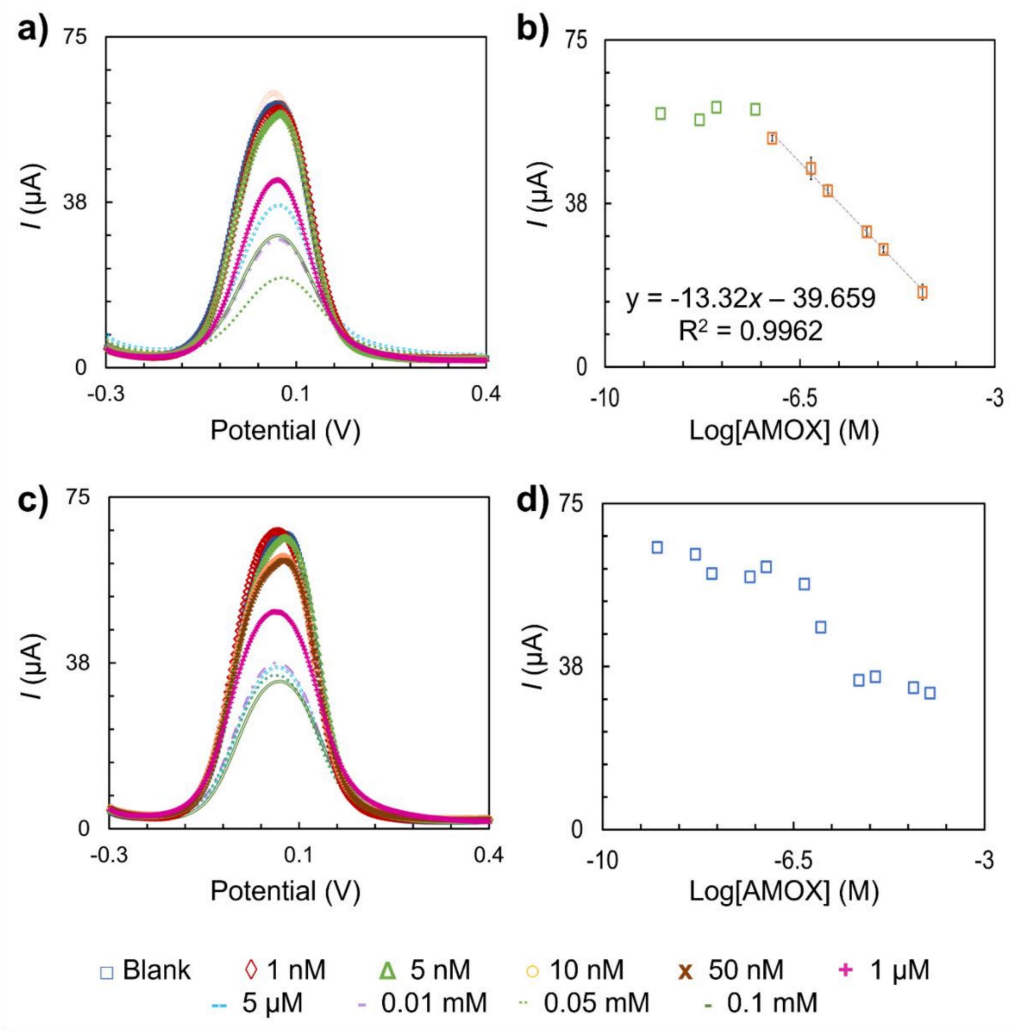

Figure 5.23 AMOX MIP analytical performance: a) SWV measurements in MIP devices with the b) corresponding calibration curves, of standard solutions of AMOX with increasing concentrations, prepared in $LiClO_4$ electrolyte; c) SWV measurements in NIP devices with the b) corresponding calibration curves, of standard solutions of AMOX with increasing concentrations, prepared in $LiClO_4$ electrolyte. Indirect readings performed with the redox probe 5.0 x 10^{-3} M $[Fe(CN)_6]^{3-/4-}$ prepared in ACN buffer.

In general, the increasing concentrations of AMOX incubated in the WE yielded decreasing current intensities of the redox probe in SWV, thereby confirming AMOX rebinding (Figure 5.23a). The corresponding calibrations curves (Figure 5.23b) revealed a linear behaviour of the current density against the logarithm of AMOX concentration. This linear range was obtained between 50 nM and 0.1 mM, with an average slope of -13.32 µA/decade. The calibration curve revealed a good square correlation coefficient ($R^2 > 0.99$), with an excellent LOD, down to the nanomolar level, of 11.98 nM.

In contrast, the NIP biosensor (acting as negative control, for monitoring the non-specific response of the sensing film) presented a random response against increasing AMOX concentrations, with lower

absolute changes in terms of current (Figure 5.23c). Despite some apparent correlation between the SWV readings and AMOX concentration, the current variation was not significant and presented an unacceptable squared correlation coefficient (Figure 5.23d). Overall, the response was dominated by the imprinted sites within the poly(EBT) film, suggesting a non-specific interaction between AMOX and the polymer.

A direct comparison with the literature on MIP-based strategies for AMOX sensing was carried out as seen in Table 5.2.

Table 5.2 Revision of proposed electrochemical MIP devices for AMOX sensing.

Preparation method	Monomer	EC readout	Linear range	Sensitivity	LOD	Author, year
IL grafting onto MWCNTs and dendritic Pt-PdNPs transference to GCE	3-propyl-1-vinylimidazolium bromide (IL)	DPV	1 nM - 1 μM and 1 – 6 μM	45.7 and 7.78 μA/μM	0.89 nM	Yang, G., 2015[426]
Precipitation polymerization and collection with a magnetic CPE	EGDMA	DPV	1.0 nM - 0.11 μM	225.21 μA/μM	0.26 nM	Zeinali, S., 2018[427]
Sol-gel polymerization, coating on GO and transference to GCE	APTES and PTES	DPV	5×10^{-10} – 9.1×10^{-7} M	4.20 μA/dec	2.9×10^{-10} M	Güney, S., 2020[428]
Precipitation polymerization, magnetic modified and transference to a CPE	AA	SWV	2.5 – 57 μM	0.24 μA/μM	0.75 μM	López, R., 2021[429]
Electropolymerization onto LIG	EBT	SWV	50 nM - 0.1 mM	39.7 μA/dec	11.98 nM	**This work**

IL: ionic liquid; MWCNTs: multi walled carbon nanotubes; GCE: glassy carbon electrode; DPV: differential pulse voltammetry; CPE: carbon paste electrode; EGDMA: ethylene glycol dimethacrylate; GO: graphene oxide; APTES: 3-Aminopropyl)triethoxysilane; PTES: phenyltriethoxysilane ; AA: acrylamide; SWV: square wave voltammetry; EBT: eriochrome black T.

As it can be seen, it was possible to obtain the widest linear range of the literature and a LOD within the current state of the art.

AA sensing material

As explained before, the AA MIP film was assembled in the second WE of the dual-LIG device, following a previously published work by Özcan, L. et al[271] with few modifications. Briefly, the electrodes were cleaned first by CV scanning in a KCl 0.1 M solution, for 100 cycles, from -0.3 to +0.95 V, with a scan-rate of 100 mV/s. The MIP film for AA was then produced by electropolymerizing pyrrole by CV in the presence of AA (Figure 5.24a), using the electrochemical conditions reported.

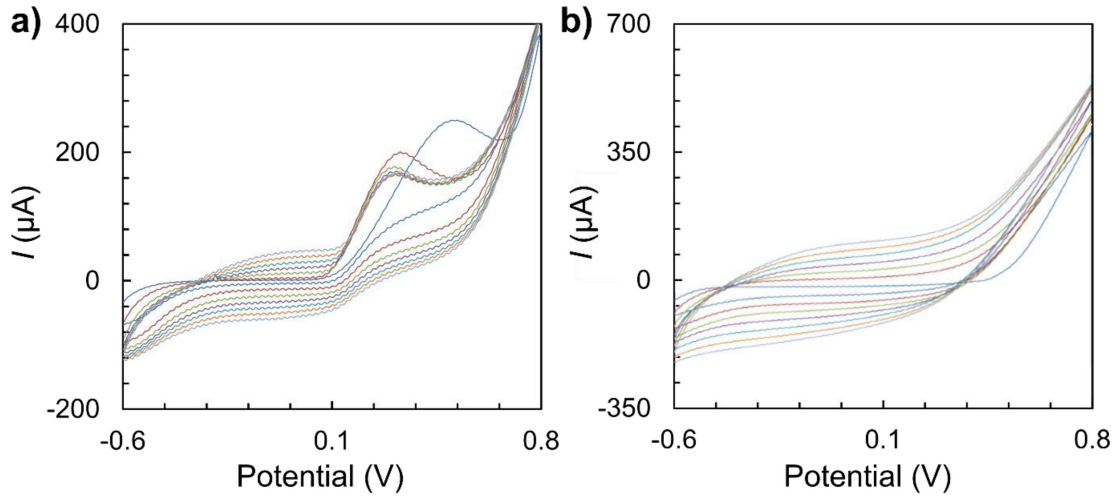

Figure 5.24 Pyrrole electropolymerization by cyclic voltammetry: a) AA MIP fabrication; b) AA NIP.

In this case, the fabrication of the AA MIP was achieved by means of the electrooxidation of pyrrole. During this process, AA molecules diffuse towards the surface of the WE and become trapped in the polymeric matrix, due to AA ability to interact with pyrrole monomers. Two types of hydrogen bonding can occur during this process: between the C=O functional group of AA and the N-H functional group of pyrrole units or, between the -OH functional group of AA and the N-H group of pyrrole.[271]

The control film (NIP) is shown in Figure 5.24b and confirms the results previously published. Finally, the template was removed, by incubating the WE in a 0.05 M phosphate buffer solution, for 30 min.

The analytical performance of the AA MIP film was followed by incubating the sensing area with increasing concentrations of AA solutions, for 20 minutes, washing it and measuring the electrical performance by SWV assays directly, without the redox probe. The typical data so obtained is shown in Figure 5.25.

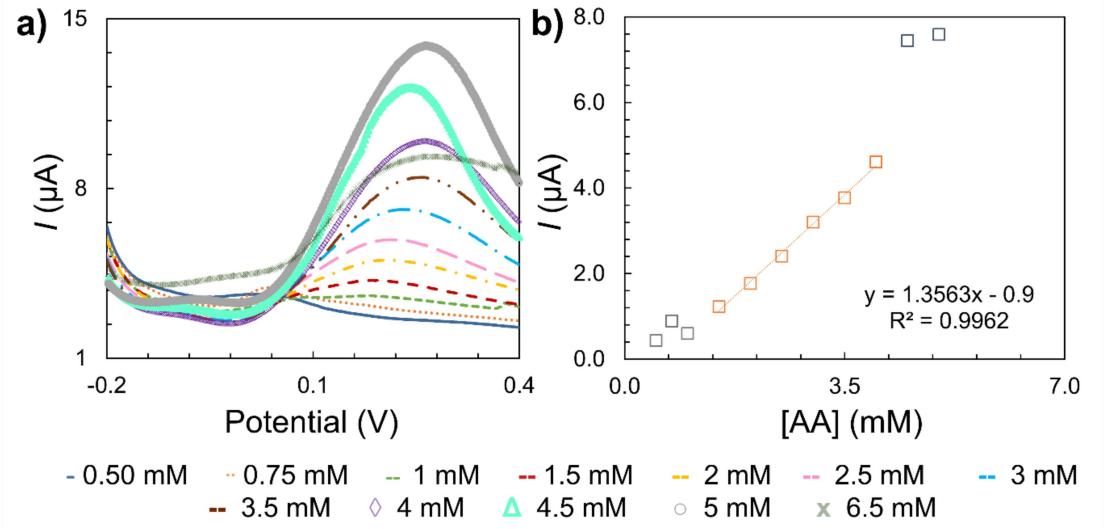

Figure 5.25 AA MIP analytical performance: a) SWV measurements in AA MIP film with increasing concentrations of AA and b) corresponding calibration curve.

The increasing concentrations of AA, incubated in the WE, increased the current intensities, thereby confirming AA rebinding (Figure 5.25a). The corresponding calibration curve (Figure 5.25b) revealed a linear behaviour of current against AA concentration. The AA sensor showed a good working linear range, between 1.5 mM and 4 mM, with an average slope of 1.356 µA/decade. Also, the calibration curve revealed a good square correlation coefficient ($R^2 > 0.99$). The linear range obtained can, however be widened, by improving the removal step, having more cavities to rebind the template with different concentrations. Also, it is possible to increase the incubation time for each standard. In addition, in case of AA, it would be possible to use a redox probe, as ruthenium-base compounds, to have indirect and more sensitive readings.

Application to binary solutions

A proof-of-concept of the dual-LIG device was conducted by testing the system in water samples with binary mixtures of AMOX and AA. For this, water from a domestic well was collected and spiked with increasing concentrations of 1:1 AMOX:AA solutions. This provided a more complex matrix than the tested standard solutions, to evaluate the behaviour of the biosensor in a close-to-real case scenario.

The general analytical procedure consisted in pre-incubating the binary samples in the WEs area. It was however clear from the previous assays that the iron redox probe used to interact with the AMOX MIP film would interfere with the direct readings of AA, because both had electroactivity properties at about 0.2 V. Thus, additional assays were performed to take advantage of the intrinsic redox properties of AMOX at higher potential values.

Thus, prior to the assessment of the dual biosensor response, the dual WEs were tested in terms of cross-response by checking the behaviour of each electrode to the other component, using individual AMOX and AA aqueous solutions. A good peak separation and lack of cross-response was observed when the two compounds were analysed in buffer, at pH 7.0 (Figure 5.26).

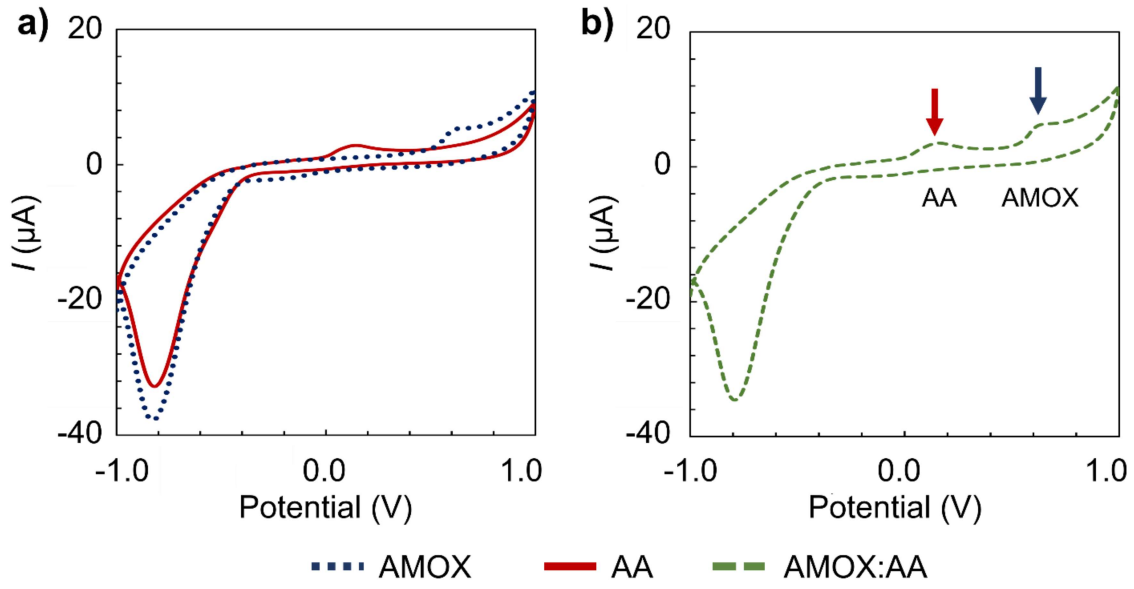

Figure 5.26 Cyclic voltammograms showing the peak separation of both molecules in a) single and b) binary solutions.

This behaviour was observed in both single (Figure 5.26a) and binary (Figure 5.26b) mixtures. Having observed such behaviour, a strategy was employed to measure both AMOX and AA in binary solutions. Thus, SWV measurements were collected by directly reading the electrochemical response of the target analytes, without the redox probe. The analytical data so obtained is shown in Figure 5.27.

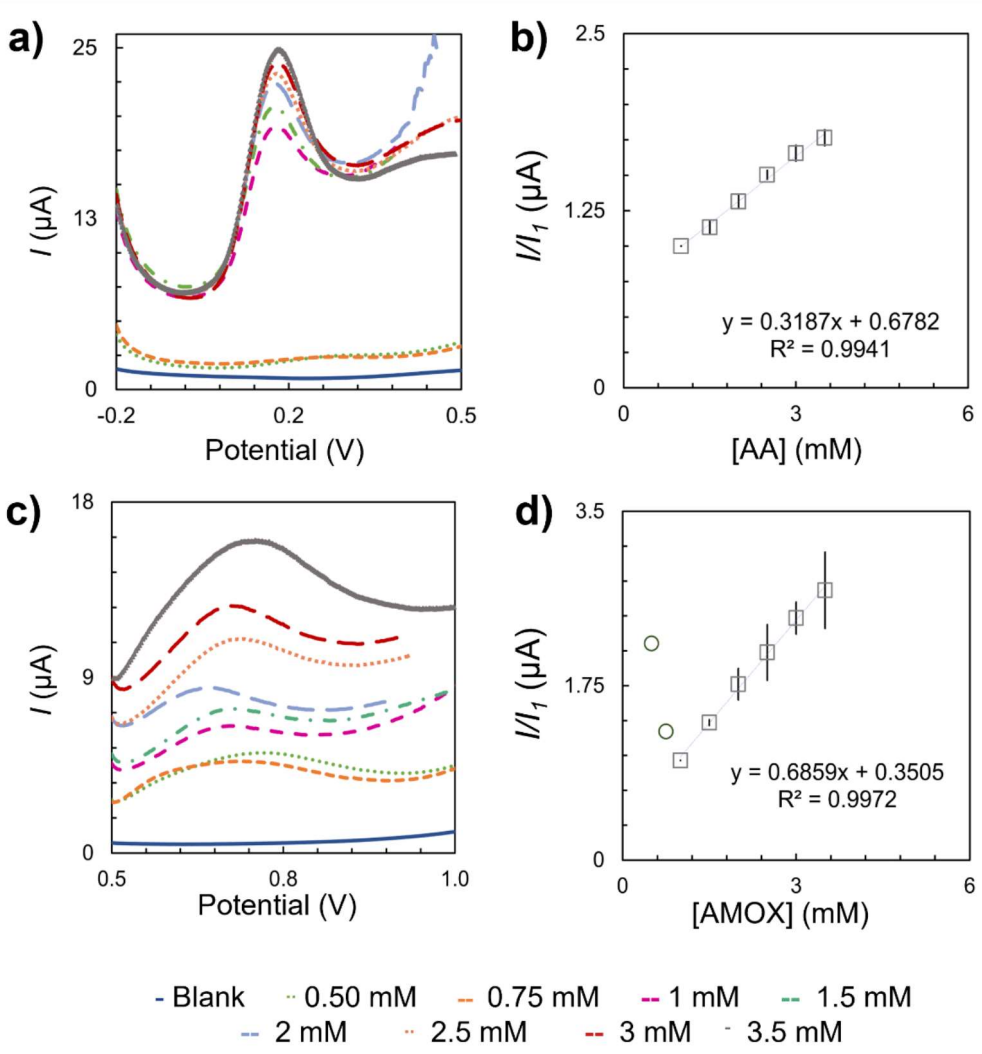

Figure 5.27 Analytical performance of the developed dual-LIG device for the simultaneously quantification of AMOX and AA: a) SWV direct readings of AA spiked in real samples and b) corresponding calibration curve; c) SWV direct readings of AMOX spiked in real samples and d) corresponding calibration curve. The SWV meausrements were carried out at 2 mV/s.

It was possible to observe a linear response for increasing concentrations of both molecules. In general, the linear response was observed from 1.0 to 3.5 mM, with a sensitivity of 0.32 µA/mM for AA and 0.69 µA/mM for AMOX. The calibration curves obtained also showed a good square correlation coefficient ($R^2 > 0.99$), which highlighted the good analytical performance of the method.

Moreover, the analysis of the spiked samples was considered by reading the current data in the obtained calibration curves. Different concentrations of AMOX and AA were added to the well's water, set both to 1.0, 1.5, 2.0, and 3.5 mM. The % errors for each concentration were calculated against the linear regression of the established calibration curves and considering the theoretical concentration according to:

$$\%error = \frac{\text{Cexperimental} - \text{Ctheorical}}{\text{Ctheorical}} \text{x} 100\% \qquad \text{(eq. 5.1)}$$

where $C_{experimental}$ is the concentration calculated from the calibration curve and $C_{theorical}$ is the theoretical concentration.

The % errors so obtained varied from -5.54% to 13.79% for AA and -5.86% to 1.16% for AMOX. Overall, these errors were suitable for all theoretical concentrations tested, being the AMOX reading more accurate for having a narrower range of error values. The highest error values for AA were obtained for the higher concentration values (2.0 and 3.5 mM), for which it would be more appropriate to analyse samples with AA in a lower concentration range. Yet, the established device, targeting two molecules at the same time may be considered accurate and precise, offering an important alternative to current SPEs systems. Moreover, although the followed strategy involved the electroactivity of both molecules in different potential ranges, which with simpler matrices the fabricated MIP layers may not be as necessary, with more complex samples, such as biological samples, the presence of the imprinted sensing materials is vital to guarantee the selectivity of the measurements.

CHAPTER 6

Conclusions and future perspectives

Chapter 6. Conclusions and future perspectives

The research work presented in this dissertation focused on the fabrication of nanobiosensing platforms, coupled with optical and electrochemical transduction mechanisms. It was divided into two main areas: development of SERS-based platforms with cellulosic materials as the support for Raman enhancement nanostructures and development of MIP-based platforms with LIG electrodes patterned onto flexible substrates.

In this chapter general conclusions about these topics and future perspectives for further development of this research area are presented.

6.1 Conclusions

To date, most biosensing platforms utilize natural bioreceptors as recognition elements. Although, in most cases, their high affinity towards the analyte of interest is undeniable, the use of these elements can carry obvious downsides, such as high cost, complexity, compromised stability on harsh environments and unavailability. The main conclusion that can be drawn from the work developed on this dissertation is the feasibility of both optical and electrochemical sensing mechanisms to use alternative recognition mechanisms that are free from natural bioreceptors. By applying different strategies, such as the one used in this work, it is possible to fabricate reliable sensing platforms with high selectivity and sensitivity, thus with equivalent performance to the ones with natural bioreceptors.

Moreover, following the current trend of scientific research on functional devices this work sought to use simple fabrication routes and low-cost and flexible materials as platforms for the developed nanobiosensors.

6.1.1 SERS-based nanobiosensing platforms

Different strategies were explored for the fabrication of SERS platforms using cellulose as substrate and both physical and chemical routes to produce nanostructures for Raman enhancement. The produced platforms were characterized in terms of Raman enhancement performance and their sensing ability was evaluated and combine with statistical data analysis protocols for label-free detection of simple molecules (tetracycline) and more complex biostructures (proteins and exosomes).

Physical route

The use of cardboard-based AgNPs for SERS sensing combined with a highly simplified sample handling and data analysis protocol was demonstrated. This platform, named here as TP@AgNPs was developed and fully characterized by our research group where its high reproducibility and stability was proven. Metal deposition by e-beam thermal evaporation was used, resulting in the direct arrangement of individual AgNPs, with a good control of size and shape, without the need for any post-thermal treatment.

All characteristic vibrational modes of milk and TET spiked milk were analysed via a global PCA-based analysis allowing to develop a peak ratio approach for the detection and quantification of TET without any sample pre-treatment. The simplification of the detection protocol allowed for a higher number of measurements within the same sample to have a better statistical representation and correlation of the spectral data to the target analyte concentration. This approach showed a sensitivity bellow 0.1 ppm, which is the maximum residue limit set by the governmental authorities. These results serve as a foundation to further explore this method for other analytes and sample types.

Chemical route

Microwave-assisted chemical synthesis was the selected approach for the in-situ growth of Raman enhancement nanostructures, namely AgNPs and AuNPs. The method offers several advantages as rapid synthesis, cost-effectiveness with energy efficiency and, ease of tunability, high-throughput and, a good control over size and shape.

As the substrate for the produced Raman active nanostructures, BNC was obtained from n*ata de coco*, which has proven to be a reliable source of nanocellulose and compared to regular cellulose, nanocellulose has not only better mechanical properties, making it easier to handle, but its nanosized fibres arrangement can render more homogeneous membranes, with reduced porosity, enhancing SERS signal reproducibility and sensitivity due to its high surface-to-volume ratio.

Microwave in-situ AgNPs synthesis proved to be successful, and through parameters optimization (such as, reactant's concentrations and reaction time), fully covered NC membranes were obtained. These membranes (NC@AgNPs) showed good results and fulfilled the goal of a low-cost substrate able to enhance Raman signal. With R6G as model molecule, the said platform was able to measure it down to 10^{-11} M with well-discriminated peaks and a reduced background noise. Biological tests with tumoral and non-tumoral exosomes were conducted and by PCA analysis, was possible to data group tumoral and non-tumoral exosomes, with 95% of confidence, even with the known high variability of exosome's

samples. These results showcase the possibility to use innovative low-cost SERS substrates with clinically relevance for cancer diagnosis and follow-up by a label-free approach.

A similar strategy was followed for AuNPs in-situ growth onto nanocellulose, through microwave irradiation, and was validated as a valuable approach for SERS sensing, while offering a high shelf-life, due to the high chemical stability of AuNPs when compared with AgNPs. In opposition to AgNPs microwave synthesis, AuNPs microwave-assisted synthesis and its performance as SERS active layers it's not so well reported in the literature. A systematic study was then performed herein by optimizing relevant parameters and study their influence in the resultant particles and SERS performance. Citrate-based AuNPs has shown to provide enhanced optical properties and stability over time, when compared with glucose-based synthesis. The fabrication approach based on an incubation step of the cellulosic substrate on the reaction mixture followed by seed-mediated growth method of AuNPs, rendered membranes with well-distributed and densely packed NPs. The method was also employed in close-to-hydrophobic and hydrophilic cellulose substrates, with better outcomes obtained with the hydrophilic ones due to the high capacity to wick the reaction mixture translating in a homogeneous distribution of particles. Still, in terms of SERS performance, nanocellulose showed superior results when compared to the hydrophilic Whatman paper due to nanocellulose' less porous content and higher surface area. Moreover, the developed workflow for SERS membranes fabrication translates in higher Raman amplifications than a 24 h immersion method of AuNPs onto nanocellulose membranes, with obvious benefits in terms of reduction of total fabrication time. Additionally, the benefits of using a three-dimensional material with high surface-to-volume ratio as SERS supporting Raman active nanostructure's matrix was demonstrated with the enhanced SERS intensities obtained with our membrane, when compared to a common glass substrate decorated with AuNPs. A calculated EF of ~10^6, with an RSD lower than 8% and an outstanding shelf life up to 7 months, with regular storage conditions, was attained. The successful label-free detection of S protein from SARS-CoV-2 virus validated the optimized NC@AuNPs membrane for SERS biosensing.

We believe that the herein developed SERS membranes offer an accurate, reliable, and inexpensive platform for biosensing that can be used in POC settings if combined with portable Raman readers. In general, the produced SERS membranes presented equivalent performance features, as a good EF, low RSD values and high shelf life, and so the approaches followed for preparation of the SERS membranes and data analysis protocols were proven to be valid for optical biosensing.

6.1.2 MIP-based nanobiosensing platforms

For the development of nanobiosensing platforms based on electrochemical transduction mechanism two novel features where combined: the use of LIG technique for electrode's patterning with MIP elements for biosensing without relying on natural bioreceptors.

The work described herein showed for the first time the combination of a simple and reproducible carbon-electrode fabrication by laser irradiation of polyimide substrates, with the on-site assembly of biorecognition elements prepared by molecular imprinting technology. The carbon material so produced is constituted by graphene and the resulting three-electrode system compared favourably to commercial devices in terms of sensitivity and linear response range.

Initially, a LIG-MIP biosensor was developed for single detection, and it showed high sensitivity against CAP, being able to detect exceptionally low concentrations of this antibiotic, down to the nanomolar range. It also showed a good selectivity against other possible interfering antibiotics (OTC, AMC, and SDZ). Afterwards, to demonstrate the versatility of the LIG technique a dual sensing platform was proposed for the detection of two molecules, AA and AMOX, that are widely used in aquaculture and its levels need to be monitored. The analytical features showed good square correlation coefficients with excellent LODs (down to the nanomolar level - 11.98 nM for AMOX). The dual-LIG MIP devices were also able to successfully monitor AA and AMOX both in binary standard solutions and in binary samples from environmental waters from a well. As output, this demonstrates that this type of platforms can be easily adopted for multi-detections systems to measure relevant molecules at the same time.

Besides the advantages in terms of analytical features, the LIG-based biosensors offer the advantages of being highly reproducible, low-cost, made of a flexible material and produced by a technique that allows freedom of design with a high resolution, allowing an easy redesign of the electrode-system, to other geometries and architectures, following the current needs of the scientific community. Moreover, due to the one-step mask-less approach for electrode's patterning, it offers potential scalability for massive biosensor platforms production The biorecognition element is also assembled by an on-site process, thereby facilitating the scalability of this specific biosensor.

Overall, the strategy proposed is considered a promising approach for the future of on-site analysis in different contexts, including environment, industrial and health applications.

6.1.3 Comparison of the developed nanobiosensing platforms with commercially available devices

The solutions found in this dissertation thesis for nanobiosensing platforms based on optical and electrochemical transductions methods, can be compared favourably with the current commercially available devices.

The developed SERS substrates combined the use of widely available cellulosic materials with low-cost techniques to produce the plasmonic nanostructures, showing in general a high shelf life and reproducibility. In particular, the use of nanocellulose membranes combined with highly stable AuNPs, produced through a solution-based process, with microwave irradiation, renders SERS substrates with a shelf-life of at least 7 months, without requiring special storage conditions, an inherent low cost (<0.025€/analysis), requirement of low sample volumes (2 μl) flexibility and conformability, which can facilitate sample collection and in-situ SERS measurements. On the other hand, the current available SERS substrates are either based on glass or silicon substrates, or even if based on cellulosic materials (as the ones from Ocean optics), they require higher sample volumes (10 μl), have a lower shelf-life of 1 – 1.5 months, while requiring storage under a desiccated environment, the paper-based sensing area is integrated in a microscope slide, thus hindering flexibility and conformability, and has a much higher associated cost (~10€/analysis).

The developed electrochemical platforms combine the use of a high throughput, versatile and low-cost production method of carbon-based electrodes that allows freedom of design with a high resolution, and the possibility to tailor the device's architecture to better suit a desired application, while offering enhanced electrochemical features when compared with the commercial counterparts, SPEs. An estimate of the cost per unit was performed accounting the cost of all materials involved, including the polyimide sheet, the silver conductive ink used for electrical contacts and the lamination pouches. The overall cost in materials was 0.15 €/unit. Even considering the costs involved in the facilities and equipment, the overall final cost of the device shall be much lower than the typical ~2 €/unit of the commercially available ceramic SPEs, because the system is highly suited to a mass-production.

6.2 Future work and perspectives

Regarding the production of nanostructures for Raman enhancement, following both physical and chemical routes, the direct deposition onto the selected substrate, without relying on post-transference methods, was successfully attained. The possibility to scale up the production methods employed needs to be further access. Moreover, adding to the Raman enhancement layers proposed in this work other strategies can be followed. In particular, the SERS membranes produced by the chemical route onto nanocellulose substrates showed very promising outputs and can be further improved by incorporating hybrid nanostructures, such as bimetallic nanocomposites of silver and gold to offer both high enhancement capabilities of Ag nanostructures with chemical stability and biocompatibility of Au, or metal oxide nanostructures decorated with either AgNPs or AuNPs to improve, for instance, the number of hotspots for Raman enhancement. Further demonstration of the capabilities of the developed SERS platforms can also be assessed, as: reusability, direct sample collection from non-flat surfaces (e.g., direct pesticides screening from fruits surfaces and/or crops), in-situ SERS measurements, among others.

The proposed devices for electrochemical biosensing using MIP films and LIG as the electrode layers was successfully demonstrated. Nonetheless, to increase sensitivities and enhance the overall performance of the LIG-based devices the WEs can be functionalized with nanostructures, such as AuNPs, that can be produced by electrodeposition or even laser irradiation. Here, polyimide substrates were used for the LIG patterning achieved by laser irradiation. Although it yields flexible high-quality electrodes for electrochemical sensing with good electric, morphological and chemical characteristics it is not obtained from renewable sources. So, it is of interest to use materials such as cellulose, that are recyclable, biodegradable, inexpensive and biocompatible, and some studies were in fact already reported in the literature on strategies to induce LIG on such substrates. Due to the observed enhanced properties of nanocellulose as SERS support membrane, as future work it may be relevant to study the rendering of LIG onto this substrate, due to its high mechanical and thermal stability and high surface area and evaluate its performance for MIP-based sensing. In fact, preliminary results on the LIG patterning onto nanocellulose were already obtained as depicted in Figure 6.1.

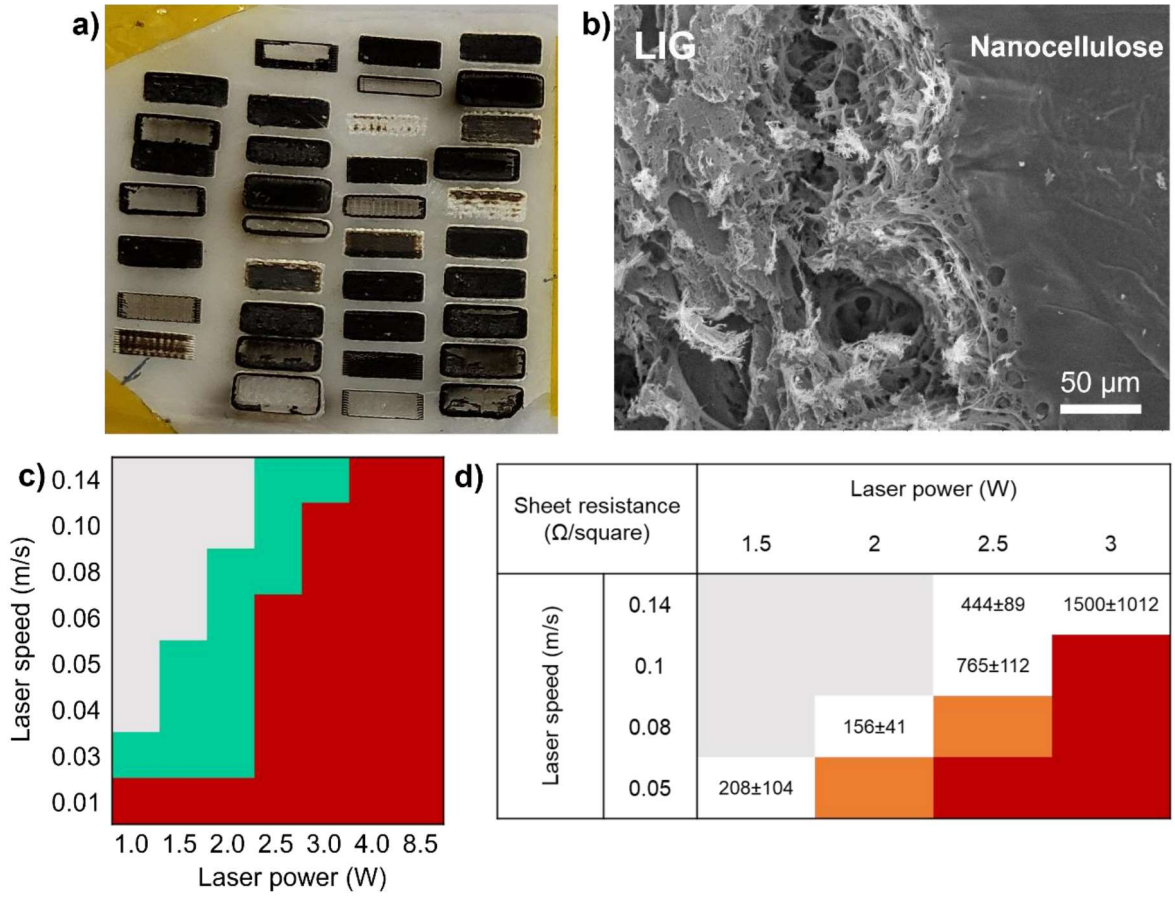

Figure 6.1 Preliminary results on LIG production onto nanocellulose membranes: a) representative photograph of the output of a optimization matrix (variation of laser power and speed); b) SEM image showing the localized LIG formation onto nanocellulose; c) output of the variation of laser conditions where ▯ represents the region of no laser effect, ▮ represents the region of LIG formation and, ▮ represents the region where the substrate is perforated or too fragile; d) sheet resistance measurements through hall effect (▮ represents the laser conditions that yielded LIG in c) but, when patterning larger areas the substrate is perforated/fragile).

The nanocellulose membranes were pre-treated with a fire-retardant, to assure that cellulose could withstand the thermal energy supplied by the laser source, thus enabling cellulose photoconversion to LIG. Tests were carried out by varying laser power and speed and the distance from the focal point (d = 0 mm, d = - 1 mm, d = +1 mm), where d = +1 mm yielded the higher number of laser conditions able to produce LIG onto nanocellulose (Figure 6.1). A laser power of 2 W and a scan rate of 0.08 m/s rendered a sheet resistance of 156 ± 41 Ω/square. Although promising, further optimizations need to be carried out to decrease the sheet resistance, and the feasibility of the rendered LIG electrodes to be used as biosensing surfaces needs to be assessed.

Moreover, testing of the endurance and robustness of the produced LIG materials is also of interest to assure that this material can be, for instance, in conformable/flexible shapes without compromising the performance of the electrodes.

The applications proposed herein with the developed nanobiosensing platforms were used as proof-of-concepts. Still, we believe that these applications are of high relevance, specifically on environmental and clinical fields, thus further developments to improve the performance of the devices and testing it with real samples, in some of the cases, is of relevance. Additionally, microfluidics can be integrated with such sensing devices to allow fluids manipulation (e.g., driving, mixing, separation, etc.), to attain autonomous samples pre-treatment.

Finally, the developed discrete nanobiosensing platforms have the potential to be incorporated in multifunctional biosensors due to the beauty of either the employed fabrication processes and used low-cost and inexpensive materials. These biosensors can be further developed to combine in the same sensing spot both transduction mechanisms (optical and electrochemical) in a synergistic way and to be integrated with other flexible devices, such as supercapacitors, for potential stand-alone sensing platforms for applications in safety, healthcare, and environment monitoring.

CHAPTER 7

Scientific outputs

This chapter shows the scientific outputs of the candidate during the thesis period, detailing the publications in peer-review periodicals and invited chapter books, oral and poster communications, research activities, courses attended, awards and master thesis guidance.

Chapter 7. Scientific outputs

During PhD activities the candidate has participated as first author or co-author in 29 peer-reviewed publications and invited chapter books translating in a h-index of 12 (Figure 7.1). The candidate also helped on the guidance of 19 master thesis and participated in several parallel international and national scientific projects within the scope of the main subject inherent to this thesis.

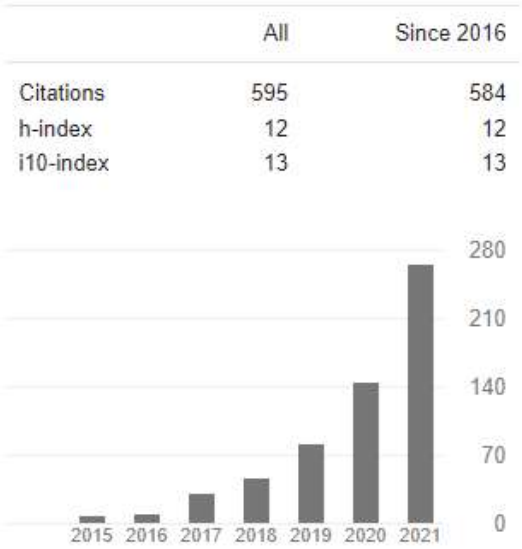

Figure 7.1 Number of citations achieved by the candidate until November 2021. Data retrieved from Google Scholar.

7.1 Publications

The publications of the candidate from which results are present in this dissertation document are listed below:

7.1.1 Peer-reviewed publications:

- **Marques, A. C.**, Pinheiro, T., Morais, M., Martins, C., Andrade, A. F., Martins, R., Sales, M. G. F., Fortunato, E., Bottom-up Microwave-assisted Seed-mediated Synthesis of Gold Nanoparticles onto Nanocellulose to Boost Stability and High Performance for SERS Applications, Applied Surface Science, **2021**, 561, 150060.

- **Marques, A. C.**, Cardoso, A. R., Martins, R., Sales, M. G. F., Fortunato, E., Laser-Induced Graphene-Based Platforms for Dual Biorecognition of Molecules. ACS Applied Nano Materials, **2020**, 3(3), 2795–2803.
- **Marques, A. C.**, Veigas, B., Araújo, A., Pagará, B., Baptista, P. V., Águas, H., Martins, R., Fortunato, E., Paper-Based SERS Platform for One-Step Screening of Tetracycline in Milk. Scientific Reports, **2019**, 9(1), 17922.
- Ferreira, N., **Marques, A. C.**, Águas, H., Bandarenka, H., Martins, R., Bodo, C., Costa-Silva, B., Fortunato, E., Label-Free Nanosensing Platform for Breast Cancer Exosome Profiling. ACS Sensors, **2019**, 4(8), 2073–2083.
- Cardoso, A. R., **Marques, A. C.**, Santos, L., Carvalho, A. F., Costa, F. M., Martins, R., Sales, M. G. F., Fortunato, E., Molecularly-Imprinted Chloramphenicol Sensor with Laser-Induced Graphene Electrodes. Biosensors&Bioelectronics, **2019**, 124–125, 167–175.
- Samouco, A., **Marques, A. C.**, Pimentel, A., Martins, R., Fortunato, E., Laser-Induced Electrodes towards Low-Cost Flexible UV ZnO Sensors. Flexible and Printed Electronics, **2018**, 3(4), 044002.

7.1.2 Invited chapter books:

- **Marques, A. C.**, Águas, H., Martins, R., Silva, B. C., Sales, M. G. F., Fortunato, E. Surface-Enhanced Raman Scattering Paper-based analytical devices. In Paper-based Analytical Devices for Chemical Analysis and Diagnostics, Elsevier, **2021**, 1, 117–168.
- **Marques, A. C.**, Pinheiro, T., Martins, G. V., Cardoso, A. R., Martins, R., Sales, M. G. F., Fortunato, E., Non-Enzymatic Lab-on-Paper Devices for Biosensing Applications. In Comprehensive Analytical Chemistry; Elsevier B.V., **2020**, 89, 189–237.

The publications of the candidate, during the thesis period, from which results are not present in this dissertation are listed below:

- Pinheiro, T., Cardoso, A. R., Sousa, C. E. A., **Marques, A. C.**, Tavares, A. P. M., Matos, A. M., Cruz, M. T., Moreira, F. T. C., Martins, R., Fortunato, E., Sales, M. G. F., Paper-based biosensors for COVID-19: A review of Innovative Tools for Controlling the Pandemic, ACS Omega, **2021**, in press.
- Pinheiro, T., Silvestre, S., Coelho, J., **Marques, A. C.**, Martins, R., Sales, M. G. F., Fortunato, E., Laser-Induced Graphene on Paper toward Efficient Fabrication of Flexible, Planar Electrodes for Electrochemical Sensing, Advanced Materials&Interfaces, **2021**, 2101502.

- Claro, P. I. C., **Marques, A. C.**, Cunha, I., Martins, R. Pereira, L., Marconcini, J. M., Mattoso, L. H. C., Fortunato, E., Tuning the Electrical Properties of Cellulose Nanocrystals through Laser-Induced Graphitization for UV Photodetectors, ACS Applied Nano Materials, **2021**, 4(8), 8262-8272.
- Nunes, D., Fragoso, A. R., Freire, T., Matias, M., **Marques, A. C.**, Martins, R., Fortunato, E., Pimentel, A., Ultrafast Microwave Synthesis of WO_3 Nanostructured Films for Solar Photocatalysis, Physica Status Solidi Rapid Research Letters, **2021**, 2100196.
- Nandy, S., Goswami, S., **Marques, A. C.**, Gaspar, D., Grey, P., Cunha, I., Nunes, D., Pimentel, A., Igreja, R., Barquinha, P., Pereira, L., Fortunato, E., Martins, R., Cellulose: A Contribution for the Zero e-Waste Challenge, Advanced Materials Technologies, **2021**, 6, 2000994.
- Freire, P.; Fragoso, A. R., Matias, M., Pinto, J. V., **Marques, A. C.**, Pimentel, A., Barquinha, P., Huertas, R., Fortunato, E., Martins, R., Enhanced Solar Photocatalysis of TiO_2 Nanoparticles and Nanostructured Thin Films Grown on Paper, Nano Express, **2021**, 2(4), 040002.
- Pinheiro, T., **Marques, A. C.**, Carvalho, P., Martins, R., Fortunato, E., Paper Microfluidics and Tailored Gold Nanoparticles for Nonenzymatic, Colorimetric Multiplex Biomarker Detection, ACS Applied Materials Interfaces, **2021**, 13, 3.
- Pereira, J. R., Araújo, D., Freitas, P., **Marques, A. C.**, Alves, V. D., Sevrin, C., Grandfils, C., Fortunato, E., Reis, M. A. M., Freitas, F., Production of Medium-chain-length Polyhydroxyalkanoates by *Pseudomonas chlororaphis* subsp. *aurantiaca*: Cultivation on Fruit Pulp Waste and Polymer Characterization, International Journal of Biological Macromolecules, **2021**, 167, 859-92.
- Concórdio-Reis, P., Pereira, C. V., Batista, M. P., Sevrin, C., Grandfils, C., **Marques, A. C.**, Fortunato, E., Gaspar, F. B., Matias, A. A., Freitas, F., et al., Silver Nanocomposites Based on the Bacterial Fucose-Rich Polysaccharide Secreted by Enterobacter A47 for Wound Dressing Applications: Synthesis, Characterization and in Vitro Bioactivity. International Journal of Biological Macromolecules, **2020**, 163, 959–969.
- Silvestre, S. L., Araújo, D., **Marques, A. C.**, Pires, C.; Matos, M., Alves, V., Martins, R.; Freitas, F., Reis, M. A. M., Fortunato, E., Microneedle Arrays of Polyhydroxyalkanoate by Laser-Based Micromolding Technique. ACS Applied Bio Materials, **2020**, 3(9), 5856–5864.
- Pinheiro, T.; Ferrão, J., **Marques, A. C.**; Oliveira, M. J., Batra, N. M., Costa, P. M. F. J., Macedo, M. P.; Águas, H., Martins, R., Fortunato, E., Paper-Based in-Situ Gold Nanoparticle Synthesis for Colorimetric, Non-Enzymatic Glucose Level Determination. Nanomaterials, **2020**, 10(10), 1–20.

- Araújo, D., Alves, V. D., **Marques, A. C.**, Fortunato, E., Reis, M. A. M., Freitas, F., Low Temperature Dissolution of Yeast Chitin-Glucan Complex and Characterization of the Regenerated Polymer. Bioengineering, **2020**, 7(1), 28.
- Pereira, M. V., **Marques, A. C.**, Marques, A. C., Oliveira, D., Oliveira, D., Martins, R., Moreira, F. T. C., Moreira, F. T. C., et al., Paper-Based Platform with an in-situ Molecularly Imprinted Polymer for β-Amyloid. ACS Omega, **2020**, 5(21), 12057-12066.
- Martins, G. V., **Marques, A. C.**, Fortunato, E., Sales, M. G. F., Paper-Based (Bio)Sensor for Label-Free Detection of 3-Nitrotyrosine in Human Urine Samples Using Molecular Imprinted Polymer. Sensing and Bio-Sensing Research, **2020**, 28, 100333.
- Pereira, J. R., Araújo, D., **Marques, A. C.**, Neves, L. A., Grandfils, C., Sevrin, C., Alves, V. D., Fortunato, E., Reis, M. A. M., Freitas, F., Demonstration of the Adhesive Properties of the Medium-Chain-Length Polyhydroxyalkanoate Produced by Pseudomonas Chlororaphis Subsp. Aurantiaca from Glycerol. International Journal of Biological Macromolecules, **2019**, 122, 1144–1151.
- Roman, C., García-Morales, M., Goswami, S., **Marques, A. C.**, Cidade, M. T., The Electrorheological Performance of Polyaniline-Based Hybrid Particles Suspensions in Silicone Oil: Influence of the Dispersing Medium Viscosity. Smart Materials and Structures, **2018**, 27(7).
- Araújo, D.; Concórdio-Reis, P., **Marques, A. C.**, Sevrin, C., Grandfils, C., Alves, V. D., Fortunato, E., Reis, M. A. M., Freitas, F., Demonstration of the Ability of the Bacterial Polysaccharide FucoPol to Flocculate Kaolin Suspensions. Environmental Technology, **2018**, 41(3), 287–295.
- Martins, G. V., **Marques, A. C.**, Fortunato, E., Sales, M. G. F., Wax-Printed Paper-Based Device for Direct Electrochemical Detection of 3-Nitrotyrosine. Electrochimica Acta, **2018**, 284, 60–68.
- **Marques, A. C.**, Santos, L., Pereira, S., Emanuele, U., Sinopoli, S., Igreja, R., Sales, G., Martins, R., Fortunato, E., A Planar Electrochromic Device Using WO_3 Nanoparticles and a Modified Paper-Based Electrolyte. Proceedings, **2018**, 2(13), 1065.
- Carvalho, A. F., Fernandes, A. J. S., Leitão, C., Deuermeier, J., **Marques, A. C.**, Martins, R., Fortunato, E., Costa, F. M., Laser-Induced Graphene Strain Sensors Produced by Ultraviolet Irradiation of Polyimide. Advanced Functional Materials, **2018**, 28(52), 1805271.
- Goswami, S., Nandy, S., Deuermeier, J., **Marques, A. C.**, Nunes, D., Patole, S. P., Costa, P. M. F. J., Martins, R., Fortunato, E., Green Nanotechnology from Waste Carbon-Polyaniline Composite: Generation of Wavelength-Independent Multiband Photoluminescence for Sensitive Ion Detection. Advanced Sustainable Systems, **2017**, 2(1), 1700137.

7.2 Oral and poster presentations

7.2.1 Oral presentations

- **Marques, A. C.**, Ferreira, N., Veigas, B., Araújo, A., Águas, H., Martins, R., Costa-Silva, B., Sales, M. G. F., Fortunato, E., Cellulose-based SERS substrates: fabrication and detection strategies, E-MRS Spring Meeting, Virtual Conference (Host: Lille, France), 2021.
- **Marques, A. C.**, Cardoso, A. R., Samouco, A., Silvestre, S., Pimentel, A., Martins, R., Sales, M. G. F., Fortunato, E., Laser direct writing as a powerful tool for sensing applications, 8th International Summer School on Trends and New Developments in Laser Technology, Fraunhofer Institute, Dresden, Germany, 2019.
- **Marques, A. C.**, Ferreira, N., Santos, L., Martins, R., Costa-Silva, B., Sales, M. G. F., Fortunato, E., Development and optimization of point-of-care nanobiosensing platforms, 7th International PhD Meeting, Fraunhofer Institute, Dresden, Germany, 2018.

7.2.2 Poster presentations

- Ferreira, N., **Marques A. C.**, Martins, R., Bodo, C., Sales, M. G. F., Costa-Silva, B., Fortunato, E., Label-free nanosensing platform for breast cancer exosome profiling, NanoBio&Med, Barcelona, Spain, 2019.
- **Marques, A. C.**, Ferreira, N., Santos, L., Martins, R., Costa-Silva, B., Sales, M. G. F., Fortunato, E., Nanobiosensing platforms towards point-of-care diagnostics, Materiais, Lisbon, Portugal, 2019.
- **Marques, A. C.**, Fernandes, A., Ferreira, N., Martins, R., Costa-Silva, B., Sales, M. G. F., Fortunato, E., Low-cost Nanobiosensing platforms, Encontro Ciência, Lisbon, Portugal, 2019.
- **Marques A. C.**, Ferreira, N., Martins R., Costa-Silva B., Sales M. G. F., Fortunato E., Development and optimization of point-of-care nanobiosensing platforms, 6th Dresden Nanoscale Symposium, Fraunhofer Institute, Dresden, Germany, 2018
- Cardoso A. R., **Marques A. C.**, Santos L., Carvalho A., Costa F., Martins, R., Sales M. G. F., Fortunato E., Ultra-sensitive laser-induced graphene flexible biosensor for aquaculture applications, Graduate Student Symposium on Molecularly Imprinting Polymers, Porto, Portugal, 2018
- **Marques, A. C.**, Coelho, B. J., Martins, R., Veiga, J. P., Fortunato, E., Lab-on-paper technology, EIT Raw Materials@Schools Annual Meeting, Bologna, Italy, 2018.
- **Marques, A. C.,** Santos, L., Pereira, S., Emanuele, U., Sinopoli, S., Igreja, R., Sales, M. G. F., Martins, R., Fortunato, E., A Planar Electrochromic Device using WO_3 Nanoparticles and a Modified Paper-Based Electrolyte, Eurosensors, Graz, Austria, 2018.

- **Marques A. C.**, Veigas B., Alves, P. U., Coelho, B. J., Pinto, J. V., Branquinho, R., Igreja, R., Águas, H., Martins, R., Fortunato, E., Biosensor Research Activity at CENIMAT/i3N, VI Annual Meeting i3N, Lisbon, Portugal, 2017

7.3 Participation in international and national research projects

- July 2015 January 2019: SYMBIOTIC – Innovative Autonomous Electrical Biosensor Synergistically Assembled Inside a Passive Direct Methanol Fuel Cell for Screening Cancer Biomarkers, H2020-FETOPEN-2014-2015-RIA, nº 60643.
- July 2020 to March 2021: ECO2COVID – Desenvolvimento de plataformas para deteção e monitorização em águas do CoronaVírus, COMPETE2020, Lisboa2020, nº 68174.
- July 2020 to November 2021: TecniCOV – Desenvolvimento de testes rápidos para monitorização de anticorpos em soro e saliva, COMPETE2020, Lisboa2020, nº 69745.

7.4 Courses

- 4th ELBYSIER Intensive Program in "Nanoelectronics and Graphene Technologies", October 9th-13th, 2017, FCT-UNL, CENIMAT, Caparica, Portugal.
- 8th International Summer School in "Trends and New Developments in Laser Technology", August 26th-30th, 2019, Fraunhofer Institute, Dresden, Germany.
- European Advanced Training Course in "Nanoscale materials - Characterization Techniques and Applications", August 27th-29th, 2018, Fraunhofer Institute, Dresden, Germany;
- Science Communication Course, May 9th-11th, 2017, NOVA Doctoral School, Lisbon, Portugal;

7.5 Awards

- 2nd prize on R2Value (Research to value) competition, 2020, IRIS, FCT-UNL, Caparica, Portugal.
- Winning team of ELGRA goes Suborbital call with the experiment: "Lab on Paper at Micro G: Testing paper microfluidic biosensor", 2020, European Low Gravity Research Association.
- Best poster award in "VI Annual Meeting i3N", 2017 Lisbon, Portugal.

7.6 Master thesis guidance

- Ana Samouco, Laser induced electrodes towards low-cost flexible electronics and its applications in a UV sensor, 2017, FCT-UNL (Supervisor: Prof. Elvira Fortunato);

- Mónica Machado, Laser induced/scribed graphene electrodes for all-printed transistors, 2017, FCT-UNL (Supervisor: Prof. Elvira Fortunato; co-supervisor: Prof. Luís Pereira)
- João Ferrão, Aplicação da tecnologia de baixo custo Lab-on-Paper a biossensores colorimétricos não enzimáticos para a deteção de glucose, 2017, FCT-UNL (Supervisor: Prof. Elvira Fortunato);
- Sara Silvestre, Biopolymer based microneedles patch by laser technology for biomedical applications, 2018, FCT-UNL (Supervisor: Prof. Elvira Fortunato; Co-supervisor: Prof. Maria Ascensão Reis);
- Carolina Pires, Biopolymer based hollow microneedles patch by laser technology for biomedical applications, 2018, FCT-UNL (Supervisor: Prof. Elvira Fortunato; Co-supervisor: Prof. Maria Ascensão Reis);
- Marta Pereira, Fabrication of 3D electrodes for biosensor applications, 2018, FCT-UNL and Biomark (Supervisor: Prof. Elvira Fortunato; Co-supervisor: Prof. Goreti Sales);
- Jaissica Vassantrai, Digital fabrication of metal electrodes for flexible applications, 2018, FCT-UNL (Supervisor: Prof. Elvira Fortunato; Co-supervisor: Prof. Joana Pinto);
- Tomás Fernandes, Digital fabrication of transparent electrodes for biosensor applications using spectroelectrochemical analysis, 2018, FCT-UNL and Biomark (Supervisor: Prof. Elvira Fortunato; Co-supervisor: Prof. Goreti Sales);
- Alexandra Fernandes, An electrochromic paper-based skin patch for the diagnostic of cystic fibrosis, 2018, FCT-UNL (Supervisor: Prof. Elvira Fortunato; Co-supervisor: Prof. Luís Pereira)
- Nuno Ferreira, In-situ green synthesis of silver nanoparticles into bacterial cellulose for SERS to be applied to breast cancer diagnostics, 2018, FCT-UNL and Champalimaud Foundation (Supervisor: Prof. Elvira Fortunato; Co-supervisor: Dr. Bruno Costa-Silva);
- Beatriz Pagará, Paper as a Colorimetric Biosensing Platform: the antibiotics case, 2018, FCT-UNL (Supervisor: Prof. Elvira Fortunato; Co-supervisor: Prof. Hugo Águas);
- Tomás Pinheiro, Desenvolvimento de um sensor colorimétrico, não-enzimático, para multideteção de glucose, colesterol e ácido úrico, 2018, FCT-UNL (Supervisor: Prof. Elvira Fortunato);
- Catarina Rijo, A paper-based low-cost label-free biosensing silver core-gold shell nanostructure for SERS to be applied to breast cancer diagnostics, 2018, FCT-UNL and Champalimaud Foundation (Supervisor: Prof. Elvira Fortunato; Co-supervisor: Dr. Bruno Costa-Silva);
- Pedro Spínola, Biopaper as a low-cost platform for colorimetric diagnostic tests, 2018, FCT-UNL (Supervisor: Prof. Elvira Fortunato; Co-supervisor: Prof. Ascensão Reis);

- Linda Câmara, Paper-based enzyme free platform for detecting falsified antibiotics using gold nanoparticles, 2019, FCT-UNL (Supervisor: Prof. Elvira Fortunato);
- João Tavares, Epidermal electronic skin strain sensor based on laser induced graphene, 2019, FCT-UNL (Supervisor: Prof. Elvira Fortunato; Co-supervisor: Prof. Rui Igreja);
- Laura Serrano, Bimetallic nanoparticles for highly sensitive colorimetric detection of glucose on paper, 2020, FCT-UNL (Supervisor: Prof. Elvira Fortunato);
- Maria Morais, Glucose biosensor using nano-enzymes based on ZnO nanostructures, 2021, FCT-UNL (Supervisor: Prof. Elvira Fortunato);
- Francisca Andrade, WO_3 nanoparticles as a potential biolabel for bioimaging applications, 2021, FCT-UNL (Supervisor: Prof. Elvira Fortunato).

7.7 Tutoring of Master practical/lab classes

- Class: Biosensors (courses: Master in Micro and Nanotechnologies Engineering; Master in Materials Engineering; Master in Biomedical Engineering; Master in Biochemistry)
    - Paper-based biosensors: fabrication and characterization
    - Immunoassays for biosensing
- Class: Nanofabrication and characterization of biomaterials (course: Master in Biomaterials and Nanomedicine)
    - Laser-induced graphene electrode's fabrication
- Class: Initiation to dissertation (course: Master in Micro and Nanotechnologies Engineering)
    - Reference manager software (Mendeley software)
    - SEM images editing (GIMP software)

Annex section

Table A1 Main characteristics of gold and silver-based SERS devices fabricated onto cellulose substrates. 167

Table A2 Examples of MIP-based biosensors produced by electropolymerization on planar electrodes for healthcare-related applications. 169

Table A3 Examples of MIP-based biosensors produced by electropolymerization on planar electrodes for environmental-related applications. 171

Table A4 Examples of LIG-based biosensors: characteristics and analytical features. 172

Table A5 Comparison of electrochemical features of C-SPE, G-SPE and LIG electrodes through cyclic voltammetry. 178

Table A6 Comparison of all substrate surface modification in terms of *Rct* values. 178

Figure A1 Cellulose-based substrates wettability: water contact angle measurements. 179

Figure A2 Cyclic voltammograms of AMOX and EBT solutions prepared in 0.2 M ACN. 179

Table A1 Main characteristics of gold and silver-based SERS devices fabricated onto cellulose substrates.

Nanomaterial	Cellulose format	Fabrication strategy	Analytes	LOD	EF	Author, year
AuNPs	Whatman grade 1 paper	In-situ seed-mediated growth	4-MPBA Brassinosteroids	10^{-11} M	1.13 x 10^{8}	Chen, M., 2017[316]
AuNRs	Cellulose nanofibers	Seed-mediated growth and deposition	R6G Thiram Tricyclazole Carbaryl	10 nM 1 nM 100 nM 1 μM	1.4 x 10^{7}	Kwon, G., 2019[144]
AuNSs	Filter and office paper	Ascorbic acid reduction and immersion	CV	1 nM	1.2 x 10^{7}	He, S. 2017[118]
GO-AuNRs	Whatman grade 1 paper	Seed-mediated growth reduction and layer-by-layer immersion	R6G Mitoxantrone	0.1 nM 5 μM	4.56 x 10^{7}	Ponlamuangdee, K., 2020[101]
AgNPs	Nanofibrillated cellulose paper	In-situ SILAR synthesis	RB 2-NT	1.3 x 10^{-12} M 172 x 10^{-15} M	1.46 x 10^{9}	Chen, L., 2019[276]
AgNSs	Office paper	Chemical synthesis and drop casting	R6G	11.4 ± 0.2 pg	3 x 10^{7}	Oliveira, M.J., 2017[93]
ZnONRs decorated with AgNPs	Cellulose paper	In-situ growth and thermal evaporation	R6G	8.9 ± 0.9 x 10^{-9} ng	10^{7}	Araújo, A., 2017[100]
AgNPs@SiO_2	Nanocrystalline cellulose	In-situ chemical synthesis	MG	0.9 nM	-	Ogundare, S.A., 2019[153]

Au@Ag core-shell NPs	Filter paper	Au Seed-mediated growth and Ag chemical synthesis and self-assembly	Estazolam	5 mg/l	-	Sha, X., 2020[96]
Au@Ag core-shell NPs	Nanofibrillar cellulose	Chemical synthesis	Thiram Paraquat	71 µg/l 46 µg/l	~10^4	Asgari, S., 2020[126]
Au/Ag alloy	Chromatography paper	In-situ thermal evaporation	Folic acid	1 pM	-	Park, M., 2018[95]
Ag@AuNPs	Whatman grade 1 paper	In-situ SILAR synthesis	R6G Aniline Sodium azide MG BCa progression	1 fM 1uM 10 nM 100 pM -	3.98 x 10^8	Kim, W., 2017[79]

AuNPs: Gold nanoparticles; 4-MPBA: 4 mercaptophenylboronic acid; AuNRs: Gold nanorods; R6G: Rhodamine 6G; AuNSs: Gold nanostars; CV: Crystal violet; GO: Graphene oxide; SILAR: Successive Ionic Layer Adsorption and Reaction; AgNPs: Silver nanoparticles; RB: Rhodamine B; 2-NT: 2-naphthalenethiol; AgNSs: Silver nanostars; ZnONRs: Zinc oxide nanorods; SiO_2: Silicon dioxide; MG: Malachite green; BCa: Breast cancer

Table A2 Examples of MIP-based biosensors produced by electropolymerization on planar electrodes for healthcare-related applications.

Analyte	Monomer	Type of electrode	EC readout technique	LOD	Linear range	Author, year
CA 15-3	Toluidine blue	Au-SPE	DPV	< 0.10 U/ml	0.1-1000 U/ml	Ribeiro, J.A., 2018[191]
Myoglobin	Phenol	Au-SPE	SWV	2.1 and 14 pg/ml	-	Ribeiro, J.A., 2017[193]
3-nitrotyrosine		C-SPE on office paper	DPV	22.3 nM	500 nM-1 mM	Martins, G.V., 2020[195]
Creatinine	Acrylamide	Au-SPE	EIS	0.016 ng/ml	0.1 ng/ml-1 µg/ml	Diouf, A., 2017[187]
Salivary glucose	Acrylamide/Bis-Acrylamide	Au-SPE	DPV	0.59 µg/ml	0.5-50 µg/ml	Diouf, A., 2019[197]
CEA	Gallic acid	Au-SPE	EIS	1.0 ng/ml	1-1000 ng/ml	Carneiro, M.C.C.G., 2019[192]
Cortisol	Pyrrole	C-SPE	CV	1 pM	-	Manickam P., 2017[202]
Cystatin C		C-SPE with MWCNTs	DPV	0.5 ng/ml	0.5-20 ng/ml	Gomes, R.S., 2021[198]
CA-125		Au-SPE	SWV	0.01 U/ml	0.01-500 U/ml	Rebelo, T., 2019[200]

Propofol		Au interdigitated electrodes	Discharging	0.1 μg/ml	0.1-30 μg/ml	Hong, C.-C., 2016[201]
Interleukin-6		C-SPE	EIS	0.02 pg/ml	-	Gonçalves, M.L., 2021[199]
Cardiac troponin T	Aniline	C-SPE with MWCNTs	DPV	0.04 pg/ml	0.1-8.0 pg/ml	Phonklam, K., 2020[194]
BSA	Eriochrome black T	C-SPE with PEDOT	EIS	4.95 x10^{-7} M	5 x 10^{-7}-1 x 10^{-5} M	Tavares, A.P.M., 2018[400]
Interleukin-1β		C-SPE with PEDOT	EIS	1.5 pM	60 pM-600 nM	Cardoso, A.R., 2019[402]
Amyloid β-42	o-phenylenediamine	C-SPE with PEDOT on office paper	SWV	0.1 ng/ml	0.1 ng/ml-1 μg/ml	Pereira, M.V., 2020[203]
Vascular endothelial growth factor		Graphite SPE	EIS	0.08 pg/ml	20-200 pg/ml	Bozal-Palabiyik, B., 2019[196]
Galectin-3	2-aminophenol	C-SPE	EIS	-	5 ng/ml-50 μg/ml	Cerqueira, S.M.V., 2021[430]

SPE: Screen-printed electrode; DPV: Differential pulse voltammetry; SWV: Square wave voltammetry; EIS: Electrochemical impedance spectroscopy; CEA: Carcinoembryonic antigen; CV: Cyclic voltammetry; MWCNTs: Multi-walled carbon nanotubes; BSA: Bovine serum albumin; PEDOT: Poly(3,4-ethylenedioxythiophene)

Table A3 Examples of MIP-based biosensors produced by electropolymerization on planar electrodes for environmental-related applications.

Analyte	Monomer	Type of electrode	EC readout technique	LOD	Linear range	Author, year
Chloramphenicol	Eriochrome black T	C-SPE with PEDOT	EIS	0.26 nM	1 nM – 100 μM	Cardoso, A.R., 2018[204]
Malathion	Acrylamide	Au-SPE	DPV	0.06 pg/ml	0.1 – 1000 pg/ml	Aghoutane, Y., 2020[189]
Lactose	Pyrrole	Graphite paper electrode	DPV	0.88 nM	1.0 – 10 nM and 25 – 125 nM	da Silva, J.L., 2021[205]
17 β-Estradiol	4-aminothiophenol	C-SPE with AuNPs	EIS	2 fM	10 fM – 100 nM	Truong, T.N.L., 2019[207]
Vitamin B_6	3-amino benzoic acid	Carbon filter paper electrode	EIS	0.01 μM	0.6 – 700 μM	Cherian, A.R., 2021[431]
17 β-Estradiol	Aniline and metanilic acid	SPE with WS_2	EIS	-	-	Lee, M.-, H., 2020[206]
Histamine	Aniline	Au-SPE	EIS	210 nM	500 nM – 1 mM	Serrano, V.M., 2020[432]

Table A4 Examples of LIG-based biosensors: characteristics and analytical features.

Application	Substrate	Laser wavelength	Assay method	Analytical features	Author, year
Glucose quantification	PI tape	450 nm	- Enzymatic EC assay (chitosan-GOx)	- Linear range up to 8 mM - Sensitivity: 43.15 μA/mM/cm^2 - LOD: 0.431 mM	Settu, K., 2021[244]
Glucose quantification	PI film coated with $CoCl_2$/PAA ink	10.6 μm	- Enzyme-free EC assay (Co_3O_4NPs)	- Linear range 1 μM – 9 mM - Sensitivity 214 μA/mM/cm^2 - LOD: 0.41 μM - Response time 0.49 sec	Zhao, J., 2021[245]
Sweat glucose quantification	PI film	10.6 μm	- Enzymatic EC assay (chitosan-GOx) - LIG modified with acetic acid and PtNPs	- Linear range up to 2.1 mM - Sensitivity: 4.622 μA/mM - LOD: < 300 nM	Yoon, H., 2020[433]
Glucose and pH quantification	PI film	10.6 μm	- Enzyme-free EC assay - LIG modified with PEDOT:PSS and Pt@Pd NPs (glucose) and PANI (pH)	Glucose: - Linear range: 10 μM– 9.2 mM - Sensitivity: 247 μA/mM/cm^2 - LOD: 3 μM pH: - Linear range: pH 4 – 7 * Sensitivity: 75.06 mV/pH	Zahed, M.A., 2020[246]

Glucose quantification	PI film	10.6 μm	- Enzymatic EC assay (GOx)	-	Pereira, S.O., 2021[223]
Glucose quantification	Phenolic resin	405 nm	- Enzymatic EC assay (GOx)	- Linear range: 0.1-10 mM	Zhang, Z., 2018[248]
Glucose quantification	Whatman paper	10.6 μm	- Enzymatic EC assay (GOx)	- Linear range: 0-1 mM and 1-15 mM - Sensitivity: 27.24 μA/mM and 5.42 μA/mM - LOD: 130 μM	Pinheiro, T., 2021[236]
Sweat glucose, lactate and alcohol detection	Lignin	10.6 μm	- Enzymatic EC assay - LIG doped with N and decorated with MXene/Prussian blue	Glucose - Sensitivity: 49.2 μA/mM/cm^2 - LOD: 0.3 μM Lactate: - Sensitivity: 21.6 μA/mM/cm^2 - LOD: 0.5 μM Alcohol: - Sensitivity: 5.78 μA/mM/cm^2	Lei, Y., 2020[249]
Wearable glucose quantification	PI film	10.6 μm	- Enzyme-free EC assay - LIG modified with nickel and gold layer	- Linear range: 0-30 mM - Sensitivity: 1080 μA/mM/cm^{-} (LIG foam); 3500 μA/mM/cm^2 (LIG fibers)	Zhu, J., 2021[434]

Several analytes: H_2O_2, glucose, lactate and choline	PI film	10.6 μm	- Electrochemiluminescence assay	- Linear range: 0.1-50; 0.1-70; 1-100; 1-100 μM - LOD: 4.36; 2.51; 5.32; 4.01 μM	Bhaiyya, M., 2021[247]
Pathogen detection (*E. coli* O157:H7)	PI film coated with metal precursors-chitosan hydrogel ink	-	- Impedimetric immunosensor - Interdigitated electrodes	- Linear range: 10^2 – 10^8 CFU/ml - LOD: 10^2 CFU/ml	You, Z., 2020[250]
Salmonella enterica monitoring	PI film	10.6 μm	- EC impedimetric assay	- Linear range: 25-10^5 CFU/ml - LOD: 13±7 CFU/ml	Soares, R.R.A., 2020[251]
Cancer diagnosis (CEA monitoring)	PI film	450 nm	- Label-free EC immunosensor assay - LIG modified with AuNPs	- Linear range: 0.01-100 ng/ml - LOD: 5.0 pg/.ml	Wang. G., 2021[252]
miRNA detection	PI tape	10.6 μm	- EC assay	- LOD: 10 fM	Wan. Z., 2020[242]
Skin-conformable sensing	PI film	10.6 μm	- Piezoresistive method	- GF: 40	Dallinger, A., 2020[435]
Thrombin detection	PI film	10.6 μm	- Aptamer-based capacitive assay - Interdigitated electrodes	- Linear range: 0.01 – 1000 nM - LOD: 0.12 pM	Yagati, A.K., 2020[253]
Ion sensing and pesticide monitoring	PI film	10.6 μm	- EC ion selective sensing	Ions:	Kucherenko, I.S., 2021[254]

			- Pesticide (atrazine) monitoring: Enzymatic EC assay (HRP)	- Sensitivity: 53.0 mV/dec (K^+); -56.6 mV/pH (H^+) - Response time: 10-15 sec Atrazine: - Sensitivity: 28.9 nA/μM	
Wearable pesticide (methyl parathion) monitoring in plants and crops surfaces	PI film	-	- EC assay (organophosphorus hydrolase) - LIG transferred to PDMS and modified with AuNPs	- Linear range: 20-500 μM - LOD: 0.01 μM	Zhao, F., 2020[255]
Nitrogen sensing in soil	PI tape	405 nm	- EC ion selective assay	- Linear range: 10^{-5}-10^{-1} M - Sensitivity: 51.7±7.8 mV/dec (NH_4^+); -54.8±2.5 mV/dec (NO_3^-) - LOD: 28.2±25.0 μM (NH_4^+); 20.6±14.8 μM (NO_3^-)	Garland, N.T., 2018[256]
Nitride detection	PI film	405 nm	- EC assay - LIG modified by MWCNT/AuNPs	- LOD: 6.75 μM	Nasraoui, S., 2019[257]
Lead quantification	Paperboard	10.6 μM	- EC assay	- LOD: 6 ppb - 4% repeatability - 5% reproducibility	Tasić, N., 2020[260]

Sulphites detection in commercial beverages	Paperboard	10.6 μM	- EC assay	- LOD: 1 mg/l	Martins, A.B., 2019[259]
Ascorbic acid and caffeic acid detection	Paperboard	10.6 μM	- EC assay	- Linear range: 0.91-2.86 mM	Araujo, W.R., 2017[235]
Estradiol detection	Phenolic paper	10.6 μM	- EC assay	- Linear range: 0.1-1.0 μM - Sensitivity: 1.61 A/M - LOD: 0.094 μM - LOQ: 0.313 μM	Mendes, L.F., 2020[436]
Dopamine detection	PI film	10.6 μM and 355 nm	- EC assay	- Sensitivity: 93 (10.6 μM) and 58 μM/cm^2 (355 nm)	Santos, N.F., 2021[384]
Dopamine detection	PI film	10.6 μM	- EC assay - LIG transferred to PDMS and modified with Pt-AuNPs	- Sensitivity: 865.80 μA/mM/cm^2 - LOD: 75 nM	Hui, X., 2019[437]
H_2O_2 sensing	PI film	10.6 μM	- EC assay - LIG modified with MWCNT	- Linear range: 2-12 mM - LOD: 2 mM	Settu, K., 2021[438]
H_2O_2 sensing	PI film	10.6 μM	- EC and PL assay - ZnO/LIG composites	- Linear range: 0.8-32.7 mM - LOD: 0.11 mM	Zanoni, J., 2021[439]
H_2O_2 sensing	PI film	10.6 μM	- EC assay - LIG modified with PtNPs	- Sensitivity: 248.4 μA/mM/cm^2 - LOD: 0.1 μM	Zhang, Y., 2019[440]

Biogenic amines detection in food	PI tape	405 nm	- EC assay - LIG modified with copper microparticles and diamine oxidase	- Sensitivity: 23.3 μA/mM - LOD: 11.6 μM - Response time: 7.3 sec	Vanegas, D.C., 2018[258]
Bisphenol A detection	PI film	10.6 μM	- MIP-EC assay	- Linear range: 0.05-20 μM - LOD: 8 nM	Beduk, T., 2020[264]
Cancer diagnosis (Her-2 monitoring)	PI film	10.6 μM	- MIP-EC assay - LIG modified with AuNPs	- Linear range: 1-200 ng/ml - LOD: 0.43 ng/ml	Lahcen, A.A., 2021[265]

PI: polyimide; EC: electrochemical; GOx: glucose oxidase; $CoCl_2$: cobalt chloridre; PAA: poly(amic acid); Co_3O_4NPs: cobalt oxide nanoparticles; PtNPs: platinum nanoparticles; PEDOT:PSS: poly(3,4-ethylenedioxythiophene) polystyrene sulfonate ; Pt@PdNPs: platinum@paladium nanoparticles; PANI: polyaniline; HRP: horseradish peroxidase; PDMS: poly(dimethylsiloxane); AuNPs: gold nanoparticles; MWCNT: multi-walled carbon nanotubes; PL: photoluminescence; ZnO: zinc oxide; H_2O_2: hydrogen peroxide.

Table A5 Comparison of electrochemical features of C-SPE, G-SPE and LIG electrodes through cyclic voltammetry.

Assembly steps	C-SPE				G-SPE				LIG			
	$i_{p.a.}$ (mA)	$i_{p.c.}$ (mA)	$E_{p.a.}$ (V)	$E_{p.c.}$ (V)	$i_{p.a.}$ (mA)	$i_{p.c.}$ (mA)	$E_{p.a.}$ (V)	$E_{p.c}$ (V)	$i_{p.a.}$ (mA)	$i_{p.c.}$ (mA)	$E_{p.a.}$ (V)	$E_{p.c.}$ (V)
Pre-treatment	+0.097	-0.097	+0.31	-0.090	+0.089	-0.090	+0.28	-0.06	+0.104	-0.105	+0.218	+0.011
PEDOT	+0.152	-0.154	+0.23	-0.030	+0.144	-0.145	+0.25	-0.04	+0.155	-0.154	+0.218	+0.028
MIP assembly	+0.108	-0.120	+0.26	-0.060	+0.083	-0.087	+0.26	-0.07	+0.079	-0.082	+0.320	-0.303
NIP assembly	+0.119	-0.123	+0.28	-0.060	+0.107	-0.111	+0.27	-0.06	+0.112	-0.109	+0.294	-0.002
Template removal (MIP)	+0.129	-0.141	+0.28	-0.060	+0.104	-0.104	+0.29	-0.04	+0.111	-0.109	+0.307	-0.020
Template removal (NIP)	+0.122	-0.134	+0.30	-0.090	+0.108	-0.110	+0.29	-0.05	+0.111	-0.110	+0.302	-0.010

Table A6 Comparison of all substrate surface modification in terms of *Rct* values.

Assembly steps	C-SPE	G-SPE	LIG
Pre-treatment	980	1254	13.8
PEDOT	11.7	71.4	12.5
MIP assembly	654	1210	802
NIP assembly	520	841	325
Template removal (MIP)	460	838	213
Template removal (NIP)	482	800	239

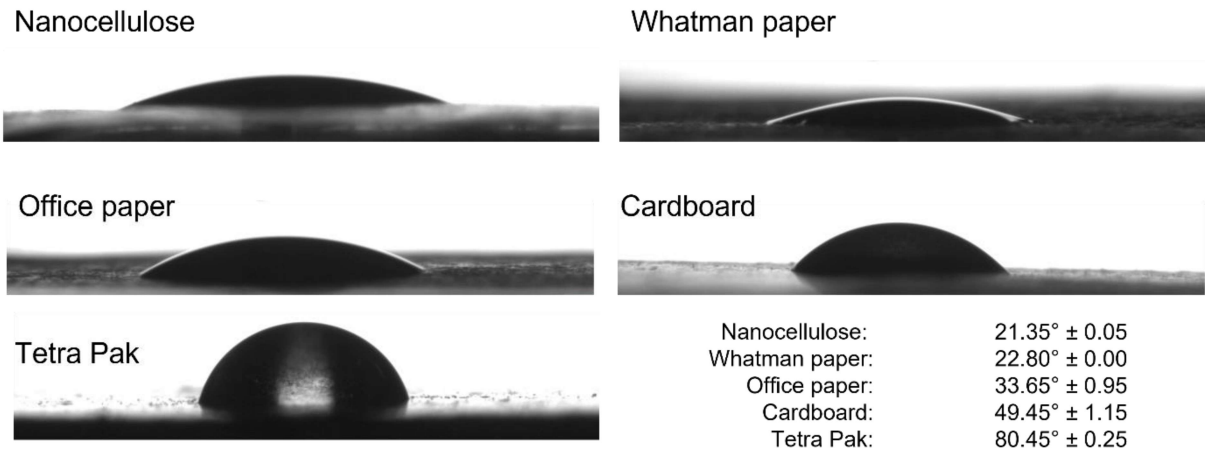

Figure A1 Cellulose-based substrates wettability: water contact angle measurements.

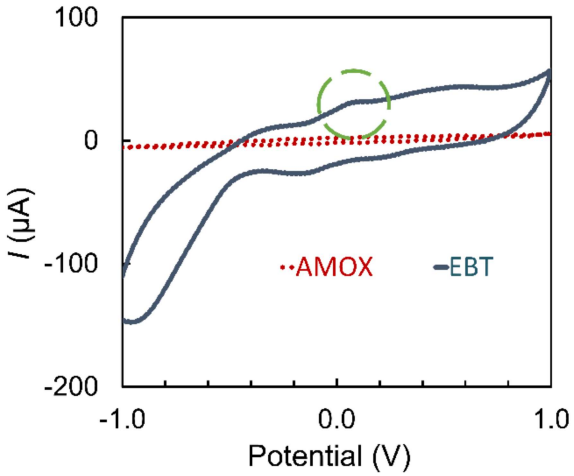

Figure A2 Cyclic voltammograms of AMOX and EBT solutions prepared in 0.2 M ACN.

References

1. World Health Organization. WHO Coronavirus Disease (COVID-19) Dashboard. https://covid19.who.int/.
2. Vigneshvar, S., Sudhakumari, C. C., Senthilkumaran, B. & Prakash, H. Recent advances in biosensor technology for potential applications - an overview. *Front. Bioeng. Biotechnol.* **4**, 1–9 (2016).
3. Mukherji, S. & Mondal, D. 5 - Lab-on-chip (LOC) devices for point of care (POC) applications. *Med. Biosens. Point Care Appl.* 99–131 (2017) doi:10.1016/B978-0-08-100072-4.00005-8.
4. Marques, A. C. *et al. Non-enzymatic lab-on-paper devices for biosensing applications*. *Comprehensive Analytical Chemistry* vol. 89 (Elsevier B.V., 2020).
5. Clark, L. C. & Lyons, C. Electrode systems for continuous monitoring in cardiovascular surgery. *Ann. N. Y. Acad. Sci.* **102**, 29–45 (1962).
6. Grand View Research. *Biosensors Market Size*. (2020).
7. Farré, M., Kantiani, L. & Barceló, D. Microfluidic Devices: Biosensors. in *Chemical Analysis of Food: Techniques and Applications* 177–217 (Elsevier, 2012). doi:10.1016/B978-0-12-384862-8.00007-8.
8. Naresh, V. & Lee, N. A review on biosensors and recent development of nanostructured materials-enabled biosensors. *Sensors (Switzerland)* **21**, 1–35 (2021).
9. Bohunicky, B. & Mousa, S. A. Biosensors: The new wave in cancer diagnosis. *Nanotechnol. Sci. Appl.* **4**, 1–10 (2011).
10. Trojanowicz, M. Impact of nanotechnology on design of advanced screen-printed electrodes for different analytical applications. *TrAC - Trends Anal. Chem.* **84**, 22–47 (2016).
11. Feynman, R. P. There's plenty of room at the bottom. *Eng. Sci.* **23**, 22–36 (1960).
12. Taniguchi, N., Arakawa, C. & Kobayashi, T. On the basic concept of nano-technology. *Proc. Int. Conf. Prod. Eng.* (1974).
13. nano.gov. National Nanotechnology Initiative (NNI). www.nano.gov.
14. Bayda, S., Adeel, M., Tuccinardi, T., Cordani, M. & Rizzolio, F. The History of Nanoscience and Nanotechnology: From Chemical–Physical Applications to Nanomedicine. *Molecules* **25**, 112 (2019).
15. Nasrollahzadeh, M., Sajadi, S. M., Sajjadi, M. & Issaabadi, Z. Applications of Nanotechnology in Daily Life. in *An Introduction to Green Nanotechnology* 113–143 (2019). doi:10.1016/B978-0-12-813586-0.00004-3.
16. Goswami, S. *et al.* Green Nanotechnology from Waste Carbon–Polyaniline Composite: Generation of Wavelength-Independent Multiband Photoluminescence for Sensitive Ion Detection. *Adv. Sustain. Syst.* 1700137--n/a doi:10.1002/adsu.201700137.
17. Marques, A. C. *et al.* Office Paper Platform for Bioelectrochromic Detection of Electrochemically Active Bacteria using Tungsten Trioxide Nanoprobes. *Sci. Rep.* **5**, 9910 (2015).
18. Gonçalves, A. *et al.* Smart optically active VO2 nanostructured layers applied in roof-type ceramic tiles for energy efficiency. *Sol. Energy Mater. Sol. Cells* **150**, 1–9 (2016).
19. Marques, A. C. *et al.* Paper-Based SERS Platform for One-Step Screening of Tetracycline in Milk. *Sci. Rep.* **9**, 17922 (2019).
20. Ferreira, N. *et al.* Label-Free Nanosensing Platform for Breast Cancer Exosome Profiling. *ACS Sensors* **4**, 2073–2083 (2019).
21. Pimentel, A. *et al.* Microwave Synthesized ZnO Nanorod Arrays for UV Sensors: A Seed Layer Annealing Temperature Study. *Materials (Basel).* **9**, 299 (2016).
22. Almeida, M. P. *et al.* Gold Nanoparticles in Analytical Chemistry. in *Gold Nanoparticles in Analytical Chemistry* 529–567 (Elsevier B.V., 2014).
23. Carpenter, A. C., Paulsen, I. T. & Williams, T. C. Blueprints for biosensors: Design, limitations,

and applications. *Genes (Basel).* **9**, (2018).
24. Águas, H., Fortunato, E., Igreja, R., Martins, R. & Oliva, A. Biosensors and Diagnostic Tests. in *From Life Moleculues to Global Health* (Principia, 2021).
25. Bhalla, N., Jolly, P., Formisano, N. & Estrela, P. Introduction to biosensors. *Essays Biochem.* **60**, 1–8 (2016).
26. Thévenot, D. R., Toth, K., Durst, R. A. & Wilson, G. S. Electrochemical biosensors: recommended definitions and classification1International Union of Pure and Applied Chemistry: Physical Chemistry Division, Commission I.7 (Biophysical Chemistry); Analytical Chemistry Division, Commission V.5 (Electroanalytical. *Biosens. Bioelectron.* **16**, 121–131 (2001).
27. Vasan, A. S. S., Doraiswami, R., Mahadeo, D. M., Huang, Y. & Pecht, M. Point-of-Care Biosensor Systems. *Front Biosci* **1**, 39–71 (2013).
28. Zhang, X., Guo, Q. & Cui, D. Recent Advances in Nanotechnology Applied to Biosensors. *Sensors* **9**, 1033–1053 (2009).
29. Suaifan, G. A. R. Y., Alhogail, S. & Zourob, M. Paper-based magnetic nanoparticle-peptide probe for rapid and quantitative colorimetric detection of Escherichia coli O157:H7. *Biosens. Bioelectron.* **92**, 702–708 (2017).
30. Badawy, M. E. I. & El-Aswad, A. F. Bioactive Paper Sensor Based on the Acetylcholinesterase for the Rapid Detection of Organophosphate and Carbamate Pesticides. *Int. J. Anal. Chem.* **2014**, 1–8 (2014).
31. Oktem, H. A., Senyurt, O., Eyidogan, F. I., Bayrac, C. & Yilmaz, R. Development of a laccase based paper biosensor for the detection of phenolic compounds. *J. Food, Agric. Environ.* **10**, 1030–1034 (2012).
32. Zhou, Q. *et al.* Development of an aptasensor for electrochemical detection of exosomes. *Methods* **97**, 88–93 (2016).
33. Veigas, B. *et al.* Gold on paper-paper platform for Au-nanoprobe TB detection. *Lab Chip* **12**, 4802–8 (2012).
34. Costa, M. N. *et al.* A low cost, safe, disposable, rapid and self-sustainable paper-based platform for diagnostic testing: lab-on-paper. *Nanotechnology* **25**, 094006 (2014).
35. Cardoso, A. R. *et al.* Molecularly-imprinted chloramphenicol sensor with laser-induced graphene electrodes. *Biosens. Bioelectron.* **124–125**, 167–175 (2019).
36. Chang, I. S., Moon, H., Jang, J. K. & Kim, B. H. Improvement of a microbial fuel cell performance as a BOD sensor using respiratory inhibitors. *Biosens. Bioelectron.* **20**, 1856–1859 (2005).
37. Hossain, S. M. Z., Luckham, R. E., McFadden, M. J. & Brennan, J. D. Reagentless bidirectional lateral flow bioactive paper sensors for detection of pesticides in beverage and food samples. *Anal. Chem.* **81**, 9055–9064 (2009).
38. Mehrotra, P. Biosensors and their applications – A review. *J. Oral Biol. Craniofacial Res.* **6**, 1–7 (2016).
39. Mabey, D., Peeling, R. W., Ustianowski, A. & Perkins, M. D. Diagnostics for the developing world. *Nat. Rev. Microbiol.* **2**, 231–240 (2004).
40. Land, K. J., Boeras, D. I., Chen, X.-S., Ramsay, A. R. & Peeling, R. W. REASSURED diagnostics to inform disease control strategies, strengthen health systems and improve patient outcomes. *Nat. Microbiol.* **4**, 46–54 (2019).
41. Grieshaber, D., MacKenzie, R., Vörös, J. & Reimhult, E. Electrochemical biosensors - Sensor principles and architectures. *Sensors* **8**, 1400–1458 (2008).
42. Hamid, M. & Khalil-ur-Rehman. Potential applications of peroxidases. *Food Chem.* **115**, 1177–1186 (2009).
43. Ali, M. *et al.* Paper-based selective and quantitative detection of uric acid using citrate-capped Pt nanoparticles (PtNPs) as a colorimetric sensing probe through a simple and remote-based device. *New J. Chem.* **43**, 7636–7645 (2019).
44. Huang, Z., Nagpal, A., Siddhanta, S. & Barman, I. Leveraging coffee-ring effect on plasmonic paper substrate for sensitive analyte detection using Raman spectroscopy. *J. Raman Spectrosc.*

49, 1552–1558 (2018).
45. Blanco-Formoso, M. & Alvarez-Puebla, R. A. Cancer Diagnosis through SERS and Other Related Techniques. *Int. J. Mol. Sci.* **21**, (2020).
46. Xian, L. *et al.* Surface-modified paper-based SERS substrates for direct-droplet quantitative determination of trace substances. *Cellulose* **27**, 1483–1495 (2020).
47. Yamada, K., Henares, T. G., Suzuki, K. & Citterio, D. Distance-Based Tear Lactoferrin Assay on Microfluidic Paper Device Using Interfacial Interactions on Surface-Modified Cellulose. *ACS Appl. Mater. Interfaces* **7**, 24864–24875 (2015).
48. Kumar, S., Bhushan, P. & Bhattacharya, S. Positively Charged Silver Nanoparticles as Labels for Paper-Based Colorimetric Detection of Heparin. in *2nd International Conference for Innovation in Biomedical Engineering and Life Sciences* 235–240 (2018). doi:10.1007/978-981-10-7554-4_41.
49. Pinheiro, T. Multiplex, Enzyme-free, Colorimetric Paper-based Device for the Measurement of Glucose, Uric Acid and Cholesterol. (NOVA University of Lisbon, 2018).
50. Pinheiro, T., Marques, A. C., Carvalho, P., Martins, R. & Fortunato, E. Paper microfluidics and tailored gold nanoparticles for nonenzymatic, colorimetric multiplex biomarker detection. *ACS Appl. Mater. Interfaces* **13**, 3576–3590 (2021).
51. Qiu, H. W. *et al.* A novel surface-enhanced Raman spectroscopy substrate based on hybrid structure of monolayer graphene and Cu nanoparticles for adenosine detection. *Appl. Surf. Sci.* **332**, 614–619 (2015).
52. Park, J. *et al.* Exosome Classification by Pattern Analysis of Surface-Enhanced Raman Spectroscopy Data for Lung Cancer Diagnosis. *Anal. Chem.* **89**, 6695–6701 (2017).
53. Xu, W., Wang, D., Li, D. & Liu, C. C. Recent Developments of Electrochemical and Optical Biosensors for Antibody Detection. (2020).
54. Shandilya, R. *et al.* Nanobiosensors: Point-of-care approaches for cancer diagnostics. *Biosens. Bioelectron.* **130**, 147–165 (2019).
55. Sur, U. K. Surface-Enhanced Raman Scattering. *Raman Spectrosc. Appl.* **27**, 241–250 (2017).
56. Ogundare, S. A. & van Zyl, W. E. A review of cellulose-based substrates for SERS: fundamentals, design principles, applications. *Cellulose* **26**, 6489–6528 (2019).
57. Fateixa, S., Nogueira, H. I. S. & Trindade, T. Hybrid nanostructures for SERS: Materials development and chemical detection. *Phys. Chem. Chem. Phys.* **17**, 21046–21071 (2015).
58. Smekal, A. Zur Quantentheorie der Streuung und Dispersion. *Naturwissenschaften* **16**, 612–613 (1923).
59. Raman, C. V & Krishnan, K. S. A New Type of Secondary Irradiation. *Nature* 501–502 (1928).
60. Raman, C. V. A new radiation. *Indian J. Phys.* **2**, 387–398 (1928).
61. The Nobel Prize in Physics 1930. *NobelPrize.org* https://www.nobelprize.org/prizes/physics/1930/summary/.
62. Indian Academy of Sciences. *C V Raman – A pictorial biography*. (1988).
63. American Chemical Society. American Chemical Society International Historic Chemical Landmarks. The Raman Effect. http://portal.acs.org/portal/PublicWebSite/education/%0Awhatischemistry/landmarks/ramaneffect/index.htm (1998).
64. Kumar, S., Kumar, P., Das, A. & Shakher Pathak, C. Surface-Enhanced Raman Scattering: Introduction and Applications. in *Recent Advances in Nanophotonics - Fundamentals and Applications* (IntechOpen, 2020). doi:10.5772/intechopen.92614.
65. Le Ru, E. & Etchegoin, P. *Principles of Surface Enhanced Raman Spectroscopy and related plasmonic effects*. (Elsevier, 2009).
66. Shvalya, V., Filipič, G., Zavašnik, J., Abdulhalim, I. & Cvelbar, U. Surface-enhanced Raman spectroscopy for chemical and biological sensing using nanoplasmonics: The relevance of interparticle spacing and surface morphology. *Appl. Phys. Rev.* **7**, 031307 (2020).
67. Mosca, S., Conti, C., Stone, N. & Matousek, P. Spatially offset Raman spectroscopy. *Nat. Rev. Methods Prim.* **1**, 21 (2021).

68. Huang, C. C., Cheng, C. Y. & Lai, Y. S. Paper-based flexible surface enhanced Raman scattering platforms and their applications to food safety. *Trends Food Sci. Technol.* **100**, 349–358 (2020).
69. Fleischmann, M., Hendra, P. J. & McQuillan, A. J. Raman spectra of pyridine adsorbed at a silver electrode. *Chem. Phys. Lett.* **26**, 163–166 (1974).
70. Jeanmaire, D. L. & Van Duyne, R. P. Surface raman spectroelectrochemistry. Part I. Heterocyclic, aromatic, and aliphatic amines adsorbed on the anodized silver electrode. *J. Electroanal. Chem.* **84**, 1–20 (1977).
71. Creighton, A. J. & Albrecht, G. M. Anomalously intense Raman spectra of pyridine at a silver electrode. *J. Am. Chem. Soc.* **99**, 5215 (1977).
72. Campion, A. & Kambhampati, P. Surface-enhanced Raman scattering. *Chem. Soc. Rev.* **27**, 241 (1998).
73. Moskovits, M. Surface-enhanced spectroscopy. *Rev. Mod. Phys.* **57**, 783–826 (1985).
74. Kambhampati, P., Child, C. M., Foster, M. C. & Campion, A. On the chemical mechanism of surface enhanced Raman scattering: Experiment and theory. *J. Chem. Phys.* **108**, 5013–5026 (1998).
75. Stiles, P. L., Dieringer, J. A., Shah, N. C. & Van Duyne, R. P. Surface-Enhanced Raman Spectroscopy. *Annu. Rev. Anal. Chem.* **1**, 601–626 (2008).
76. Jensen, L., Aikens, C. M. & Schatz, G. C. Electronic structure methods for studying surface-enhanced Raman scattering. *Chem. Soc. Rev.* **37**, 1061 (2008).
77. Lis, D. & Cecchet, F. Localized surface plasmon resonances in nanostructures to enhance nonlinear vibrational spectroscopies: towards an astonishing molecular sensitivity. *Beilstein J. Nanotechnol.* **5**, 2275–2292 (2014).
78. Sanguansap, Y., Karn-orachai, K. & Laocharoensuk, R. Tailor-made porous striped gold-silver nanowires for surface enhanced Raman scattering based trace detection of β-hydroxybutyric acid. *Appl. Surf. Sci.* **500**, (2020).
79. Kim, W. *et al.* Low-Cost Label-Free Biosensing Bimetallic Cellulose Strip with SILAR-Synthesized Silver Core-Gold Shell Nanoparticle Structures. *Anal. Chem.* **89**, 6448–6454 (2017).
80. Kim, W., Kim, Y. H., Park, H. K. & Choi, S. Facile Fabrication of a Silver Nanoparticle Immersed, Surface-Enhanced Raman Scattering Imposed Paper Platform through Successive Ionic Layer Absorption and Reaction for On-Site Bioassays. *ACS Appl. Mater. Interfaces* **7**, 27910–27917 (2015).
81. Ngo, Y. H., Li, D., Simon, G. P. & Garnier, G. Gold nanoparticle-paper as a three-dimensional surface enhanced raman scattering substrate. *Langmuir* **28**, 8782–8790 (2012).
82. Suntornsuk, W. & Suntornsuk, L. Recent applications of paper-based point-of-care devices for biomarker detection. *Electrophoresis* **41**, 287–305 (2020).
83. Tomazelli Coltro, W. K., Cheng, C. M., Carrilho, E. & de Jesus, D. P. Recent advances in low-cost microfluidic platforms for diagnostic applications. *Electrophoresis* **35**, 2309–2324 (2014).
84. Ozer, T., McMahon, C. & Henry, C. S. Advances in Paper-Based Analytical Devices. *Annu. Rev. Anal. Chem.* **13**, 061318–114845 (2020).
85. Vicente, A. T. *et al.* Optoelectronics and Bio Devices on Paper Powered by Solar Cells. in *Nanostructured Solar Cells* 33–65 (InTech, 2017). doi:10.5772/66695.
86. B. Pinto, R. J., C., M., Pascoal, C. & Trindade, T. Composites of Cellulose and Metal Nanoparticles. in *Nanocomposites - New Trends and Developments* (ed. Ebrahimi, F.) (InTechOpen, 2012). doi:10.5772/50553.
87. Vo-Dinh, T., Hiromoto, M. Y. K., Begun, G. M. & Moody, R. L. Surface-enhanced Raman spectrometry for trace organic analysis. *Anal. Chem.* **56**, 1667–1670 (1984).
88. Tran, C. D. Subnanogram detection of dyes on filter paper by surface-enhanced Raman scattering spectrometry. *Anal. Chem.* **56**, 824–826 (1984).
89. Meng, Y., Lai, Y., Jiang, X., Zhao, Q. & Zhan, J. Silver nanoparticles decorated filter paper via self-sacrificing reduction for membrane extraction surface-enhanced Raman spectroscopy detection. *Analyst* **138**, 2090–2095 (2013).

90. Lu, Y. *et al.* Ag-coated cellulose fibers as Surface-enhanced Raman scattering substrates for adsorptive detection of malachite green. *Materials (Basel).* **11**, (2018).
91. Martins, N. C. T., Fateixa, S., Fernandes, T., Nogueira, H. I. S. & Trindade, T. Inkjet Printing of Ag and Polystyrene Nanoparticle Emulsions for the One-Step Fabrication of Hydrophobic Paper-Based Surface-Enhanced Raman Scattering Substrates. *ACS Appl. Nano Mater.* **4**, 4484–4495 (2021).
92. Marques, P. A. A. P., Nogueira, H. I. S., Pinto, R. J. B., Neto, C. P. & Trindade, T. Silver-bacterial cellulosic sponges as active SERS substrates. *J. Raman Spectrosc.* **39**, 439–443 (2008).
93. Oliveira, M. J. *et al.* Office paper decorated with silver nanostars-an alternative cost effective platform for trace analyte detection by SERS. *Sci. Rep.* **7**, 2480 (2017).
94. Lartey, J. A. *et al.* Sandwiching analytes with structurally diverse plasmonic nanoparticles on paper substrates for surface enhanced Raman spectroscopy. *RSC Adv.* **9**, 32535–32543 (2019).
95. Park, M., Hwang, C. S. H. & Jeong, K. H. Nanoplasmonic Alloy of Au/Ag Nanocomposites on Paper Substrate for Biosensing Applications. *ACS Appl. Mater. Interfaces* **10**, 290–295 (2018).
96. Sha, X. *et al.* A rapid detection method for on-site screening of estazolam in beverages with Au@Ag core-shell nanoparticles paper-based SERS substrate. *Anal. Sci.* **36**, 667–674 (2020).
97. Kim, W. *et al.* Paper-Based Surface-Enhanced Raman Spectroscopy for Diagnosing Prenatal Diseases in Women. *ACS Nano* **12**, 7100–7108 (2018).
98. Kang, S., Rahman, A., Boeding, E. & Vikesland, P. J. Synthesis and SERS application of gold and iron oxide functionalized bacterial cellulose nanocrystals (Au@Fe3O4@BCNCs). *Analyst* **145**, 4358–4368 (2020).
99. Mekonnen, M. L., Su, W. N., Chen, C. H. & Hwang, B. J. Ag@SiO2 nanocube loaded miniaturized filter paper as a hybrid flexible plasmonic SERS substrate for trace melamine detection. *Anal. Methods* **9**, 6823–6829 (2017).
100. Araújo, A. *et al.* Direct growth of plasmonic nanorod forests on paper substrates for low-cost flexible 3D SERS platforms. *Flex. Print. Electron.* **2**, (2017).
101. Ponlamuangdee, K., Hornyak, G. L., Bora, T. & Bamrungsap, S. Graphene oxide/gold nanorod plasmonic paper – a simple and cost-effective SERS substrate for anticancer drug analysis. *New J. Chem.* **44**, 14087–14094 (2020).
102. Pan, X. *et al.* A graphene oxide-gold nanostar hybrid based-paper biosensor for label-free SERS detection of serum bilirubin for diagnosis of jaundice. *Biosens. Bioelectron.* **145**, (2019).
103. Bharadwaj, S., Pandey, A., Yagci, B., Ozguz, V. & Qureshi, A. Graphene nano-mesh-Ag-ZnO hybrid paper for sensitive SERS sensing and self-cleaning of organic pollutants. *Chem. Eng. J.* **336**, 445–455 (2018).
104. Yang, C. *et al.* Multifunctional paper strip based on GO-veiled Ag nanoparticles with highly SERS sensitive and deliverable properties for high-performance molecular detection. *Opt. Express* **26**, 10023 (2018).
105. Chen, M., Yang, H., Rong, L. & Chen, X. A gas-diffusion microfluidic paper-based analytical device (μPAD) coupled with portable surface-enhanced Raman scattering (SERS): Facile determination of sulphite in wines. *Analyst* **141**, 5511–5519 (2016).
106. Lan, L., Hou, X., Gao, Y., Fan, X. & Qiu, T. Inkjet-printed paper-based semiconducting substrates for surface-enhanced Raman spectroscopy. *Nanotechnology* **31**, (2020).
107. Kim, D. *et al.* 2,2,6,6-Tetramethylpiperidine-1-oxy-Oxidized Cellulose Nanofiber-Based Nanocomposite Papers for Facile in Situ Surface-Enhanced Raman Scattering Detection. *ACS Sustain. Chem. Eng.* **7**, 15640–15647 (2019).
108. Liou, P., Nayigiziki, F. X., Kong, F., Mustapha, A. & Lin, M. Cellulose nanofibers coated with silver nanoparticles as a SERS platform for detection of pesticides in apples. *Carbohydr. Polym.* **157**, 643–650 (2017).
109. Oliveira, M. J. *et al.* Reusable and highly sensitive SERS immunoassay utilizing gold nanostars and a cellulose hydrogel-based platform. *J. Mater. Chem. B* (2021) doi:10.1039/D1TB01404H.
110. Peinado, H., Lavotshkin, S. & Lyden, D. The secreted factors responsible for pre-metastatic niche

formation: Old sayings and new thoughts. *Semin. Cancer Biol.* **21**, 139–146 (2011).
111. Selwyna, P. G. C., Loganathan, P. R. & Begam, K. H. Development of electrochemical biosensor for breast cancer detection using gold nanoparticle doped CA 15-3 antibody and antigen interaction. *Int. Conf. Signal Process. Image Process. Pattern Recognit. 2013, ICSIPR 2013* **1**, 1–7 (2013).
112. Hu, S. W. *et al.* A paper-based SERS test strip for quantitative detection of Mucin-1 in whole blood. *Talanta* **179**, 9–14 (2018).
113. Villa, J. E. L., Pasquini, C. & Poppi, R. J. Surface-enhanced Raman spectroscopy and MCR-ALS for the selective sensing of urinary adenosine on filter paper. *Talanta* **187**, 99–105 (2018).
114. Urinary nucleosides as biomarkers of breast, colon, lung, and gastric cancer in Taiwanese. *PLoS One* (2013).
115. Turkevich, J., Stevenson, P. C. & Hillier, J. A study of the nucleation and growth processes in the synthesis of colloidal gold. *Discuss. Faraday Soc.* **11**, 55–75 (1951).
116. Díaz-Liñán, M. C., García-Valverde, M. T., López-Lorente, A. I., Cárdenas, S. & Lucena, R. Silver nanoflower-coated paper as dual substrate for surface-enhanced Raman spectroscopy and ambient pressure mass spectrometry analysis. *Anal. Bioanal. Chem.* **412**, 3547–3557 (2020).
117. Reokrungruang, P., Chatnuntawech, I., Dharakul, T. & Bamrungsap, S. A simple paper-based surface enhanced Raman scattering (SERS) platform and magnetic separation for cancer screening. *Sensors Actuators, B Chem.* **285**, 462–469 (2019).
118. He, S., Chua, J., Tan, E. K. M. & Kah, J. C. Y. Optimizing the SERS enhancement of a facile gold nanostar immobilized paper-based SERS substrate. *RSC Adv.* **7**, 16264–16272 (2017).
119. Liu, Q. *et al.* Paper-based plasmonic platform for sensitive, noninvasive, and rapid cancer screening. *Biosens. Bioelectron.* **54**, 128–134 (2014).
120. Xu, Y. *et al.* Synthesis of the 3D AgNF/AgNP arrays for the paper-based surface enhancement Raman scattering application. *Sensors Actuators, B Chem.* **265**, 302–309 (2018).
121. Lu, D. *et al.* SERS spectroscopy using Au-Ag nanoshuttles and hydrophobic paper-based Au nanoflower substrate for simultaneous detection of dual cervical cancer–associated serum biomarkers. *Anal. Bioanal. Chem.* (2020) doi:10.1007/s00216-020-02843-x.
122. Lim, W. Y., Goh, C. H., Thevarajah, T. M., Goh, B. T. & Khor, S. M. Using SERS-based microfluidic paper-based device (μPAD) for calibration-free quantitative measurement of AMI cardiac biomarkers. *Biosens. Bioelectron.* **147**, (2020).
123. Berger, A. G., Restaino, S. M. & White, I. M. Vertical-flow paper SERS system for therapeutic drug monitoring of flucytosine in serum. *Anal. Chim. Acta* **949**, 59–66 (2017).
124. Ahn, Y. J., Gil, Y. G., Lee, Y. J., Jang, H. & Lee, G. J. A dual-mode colorimetric and SERS detection of hydrogen sulfide in live prostate cancer cells using a silver nanoplate-coated paper assay. *Microchem. J.* **155**, 104724 (2020).
125. Sivashanmugan, K. *et al.* Bimetallic nanoplasmonic gap-mode SERS substrate for lung normal and cancer-derived exosomes detection. *J. Taiwan Inst. Chem. Eng.* **80**, 149–155 (2017).
126. Asgari, S. *et al.* Nanofibrillar cellulose/Au@Ag nanoparticle nanocomposite as a SERS substrate for detection of paraquat and thiram in lettuce. *Microchim. Acta* **187**, (2020).
127. Rijo, C. A paper-based low-cost label-free biosensing silver core-gold shell nanostructure for SERS to be applied to breast cancer diagnostics. (NOVA University of Lisbon, 2018).
128. Mc Namara, K., Alzubaidi, H. & Jackson, J. K. Cardiovascular disease as a leading cause of death: how are pharmacists getting involved? *Integr. Pharm. Res. Pract.* **8**, 1–11 (2019).
129. Mabbott, S. *et al.* Detection of cardiovascular disease associated miR-29a using paper-based microfluidics and surface enhanced Raman scattering. *Analyst* **145**, 983–991 (2020).
130. Yokoyama, M. *et al.* Feasibility study of paper-based surface enhanced Raman spectroscopy of tear fluids for onsite therapeutic drug monitoring. in *World Automation Congress Proceedings* 474–477 (2014). doi:10.1109/WAC.2014.6936005.
131. Yokoyama, M. *et al.* Paper-basd surface enhanced Raman spectroscopy of pnenobarbital sodium for point-of-care therapeutic drug monitoring. in *Optical Diagnostics and Sensing XV: Toward*

Point-of-Care Diagnostics (ed. Cote, GL) vol. 9332 933210 (2015).
132. Locke, A. K., Coté, G. L. & Deutz, N. E. P. Development of a paper-based vertical flow SERS assay for citrulline detection using aptamer-conjugated gold nanoparticles. in *OPTICAL DIAGNOSTICS AND SENSING XVIII: TOWARD POINT-OF-CARE DIAGNOSTICS* (ed. Cote, GL) vol. 10501 4 (2018).
133. Villa, J. E. L. & Poppi, R. J. A portable SERS method for the determination of uric acid using a paper-based substrate and multivariate curve resolution. *Analyst* **141**, 1966–1972 (2016).
134. Kim, W. S., Shin, J. H., Park, H. K. & Choi, S. A low-cost, monometallic, surface-enhanced Raman scattering-functionalized paper platform for spot-on bioassays. *Sensors Actuators, B Chem.* **222**, 1112–1118 (2016).
135. Zou, Y. *et al.* Portable and Label-Free Detection of Blood Bilirubin with Graphene-Isolated-Au-Nanocrystals Paper Strip. *Anal. Chem.* **90**, 13687–13694 (2018).
136. Chamuah, N., Hazarika, A., Hatiboruah, D. & Nath, P. SERS on paper: An extremely low cost technique to measure Raman signal. *J. Phys. D. Appl. Phys.* **50**, (2017).
137. Lu, D., Deng, Z., Xia, J. & Cao, X. SERS immunoassay for detection of procalcitonion in serum from patients with premature rupture of membranes using hollow Au nanocages and Ag nanowires-decorated filter paper. *Vib. Spectrosc.* **104**, (2019).
138. Russo, L. *et al.* Detection of resistance protein A (MxA) in paper-based immunoassays with surface enhanced Raman spectroscopy with AuAg nanoshells. *Nanoscale* **11**, 10819–10827 (2019).
139. Mebdoua, S. Pesticide Residues in Fruits and Vegetables. in *Bioactive Molecules in Food* (eds. Mérillon, J. & Ramawat, K.) 1–39 (Springer, Cham, 2018). doi:10.1007/978-3-319-54528-8_76-1.
140. Monitoring of Pesticide Residues in Commonly Used Fruits and Vegetables in Kuwait. *Int. J. Environ. Res. Public Health* **14**, 833 (2017).
141. Okocha, R. C., Olatoye, I. O. & Adedeji, O. B. Food safety impacts of antimicrobial use and their residues in aquaculture. *Public Health Rev.* **39**, 21 (2018).
142. Rai, P. K., Lee, S. S., Zhang, M., Tsang, Y. F. & Kim, K.-H. Heavy metals in food crops: Health risks, fate, mechanisms, and management. *Environ. Int.* **125**, 365–385 (2019).
143. Xiong, Z., Lin, M., Lin, H. & Huang, M. Facile synthesis of cellulose nanofiber nanocomposite as a SERS substrate for detection of thiram in juice. *Carbohydr. Polym.* **189**, 79–86 (2018).
144. Kwon, G. *et al.* Nanoporous cellulose paper-based SERS platform for multiplex detection of hazardous pesticides. *Cellulose* **26**, 4935–4944 (2019).
145. Yang, G. *et al.* Fabrication of paper-based SERS substrates by spraying silver and gold nanoparticles for SERS determination of malachite green, methylene blue, and crystal violet in fish. *Microchim. Acta* **187**, (2020).
146. Luo, W. *et al.* In situ synthesis of gold nanoparticles on pseudo-paper films as flexible SERS substrate for sensitive detection of surface organic residues. *Talanta* **197**, 225–233 (2019).
147. Godoy, N. V. *et al.* Ultrasensitive inkjet-printed based SERS sensor combining a high-performance gold nanosphere ink and hydrophobic paper. *Sensors Actuators, B Chem.* **320**, (2020).
148. Lee, D. J. & Kim, D. Y. Hydrophobic paper-based SERS sensor using gold nanoparticles arranged on graphene oxide flakes. *Sensors (Switzerland)* **19**, (2019).
149. Zhu, Y., Li, M., Yu, D. & Yang, L. A novel paper rag as 'D-SERS' substrate for detection of pesticide residues at various peels. *Talanta* **128**, 117–124 (2014).
150. Ma, Y. *et al.* Rapid and sensitive on-site detection of pesticide residues in fruits and vegetables using screen-printed paper-based SERS swabs. *Anal. Methods* **10**, 4655–4664 (2018).
151. Sun, M. *et al.* Performance enhancement of paper-based SERS chips by shell-isolated nanoparticle-enhanced Raman spectroscopy. *J. Mater. Sci. Technol.* **35**, 2207–2212 (2019).
152. Lin, X. *et al.* Lab-on-paper surface-enhanced Raman spectroscopy platform based on self-assembled Au@Ag nanocube monolayer for on-site detection of thiram in soil. *J. Raman Spectrosc.* **50**, 916–925 (2019).
153. Ogundare, S. A. & van Zyl, W. E. Amplification of SERS "hot spots" by silica clustering in a

silver-nanoparticle/nanocrystalline-cellulose sensor applied in malachite green detection. *Colloids Surfaces A Physicochem. Eng. Asp.* **570**, 156–164 (2019).
154. Yu, Q. *et al.* Multi-functional regenerated cellulose fibers decorated with plasmonic Au nanoparticles for colorimetry and SERS assays. *Cellulose* **25**, 6041–6053 (2018).
155. Zhu, Y., Zhang, L. & Yang, L. Designing of the functional paper-based surface-enhanced Raman spectroscopy substrates for colorants detection. *Mater. Res. Bull.* **63**, 199–204 (2015).
156. Purwidyantri, A. *et al.* Facile Bacterial Cellulose Nanofibrillation for the Development of a Plasmonic Paper Sensor. *ACS Biomater. Sci. Eng.* **6**, 3122–3131 (2020).
157. Zhang, L., Liu, J., Zhou, G. & Zhang, Z. Controllable in-situ growth of silver nanoparticles on filter paper for flexible and highly sensitive sers sensors for malachite green residue detection. *Nanomaterials* **10**, (2020).
158. Gu, J. & Dichiara, A. Hybridization between cellulose nanofibrils and faceted silver nanoparticles used with surface enhanced Raman scattering for trace dye detection. *Int. J. Biol. Macromol.* **143**, 85–92 (2020).
159. Das, D., Senapati, S. & Nanda, K. K. 'rinse, Repeat': An Efficient and Reusable SERS and Catalytic Platform Fabricated by Controlled Deposition of Silver Nanoparticles on Cellulose Paper. *ACS Sustain. Chem. Eng.* **7**, 14089–14101 (2019).
160. Kumar, A. & Santhanam, V. Paper swab based SERS detection of non-permitted colourants from dals and vegetables using a portable spectrometer. *Anal. Chim. Acta* **1090**, 106–113 (2019).
161. Deng, D. *et al.* Rapid detection of malachite green residues in fish using a surface-enhanced Raman scattering-active glass fiber paper prepared by in situ reduction method. *Talanta* **200**, 272–278 (2019).
162. Zhang, W. *et al.* Brushing, a simple way to fabricate SERS active paper substrates. *Anal. Methods* **6**, 2066–2071 (2014).
163. Xiong, Z. *et al.* Development of nanofibrillated cellulose coated with gold nanoparticles for measurement of melamine by SERS. *Cellulose* **24**, 2801–2811 (2017).
164. Zhang, C. *et al.* Hydrophobic paper-based SERS platform for direct-droplet quantitative determination of melamine. *Food Chem.* **287**, 363–368 (2019).
165. Li, D., Duan, H., Ma, Y. & Deng, W. Headspace-Sampling Paper-Based Analytical Device for Colorimetric/Surface-Enhanced Raman Scattering Dual Sensing of Sulfur Dioxide in Wine. *Anal. Chem.* **90**, 5719–5727 (2018).
166. Huang, D. *et al.* Black phosphorus-Au filter paper-based three-dimensional SERS substrate for rapid detection of foodborne bacteria. *Appl. Surf. Sci.* **497**, (2019).
167. Song, Y. *et al.* Au Sputtered Paper Chromatography Tandem Raman Platform for Sensitive Detection of Heavy Metal Ions. *ACS Sensors* **5**, 1455–1464 (2020).
168. Ameku, W. A., De Araujo, W. R., Rangel, C. J., Ando, R. A. & Paixão, T. R. L. C. Gold Nanoparticle Paper-Based Dual-Detection Device for Forensics Applications. *ACS Appl. Nano Mater.* **2**, 5460–5468 (2019).
169. Moram, S. S. B., Byram, C. & Soma, V. R. Gold-nanoparticle- and nanostar-loaded paper-based SERS substrates for sensing nanogram-level Picric acid with a portable Raman spectrometer. *Bull. Mater. Sci.* **43**, (2020).
170. Moram, S. S. B., Byram, C., Shibu, S. N., Chilukamarri, B. M. & Soma, V. R. Ag/Au Nanoparticle-Loaded Paper-Based Versatile Surface-Enhanced Raman Spectroscopy Substrates for Multiple Explosives Detection. *ACS Omega* **3**, 8190–8201 (2018).
171. Wang, C., Liu, B. & Dou, X. Silver nanotriangles-loaded filter paper for ultrasensitive SERS detection application benefited by interspacing of sharp edges. *Sensors Actuators, B Chem.* **231**, 357–364 (2016).
172. Sallum, L. F., Soares, F. L. F., Ardila, J. A. & Carneiro, R. L. Optimization of SERS scattering by Ag-NPs-coated filter paper for quantification of nicotinamide in a cosmetic formulation. *Talanta* **118**, 353–358 (2014).
173. Doherty, B., Brunetti, B. G., Sgamellotti, A. & Miliani, C. A detachable SERS active cellulose film:

A minimally invasive approach to the study of painting lakes. *J. Raman Spectrosc.* **42**, 1932–1938 (2011).
174. Bernalte, E. *et al.* Pencil It in: Exploring the Feasibility of Hand-Drawn Pencil Electrochemical Sensors and Their Direct Comparison to Screen-Printed Electrodes. *Biosensors* **6**, 45–65 (2016).
175. Arduini, F. *et al.* Electrochemical biosensors based on nanomodified screen-printed electrodes: Recent applications in clinical analysis. *TrAC - Trends Anal. Chem.* **79**, 114–126 (2016).
176. Taleat, Z., Khoshroo, A. & Mazloum-Ardakani, M. Screen-printed electrodes for biosensing: A review (2008-2013). *Microchim. Acta* **181**, 865–891 (2014).
177. Hayat, A. & Marty, J. L. Disposable screen printed electrochemical sensors: Tools for environmental monitoring. *Sensors (Switzerland)* **14**, 10432–10453 (2014).
178. Malitesta, C. *et al.* MIP sensors – the electrochemical approach. *Anal. Bioanal. Chem.* **402**, 1827–1846 (2012).
179. Ahmad, O. S., Bedwell, T. S., Esen, C., Garcia-Cruz, A. & Piletsky, S. A. Molecularly Imprinted Polymers in Electrochemical and Optical Sensors. *Trends Biotechnol.* **37**, 294–309 (2019).
180. Sharma, P. S., Pietrzyk-Le, A., D'Souza, F. & Kutner, W. Electrochemically synthesized polymers in molecular imprinting for chemical sensing. *Anal. Bioanal. Chem.* **402**, 3177–3204 (2012).
181. Refaat, D. *et al.* Strategies for molecular imprinting and the evolution of MIP nanoparticles as plastic antibodies—synthesis and applications. *Int. J. Mol. Sci.* **20**, (2019).
182. Crapnell, R. *et al.* Recent Advances in Electrosynthesized Molecularly Imprinted Polymer Sensing Platforms for Bioanalyte Detection. *Sensors* **19**, 1204 (2019).
183. Piletsky, S. A., Butovich, I. A. & Kukhar, V. P. Design of molecular sensors on the basis of substrate-selective polymer membranes. *Zh. Anal. Khim.* **47**, 1681–1684 (1992).
184. Yamanaka, K., Vestergaard, M. M. C. & Tamiya, E. Printable electrochemical biosensors: A focus on screen-printed electrodes and their application. *Sensors (Switzerland)* **16**, 1–16 (2016).
185. Yoo, E.-H. & Lee, S.-Y. Glucose biosensors: an overview of use in clinical practice. *Sensors (Basel).* **10**, 4558–76 (2010).
186. Rackus, D. G., Shamsi, M. H. & Wheeler, A. R. Electrochemistry, biosensors and microfluidics: a convergence of fields. *Chem. Soc. Rev.* **44**, 5320–5340 (2015).
187. Diouf, A., Motia, S., El Alami El Hassani, N., El Bari, N. & Bouchikhi, B. Development and characterization of an electrochemical biosensor for creatinine detection in human urine based on functional molecularly imprinted polymer. *J. Electroanal. Chem.* **788**, 44–53 (2017).
188. Khan, M. A. R. *et al.* Plastic antibody for the electrochemical detection of bacterial surface proteins. *Sensors Actuators B Chem.* **233**, 697–704 (2016).
189. Aghoutane, Y., Diouf, A., Österlund, L., Bouchikhi, B. & El Bari, N. Development of a molecularly imprinted polymer electrochemical sensor and its application for sensitive detection and determination of malathion in olive fruits and oils. *Bioelectrochemistry* **132**, (2020).
190. Grothe, R. A. *et al.* Electroanalytical profiling of cocaine samples by imprinted polymer using benzocaine as the template molecule. *Analyst* 1747–1759 (2021) doi:10.1039/d0an02274h.
191. Ribeiro, J. A., Pereira, C. M., Silva, A. F. & Sales, M. G. F. Disposable electrochemical detection of breast cancer tumour marker CA 15-3 using poly(Toluidine Blue) as imprinted polymer receptor. *Biosens. Bioelectron.* **109**, 246–254 (2018).
192. Carneiro, M. C. C. G., Sousa-Castillo, A., Correa-Duarte, M. A. & Sales, M. G. F. Dual biorecognition by combining molecularly-imprinted polymer and antibody in SERS detection. Application to carcinoembryonic antigen. *Biosens. Bioelectron.* **146**, 111761 (2019).
193. Ribeiro, J. A., Pereira, C. M., Silva, A. F. & Sales, M. G. F. Electrochemical detection of cardiac biomarker myoglobin using polyphenol as imprinted polymer receptor. *Anal. Chim. Acta* **981**, 41–52 (2017).
194. Phonklam, K., Wannapob, R., Sriwimol, W., Thavarungkul, P. & Phairatana, T. A novel molecularly imprinted polymer PMB/MWCNTs sensor for highly-sensitive cardiac troponin T detection. *Sensors Actuators, B Chem.* **308**, (2020).
195. Martins, G. V., Marques, A. C., Fortunato, E. & Sales, M. G. F. Paper-based (bio)sensor for label-

free detection of 3-nitrotyrosine in human urine samples using molecular imprinted polymer. *Sens. Bio-Sensing Res.* **28**, 100333 (2020).
196. Bozal-Palabiyik, B., Lettieri, M., Uslu, B. & Marrazza, G. Electrochemical Detection of Vascular Endothelial Growth Factor by Molecularly Imprinted Polymer. *Electroanalysis* **31**, 1475–1481 (2019).
197. Diouf, A., Bouchikhi, B. & El Bari, N. A nonenzymatic electrochemical glucose sensor based on molecularly imprinted polymer and its application in measuring saliva glucose. *Mater. Sci. Eng. C* **98**, 1196–1209 (2019).
198. Gomes, R. S. *et al.* Plastic antibody of polypyrrole/multiwall carbon nanotubes on screen-printed electrodes for cystatin C detection. *Biosensors* **11**, (2021).
199. Gonçalves, M. de L., Truta, L. A. N., Sales, M. G. F. & Moreira, F. T. C. Electrochemical Point-of Care (PoC) Determination of Interleukin-6 (IL-6) Using a Pyrrole (Py) Molecularly Imprinted Polymer (MIP) on a Carbon-Screen Printed Electrode (C-SPE). *Anal. Lett.* **54**, 2611–2623 (2021).
200. Rebelo, T. S. C. R. *et al.* Molecularly imprinted polymer SPE sensor for analysis of CA-125 on serum. *Anal. Chim. Acta* **1082**, 126–135 (2019).
201. Hong, C. C. *et al.* Handheld analyzer with on-chip molecularly-imprinted biosensors for electrical detection of propofol in plasma samples. *Biosens. Bioelectron.* **86**, 623–629 (2016).
202. Manickam, P., Pasha, S. K., Snipes, S. A. & Bhansali, S. A Reusable Electrochemical Biosensor for Monitoring of Small Molecules (Cortisol) Using Molecularly Imprinted Polymers. *J. Electrochem. Soc.* **164**, B54–B59 (2017).
203. Pereira, M. V. *et al.* Paper-Based Platform with an in Situ Molecularly Imprinted Polymer for β-Amyloid. *ACS Omega* **5**, 12057–12066 (2020).
204. Cardoso, A. R., Tavares, A. P. M. & Sales, M. G. F. In-situ generated molecularly imprinted material for chloramphenicol electrochemical sensing in waters down to the nanomolar level. *Sensors Actuators B Chem.* **256**, 420–428 (2018).
205. da Silva, J. L. *et al.* Non-enzymatic lactose molecularly imprinted sensor based on disposable graphite paper electrode. *Anal. Chim. Acta* **1143**, 53–64 (2021).
206. Lee, M.-H. *et al.* Doping of transition metal dichalcogenides in molecularly imprinted conductive polymers for the ultrasensitive determination of 17β-estradiol in eel serum. *Biosens. Bioelectron.* **150**, 111901 (2020).
207. Truong, T. N. L., Van Toan, P. & Hao, N. Q. Using AuNPs-modified screen-printed electrode in the development of molecularly imprinted polymer for artificial bioreceptor fabrication to improve biosensor sensitivity for 17β-estradiol detection. *Adv. Nat. Sci. Nanosci. Nanotechnol.* **10**, (2019).
208. Chang, T. L., Chen, Z. C. & Tseng, S. F. Laser micromachining of screen-printed graphene for forming electrode structures. *Appl. Surf. Sci.* **374**, 305–311 (2016).
209. Novoselov, K. S. *et al.* Electric field in atomically thin carbon films. *Science (80-.).* **306**, 666–669 (2004).
210. Ye, R. Q. *et al.* In Situ Formation of Metal Oxide Nanocrystals Embedded in Laser-Induced Graphene. *ACS Nano* **9**, 9244–9251 (2015).
211. Singh, S. P. *et al.* Laser-Induced Graphene Layers and Electrodes Prevents Microbial Fouling and Exerts Antimicrobial Action. *ACS Appl. Mater. Interfaces* **9**, 18238–18247 (2017).
212. Ye, R., James, D. K. & Tour, J. M. Laser-Induced Graphene. *Acc. Chem. Res.* **51**, 1609–1620 (2018).
213. Wang, F. *et al.* Laser-induced graphene: preparation, functionalization and applications. *Mater. Technol.* **33**, 340–356 (2018).
214. Vivaldi, F. M. *et al.* Three-Dimensional (3D) Laser-Induced Graphene: Structure, Properties, and Application to Chemical Sensing. *ACS Appl. Mater. Interfaces* acsami.1c05614 (2021) doi:10.1021/acsami.1c05614.
215. Wan, Z., Nguyen, N.-T., Gao, Y. & Li, Q. Laser induced graphene for biosensors. *Sustain. Mater. Technol.* **25**, e00205 (2020).
216. Ye, R., James, D. K. & Tour, J. M. Laser-Induced Graphene: From Discovery to Translation. *Adv.*

Mater. **31**, 1–15 (2019).
217. Lin, J. *et al.* Laser-induced porous graphene films from commercial polymers. *Nat. Commun.* **5**, 1–8 (2014).
218. Xu, G., Jarjes, Z. A., Desprez, V., Kilmartin, P. A. & Travas-Sejdic, J. Sensitive, selective, disposable electrochemical dopamine sensor based on PEDOT-modified laser scribed graphene. *Biosens. Bioelectron.* **107**, 184–191 (2018).
219. Nayak, P., Kurra, N., Xia, C. & Alshareef, H. N. Highly Efficient Laser Scribed Graphene Electrodes for On-Chip Electrochemical Sensing Applications. *Adv. Electron. Mater.* **2**, 1600185 (2016).
220. Hong, Q., Yang, L., Ge, L., Liu, Z. & Li, F. Direct-laser-writing of three-dimensional porous graphene frameworks on indium-tin oxide for sensitive electrochemical biosensing. *Analyst* **143**, 3327–3334 (2018).
221. Zhang, C., Xie, Y., Zhang, C. & Lin, J. Upgrading coal to multifunctional graphene based materials by direct laser scribing. *Carbon N. Y.* **153**, 585–591 (2019).
222. Marques, A. C., Cardoso, A. R., Martins, R., Sales, M. G. F. & Fortunato, E. Laser-Induced Graphene-Based Platforms for Dual Biorecognition of Molecules. *ACS Appl. Nano Mater.* **3**, 2795–2803 (2020).
223. Pereira, S. O., Santos, N. F., Carvalho, A. F., Fernandes, A. J. S. & Costa, F. M. Electrochemical Response of Glucose Oxidase Adsorbed on Laser-Induced Graphene. *Nanomaterials* **11**, 1893 (2021).
224. Tehrani, F. & Bavarian, B. Facile and scalable disposable sensor based on laser engraved graphene for electrochemical detection of glucose. *Sci. Rep.* **6**, 27975 (2016).
225. Li, L. *et al.* High-Performance Pseudocapacitive Microsupercapacitors from Laser-Induced Graphene. *Adv. Mater.* **28**, 838–845 (2016).
226. Peng, Z. *et al.* Flexible Boron-Doped Laser-Induced Graphene Microsupercapacitors. *ACS Nano* **9**, 5868–5875 (2015).
227. Peng, Z., Lin, J., Ye, R., Samuel, E. L. G. & Tour, J. M. Flexible and stackable laser-induced graphene supercapacitors. *ACS Appl. Mater. Interfaces* **7**, 3414–3419 (2015).
228. Zhang, J. *et al.* Efficient Water-Splitting Electrodes Based on Laser-Induced Graphene. *ACS Appl. Mater. Interfaces* **9**, 26840–26847 (2017).
229. Rathinam, K. *et al.* Polyimide derived laser-induced graphene as adsorbent for cationic and anionic dyes. *Carbon N. Y.* **124**, 515–524 (2017).
230. Huang, L. *et al.* Self-Reporting and Photothermally Enhanced Rapid Bacterial Killing on a Laser-Induced Graphene Mask. *ACS Nano* **14**, 12045–12053 (2020).
231. Samouco, A., Marques, A. C., Pimentel, A., Martins, R. & Fortunato, E. Laser-induced electrodes towards low-cost flexible UV ZnO sensors. *Print. Electron.* **3**, 044002 (2018).
232. Samouco, A., Marques, A. C., Pimentel, A., Martins, R. & Fortunato, E. Laser-induced electrodes towards low-cost flexible UV ZnO sensors. *Flex. Print. Electron.* **3**, 044002 (2018).
233. Chyan, Y. *et al.* Laser-Induced Graphene by Multiple Lasing: Toward Electronics on Cloth, Paper, and Food. *ACS Nano* **12**, 2176–2183 (2018).
234. Ye, R. *et al.* Laser-Induced Graphene Formation on Wood. *Adv. Mater.* **29**, 1–7 (2017).
235. Araujo, W. R. *et al.* Single-Step Reagentless Laser Scribing Fabrication of Electrochemical Paper-Based Analytical Devices. *Angew. Chemie* **129**, 15309–15313 (2017).
236. Pinheiro, T. *et al.* Laser-Induced Graphene on Paper toward Efficient Fabrication of Flexible, Planar Electrodes for Electrochemical Sensing. *Adv. Mater. Interfaces* 2101502 (2021) doi:10.1002/admi.202101502.
237. Rocha, D. P. *et al.* Reagentless and sub-minute laser-scribing treatment to produce enhanced disposable electrochemical sensors via additive manufacture. *Chem. Eng. J.* **425**, 130594 (2021).
238. Tasic, N. *et al.* Insights into electrochemical behavior in laser-scribed electrochemical paper-based analytical devices. *Electrochem. commun.* **121**, 106872 (2020).
239. Ge, L., Hong, Q., Li, H., Liu, C. & Li, F. Direct-Laser-Writing of Metal Sulfide-Graphene

Nanocomposite Photoelectrode toward Sensitive Photoelectrochemical Sensing. *Adv. Funct. Mater.* **29**, (2019).
240. Kucherenko, I. S. *et al.* Ion-Selective Sensors Based on Laser-Induced Graphene for Evaluating Human Hydration Levels Using Urine Samples. *Adv. Mater. Technol.* **5**, (2020).
241. Mamleyev, E. R. *et al.* Laser-induced hierarchical carbon patterns on polyimide substrates for flexible urea sensors. *npj Flex. Electron.* **3**, (2019).
242. Wan, Z. *et al.* Laser induced self-N-doped porous graphene as an electrochemical biosensor for femtomolar miRNA detection. *Carbon N. Y.* **163**, 385–394 (2020).
243. Fenzl, C. *et al.* Laser-Scribed Graphene Electrodes for Aptamer-Based Biosensing. *ACS Sensors* **2**, 616–620 (2017).
244. Settu, K., Chiu, P. T. & Huang, Y. M. Laser-induced graphene-based enzymatic biosensor for glucose detection. *Polymers (Basel).* **13**, (2021).
245. Zhao, J. *et al.* Co3O4 nanoparticles embedded in laser-induced graphene for a flexible and highly sensitive enzyme-free glucose biosensor. *Sensors Actuators B Chem.* **347**, 130653 (2021).
246. Zahed, M. A. *et al.* Highly flexible and conductive poly (3, 4-ethylene dioxythiophene)-poly (styrene sulfonate) anchored 3-dimensional porous graphene network-based electrochemical biosensor for glucose and pH detection in human perspiration. *Biosens. Bioelectron.* **160**, 112220 (2020).
247. Bhaiyya, M., Pattnaik, P. K. & Goel, S. Portable Electrochemiluminescence Platform with Laser-Induced Graphene-Based U-Shaped Bipolar Electrode for Selective Sensing of Various Analytes. *IEEE Trans. Electron Devices* **68**, 2447–2454 (2021).
248. Zhang, Z. *et al.* Visible light laser-induced graphene from phenolic resin: A new approach for directly writing graphene-based electrochemical devices on various substrates. *Carbon N. Y.* **127**, 287–296 (2018).
249. Lei, Y., Alshareef, A. H., Zhao, W. & Inal, S. Laser-Scribed Graphene Electrodes Derived from Lignin for Biochemical Sensing. *ACS Appl. Nano Mater.* **3**, 1166–1174 (2020).
250. You, Z. *et al.* Laser-induced noble metal nanoparticle-graphene composites enabled flexible biosensor for pathogen detection. *Biosens. Bioelectron.* **150**, 111896 (2020).
251. Soares, R. R. A. *et al.* Laser-Induced Graphene Electrochemical Immunosensors for Rapid and Label-Free Monitoring of Salmonella enterica in Chicken Broth. *ACS Sensors* **5**, 1900–1911 (2020).
252. Wang, G., Chen, J., Huang, L., Chen, Y. & Li, Y. A laser-induced graphene electrochemical immunosensor for label-free CEA monitoring in serum. *Analyst* 6631–6642 (2021) doi:10.1039/d1an01011e.
253. Yagati, A. K. *et al.* Laser-induced graphene interdigitated electrodes for label-free or nanolabel-enhanced highly sensitive capacitive aptamer-based biosensors. *Biosens. Bioelectron.* **164**, 112272 (2020).
254. Kucherenko, I. S. *et al.* Laser-induced graphene electrodes for electrochemical ion sensing, pesticide monitoring, and water splitting. *Anal. Bioanal. Chem.* **413**, 6201–6212 (2021).
255. Zhao, F. *et al.* Smart plant-wearable biosensor for in-situ pesticide analysis. *Biosens. Bioelectron.* **170**, 112636 (2020).
256. Garland, N. T. *et al.* Flexible Laser-Induced Graphene for Nitrogen Sensing in Soil. *ACS Appl. Mater. Interfaces* **10**, 39124–39133 (2018).
257. Nasraoui, S. *et al.* Investigation of Laser Induced Graphene Electrodes Modified by MWNT/AuNPs for Detection of Nitrite. *16th Int. Multi-Conference Syst. Signals Devices, SSD 2019* 615–620 (2019) doi:10.1109/SSD.2019.8893191.
258. Vanegas, D. *et al.* Laser Scribed Graphene Biosensor for Detection of Biogenic Amines in Food Samples Using Locally Sourced Materials. *Biosensors* **8**, 42 (2018).
259. Martins, A. B. *et al.* Laser-pyrolyzed electrochemical paper-based analytical sensor for sulphite analysis. *Electrochem. commun.* **107**, 106541 (2019).
260. Tasić, N., Sousa, L. De, Thiago, D. O. & Gonçalves, L. M. Laser-pyrolysed paper electrodes for the square-wave anodic stripping voltammetric detection of lead. *Med. Devices Sensors* **3**, e10115

(2020).
261. Yang, Y. *et al.* A laser-engraved wearable sensor for sensitive detection of uric acid and tyrosine in sweat. *Nat. Biotechnol.* **38**, 217–224 (2020).
262. Xuan, X. *et al.* A highly stretchable and conductive 3D porous graphene metal nanocomposite based electrochemical-physiological hybrid biosensor. *Biosens. Bioelectron.* **120**, 160–167 (2018).
263. Yu, Y., Joshi, P. C., Wu, J. & Hu, A. Laser-Induced Carbon-Based Smart Flexible Sensor Array for Multiflavors Detection. *ACS Appl. Mater. Interfaces* **10**, 34005–34012 (2018).
264. Beduk, T., Ait Lahcen, A., Tashkandi, N. & Salama, K. N. One-step electrosynthesized molecularly imprinted polymer on laser scribed graphene bisphenol a sensor. *Sensors Actuators B Chem.* **314**, 128026 (2020).
265. Lahcen, A. A. *et al.* Laser-scribed graphene sensor based on gold nanostructures and molecularly imprinted polymers: Application for Her-2 cancer biomarker detection. *Sensors Actuators B Chem.* **347**, 1–12 (2021).
266. Pimentel, A. *et al.* 3D ZnO/Ag surface-enhanced Raman scattering on disposable and flexible cardboard platforms. *Materials (Basel).* **10**, (2017).
267. Araújo, A. *et al.* Highly efficient nanoplasmonic SERS on cardboard packaging substrates. *Nanotechnology* **25**, 415202 (2014).
268. C., M. A., K. P., F., Singh, S. & Baik, S. Hierarchically-structured silver nanoflowers for highly conductive metallic inks with dramatically reduced filler concentration. *Sci. Rep.* **6**, 34894 (2016).
269. Samouco, A. Laser induced electrodes towards low cost flexible electronics and its applications in a UV sensor. (NOVA University of Lisbon, 2017).
270. Harvey, D. Modern Analytic Chemistry. 797 (2000).
271. Özcan, L., Şahin, M. & Şahin, Y. Electrochemical preparation of a molecularly imprinted polypyrrole-modified pencil graphite electrode for determination of ascorbic acid. *Sensors* **8**, 5792–5805 (2008).
272. Chen, X. *et al.* Superhydrophobic SERS substrates based on silicon hierarchical nanostructures. *J. Opt.* **20**, 024012 (2018).
273. Nemciauskas, K., Traksele, L., Salaseviciene, A. & Snitka, V. A silicon membrane-silver nanoparticles SERS chip for trace molecules detection. *Microelectron. Eng.* **225**, 111282 (2020).
274. Yue, X. *et al.* Synthesis of a low-cost, stable, silicon-based SERS substrate for rapid, nondestructive biosensing. *Optik (Stuttg).* **192**, 162959 (2019).
275. Yin, G. *et al.* Highly Sensitive and Stable SERS Substrate Fabricated by Co-sputtering and Atomic Layer Deposition. *Nanoscale Res. Lett.* **14**, 168 (2019).
276. Chen, L., Ying, B., Song, P. & Liu, X. A Nanocellulose-Paper-Based SERS Multiwell Plate with High Sensitivity and High Signal Homogeneity. *Adv. Mater. Interfaces* **6**, (2019).
277. Fan, M., Andrade, G. F. S. & Brolo, A. G. A review on the fabrication of substrates for surface enhanced Raman spectroscopy and their applications in analytical chemistry. *Anal. Chim. Acta* **693**, 7–25 (2011).
278. Cao, W. & Elsayed-Ali, H. E. Stability of Ag nanoparticles fabricated by electron beam lithography. *Mater. Lett.* **63**, 2263–2266 (2009).
279. Crupi, S. M. and M. J. M. and S. M. and F. S. and F. P. and I. Self-assembled silver nanoparticles for plasmon-enhanced solar cell back reflectors: correlation between structural and optical properties. *Nanotechnology* **24**, 265601 (2013).
280. Komarala, E. T. and N. C. and V. D. and V. K. Optical properties of Ag nanoparticle layers deposited on silicon substrates. *J. Opt.* **15**, 35005 (2013).
281. Temple, T. L., Mahanama, G. D. K., Reehal, H. S. & Bagnall, D. M. Influence of localized surface plasmon excitation in silver nanoparticles on the performance of silicon solar cells. *Sol. Energy Mater. Sol. Cells* **93**, 1978–1985 (2009).
282. Gajda, A., Nowacka-Kozak, E., Gbylik-Sikorska, M. & Posyniak, A. Tetracycline antibiotics transfer from contaminated milk to dairy products and the effect of the skimming step and pasteurisation process on residue concentrations. *Food Addit. Contam. - Part A Chem. Anal.*

Control. Expo. Risk Assess. **35**, 66–76 (2018).
283. Sivakesava, S. & Irudayaraj, J. Rapid Determination of Tetracycline in Milk by FT-MIR and FT-NIR Spectroscopy. *J. Dairy Sci.* **85**, 487–493 (2002).
284. Chen, Y. *et al.* High sensitive detection of penicillin G residues in milk by surface-enhanced Raman scattering. *Talanta* **167**, 236–241 (2017).
285. Piper, T. *et al.* Determination of 13C/12C ratios of endogenous urinary steroids: methd validation, reference population and application to doping control purposes. *Rapid Commun. Mass Spectrom.* **22**, 2161–2175 (2008).
286. Borghi, A. A. & Palma, M. S. A. Tetracycline: Production, waste treatment and environmental impact assessment. *Brazilian J. Pharm. Sci.* **50**, 25–40 (2014).
287. Dhakal, S. *et al.* A simple surface-enhanced raman spectroscopic method for on-site screening of tetracycline residue in whole milk. *Sensors (Switzerland)* **18**, (2018).
288. de Albuquerque Fernandes, S. A. *et al.* Daily ingestion of tetracycline residue present in pasteurized milk: a public health problem. *Environ. Sci. Pollut. Res.* **21**, 3427–3434 (2014).
289. Kurittu, J., Lonberg, S., Virta, M. & Karp, M. Qualitative Detection of Tetracycline Residues in Milk with a Luminescence-Based Microbial Method: The Effect of Milk Composition and Assay Performance in Relation to an Immunoassay and a Microbial Inhibition Assay. *J. Food Prot.* **63**, 953–957 (2000).
290. Pikkemaat, M. G., Dijk, S. O., Schouten, J., Rapallini, M. & van Egmond, H. J. A new microbial screening method for the detection of antimicrobial residues in slaughter animals: The Nouws antibiotic test (NAT-screening). *Food Control* **19**, 781–789 (2008).
291. Zhou, L., Li, D.-J., Gai, L., Wang, J.-P. & Li, Y.-B. Electrochemical aptasensor for the detection of tetracycline with multi-walled carbon nanotubes amplification. *Sensors Actuators B Chem.* **162**, 201–208 (2012).
292. Luo, Y. *et al.* A novel colorimetric aptasensor using cysteamine-stabilized gold nanoparticles as probe for rapid and specific detection of tetracycline in raw milk. *Food Control* **54**, 7–15 (2015).
293. Cinquina, A. L., Longo, F., Anastasi, G., Giannetti, L. & Cozzani, R. Validation of a high-performance liquid chromatography method for the determination of oxytetracycline, tetracycline, chlortetracycline and doxycycline in bovine milk and muscle. *J. Chromatogr. A* **987**, 227–233 (2003).
294. Fritz, J. W. & Zuo, Y. Simultaneous determination of tetracycline, oxytetracycline, and 4-epitetracycline in milk by high-performance liquid chromatography. *Food Chem.* **105**, 1297–1301 (2007).
295. Andersen, W. C. *et al.* Determination of tetracycline residues in shrimp and whole milk using liquid chromatography with ultraviolet detection and residue confirmation by mass spectrometry. *Anal. Chim. Acta* **529**, 145–150 (2005).
296. Blasco, C., Corcia, A. Di & Picó, Y. Determination of tetracyclines in multi-specie animal tissues by pressurized liquid extraction and liquid chromatography–tandem mass spectrometry. *Food Chem.* **116**, 1005–1012 (2009).
297. Araújo, A. Plasmonic Silver Nanoparticles by Dewetting process : Applications in SERS and Thin Film Solar Cells. (Universidade NOVA de Lisboa, 2018).
298. Jin, D. *et al.* SERS detection of expired tetracycline hydrochloride with an optical fiber nano-probe. *Anal. Methods* **7**, 1307–1312 (2015).
299. Pinheiro, P., Fateixa, S., Nogueira, H. & Trindade, T. Magnetite-Supported Gold Nanostars for the Uptake and SERS Detection of Tetracycline. *Nanomaterials* **9**, 31 (2018).
300. McGoverin, C. M., Clark, A. S. S., Holroyd, S. E. & Gordon, K. C. Raman spectroscopic quantification of milk powder constituents. *Anal. Chim. Acta* **673**, 26–32 (2010).
301. De Gelder, J., De Gussem, K., Vandenabeele, P. & Moens, L. Reference database of Raman spectra of biological molecules. *J. Raman Spectrosc.* **38**, 1133–1147 (2007).
302. Kuang, Y., Jia, H., Miyanaga, K. & Tanji, Y. Effect of milk on antibacterial activity of tetracycline against Escherichia coli and Staphylococcus aureus isolated from bovine mastitis. *Appl.*

Microbiol. Biotechnol. **84**, 135–142 (2009).
303. Li, H. *et al.* A magnetite/PMAA nanospheres-targeting SERS aptasensor for tetracycline sensing using mercapto molecules embedded core/shell nanoparticles for signal amplification. *Biosens. Bioelectron.* **92**, 192–199 (2017).
304. Ouyang, Q. *et al.* Rapid and specific sensing of tetracycline in food using a novel upconversion aptasensor. *Food Control* **81**, 156–163 (2017).
305. Granados-Chinchilla, F. & Rodríguez, C. Tetracyclines in Food and Feedingstuffs: From Regulation to Analytical Methods, Bacterial Resistance, and Environmental and Health Implications. *J. Anal. Methods Chem.* **2017**, (2017).
306. Food and Drug Administration. Milk Drug Residue Sampling Survey. *Silver Spring* 10 (2015).
307. Lux, C., Lubio, A., Ruediger, A., Robert, S. & Muehlethaler, C. Optimizing the analysis of dyes by Surface-Enhanced Raman Spectroscopy (SERS) using a conventional-microwave silver nanoparticles synthesis. *Forensic Chem.* **16**, (2019).
308. Hsu, K. C. & Chen, D. H. Microwave-assisted green synthesis of Ag/reduced graphene oxide nanocomposite as a surface-enhanced Raman scattering substrate with high uniformity. *Nanoscale Res. Lett.* **9**, 1–9 (2014).
309. Xia, L. *et al.* Microwave-assisted synthesis of sensitive silver substrate for surface-enhanced Raman scattering spectroscopy. *J. Chem. Phys.* **129**, 1–8 (2008).
310. Jiang, T., Li, J., Zhang, L., Wang, B. & Zhou, J. Microwave assisted in situ synthesis of Ag-NaCMC films and their reproducible surface-enhanced Raman scattering signals. *J. Alloys Compd.* **602**, 94–100 (2014).
311. Dong, S. *et al.* Beehive-Inspired Macroporous SERS Probe for Cancer Detection through Capturing and Analyzing Exosomes in Plasma. *ACS Appl. Mater. Interfaces* **12**, 5136–5146 (2020).
312. Jiang, J. *et al.* A Highly Sensitive and Stable SERS Sensor for Malachite Green Detection Based on Ag Nanoparticles In Situ Generated on 3D MoS2 Nanoflowers. *ChemistrySelect* **5**, 354–359 (2020).
313. Su, S. *et al.* Creating SERS hot spots on MoS2 nanosheets with in situ grown gold nanoparticles. *ACS Appl. Mater. Interfaces* **6**, 18735–18741 (2014).
314. Ghosh, P. *et al.* Directed Microwave-Assisted Self-Assembly of Au–Graphene–Au Plasmonic Dimers for SERS Applications. *Adv. Mater. Interfaces* **6**, 1–9 (2019).
315. Li, H. *et al.* Microwave method synthesis of magnetic ionic liquid/gold nanoparticles as ultrasensitive SERS substrates for trace clopidol detection. *Anal. Bioanal. Chem.* **412**, 3063–3071 (2020).
316. Chen, M. *et al.* In situ fabrication of label-free optical sensing paper strips for the rapid surface-enhanced Raman scattering (SERS) detection of brassinosteroids in plant tissues. *Talanta* **165**, 313–320 (2017).
317. Pinto, R. J. B., Marques, P. A. A. P., Barros-Timmons, A. M., Trindade, T. & Neto, C. P. Novel SiO2/cellulose nanocomposites obtained by in situ synthesis and via polyelectrolytes assembly. *Compos. Sci. Technol.* **68**, 1088–1093 (2008).
318. Kang, L. *et al.* Nanoporous thermochromic VO2 films with low optical constants, enhanced luminous transmittance and thermochromic properties. *ACS Appl. Mater. Interfaces* **3**, 135–138 (2011).
319. Wu, M. *et al.* Functional paper-based SERS substrate for rapid and sensitive detection of Sudan dyes in herbal medicine. *Spectrochim. Acta - Part A Mol. Biomol. Spectrosc.* **196**, 110–116 (2018).
320. Klemm, D. *et al.* Nanocelluloses: A New Family of Nature-Based Materials. *Angew. Chemie Int. Ed.* **50**, 5438–5466 (2011).
321. Molina-Ramírez, C., Álvarez, J., Zuluaga, R., Castro, C. & Gañán, P. A Novel Approach Using Conventional Methodologies to Scale up BNC Production Using Komagataeibacter medellinensis and Rotten Banana Waste as Alternative. *Processes* **8**, 1469 (2020).
322. Gama, F. M., Gatenholm, P. & Klemm, D. *Bacterial nanocellulose: A sophisticated multifunctional material*. *Bacterial NanoCellulose: A Sophisticated Multifunctional Material* (2016).

323. Parnsubsakul, A. *et al.* Silver nanoparticle/bacterial nanocellulose paper composites for paste-and-read SERS detection of pesticides on fruit surfaces. *Carbohydr. Polym.* **235**, (2020).
324. Huo, D. *et al.* Ag-Nanoparticles@Bacterial Nanocellulose as a 3D Flexible and Robust Surface-Enhanced Raman Scattering Substrate. *ACS Appl. Mater. Interfaces* **12**, 50713–50720 (2020).
325. Rodríguez-Sevilla, E., Vázquez, G. V. & Morales-Narváez, E. Simple, Flexible, and Ultrastable Surface Enhanced Raman Scattering Substrate Based on Plasmonic Nanopaper Decorated with Graphene Oxide. *Adv. Opt. Mater.* **6**, 1–9 (2018).
326. Zhou, X. *et al.* Photoinduced synthesis of gold nanoparticle–bacterial cellulose nanocomposite and its application for in-situ detection of trace concentration of dyes in textile and paper. *Cellulose* **25**, 3941–3953 (2018).
327. Wei, H. & Vikesland, P. J. PH-Triggered Molecular Alignment for Reproducible SERS Detection via an AuNP/Nanocellulose Platform. *Sci. Rep.* **5**, 1–10 (2015).
328. Wei, H., Rodriguez, K., Renneckar, S., Leng, W. & Vikesland, P. J. Preparation and evaluation of nanocellulose-gold nanoparticle nanocomposites for SERS applications. *Analyst* **140**, 5640–5649 (2015).
329. Tian, L. *et al.* Bacterial Nanocellulose-Based Flexible Surface Enhanced Raman Scattering Substrate. *Adv. Mater. Interfaces* **3**, 1–8 (2016).
330. Wu, J., Feng, Y., Zhang, L. & Wu, W. Nanocellulose-based Surface-enhanced Raman spectroscopy sensor for highly sensitive detection of TNT. *Carbohydr. Polym.* **248**, 116766 (2020).
331. Wu, J. *et al.* In situ synthesis of silver-nanoparticles/bacterial cellulose composites for slow-released antimicrobial wound dressing. *Carbohydr. Polym.* **102**, 762–771 (2014).
332. Nugroho, D. A. & Aji, P. Characterization of Nata de Coco Produced by Fermentation of Immobilized Acetobacter xylinum. *Agriculture and Agricultural Science Procedia* vol. 3 278–282 (2015).
333. G. Miguel, D. Fernando, B. S. *Bacterial Nanocellulose: From biotechnology to Bio-Economy*. (2016).
334. Lorusso, S. *Ancient and Modern Paper Characterization by FTIR and Micro-Raman Spectroscopy*. (2010).
335. Manente, S., Micheluz, A., Ganzerla, R., Ravagnan, G. & Gambaro, A. Chemical and biological characterization of paper: A case study using a proposed methodological approach. *Int. Biodeterior. Biodegradation* **74**, 99–108 (2012).
336. Li, Z. *et al.* Facilely green synthesis of silver nanoparticles into bacterial cellulose. *Cellulose* **22**, 373–383 (2015).
337. Oliveira, R. L. *et al.* Synthesis and characterization of methylcellulose produced from bacterial cellulose under heterogeneous condition. *J. Braz. Chem. Soc.* **26**, 1861–1870 (2015).
338. International Agency for Research on Cancer, W. H. O. *Cancer fact sheets*. (2020).
339. Costa-Silva, B. *et al.* Pancreatic cancer exosomes initiate pre-metastatic niche formation in the liver. *Nat. Cell Biol.* **17**, 1–7 (2015).
340. Thakur, B. K. *et al.* Double-stranded DNA in exosomes: a novel biomarker in cancer detection. *Cell Res.* **24**, 766–9 (2014).
341. Sharma, S. *et al.* Structural-Mechanical Characterization of Nanoparticle Exosomes in Human Saliva, Using Correlative AFM, FESEM, and Force Spectroscopy. *ACS Nano* **4**, 1921–1926 (2010).
342. Jeong, S. *et al. Integrated Magneto-Electrochemical Sensor for Exosome Analysis*. *ACS Nano* vol. 10 (2016).
343. Im, H. *et al.* Label-free detection and molecular profiling of exosomes with a nano-plasmonic sensor. *Nat. Biotechnol.* **32**, 490–5 (2014).
344. Zhu, L. *et al.* Label-free quantitative detection of tumor-derived exosomes through surface plasmon resonance imaging. *Anal. Chem.* **86**, 8857–8864 (2014).
345. Lee, C. *et al.* 3D plasmonic nanobowl platform for the study of exosomes in solution. *Nanoscale* **7**, 9290–7 (2015).
346. Lee, C., Carney, R., Lam, K. & Chan, J. W. SERS analysis of selectively captured exosomes using an integrin-specific peptide ligand. *J. Raman Spectrosc.* **48**, 1771–1776 (2017).

347. Guerrini, L., Garcia-Rico, E., O'Loghlen, A., Giannini, V. & Alvarez-Puebla, R. A. Surface-Enhanced Raman Scattering (SERS) Spectroscopy for Sensing and Characterization of Exosomes in Cancer Diagnosis. *Cancers (Basel).* **13**, 2179 (2021).
348. Roy, S., Muhammed Ajmal, C., Baik, S. & Kim, J. Silver nanoflowers for single-particle SERS with 10 pM sensitivity. *Nanotechnology* **28**, 0–23 (2017).
349. Mehtab, S., Zaidi, M. G. H. & Irshad Siddiqi, T. Designing Fructose Stabilized Silver Nanoparticles for Mercury(II) Detection and Potential Antibacterial Agents. *Mater. Sci. Res. India* **15**, 241–249 (2018).
350. Woo, J., Sharma, S. & Gimzewski, J. The Role of Isolation Methods on a Nanoscale Surface Structure and its Effect on the Size of Exosomes. *J. Circ. Biomarkers* **5**, 11 (2016).
351. Mahesh, G. Paper-based Diagnostics for COVID-19 Developed by CSIR-IGIB. *Sicence Report.* 28–29 (2020).
352. Udugama, B. *et al.* Diagnosing COVID-19: The Disease and Tools for Detection. *ACS Nano* **14**, 3822–3835 (2020).
353. Baker, A. N. *et al.* The SARS-COV-2 Spike Protein Binds Sialic Acids and Enables Rapid Detection in a Lateral Flow Point of Care Diagnostic Device. *ACS Cent. Sci.* **6**, 2046–2052 (2020).
354. Hristov, D. R., Rijal, H., Gomez-Marquez, J. & Hamad-Schifferli, K. Developing a paper-based antigen assay to differentiate between coronaviruses and SARS-CoV-2 Spike variants. *ChemRxiv* (2020) doi:10.26434/chemrxiv.13476738.v1.
355. Ou, X. *et al.* Characterization of spike glycoprotein of SARS-CoV-2 on virus entry and its immune cross-reactivity with SARS-CoV. *Nat. Commun.* **11**, (2020).
356. Zhang, D. *et al.* Ultra-fast and onsite interrogation of severe acute respiratory syndrome coronavirus 2 (SARS-CoV-2) in environmental specimens via surface enhanced Raman scattering (SERS). *medRxiv* (2020) doi:10.1101/2020.05.02.20086876.
357. Peng, Y. *et al.* Charge-Transfer Resonance and Electromagnetic Enhancement Synergistically Enabling MXenes with Excellent SERS Sensitivity for SARS-CoV-2 S Protein Detection. *Nano-Micro Lett.* **13**, 52 (2021).
358. Unser, S., Campbell, I., Jana, D. & Sagle, L. Direct glucose sensing in the physiological range through plasmonic nanoparticle formation. *Analyst* **140**, 590–599 (2015).
359. Pinheiro, T. *et al.* Paper-Based In-Situ Gold Nanoparticle Synthesis for Colorimetric, Non-Enzymatic Glucose Level Determination. *Nanomaterials* **10**, 2027 (2020).
360. Tran, M., DePenning, R., Turner, M. & Padalkar, S. Effect of citrate ratio and temperature on gold nanoparticle size and morphology. *Mater. Res. Express* **3**, 105027 (2016).
361. Ishizaka, T., Ishigaki, A., Kawanami, H., Suzuki, A. & Suzuki, T. M. Dynamic control of gold nanoparticle morphology in a microchannel flow reactor by glucose reduction in aqueous sodium hydroxide solution. *J. Colloid Interface Sci.* **367**, 135–138 (2012).
362. Suvarna, S. *et al.* Synthesis of a novel glucose capped gold nanoparticle as a better theranostic candidate. *PLoS One* **12**, 1–15 (2017).
363. Park, J.-W. & Shumaker-Parry, J. S. Structural Study of Citrate Layers on Gold Nanoparticles: Role of Intermolecular Interactions in Stabilizing Nanoparticles. *J. Am. Chem. Soc.* **136**, 1907–1921 (2014).
364. Polte, J. Fundamental growth principles of colloidal metal nanoparticles - a new perspective. *CrystEngComm* **17**, 6809–6830 (2015).
365. Liu, J., Qin, G., Raveendran, P. & Ikushima, Y. Facile 'green' synthesis, characterization, and catalytic function of β-D-glucose-stabilized Au nanocrystals. *Chem. - A Eur. J.* **12**, 2131–2138 (2006).
366. Britto Hurtado, R. *et al.* Instant synthesis of gold nanoparticles at room temperature and SERS applications. *Phys. Lett. Sect. A Gen. At. Solid State Phys.* **380**, 2658–2663 (2016).
367. Chen, F., Wang, Y., Ma, J. & Yang, G. A biocompatible synthesis of gold nanoparticles by Tris(hydroxymethyl)aminomethane. *Nanoscale Res. Lett.* **9**, 220 (2014).
368. Bayazit, M. K., Yue, J., Cao, E., Gavriilidis, A. & Tang, J. Controllable Synthesis of Gold

Nanoparticles in Aqueous Solution by Microwave Assisted Flow Chemistry. *ACS Sustain. Chem. Eng.* **4**, 6435–6442 (2016).
369. Seol, S. K., Kim, D., Jung, S. & Hwu, Y. Microwave synthesis of gold nanoparticles: Effect of applied microwave power and solution pH. *Mater. Chem. Phys.* **131**, 331–335 (2011).
370. Kumar, S., Gandhi, K. S. & Kumar, R. Modeling of formation of gold nanoparticles by citrate method. *Ind. Eng. Chem. Res.* **46**, 3128–3136 (2007).
371. Ankamwar, B. Gold and silver nanoparticles used for SERS detection of S. aureus and E. coli . *Nano Express* **1**, 010020 (2020).
372. Rodríguez-León, E. *et al.* Synthesis of Gold Nanoparticles Using Mimosa tenuiflora Extract, Assessments of Cytotoxicity, Cellular Uptake, and Catalysis. *Nanoscale Res. Lett.* **14**, 334 (2019).
373. Alegria, E. *et al.* Effect of Phenolic Compounds on the Synthesis of Gold Nanoparticles and its Catalytic Activity in the Reduction of Nitro Compounds. *Nanomaterials* **8**, 320 (2018).
374. Casaletto, M. P., Longo, A., Martorana, A., Prestianni, A. & Venezia, A. M. XPS study of supported gold catalysts: the role of Au0 and Au+δ species as active sites. *Surf. Interface Anal.* **38**, 215–218 (2006).
375. Moulder, J., Stickle, W., Sobol, P. & Bomben, K. *Handbook of X-ray Photoelectron Spectroscopy*. (Perkin-Elmer Corporation, 1992).
376. Villa, J. E. L., Quiñones, N. R., Fantinatti-Garboggini, F. & Poppi, R. J. Fast discrimination of bacteria using a filter paper–based SERS platform and PLS-DA with uncertainty estimation. *Anal. Bioanal. Chem.* **411**, 705–713 (2019).
377. Dalla Marta, S., Novara, C., Giorgis, F., Bonifacio, A. & Sergo, V. Optimization and characterization of paper-made Surface Enhanced Raman Scattering (SERS) substrates with Au and Ag NPs for quantitative analysis. *Materials (Basel).* **10**, (2017).
378. Lee, C. H., Tian, L. & Singamaneni, S. Paper-based SERS swab for rapid trace detection on real-world surfaces. *ACS Appl. Mater. Interfaces* **2**, 3429–3435 (2010).
379. KONG, J. & YU, S. Fourier Transform Infrared Spectroscopic Analysis of Protein Secondary Structures. *Acta Biochim. Biophys. Sin. (Shanghai).* **39**, 549–559 (2007).
380. Rygula, A. *et al.* Raman spectroscopy of proteins: a review. *J. Raman Spectrosc.* **44**, 1061–1076 (2013).
381. Marchant, A. L. Experimental and theoretical studies of surface and volume changes in dielectrics induced by long-pulse RF CO 2 laser irradiation by. **c**, (2012).
382. Muzyka, K. & Xu, G. Laser-Induced Graphene in Facts, Numbers, and Notes in View of Electroanalytical Applications: A Review. *Electroanalysis* **33**, 1–17 (2021).
383. Wang, L., Wang, Z., Bakhtiyari, A. N. & Zheng, H. A comparative study of laser-induced graphene by CO2 infrared laser and 355 nm ultraviolet (UV) laser. *Micromachines* **11**, 1–9 (2020).
384. Santos, N. F. *et al.* IR and UV Laser-Induced Graphene: Application as Dopamine Electrochemical Sensors. *Adv. Mater. Technol.* **6**, 1–13 (2021).
385. Xu, J., Wang, Y. & Hu, S. Nanocomposites of graphene and graphene oxides: Synthesis, molecular functionalization and application in electrochemical sensors and biosensors. A review. *Microchim. Acta* **184**, (2017).
386. Żelechowska, K., Kondratowicz, I. & Sadowski, W. 3D porous graphene-based structures - synthesis and applications. in *Carbon nanotechnology* 210–241 (2014).
387. Ma, Y. & Chen, Y. Three-dimensional graphene networks : synthesis, properties and applications. *Natl. Sci. Rev.* **2**, 40–53 (2015).
388. Yang, Y. *et al.* Surface Morphology and Raman Analysis of the Polyimide Film Aged Under Bipolar Pulse Voltage. 1–6 (2013) doi:10.1002/pen.
389. Carvalho, A. F. *et al.* Simultaneous CVD synthesis of graphene-diamond hybrid films. *Carbon N. Y.* **98**, 99–105 (2016).
390. Rao, R. *et al.* Effects of layer stacking on the combination raman modes in graphene. *ACS Nano* **5**, 1594–1599 (2011).
391. Ferrari, A. C. & Basko, D. M. Raman spectroscopy as a versatile tool for studying the properties

of graphene. *Nat. Nanotechnol.* **8**, 235–246 (2013).
392. Li, W., Tan, C., Lowe, M. A., Abruña, H. D. & Ralph, D. C. Electrochemistry of individual monolayer graphene sheets. *ACS Nano* **5**, 2264–2270 (2011).
393. Fang, Y. *et al.* A bio-enabled maximally mild layer-by-layer Kapton surface modification approach for the fabrication of all-inkjet-printed flexible electronic devices. *Nat. Publ. Gr.* 1–9 (2016) doi:10.1038/srep39909.
394. Samsonova, J. V., Cannavan, A. & Elliott, C. T. A Critical Review of Screening Methods for the Detection of Chloramphenicol, Thiamphenicol, and Florfenicol Residues in Foodstuffs. *Crit. Rev. Anal. Chem.* **42**, 50–78 (2012).
395. Zhou, B. *et al.* A new sensitive method for the detection of chloramphenicol in food using time-resolved fluoroimmunoassay. *Eur. Food Res. Technol.* **240**, 619–625 (2015).
396. Ashwin, H. M. *et al.* Development and validation of screening and confirmatory methods for the detection of chloramphenicol and chloramphenicol glucuronide using SPR biosensor and liquid chromatography-tandem mass spectrometry. *Anal. Chim. Acta* **529**, 103–108 (2005).
397. Abnous, K., Danesh, N. M., Ramezani, M., Emrani, A. S. & Taghdisi, S. M. A novel colorimetric sandwich aptasensor based on an indirect competitive enzyme-free method for ultrasensitive detection of chloramphenicol. *Biosens. Bioelectron.* **78**, 80–86 (2016).
398. Xia, X. *et al.* A highly sensitive europium nanoparticle-based lateral flow immunoassay for detection of chloramphenicol residue. *Anal. Bioanal. Chem.* **405**, 7541–7544 (2013).
399. Mostafiz, B., Fotouhi, L. & Dorraji, P. S. An electrochemical sensor based on an Eriochrome Black T polymer and deep eutectic solvent for the simultaneous determination of omeprazole and lansoprazole. *Anal. Methods* **12**, 4072–4079 (2020).
400. Tavares, A. P. M. & Sales, M. G. F. Novel electro-polymerized protein-imprinted materials using Eriochrome black T: Application to BSA sensing. *Electrochim. Acta* **262**, 214–225 (2018).
401. Zhao, Q., Jamal, R., Zhang, L., Wang, M. & Abdiryim, T. The structure and properties of PEDOT synthesized by template-free solution method. *Nanoscale Res. Lett.* **9**, 557 (2014).
402. Cardoso, A. R., de Sá, M. H. & Sales, M. G. F. An impedimetric molecularly-imprinted biosensor for Interleukin-1β determination, prepared by in-situ electropolymerization on carbon screen-printed electrodes. *Bioelectrochemistry* **130**, 107287 (2019).
403. Hughes, G. *et al.* Recent advances in the fabrication and application of screen-printed electrochemical (bio)sensors based on carbon materials for biomedical, agri-food and environmental analyses. *Biosensors* **6**, (2016).
404. Da Silva, J. L., Beluomini, M. A. & Ramos Stradiotto, N. Cathodic electrochemical determination of furfural in sugarcane bagasse using an electrode modified with nickel nanoparticles. *Anal. Methods* **9**, 826–834 (2017).
405. Vu, V.-P. *et al.* Possible detection of antibiotic residue using molecularly imprinted polyaniline-based sensor. *Vietnam J. Chem.* **57**, 328–333 (2019).
406. Roushani, M., Rahmati, Z., Hoseini, S. J. & Hashemi Fath, R. Impedimetric ultrasensitive detection of chloramphenicol based on aptamer MIP using a glassy carbon electrode modified by 3-ampy-RGO and silver nanoparticle. *Colloids Surfaces B Biointerfaces* **183**, (2019).
407. Edanõl, Y. D. G., Ferrer, M. R. R., Raguindin, R. K. M. & Arco, S. D. Potentiometric determination of a regulated veterinary drug via MIP-modified electrode. *ACM Int. Conf. Proceeding Ser.* 71–74 (2016) doi:10.1145/3022702.3022723.
408. Yang, G. & Zhao, F. Electrochemical sensor for chloramphenicol based on novel multiwalled carbon nanotubes@molecularly imprinted polymer. *Biosens. Bioelectron.* **64**, 416–422 (2015).
409. Längin, A., Alexy, R., König, A. & Kümmerer, K. Deactivation and transformation products in biodegradability testing of ß-lactams amoxicillin and piperacillin. *Chemosphere* **75**, 347–354 (2009).
410. Elizalde-Velázquez, A. *et al.* Amoxicillin in the Aquatic Environment, Its Fate and Environmental Risk. in *Environmental Health Risk - Hazardous Factors to Living Species - Intech* 247–267 (2016). doi:http://dx.doi.org/10.5772/57353.

411. Romero, J., Gloria, C. & Navarrete, P. Antibiotics in Aquaculture – Use, Abuse and Alternatives. in *Health and Environment in Aquaculture* (InTech, 2012). doi:10.5772/28157.
412. Dawood, M. A. O. & Koshio, S. Vitamin C supplementation to optimize growth, health and stress resistance in aquatic animals. *Rev. Aquac.* **10**, 334–350 (2018).
413. Li, S., Cowey, C. B. & Woo, P. T. K. Effects of dietary ascorbic acid deficiency on Cryptobia salmositica infection and on vaccination against cryptobiosis in Oncorhynchus mykiss. *Dis. Aquat. Organ.* **24**, 11–16 (1996).
414. Mohammed, A. & Ahmed, M. Effects of Different Dietary Levels of Vitamin C (Ascorbic Acid) On Growth Performance of Tilapia Fry (Oreochromis niloticus). **2017**, 10–12 (2017).
415. Bard, A. & Faulkner, L. *Electrochemical methods, fundamentals and applications*. *Journal of Chemical Education* vol. 60 (1983).
416. Zoski, C. G. *Handbook of Electrochemistry*. (2016).
417. Carneiro, M. C. C. G., Moreira, F. T. C., Dutra, R. A. F., Fernandes, R. & Sales, M. G. F. Homemade 3-carbon electrode system for electrochemical sensing: Application to microRNA detection. *Microchem. J.* **138**, 35–44 (2018).
418. Ağın, F. Electrochemical Determination of Amoxicillin on a Poly(Acridine Orange) Modified Glassy Carbon Electrode. *Anal. Lett.* **49**, 1366–1378 (2016).
419. Fouladgar, M. *et al.* Voltammetric determination of amoxicillin at the electrochemical sensor ferrocenedicarboxylic acid multi wall carbon nanotubes paste electrode. *Int. J. Electrochem. Sci.* **6**, 1355–1366 (2011).
420. Ayankojo, A. G., Reut, J., Öpik, A., Furchner, A. & Syritski, V. Hybrid molecularly imprinted polymer for amoxicillin detection. *Biosens. Bioelectron.* **118**, 102–107 (2018).
421. Jamieson, O. *et al.* Screen printed electrode based detection systems for the antibiotic amoxicillin in aqueous samples utilising molecularly imprinted polymers as synthetic receptors. *Chemosensors* **8**, 5 (2020).
422. Ayankojo, A. G., Reut, J., Boroznjak, R., Öpik, A. & Syritski, V. Molecularly imprinted poly(meta-phenylenediamine) based QCM sensor for detecting Amoxicillin. *Sensors Actuators B Chem.* **258**, 766–774 (2018).
423. Ferrari, A. C. Raman spectroscopy of graphene and graphite: Disorder, electron-phonon coupling, doping and nonadiabatic effects. *Solid State Commun.* **143**, 47–57 (2007).
424. Ferrari, A. C. *et al.* Raman Spectrum of Graphene and Graphene Layers. *Phys. Rev. Lett.* **97**, 187401 (2006).
425. Xu, B. *et al.* Functional solid additive modified PEDOT:PSS as an anode buffer layer for enhanced photovoltaic performance and stability in polymer solar cells. *Sci. Rep.* **7**, 45079 (2017).
426. Yang, G. & Zhao, F. Molecularly imprinted polymer grown on multiwalled carbon nanotube surface for the sensitive electrochemical determination of amoxicillin. *Electrochim. Acta* **174**, 33–40 (2015).
427. Zeinali, S., Khoshsafar, H., Rezaei, M. & Bagheri, H. Fabrication of a selective and sensitive electrochemical sensor modified with magnetic molecularly imprinted polymer for amoxicillin. *Anal. Bioanal. Chem. Res.* **5**, 195–204 (2018).
428. Güney, S., Arslan, T., Yanık, S. & Güney, O. An Electrochemical Sensing Platform Based on Graphene Oxide and Molecularly Imprinted Polymer Modified Electrode for Selective Detection of Amoxicillin. *Electroanalysis* **33**, 46–56 (2021).
429. López, R., Khan, S., Wong, A., Sotomayor, M. del P. T. & Picasso, G. Development of a New Electrochemical Sensor Based on Mag-MIP Selective Toward Amoxicillin in Different Samples. *Front. Chem.* **9**, (2021).
430. Cerqueira, S. M. V., Fernandes, R., Moreira, F. T. C. & Sales, M. G. F. Development of an electrochemical biosensor for Galectin-3 detection in point-of-care. *Microchem. J.* **164**, (2021).
431. Cherian, A. R., Benny, L., Varghese, A., John, N. S. & Hegde, G. Molecularly Imprinted Scaffold Based on poly (3-aminobenzoic acid) for Electrochemical Sensing of Vitamin B 6 . *J. Electrochem. Soc.* **168**, 077512 (2021).

432. Serrano, V. M., Cardoso, A. R., Diniz, M. & Sales, M. G. F. In-situ production of Histamine-imprinted polymeric materials for electrochemical monitoring of fish. *Sensors Actuators, B Chem.* **311**, (2020).
433. Yoon, H. *et al.* A chemically modified laser-induced porous graphene based flexible and ultrasensitive electrochemical biosensor for sweat glucose detection. *Sensors Actuators, B Chem.* **311**, 127866 (2020).
434. Zhu, J. *et al.* Laser-induced graphene non-enzymatic glucose sensors for on-body measurements. *Biosens. Bioelectron.* **193**, 113606 (2021).
435. Dallinger, A., Keller, K., Fitzek, H. & Greco, F. Stretchable and Skin-Conformable Conductors Based on Polyurethane/Laser-Induced Graphene. *ACS Appl. Mater. Interfaces* **12**, 19855–19865 (2020).
436. Francine, L. M., Siervo, A., Araujo, W. R. & Paixão, T. R. L. C. Reagentless fabrication of a porous graphene-like electrochemical device from phenolic paper using laser-scribing. *Carbon N. Y.* **159**, 110–118 (2020).
437. Hui, X., Xuan, X., Kim, J. & Park, J. Y. A highly flexible and selective dopamine sensor based on Pt-Au nanoparticle-modified laser-induced graphene. *Electrochim. Acta* **328**, 135066 (2019).
438. Settu, K., Lai, Y. C. & Liao, C. T. Carbon nanotube modified laser-induced graphene electrode for hydrogen peroxide sensing. *Mater. Lett.* **300**, 130106 (2021).
439. Zanoni, J. *et al.* Dual transduction of h2o2 detection using zno/laser-induced graphene composites. *Chemosensors* **9**, (2021).
440. Zhang, Y. *et al.* Laser-induced Graphene-based Non-enzymatic Sensor for Detection of Hydrogen Peroxide. *Electroanalysis* **31**, 1334–1341 (2019).